~~RL-867~~
RL-985

DISCONTINUITY CHARACTERIZATION IN SHIELDED MICROSTRIP: A THEORETICAL AND EXPERIMENTAL STUDY

by

Lawrence Patrick Dunleavy

A dissertation submitted in partial fulfillment
of the requirements for the degree of
Doctor of Philosophy
(Electrical Engineering)
in The University of Michigan
1988

ABSTRACT

DISCONTINUITY CHARACTERIZATION IN SHIELDED MICROSTRIP: A THEORETICAL AND EXPERIMENTAL STUDY

by
Lawrence Patrick Dunleavy

Chairperson: Pisti B. Katehi

The need for more accurate modeling of microstrip discontinuity structures has become apparent with the advent of Monolithic Microwave Integrated Circuits (MMICs) as well as the push to higher millimeter-wave frequencies. The development of accurate microstrip discontinuity models, based on full-wave analyses, is key to improving circuit simulations and reducing lengthy design cycle costs. In most applications, radiation and electromagnetic interference are avoided by enclosing microstrip circuitry in a shielding cavity (or housing). The effects of the shielding can be significant, even when the top of the cavity is several substrate heights above the circuitry. Shielding effects are not adequately accounted for in the discontinuity models used in most microwave CAD software.

A new integral equation method is described for the full-wave analysis of shielded microstrip discontinuities. The integral equation is derived by an application of the reciprocity theorem and then solved by the method of moments. Two types of circuit excitation are considered: a coaxial excitation method developed here, and the widely used gap generator method. Several numerical experiments are presented that lead to very useful relationships governing the convergence and stability of the method of moments analysis of this problem. Most significantly, an optimum sampling range is defined that provides the most accuracy in the matrix solution.

Numerical and measured results are presented for microstrip effective dielectric constants, and the network parameters of open-end and series gap discontinuities, and two coupled line filters. For the effective dielectric constant, as the size of the shielding cavity is reduced, the difference between the numerical and CAD package results becomes significant. Conversely, for an open-end discontinuity, choosing a smaller shielding cavity extends the frequency range over which the equivalent capacitance is relatively constant. The numerical results are in excellent agreement with measured data obtained using a variation of the thru-short-delay de-embedding technique. A case in point is that of a four resonator coupled line filter. The numerical results accurately predict the filter performance in every way, whereas discrepancies are observed in the CAD model predictions. It is demonstrated that these discrepancies are due to shielding effects.

To my parents and to the memory of my brother Michael

ACKNOWLEDGEMENTS

I have many to thank for helping me along the Ph.D. journey. First I thank my advisor, her constant optimism and good nature greatly eased the difficult times. I also extend my sincere gratitude to the other members of my dissertation committee for their time and their consideration.

There are several other professors whose inspiration and advise have left their mark on my career. Among these are Dr. T.B.A. Senior, Dr. Chen-To Tai (my favorite tennis rival), Dr. Val Liepa, and Dr. Emmett Leith. I also thank Dr. W.A. Fordon and Dr. Jon Soper of Michigan Technological University.

I am indebted to my friends and colleagues who contributed in various ways to this work especially Mlle. Emilie van Deventer, Mr. Tim Peters , Mr. Marcel Tutt, Mr. Mike Dunn, Ms. Jeanette Vecchio, and Mr. Jim Morgan. The insightful conversations held with Dr. Tom Willis, Mr. Norm VandenBerg, and Mr. Tom Livernois helped form some of the ideas presented. I also thank Mr. Jim Schellenberg, Mr. Ed Watkins and Mr. Doug Dunn of Hughes Aircraft Company for their inputs to the experimental part of this work.

Finally, I thank my family. Though they openly feared I would be a professional student for life, my parents, brothers, sisters, and other relatives always gave love, support, and encouragement. For this, I also extend my appreciation to my friends The Buschellmans, The van Deventers, The Heeremas, and The Linquists.

This work was sponsored in part through a Howard Hughes Doctoral Fellowship. Additional support was provided by The National Science Foundation (Contract. No. ECS-8602530) and the Army Research Office (Contract No. DAAL03-87-K-0088).

TABLE OF CONTENTS

CHAPTER

LIST OF FIGURES

Figure

LIST OF TABLES

Table

LIST OF APPENDICES

Appendix

LIST OF SYMBOLS

a = Dimension of cavity along longitudinal (x) direction of microstrip

$\bar{A}^i$ = Magnetic vector potential

$A^{(i)}_{mn}$ = Complex coefficients for series representation for $G^{(i)}_{xx}$

b = Dimension of cavity along transverse (y) direction of microstrip

$B^{(i)}_{mn}$ = Complex coefficients for series representation for $G^{(i)}_{xz}$

c = Dimension of cavity along direction perpendicular to substrate (z-direction)

c'' = Distance from the center of the feed to the top of the cavity ($c'' = c - h_c$)

c_{nq} = Variable multiplier function of n and q used to simplify expressions for magnetic field $\bar{H}_q$ at coaxial aperture

c_{op} = Normalized equivalent capacitance for open end discontinuity

$c^{(i)}_{ymn}$ = Complex coefficients associated with the y-component of the magnetic field $\bar{H}^{(i)}_q$

$c^{(i)}_{zmn}$ = Complex coefficients associated with the z-component of the magnetic field $\bar{H}^{(i)}_q$

d_{1mn} = First denominator function of complex Green's function coefficients

d_{2mn} = Second denominator function of complex Green's function coefficients

$\bar{E}^i$ = Electric field in the i^{th} region of the cavity

$\bar{E}_q$ = Electric field associated with the test current $\bar{J}_q$

E_{qx} = x-component of the electric field due to the test source $\bar{J}_q$ evaluated at the substrate/air interface

$\bar{E}^{tot}$ = Total electric field inside shielding cavity

f = Frequency of operation (Hz)

f = Cut-off frequency for non-evanescent waveguide modes (GHz)

f_{mn} = Numerator function used in expression for Γ_{xx}

$\bar{\bar{G}}^i$ = Dyadic Green's function of i^{th} region

$G_{xx}^{(i)}$ = xx- component of dyadic Green's in region i

$G_{xz}^{(i)}$ = xz- component of dyadic Green's in region i

h = Thickness of microstrip substrate

h_c = z-coordinate of center of coaxial feed

$\bar{H}^i$ = Magnetic field in i^{th} region of cavity

$\bar{H}_q$ = Magnetic field associated with the test current $\bar{J}_q$

H_{q0} = Common variable multiplier function of q used to simplify expressions for magnetic field $\bar{H}_q$ at coaxial aperture.

$\bar{H}_{qt}$ = Projection of magnetic field onto the plane of the feed aperture

$[\mathbf{I}]$ = Unknown current vector comprised of complex coefficients for current

$[\mathbf{I}_d]$ = Unknown current vector for general dual excitation

$[\mathbf{I}_e]$ = Unknown current vector for even excitation

$[\mathbf{I}_o]$ = Unknown current vector for odd excitation

I_p = Complex coefficients current expansion into series of basis functions (= components of I).

$\mathcal{I}_{qmn}$ = Surface integral encountered in the evaluation of E_{qx}

$\bar{J}$ = Electric current distribution in cavity

$\bar{J}_q$ = Test current source (weighting function in method of moments)

$\bar{J}_s$ = Surface current distribution on microstrip conductors

k_i = Complex wave number in region i

k_x = Eigenvalues for the x-variation of the Green's function $(= \frac{n\pi}{a})$

k_y = Eigenvalues for the y-variation of the Green's function $(= \frac{m\pi}{b})$

$k_z^{(i)}$ = Eigenvalues for the z-variation of the Green's function in region i

K = Wave number used in the sinusoidal subsectional expansion of the current (equal to the real part of the wave number in the dielectric region)

l_x = Length of each subsection

L_1 = Length of input uniform line section section for series gap or filter

L_{eff} = Effective length extension for open end discontinuity

L_{in} = Length of the microstrip line in inches (for an open end or thru line).

L' = Normalized length of the microstip line ($=L_{in}/\lambda_d$)

L_{mn} = mn^{th} term of series used to compute $LN(n)$

$LN(n)$ = Storage vector used in computation of the impedance matrix

M_{mn} = mn^{th} term of series used to compute $MN(n)$

$\mathcal{M}^i_{mn}$ = Integrand for numerical integration performed to compute M_{mn}

$MN(n)$ = Storage vector used in computation of the impedance matrix

$\bar{M}_s$ = Magnetic frill current existing over aperture of coaxial feed

$\bar{M}_{sl}$ = Magnetic frill current existing over aperture of coaxial feed on left, for case of dual excitation

$\bar{M}_{sr}$ = Magnetic frill current existing over aperture of coaxial feed on right, for case of dual excitation

$\bar{M}_\phi$ = Component of magnetic frill current in the $\hat{\phi}$ direction

$MSTOP$ = Index for truncation of m-series used to compute $LN(n)$, and $MN(n)$

$\bar{M}_s$ = Equivalent magnetic surface current distribution at coaxial aperture

$NSTOP$ = Index for truncation of n-series used to compute Z_{qp} and V_q

N_s = Number of subsections that strip is divided

N_x = Number of samples per dielectric wavelength ($= 1/l_x$)

$\bar{r}$ = Position vector anywhere inside cavity

$\bar{r}'$ = Position vector of assumed infinitesimal current source

r_a = Radius of inner conductor of coaxial feed

r_b = Radius of outer conductor of coaxial feed

RC = Reciprocal matrix condition number

R_{1n} = Argument of first Sinc function of expression for $\mathcal{I}_{qmn}$ ($= \left[\frac{1}{2}(k_x + K)l_x\right]$)

R_{2n} = Argument of second Sinc function of expression for $\mathcal{I}_{qmn}$ ($= \left[\frac{1}{2}(k_x - K)l_x\right]$)

s = Estimated standard deviation (used for experimental data analysis)

S_{ij} = Scattering parameters ($i, j = 1, 2$)

S_f = Surface of coaxial aperture

$S_f^{(i)}$ = Portion of coaxial aperture surface lying in region i

S_{lf} = Surface of coaxial aperture for feed on left hand side ($x = 0$ side) of cavity

S_q = Surface of the q^{th} strip subsection

S_{rf} = Surface of coaxial aperture for feed on right hand side ($x = a$ side) of cavity

S_{strip} = Surface of conducting strip

SWR = Standing wave ratio on microstrip line

$\tan \delta_d$ = Loss tangent of substrate material ($= \frac{\sigma}{\omega \epsilon_{r1} \epsilon_0}$)

V = Volume of shielding cavity

V_0 = Complex voltage present in the coaxial line at the feeding point

[V] = Excitation vector used in method of moments solution

$[\mathbf{V_l}]$ = Excitation vector associated with left hand feed

$[\mathbf{V_r}]$ = Excitation vector associated with right hand feed

$[\mathbf{V}_d]$ = Combined excitation vector for dual excitation

$[\mathbf{V}_e]$ = Even excitation vector

$[\mathbf{V}_o]$ = Odd excitation vector

$V_q = q^{th}$ element of the excitation vector

$V_{ql} = q^{th}$ element of the excitation vector corresponding to left hand feed for case of dual excitation

$V_{qr} = q^{th}$ element of the excitation vector corresponding to right hand feed for case of dual excitation

W = Width of microstrip line

x_p = Position vector giving x-coordinate of the p^{th} subsection

Y_0 = y-coordinate of the center of the strip with respect to the origin

Y_c = y-coordinate of center of coaxial feed

y_{ij} = Normalized admittance parameters $(i, j = 1, 2)$

$z(x)$= Input impedance at position x looking toward the discontinuity

z_{ij} = Normalized impedance parameters $(i, j = 1, 2)$

[Z]= Impedance matrix used in method of moments solution

Z_{qp} = The $q - p$ element of the impedance matrix

α_g = Loss factor of microstrip transmission line

α_p = Subsectional sinusoidal basis functions used for series expansion of current in the longitudinal (x) direction

β_g = Phase constant of microstrip transmission line

γ_g = Complex propagation constant of microstrip transmission line

$\bar{\bar{\Gamma}}^i$ = Modified dyadic Green's function in region i

$\Gamma(x)$= Input voltage reflection coefficient at position x looking toward the discontinuity

Γ_{xx} = xx-component of modified dyadic Green's function in either region evaluated at substrate/air interface ($z = h$)

ϵ_0 = Free space permittivity ($= 8.854 \times 10^{-12}$ F/cm)

ϵ_i = Complex permittivity of material in i^{th} region of cavity

ϵ_r^* = Complex relative dielectric constant of substrate material ($= \frac{\epsilon_i}{\epsilon_0}$)

ϵ_{r1} = Real part of ϵ_r^*

ζ_q = Variable multiplier used in expression for $\mathcal{I}_{qmn}$

θ_{op}= Angle of reflection coefficient for open-end discontinuity

λ_0 = Wavelength in air ($\epsilon_r = 1$)

λ_d = Wavelength in dielectric ($\epsilon_r = \epsilon_{r1}$)

λ_g = Microstrip wavelength ($\epsilon_r = \epsilon_{eff}$)

μ_i = Permeability of material in i^{th} region of cavity

μ_0 = Free space permeability ($= 4\pi \times 10^{-7}$ H/m)

ρ = Volume charge density in cavity

σ= Conductivity of substrate material

φ_n = Variable multiplier for complex Green's function coefficients

ψ = Function describing variation of microstrip current in the transverse(y) direction

ω = Radian frequency ($= 2\pi f$)

CHAPTER I

INTRODUCTION

1.1 Motivation

Millimeter-wave integrated circuits are important for a variety of scientific and military applications, and a wide range of solid state circuitry has been developed in both hybrid and monolithic form. However, the inability to accurately predict the electrical characteristics of various circuit components is a serious barrier to the widespread and cost effective application of these technologies. In fact, even at microwave frequencies, computer simulations of Monolithic Microwave Integrated Circuit (MMIC) components are often inadequate leading to lengthy design cycles with many costly circuit design iterations. The development of more accurate microstrip discontinuity models, based on full-wave analyses, is key to improving microwave and millimeter-wave circuit simulations and reducing lengthy design cycle costs.

Typical microwave and millimeter-wave IC's contain various active and passive elements interconnected by microstrip transmission lines as illustrated in Figure 1.1. In the vicinity of transmission line junctions and other discontinuities, parasitic effects occur that can significantly modify circuit operation. These discontinuity effects can be modeled by the use of lumped equivalent circuits or by

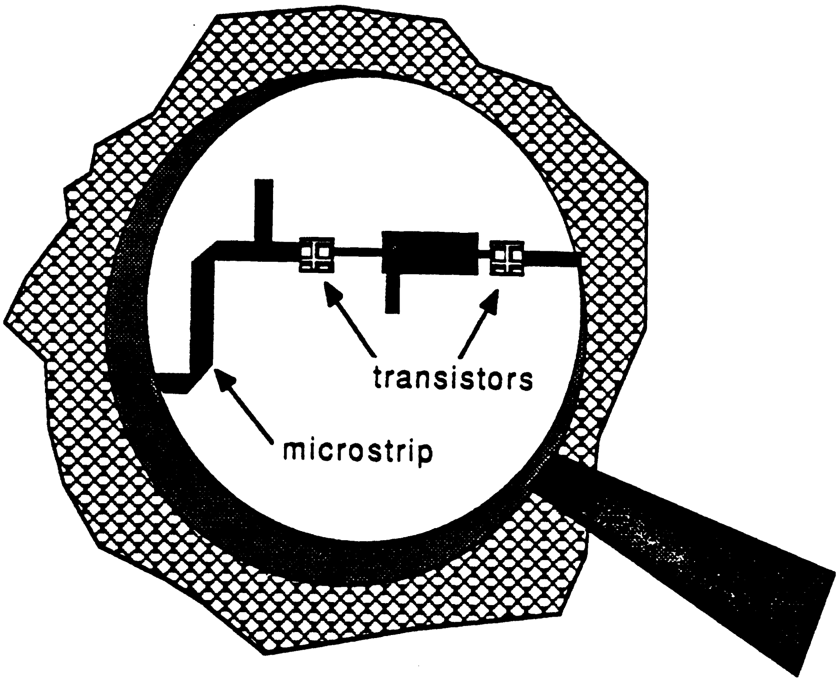

Figure 1.1: Typical millimeter-wave integrated circuit structure. Accurate modeling of discontinuities is key to cost effective designs.

generalized matrix representations; however, the models are only as accurate as the analysis technique used to derive them. Several techniques have been applied, and approximate models exist for most common discontinuities. However, for MMICs and for both hybrid and Monolithic Millimeter-wave Integrated Circuits (M^3ICs), additional theoretical and experimental research is needed to establish the accuracy of these models and to develop improved models where needed.

One area where this is true is for shielded microstrip discontinuities. As shown in Figure 1.2, there are three basic classes of microstrip. In open microstrip the top of the substrate is left open to the air. In this case, surface waves and radiation from circuit elements is unavoidable. In covered microstrip, a conducting cover is present, but no side walls are present, and in shielded microstrip the circuitry is enclosed in a rectangular waveguide.

This last category, shielded microstrip, is the most common for practical applications. In fact, usually the microstrip circuit is completely enclosed in a shielding cavity (or housing) as shown in Figure 1.3. This prevents radiation and electromagnetic interference and it also supresses surface wave modes.

The effect of the shielding on discontinuity behavior can be significant, and requires accurate modeling, at high frequencies. There are two main conditions where this is true. The first occurs when the frequency approaches or is above the cutoff frequency above which higher order modes can propagate within the shielded structure. The second occurs when the metal enclosure is physically close to the circuitry. A full-wave analysis is required to accurately model shielding effects. These effects are not adequately accounted for in the discontinuity models used in most available CAD packages. The theoretical part of this thesis addresses this area.

There is also a great need for experimental data. Published experimental data on microstrip discontinuites is very limited, especially for high microwave (above X-band) and millimeter-wave frequencies. Such measurements are not trivial, but are essential to verifying the accuracy or at least the reasonableness of theoretical results. This was the motivation for the experimental part of this work.

1.2 Thesis Objectives

The overall goal of this research is to use full-wave analysis techniques combined with experimental data to study some relatively basic shielded microstrip discontinuities. This research is intended to aid in the development of an accurate data base for all kinds of microstrip discontinuities. Such a data base has several uses: 1) existing CAD models can be checked against it to determine their regions of validity, 2) it can be used to develop new and more accurate, C.A.D. models , and 3) it can be used to improve experimental methodology. For example, it can

a) Open microstrip

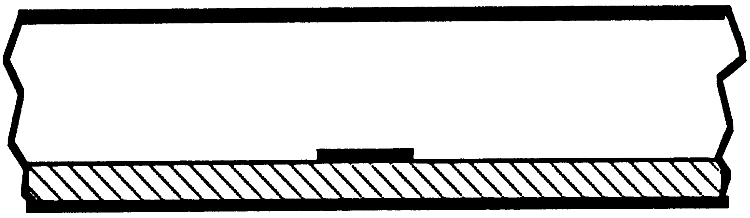

b) Covered microstrip

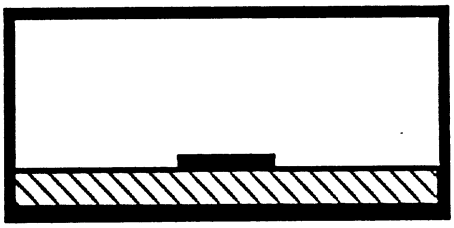

c) Shielded microstrip

Figure 1.2: Three basic classes of microstrip.

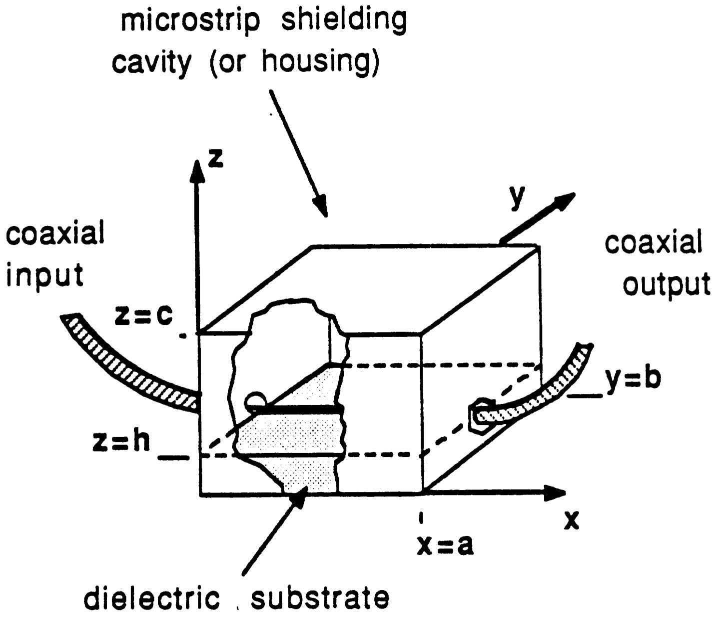

Figure 1.3: Basic geometry for the shielded microstrip cavity problem.

be used to help characterize microstrip standards for measurement calibration and verification.

The specific objectives of the present research may be summarized as follows:

- Develop a new theoretical method for computational analysis of shielded microstrip discontinuities
- Explore the use of a practical excitation mechanism
- Investigate high frequency microstrip measurement techniques
- Conduct an experimental study in close correlation with the theoretical work

The primary objective is to develop an accurate and computer efficient method for full-wave analysis of discontinuities in shielded microstrip. This method is to be demonstrated by obtaining numerical results for practical discontinuity structures for which the thin-strip approximation [1] applies.

Another objective is to investigate ways to use practical circuit excitation mechanisms in the theoretical solution. To date, all full-wave analyses of microstrip discontinuities use either a gap generator excitation method [5,11], or use a cavity resonance technique (without actually exciting the circuit)[8,10] to determine discontinuity parameters. Both of these techniques are purely mathematical tools. The former has no physical basis relative to an actual circuit. The latter is also abstract, since in any practical circuit some form of excitation is present. To derive a more realistically based formulation, the use of a coaxial excitation mechanism is to be explored and compared to the gap generator method.

A final objective is to conduct an experimental study to aid in the verification of the theory. As part of this study, a number of techniques are to be assessed qualitatively as to their suitability for high frequency (X-band and higher) measurements. Limitations on measurement accuracy are also to be addressed.

1.3 Accomplishments

In this thesis, the research objectives outlined above are accomplished as follows. A new method is developed for the analysis of discontinuities in shielded microstrip. In the analysis one of two different types of excitation can be used: the first is a coaxial excitation method, and the second is the gap generator approach discussed above. It is shown that with gap generator excitation, the current is disrupted over the region surrounding it; while with coaxial excitation, the current is undisturbed and uniform along the length of the strip. However, for the evaluation of discontinuity parasitics, the final results appear to be unaffected by the method of excitation. The validity of the thin-strip approximation for the

---

[1] The thin-strip approximation assumes that the width of the conducting strips is small compared to a wavelength.

structures considered in this thesis is also examined.

To demonstrate the method, numerical results are presented for open-end and series gap discontinuities, and a four resonator coupled line filter. These results are compared to other full-wave analyses, to data from *Super Compact* and *Touchstone* [2], and to measurements. The measurements were performed by the author using a variation of the TSD de-embedding technique [44].

The contribution of this thesis is in three areas: theoretical, computational, and experimental. The theoretical contribution is in the derivation of the method of moments solution for the problem of Figure 1.3. This derivation is based on modeling the coaxial feed with a magnetic frill current (Chapter 2). To the author's knowledge, this is the first time that the frill current approach has been applied to the shielded microstrip problem. From a computational point of view, extensive numerical convergence experiments were performed that lead to some surprisingly simple relationships governing the convergence and stability behavior of the method of moments solution for this problem (Chapter 3). Finally, as part of the experimental study, a novel perturbation analysis was applied to study the effect of connection repeatability errors on microstrip de-embedding accuracy (Chapter 4). The experimental results demonstrate the accuracy and usefulness of the theory developed here and also suggest some areas where improvements can be made (Chapter 5).

1.4 Brief Review of Theoretical Approaches

As mentioned above, several approximate techniques exist for microstrip discontinuity analysis. The published literature on this subject is voluminous. However, a few comments are in order before discussing full-wave solutions.

---

[2] *Super Compact* and *Touchstone* are microwave CAD software packages available from Compact Software and EESOF respectively.

1.4.1 Quasi-Static Techniques

Quasi-static techniques are well established and described in standard texts [1]-[3]. With these techniques, equivalent circuits are derived in terms of static capacitances and low frequency inductances. Convenient analytical formulas for discontinuity parasitics are possible, yet their accuracy is questionable for frequencies above a few GHz. Also, most existing models based on these techniques ignore shielding effects.

1.4.2 Planar Waveguide Models

Planar waveguide models provide a frequency dependent solution. In this approach, an equivalent planar waveguide geometry is proposed for the microstrip problem. The transformed problem is then solved using an appropriate analytical technique, such as mode matching [4]. Models derived from this technique are generally considered accurate to higher frequencies than those derived from quasi-static models.

However, the method does not provide an adequate model for shielded microstrip. As discussed in Chapter 5, the higher order modes in shielded microstrip are essentially rectangular waveguide modes. The mode behavior of a planar waveguide is quite different than for rectangular waveguide. Its applicability even for the dominant microstrip mode is questionable, since the dominant mode in shielded microstrip is the result of an infinite summation of evanescent waveguide modes. This is not to say that reasonable predictions are not possible with this method, only that its application for the shielded microstrip problem is not rigorous.

1.4.3 Rigorous Full-Wave Solutions

As described above, for many applications, the limitations of the above two techniques cannot be tolerated, and a more accurate solution is required.

A full-wave solution[3] that meets this requirement was developed by Katehi to treat discontinuites in open microstrip [5,6]. This technique has so far been applied to solve for various discontinuities in open microstrip. The new analytical methodology presented here is an extension of the approach of Katehi to shielded microstrip configurations.

While rigorous solutions to shielded discontinuities have been advanced by others, their is a need for further research in this area. The most extensive work has been performed by Jansen et al. [7]-[9]. Although reasonable results have been demonstrated for several microstrip structures, there has been little accompanying experimental verification, and only limited comparisons to other rigorous numerical solutions. The primary reasons for this have most likely been the difficulties of performing the measurements, as discussed herein, and the existence of only a few other rigorous solutions ([10]-[12]). Further, the only published results from the other rigorous solutions that the author is aware of is for the open-end discontinuity.

1.5 Description of Theoretical Methods

The theoretical method developed here is addressed to the shielded microstrip geometry shown in Figure 1.3. The shielding box forms a rectangular cavity, which -for most practical uses- is cutoff for the highest frequency of operation. That is, the cavity dimensions are usually such that the coupling of microstrip

---

[3] A full-wave solution, refers to the application of a rigorous electromagnetic analysis to the microstrip geometry, making as few assumptions as possible.

modes into higher order waveguide modes is avoided. However, as far as the the current distribution is concerned, the solution presented here is accurate whether the cavity is cutoff or not. Above this cutoff frequency the onset of higher order modes distort the current distribution and the definition of circuit behavior in the usual way, by a transmission line model, becomes ambiguous.

The theoretical method is based on Galerkin's implementation of the method of moments. A flow chart illustrating the method is shown in Figure 1.4. First, the required matrix equation is derived. In this derivation, the coaxial feed is represented by an equivalent magnetic current source. The reciprocity theorem is then applied to establish an integral equation that relates this magnetic current source and the electric current on the conducting strips to the electromagnetic fields inside the cavity. By expanding the electric current into a series of sinusoidal subsectional basis functions, the integral equation is transformed into a matrix equation. In a similar way, the reciprocity theorem is applied for the case of gap generator, and an identical form results for the elements of the impedance matrix.

Next, the Green's function is derived and used to evaluate the electric and magnetic fields within the cavity. The Green's function is derived by applying boundary conditions to the problem of Figure 1.3 with the conducting strips replaced by an infinitesimal current source on the substrate/air interface. This is a common approach in solving boundary conditions of this type [16].

Finally, the matrix equation is solved to compute the current distribution. Based on the current, either an equivalent circuit or scattering parameters are derived to characterize the discontinuity being considered.

1.6 Description of Experimental Study

To obtain verification data for the theoretical method of this thesis, an ex-

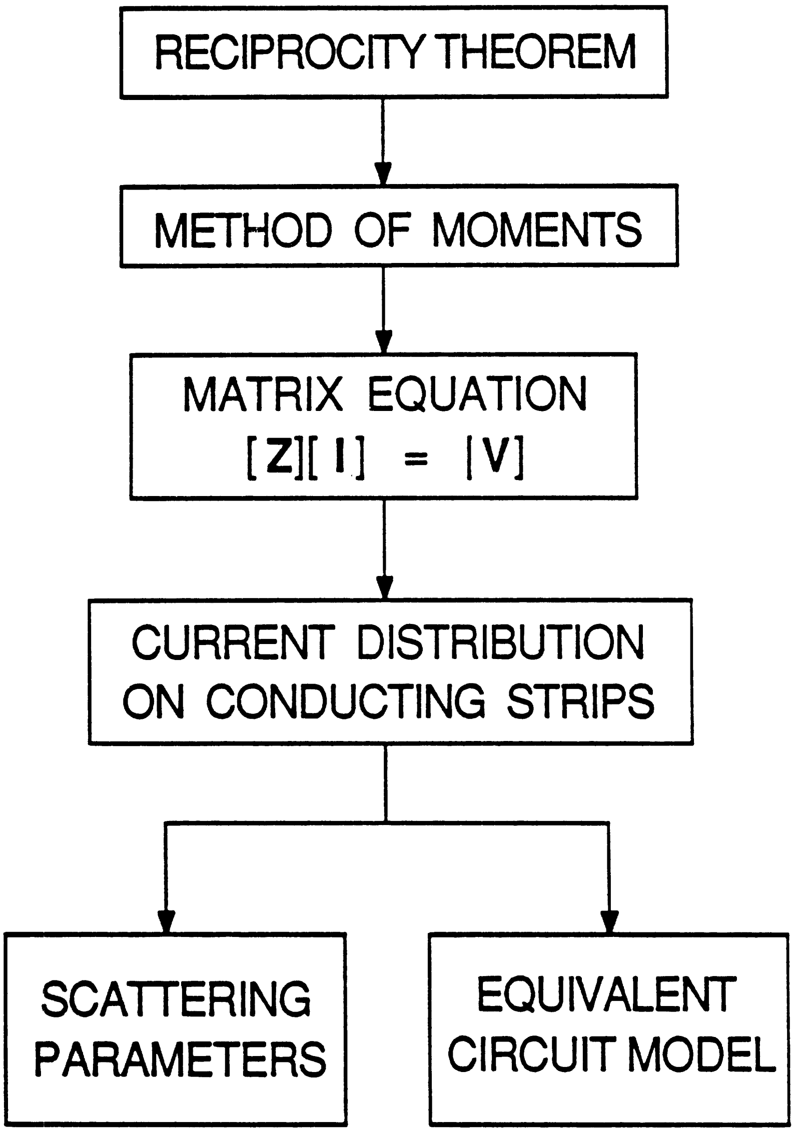

Figure 1.4: Flow chart illustrating theoretical approach for characterizing microstrip discontinuities.

perimental study was conducted in cooperation with Hughes Aircraft Company [4]. As discussed in Chapter 4, the lack of experimental data on microstrip discontinuities is mainly due to the difficulties with removing test fixture parasitics from the measurements (called de-embedding), and the non-repeatability of microstrip connections. To address these issues, a study of de-embedding techniques was conducted, from which it has been concluded that the most suitable technique for the measurements of this thesis is the thru-short-delay (TSD) method. Also, a connection repeatability study was carried out [14,15], and the results were used to decide on how to best implement TSD de-embedding, and they were used to approximate the associated uncertainty in de-embedding accuracy. S-parameter measurements were then obtained for an open-end discontinuity, three series gap discontinuities with different gap widths, and two coupled line band pass filter structures.

---

[4] Hughes Aircraft Company, Microwave Products Division, Torrance, California.

CHAPTER II

THEORETICAL METHODOLOGY

2.1 Assumptions

In this solution, a few simplifying assumptions are made to reduce unnecessary complexity, and excessive computer time. Throughout the analysis, it is assumed that the width of the conducting strips is small compared to the microstrip wavelength λ_g. In this case, unidirectional currents may be assumed with negligible loss in accuracy. While substrate losses are accounted for, it is assumed that the strip conductors and the walls of the shielding box are lossless, and that the strip thickness is negligible. For the computation of two-port network parameters (Section 2.7.2), the strip geometry is assumed to be physically symmetric with respect to the center of the cavity (in both the x and y directions of Figure 1.3). Also, to simplify notation, the assumed time dependence is $e^{j\omega t}$, and it is suppressed throughout the dissertation.

The above assumptions are valid for the high frequency analysis of the microstrip structures of Figure 2.1, provided good conductors are used in the metalized areas. The first three structures of Figure 2.1, the open-end, the series gap and the coupled lines are discontinuity structures. The last one, the thru-line,

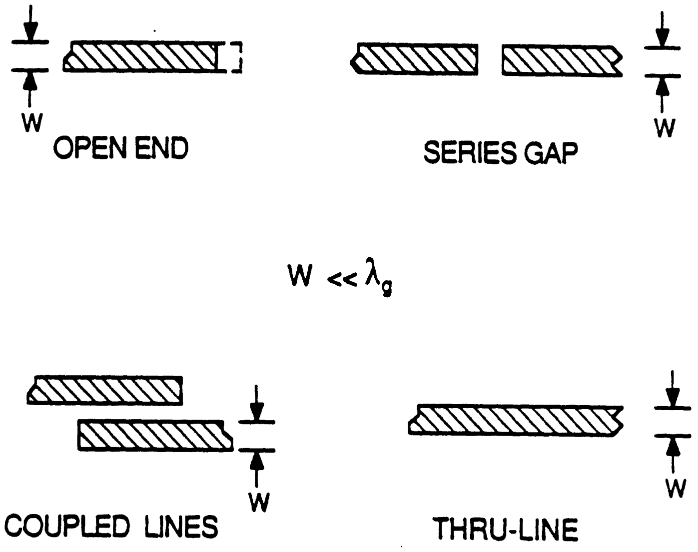

Figure 2.1: Microstrip structures for which thin-strip approximation is valid.

is not. The thru-line is included since it is a useful test case, and it is used to determine the microstrip propagation constant γ_g.

2.2 Method of Moments Formulation

The method of moments is a well established numerical technique for solving electromagnetic problems [17],[18]. A review of the basic approach is given in Appendix A. This section makes use of the method of moments to set up a matrix equation that provides for a computer solution to shielded microstrip discontinuity problems.

For the most part, the theory presented applies to the use of a coaxial excitation mechanism, based on the frill current model. A few comments are made, however, to indicate how the theory differs for the use of a gap generator excitation model. In the matrix equation, the only significant difference is the excitation vector used.

2.2.1 Application of Reciprocity Theorem

Reciprocity Theorem for Coaxial Excitation

Consider the geometry of Figure 1.3. In most cases the coaxial feed, or "launcher", is designed to allow only transverse electromagnetic (TEM) propagation, and the feed's center conductor is small compared to a wavelength. In these cases, the radial electric field will be dominant on the aperture and we can replace the feed by an equivalent magnetic surface current, sometimes called a "frill" current, whose only component is in the $\hat{\phi}$ direction (i.e.$\bar{M}_s = M_\phi \hat{\phi}$) [1]. This method of modeling the feed with a magnetic current source will be discussed further in Section 2.5. The magnetic current source is coupled with the current distribution $\bar{J}_s$ on the conducting strip to produce the total electric field $\bar{E}^{tot}$ and the total magnetic field $\bar{H}^{tot}$ inside the cavity as indicated in Figure 2.3.

We now propose an independent test current source $\bar{J}_q$ existing only on a small subsection of the conducting strip as shown in Figure 2.4. Using the reciprocity theorem, the two sets of current sources are related according to

$$\int\int\int_V \left(\bar{J}_s \cdot \bar{E}_q - \bar{H}_q \cdot \bar{M}_s\right) dv = \int\int\int_V \bar{J}_q \cdot \bar{E}^{tot} dv \tag{2.1}$$

where the volume V is the interior of the cavity.

Since $\bar{J}_q$ is x-directed and zero everywhere except over one subsection of the conducting strip, the right hand side of (2.1) reduces to

$$\int\int\int_V \bar{J}_q \cdot \bar{E}^{tot} dv = \int\int_{S_q} \left|\bar{J}_q\right| E_x^{tot}(z = h) ds = 0 \tag{2.2}$$

---

[1] $\hat{\phi}$ refers to the cylindrical coordinate referenced to the center of the feeding aperture (see Figure 2.2.)

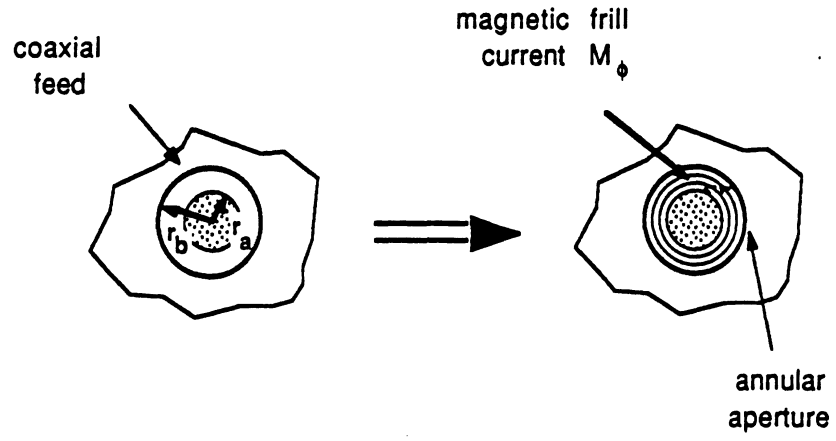

Figure 2.2: Representation of coaxial feed by a circular aperture with magnetic frill current M_ϕ.

where S_q is the surface of an arbitrary subsection and $E_x^{tot}(z = h)$ is the x-component of the total electric field which must vanish on the surface of the conductors ($z = h$) since they are assumed to be perfectly conducting.

Reducing the remaining volume integrals in (2.1) to surface integrals results in

$$\int\int_{S_{strip}} \bar{E}_q(z = h) \cdot \bar{J}_s ds = \int\int_{S_f} \bar{H}_q(x = 0) \cdot \bar{M}_s ds \tag{2.3}$$

where S_{strip} is the surface of the conducting strip and S_f is the surface of the coaxial aperture. Note that this equation is not explicitly in the form of the operator equation of (A.1). This is because in using the reciprocity theorem formulation we have inherently placed it in the inner product form of (A.3).

Reciprocity Theorem for Gap Generator Excitation

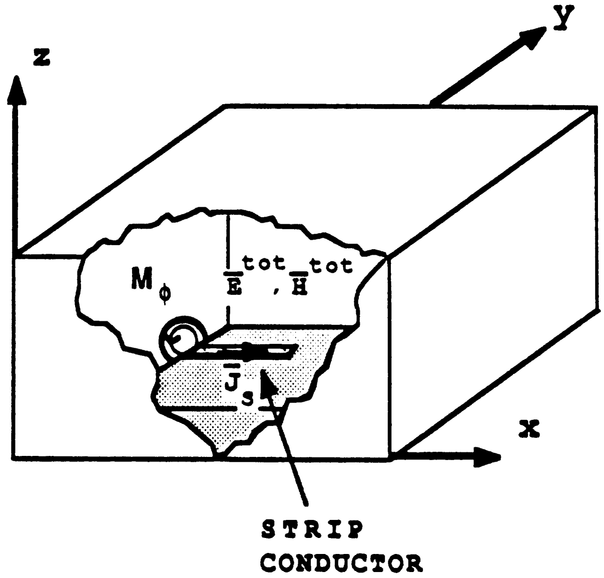

Figure 2.3: Total fields $\bar{E}^{tot}$, $\bar{H}^{tot}$ inside cavity are produced by magnetic current source M_ϕ at aperture and electric current distribution $\bar{J}_s$ on the conducting strip.

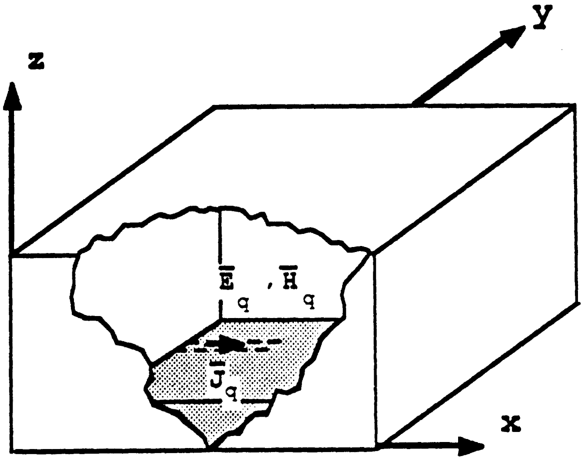

Figure 2.4: Test current $\bar{J}_q$ on conducting strip and associated fields $\bar{E}_q$, $\bar{H}_q$ inside the cavity.

The formulation for the case of gap generator excitation can also be derived from reciprocity theorem. In this case, it is assumed that E_x is non-zero at one point (x_g) on the strip, between two subsections. Setting $\bar{M}_s = 0$ in 2.1, and reducing the resulting volume integrals to surface integrals yields

$$\int\int_{S_{strip}} \bar{E}_q(z=h)\cdot\bar{J}_s ds = \int\int_{S_q} \left|\bar{J}_q\right| E_x^{tot}(z=h) ds \tag{2.4}$$

Since $E_x = 0$ everywhere except x_g, the right hand side of 2.4 vanishes everywhere except over the the subsectional surface containing x_g. This surface integral we arbitrarily set equal to unity. That is

$$\int\int_{S_q} \left|\bar{J}_q\right| E_x^{tot}(z=h) ds = \begin{cases} 1 & \text{for } q = g \\ 0 & \text{else} \end{cases} \tag{2.5}$$

where g is the index corresponding to the position of the gap generator.

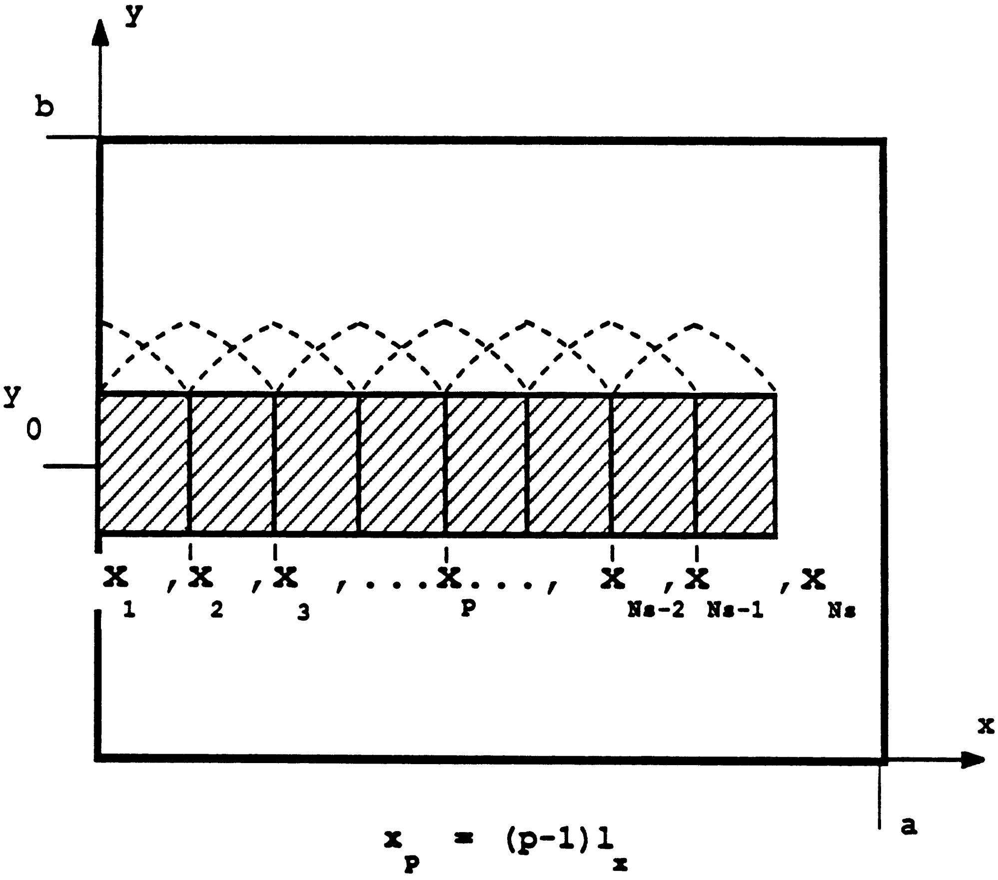

Figure 2.5: Strip geometry for use in basis function expansion of current for the case of an open-ended line.

2.2.2 Expansion of Current with Sinusoidal Basis Functions

In order to solve the integral equation (2.3), the current distribution $\bar{J}_s$ is expanded into a series of orthogonal functions as follows. Consider the strip geometry shown in Figure 2.5, let

$$\bar{J}_s = \psi(y) \sum_{p=1}^{N_s} I_p \alpha_p(x) \hat{x} \tag{2.6}$$

where I_p are unknown current coefficients. The function $\psi(y)$ describes the variation of the current in the transverse direction and is given by

$$\psi(y) = \begin{cases} \dfrac{\frac{2}{\pi W}}{\sqrt{1-\left[\frac{2(y-Y_0)}{W}\right]^2}} & Y_0 - W/2 \leq y \leq Y_0 + W/2 \\ 0 & \text{else} \end{cases} \tag{2.7}$$

This variation was chosen to agree with that derived by Maxwell for the charge density distribution on an isolated conducting strip [20], and it has been used successfully by others to describe the transverse variation of microstrip currents [5,21,22].

The basis functions $\alpha_p(x)$ comprise an orthonormal set and are described by

$$\alpha_p(x) = \begin{cases} \frac{\sin[K(x_{p+1}-x)]}{\sin(Kl_x)} & x_p \leq x \leq x_{p+1} \\ \frac{\sin[K(x-x_{p-1})]}{\sin(Kl_x)} & x_{p-1} \leq x \leq x_p \\ 0 & \text{else} \end{cases} \tag{2.8}$$

for $p \neq 1$, and

$$\alpha_1(x) = \begin{cases} \frac{\sin[K(l_x-x)]}{\sin(Kl_x)} & 0 \leq x \leq l_x \\ 0 & \text{else} \end{cases} \tag{2.9}$$

for $p = 1$, where

$K = \omega\sqrt{\mu_o \epsilon_{r1} \epsilon_0}$ is the real part of the wave number in the dielectric region

W is the width of the microstrip line

Y_0 is the y-coordinate of the center of the strip with respect to the origin in Figure 1.3

x_p is the x-coordinate of the pth subsection $(=(p-1)l_x)$

l_x is the subsection length $(l_x = x_{p+1} - x_p)$.

2.2.3 Transformation of Integral Equation into a Matrix Equation

The integral equation (2.3) can now be transformed into a matrix equation by substituting the expansion of (2.6) for the current $\bar{J}_s$. This results in the following:

$$\sum_{p=1}^{N_s} \left[\int\int_{S_p} \bar{E}_q(z=h) \cdot \psi(y)\, \alpha_p(x)\, \hat{x} ds \right] I_p = \int\int_{S_f} \bar{H}_q \cdot \bar{M}_s ds \qquad (2.10)$$

where S_p is the surface area of the p^{th} subsection, and N_s is the number of sections that the strip is divided into for computation.

We may now express (2.10) as

$$[\mathbf{Z}]\,[\mathbf{I}] = [\mathbf{V}] \; . \qquad (2.11)$$

In the above, $[\mathbf{Z}]$ is called the impedance matrix, and has the form

$$[\mathbf{Z}] = \begin{bmatrix} Z_{11} & Z_{12} & \cdots & Z_{1N_s} \\ Z_{21} & Z_{22} & & Z_{2N_s} \\ \vdots & & \ddots & \vdots \\ Z_{N_s1} & Z_{N_s2} & \cdots & Z_{N_sN_s} \end{bmatrix} \qquad (2.12)$$

$[\mathbf{V}]$ is called the excitation vector and may be expressed as

$$[\mathbf{V}] = \begin{bmatrix} V_1 & V_2 & \cdots & V_{N_s} \end{bmatrix}^T . \qquad (2.13)$$

$[\mathbf{I}]$ is the current vector comprised of the unknown current coefficients as follows:

$$[\mathbf{I}] = \begin{bmatrix} I_1 & I_2 & \cdots & I_{N_s} \end{bmatrix}^T . \qquad (2.14)$$

The individual elements of the impedance matrix are given by

$$Z_{qp} = \int \int_{S_p} \bar{E}_q(z = h) \cdot \psi(y) \, \alpha_p(x) \, \hat{x} ds \, . \qquad (2.15)$$

The elements of the excitation vector (coaxial excitation) are given by

$$V_q = \int \int_{S_f} \bar{H}_q \cdot \bar{M}_s ds \, . \qquad (2.16)$$

We can now solve for the current vector by matrix inversion and multiplication according to

$$[\mathrm{I}] = [\mathrm{Z}]^{-1} [\mathrm{V}] \, . \qquad (2.17)$$

For gap generator excitation, the impedance matrix elements are also given by (2.15); however, the elements of the excitation vector are given by the right hand side of (2.5).

2.3 Derivation of the Green's Function

To compute the elements of the impedance matrix, we must derive the Green's function associated with the electric and magnetic fields $\bar{E}_q$, $\bar{H}_q$. We will first define the problem geometry and outline the electromagnetic theory to be used. Then, the boundary value problem will be solved for the Green's function.

2.3.1 Geometry and Electromagnetic Theory

The geometry used in the Green's function derivation is shown in Figure 2.6. The cavity is divided into two regions: Region 1 consists of the volume contained within the substrate ($z < h$), while region 2 is the volume above the substrate surface ($z > h$). Notice, as discussed in Section 1.5, the conducting strips have been replaced by an infinitesimal current source $\bar{J}$.

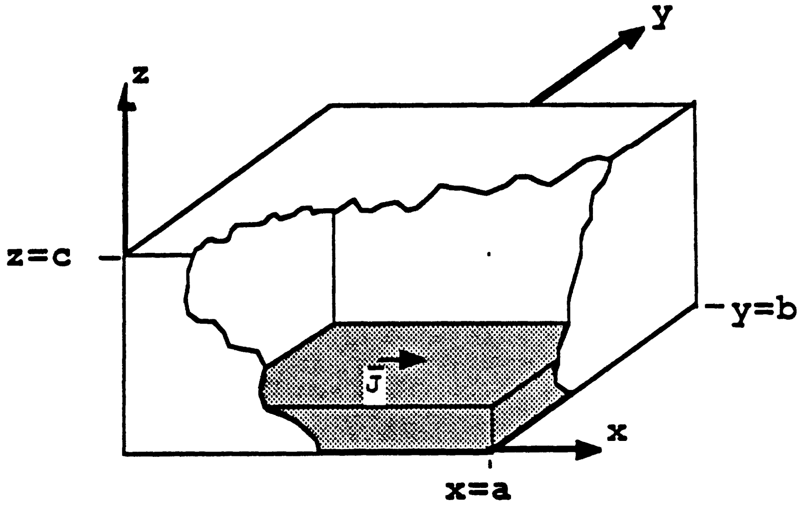

a) Cutaway view

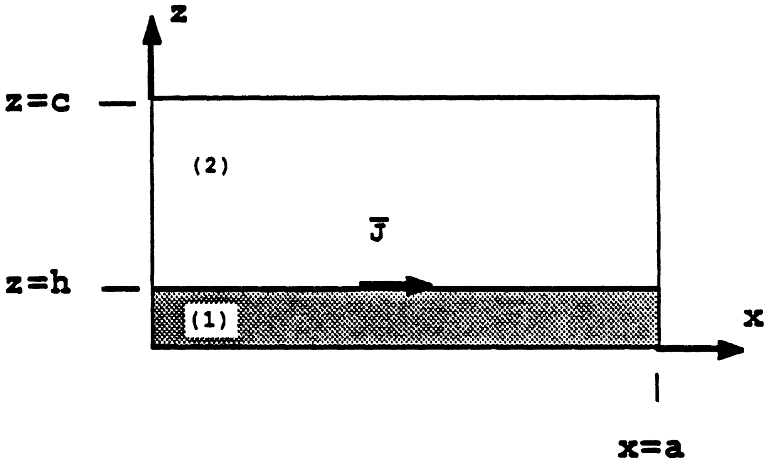

b) Cross section in x-z plane

Figure 2.6: Geometry used in derivation of the Green's function.

The Green's function will be defined as the electric field due to an infinitesimal current source located on the substrate surface of Figure 2.6. After deriving the Green's function, the fields associated with the test source $\bar{J}_q$ will be evaluated by integrating over the surface of the q^{th} subsection.

The test source $\bar{J}_q$ and the associated fields within the cavity ($\bar{E}_q$,$\bar{H}_q$) are related through Maxwell's equations, which may be put in the following form:

$$\begin{aligned}
\bar{\nabla} \times \bar{E}^i &= -j\omega\mu_i\bar{H}^i && (2.18)\\
\bar{\nabla} \times \bar{H}^i &= j\omega\epsilon_i\bar{E}^i + \bar{J} && (2.19)\\
\bar{\nabla} \cdot \bar{J} &= -j\omega\rho && (2.20)\\
\bar{\nabla} \cdot \left(\epsilon_i\bar{E}^i\right) &= \rho && (2.21)\\
\bar{\nabla} \cdot \left(\mu_i\bar{H}^i\right) &= 0\,. && (2.22)
\end{aligned}$$

In the above, $i = 1,2$ indicates that these equations hold in each of the regions respectively. Also, to simplify the notation of this subsection, the subscript q is suppressed with the understanding that all the field quantities discussed here are associated with the test source $\bar{J}_q$ (i.e. $\bar{E}^i = \bar{E}^i_q$ etc.). Further, since it is assumed that both regions are non-magnetic and that region 2 is air, we have

$$\mu_1 = \mu_2 = \mu_0 \qquad (2.23)$$

$$\epsilon_i = \begin{cases} \epsilon_r^*\epsilon_0 & for\ i=1 \\ \epsilon_0 & for\ i=2 \end{cases} \qquad (2.24)$$

where

$$\epsilon_r^* = \epsilon_{r1} - j\frac{\sigma}{\omega\epsilon_0} = \epsilon_{r1}\left(1 - j\tan\delta_d\right)\,. \qquad (2.25)$$

In the above, $\tan\delta_d = \frac{\sigma}{\omega\epsilon_{r1}\epsilon_0}$ is referred to as the dielectric loss tangent of the dielectric region, δ_d is called the dissipation angle.

2.3.2 Solution to Boundary Value Problem for the Green's Function

We now introduce the vector potentials $\bar{A}^i$ such that

$$\bar{H}^i = \frac{1}{\mu_o}\bar{\nabla} \times \bar{A}^i . \tag{2.26}$$

In view of (2.26), the electric field may be written as (B.13)

$$\bar{E}^i = -j\omega\left(1 + \frac{1}{k_i^2}\bar{\nabla}\bar{\nabla}\cdot\right)\bar{A}^i \tag{2.27}$$

where $\bar{A}^i$ satisfies the inhomogeneous wave equation

$$\nabla^2 \bar{A}^i + k_i^2 \bar{A}^i = -\mu_0 \bar{J} . \tag{2.28}$$

The integral form of the electric field is derived in Appendix B, and is given by (B.21)

$$\bar{E}^i = -j\omega\mu_0 \int\int\int_V \left[\left(1 + \frac{1}{k_i^2}\bar{\nabla}\bar{\nabla}\cdot\right)(\bar{\bar{G}}^i)^T\right] \cdot \bar{J} dv' \tag{2.29}$$

where $k_i^2 = \omega^2\mu_0\epsilon_i$, and $\bar{\bar{G}}^i$ is a dyadic Green's function [23] satisfying the following equation

$$\nabla^2 \bar{\bar{G}}^i + k_i^2 \bar{\bar{G}}^i = -\bar{\bar{I}}\delta(\bar{r} - \bar{r}') . \tag{2.30}$$

In (2.30), $\bar{\bar{I}}$ is the unit dyadic given by $\hat{x}\hat{x} + \hat{y}\hat{y} + \hat{z}\hat{z}$.

Because of the air/dielectric interface, a two component vector potential is necessary to satisfy the boundary conditions [24]. Accordingly, let

$$\bar{A}^i = A_x^i\hat{x} + A_z^i\hat{z} . \tag{2.31}$$

From (B.17) $\bar{A}^i$ is related to $\bar{\bar{G}}^i$ by the following volume integral:

$$\bar{A}^i = \mu \int\int\int_V \bar{J} \cdot \bar{\bar{G}}^i dv' . \tag{2.32}$$

$\bar{\bar{G}}^i$ may be expressed in most general form as follows:

$$\bar{\bar{G}}^i = \begin{pmatrix} G_{xx}^i\hat{x}\hat{x} & + & G_{xy}^i\hat{x}\hat{y} & + & G_{xz}^i\hat{x}\hat{z} \\ +\,G_{yx}^i\hat{y}\hat{x} & + & G_{yy}^i\hat{y}\hat{y} & + & G_{yz}^i\hat{y}\hat{z} \\ +\,G_{zx}^i\hat{z}\hat{x} & + & G_{zy}^i\hat{z}\hat{y} & + & G_{zz}^i\hat{z}\hat{z} \end{pmatrix} . \tag{2.33}$$

Assuming an infinitesimal x-directed current source given by

$$\bar{J} = \delta(\bar{r} - \bar{r}')\,\hat{x} \tag{2.34}$$

in (2.32) allows for reducing $\bar{\bar{G}}^i$ to

$$\bar{\bar{G}}^i = G^i_{xx}\hat{x}\hat{x} + G^i_{xz}\hat{x}\hat{z}\,. \tag{2.35}$$

The dyadic components of (2.35) are found by applying appropriate boundary conditions at the walls: $x = 0$, and a ; $y = 0$, and b ; and $z = 0$, and c. As detailed in Appendix C, these components may be expressed as

$$\begin{aligned}
G^{(1)}_{xx} &= \sum_{m=1}^{\infty}\sum_{n=0}^{\infty} A^{(1)}_{mn} \cos k_x x \, \sin k_y y \, \sin k^{(1)}_z z && (2.36)\\
G^{(1)}_{xz} &= \sum_{m=1}^{\infty}\sum_{n=0}^{\infty} B^{(1)}_{mn} \sin k_x x \, \sin k_y y \, \cos k^{(1)}_z z && (2.37)\\
G^{(2)}_{xx} &= \sum_{m=1}^{\infty}\sum_{n=0}^{\infty} A^{(2)}_{mn} \cos k_x x \, \sin k_y y \, \sin k^{(2)}_z (z - c) && (2.38)\\
G^{(2)}_{xz} &= \sum_{m=1}^{\infty}\sum_{n=0}^{\infty} B^{(2)}_{mn} \sin k_x x \, \sin k_y y \, \cos k^{(2)}_z (z - c) && (2.39)
\end{aligned}$$

where

$$\begin{aligned}
k_x &= n\pi/a && (2.40)\\
k_y &= m\pi/b && (2.41)\\
k^{(1)}_z &= \sqrt{k_1^2 - k_x^2 - k_y^2} && (2.42)\\
k^{(2)}_z &= \sqrt{k_0^2 - k_x^2 - k_y^2} && (2.43)\\
k_1 &= \omega\sqrt{\mu_0\epsilon_1} && (2.44)\\
k_0 &= \omega\sqrt{\mu_0\epsilon_0}\,. && (2.45)
\end{aligned}$$

The coefficients $A^{(1)}_{mn}$, $A^{(2)}_{mn}$, $B^{(1)}_{mn}$, and $B^{(2)}_{mn}$ are found by applying boundary conditions at the air/dielectric interface. The details of this analysis can be found in Appendix D. The results are:

$$A^{(1)}_{mn} = \frac{-\varphi_n \cos k_x x' \sin k_y y' \tan k^{(2)}_z (h - c)}{abd_{1mn} \cos k^{(1)}_z h} \tag{2.46}$$

$$A_{mn}^{(2)} = \frac{-\varphi_n \cos k_x x' \sin k_y y' \tan k_z^{(1)} h}{abd_{1mn} \cos k_z^{(2)}(h-c)} \tag{2.47}$$

$$B_{mn}^{(1)} = \frac{-\varphi_n(1-\epsilon_r^*)k_x \cos k_x x' \sin k_y y' \tan k_z^{(1)} h \tan k_z^{(2)}(h-c)}{abd_{1mn}d_{2mn} \cos k_z^{(1)} h} \tag{2.48}$$

$$B_{mn}^{(2)} = \frac{-\varphi_n(1-\epsilon_r^*)k_x \cos k_x x' \sin k_y y' \tan k_z^{(1)} h \tan k_z^{(2)}(h-c)}{abd_{1mn}d_{2mn} \cos k_z^{(2)}(h-c)} \tag{2.49}$$

where

$$\varphi_n = \begin{cases} 2 & \text{for } n = 0 \\ 4 & \text{for } n \neq 0 \end{cases} \tag{2.50}$$

$$d_{1mn} = k_z^{(2)} \tan k_z^{(1)} h - k_z^{(1)} \tan k_z^{(2)}(h-c) \tag{2.51}$$

$$d_{2mn} = k_z^{(2)}\epsilon_r^* \tan k_z^{(2)}(h-c) - k_z^{(1)} \tan k_z^{(1)} h\ . \tag{2.52}$$

Having derived the Green's function, we are now ready to proceed to the formulation for the elements of the impedance matrix and excitation vector.

2.4 Impedance Matrix Formulation

The elements of the impedance matrix are given by (2.15)

$$Z_{qp} = \int\int_{S_p} \bar{E}_q(z=h) \cdot \psi(y')\, \alpha_p(x')\, \hat{x} ds' \tag{2.53}$$

which reduces to

$$Z_{qp} = \int\int_{S_p} E_{qx}(z=h) \psi(y')\, \alpha_p(x')\, ds'\ . \tag{2.54}$$

To evaluate the impedance matrix elements we need only $E_{qx}(z=h)$; that is, the x-component of the electric field due to the test currents $\bar{J}_q$ at the air/dielectric interface.

2.4.1 Evaluation of the Electric Field Due to the Test Currents

Since $\bar{J}_q$ is a surface current distribution, the volume integral in (2.29) is reduced to the following surface integral:

$$\bar{E}_q{}^i = -j\omega\mu_0 \int\int_{S_q} \left[\left(1 + \frac{1}{k_i^2} \bar{\nabla}\bar{\nabla}\cdot \right) (\bar{\bar{G}}^i)^T \right] \cdot \bar{J}_q dx'dy' \tag{2.55}$$

where S_q is the surface of the q^{th} subsection.

For best accuracy in applying the method of moments, the test currents $\bar{J}_q$ are expressed in terms of functions which are identical to the basis functions (Galerkin's method)

$$\bar{J}_q = \psi(y')\alpha_q(x')\hat{x} \tag{2.56}$$

where $\psi(y')$ is given by (2.7) with y replaced by y', and $\alpha_q(x')$ is given by (2.8) and (2.9) with p replaced by q and x replaced by x'.

We now substitute from (2.56) for $\bar{J}_q$ in (2.55) to yield

$$\bar{E}_q{}^i = -j\omega\mu_0 \int\int_{S_q} \left[\left(1 + \frac{1}{k_i^2} \bar{\nabla}\bar{\nabla}\cdot \right) (\bar{\bar{G}}^i)^T \right] \cdot \psi(y')\alpha_q(x')\hat{x} dx'dy' \tag{2.57}$$

Let us define a *modified dyadic Green's function* $\bar{\bar{\Gamma}}^i$ by

$$\bar{\bar{\Gamma}}^i = -j\omega\mu_0 \left[\left(1 + \frac{1}{k_i^2} \bar{\nabla}\bar{\nabla}\cdot \right) (\bar{\bar{G}}^i)^T \right] . \tag{2.58}$$

Then, $\bar{E}_q^i$ can be expressed as

$$\bar{E}_q^i = \int\int_{S_q} \bar{\bar{\Gamma}}^i \cdot \psi(y')\alpha_q(x')\hat{x} dx'dy' . \tag{2.59}$$

The dyadic transpose of (2.35) yields

$$(\bar{\bar{G}}^i)^T = G_{xx}^i \hat{x}\hat{x} + G_{zx}^i \hat{z}\hat{x} . \tag{2.60}$$

When this expression is substituted in (2.58) and the divergence and gradient operations are performed we can express $\bar{\bar{\Gamma}}^i$ as (see Appendix E, (E.3))

$$\bar{\bar{\Gamma}}^i = \Gamma_{xx}^i \hat{x}\hat{x} + \Gamma_{yx}^i \hat{y}\hat{x} + \Gamma_{zx}^i \hat{z}\hat{x} \tag{2.61}$$

where

$$\Gamma^i_{xx} = G^i_{xx} + \frac{1}{k_i^2}\frac{\partial}{\partial x}\left(\frac{\partial G^i_{xx}}{\partial x} + \frac{\partial G^i_{xz}}{\partial z}\right) \tag{2.62}$$

$$\Gamma^i_{yx} = \frac{1}{k_i^2}\frac{\partial}{\partial y}\left(\frac{\partial G^i_{xx}}{\partial x} + \frac{\partial G^i_{xz}}{\partial z}\right) \tag{2.63}$$

$$\Gamma^i_{zx} = G^i_{xz} + \frac{1}{k_i^2}\frac{\partial}{\partial z}\left(\frac{\partial G^i_{xx}}{\partial x} + \frac{\partial G^i_{xz}}{\partial z}\right) . \tag{2.64}$$

Substituting this expression into (2.59) gives

$$\begin{aligned} \bar{E}^i_q &= \int\!\!\int_{S_q} \Gamma^i_{xx}\psi(y')\alpha_q(x')dx'dy'\ \hat{x} \\ &\quad + \int\!\!\int_{S_q} \Gamma^i_{yx}\psi(y')\alpha_q(x')dx'dy'\ \hat{y} \\ &\quad + \int\!\!\int_{S_q} \Gamma^i_{zx}\psi(y')\alpha_q(x')dx'dy'\ \hat{z} . \end{aligned} \tag{2.65}$$

Recall that we only need the x-component of this field which is given by

$$E^i_{qx} = \int\!\!\int_{S_q} \Gamma^i_{xx}\psi(y')\alpha_q(x')dx'dy' . \tag{2.66}$$

Furthermore, at $z = h$, boundary conditions require that $E^{(1)}_{qx}(z = h)$ and $E^{(2)}_{qx}(z = h)$ be identical. From the above equation it is obvious that this implies

$$\Gamma^{(1)}_{xx}(z = h) = \Gamma^{(2)}_{xx}(z = h) = \Gamma_{xx}(z = h). \tag{2.67}$$

This equality is verified in Appendix E, and the result of (E.7) may be put in the form

$$\begin{aligned} &\Gamma_{xx}(z = h) = \\ &\qquad j\omega\mu_0 \sum_{m=1}^{\infty}\sum_{n=0}^{\infty} \frac{f_{mn}}{abd_{1mn}d_{2mn}} \left[\cos k_x x\ \sin k_y y\ \cos k_x x'\ \sin k_y y'\right] \end{aligned} \tag{2.68}$$

where

$$\begin{aligned} f_{mn} &= \varphi_n \tan k_z^{(1)}h\ \tan k_z^{(2)}(h - c)\left[k_z^{(2)}\epsilon_r^*\left(1 - \frac{k_x^2}{k_1^2}\right)\ \tan k_z^{(2)}(h - c)\right. \\ &\qquad \left. - k_z^{(1)}\left(1 - \frac{k_x^2}{k_0^2}\right)\ \tan k_z^{(1)}h\right] . \end{aligned} \tag{2.69}$$

If we place (2.68) into (2.66) we obtain

$$\begin{aligned} E^{(1)}_{qx}(z=h) &= E^{(2)}_{qx}(z=h) = \\ E_{qx}(z=h) &= j\omega\mu_0 \sum_{m=1}^{\infty}\sum_{n=0}^{\infty} \frac{f_{mn}}{abd_{1mn}d_{2mn}} \cos k_x x \ \sin k_y y \ \mathcal{I}_{qmn} \, . \end{aligned} \tag{2.70}$$

where

$$\mathcal{I}_{qmn} = \int\int_{S_q} \cos k_x x' \sin k_y y' \psi(y') \alpha_q(x') dx' dy' \, . \tag{2.71}$$

This surface integration is evaluated in closed form in Appendix F; the result is

$$\begin{aligned} \mathcal{I}_{qmn} &= -\frac{\zeta_q K l_x^2 \cos k_x x_q}{4 \sin K l_x} \operatorname{Sinc}\left[\frac{1}{2}(k_x + K) l_x\right] \operatorname{Sinc}\left[\frac{1}{2}(k_x - K) l_x\right] \\ &\quad \cdot \sin k_y Y_0 \, J_0(k_y \frac{W}{2}) \, . \end{aligned} \tag{2.72}$$

where

$$\operatorname{Sinc}(t) = \begin{cases} \frac{\sin t}{t} & \text{for } t \neq 0 \\ 1 & \text{for } t = 0 \, . \end{cases} \tag{2.73}$$

$$\zeta_q = \begin{cases} 2 & \text{for } q = 1 \\ 4 & \text{else} \end{cases} \tag{2.74}$$

$$K = \omega\sqrt{\mu_0 \epsilon_0 \epsilon_{r1}} \tag{2.75}$$

$$R_{1n} = \frac{1}{2}(k + k_x) l_x \tag{2.76}$$

$$R_{2n} = \frac{1}{2}(k - k_x) l_x \, . \tag{2.77}$$

The position vector x_q gives the x-coordinate of the q^{th} strip subsection. As will be outlined in Section 3.1.3, the functional dependence of this vector varies with the type of structure being analyzed.

We are now ready to evaluate the impedance elements.

2.4.2 Evaluation of the Impedance Matrix Elements

From (2.70) and (2.54) we have

$$Z_{qp} = j\omega\mu_0 \sum_{m=1}^{\infty}\sum_{n=0}^{\infty} \frac{f_{mn}\mathcal{I}_{qmn}}{abd_{1mn}d_{2mn}} \mathcal{I}_{pmn} \tag{2.78}$$

where

$$\mathcal{I}_{pmn} = \int\int_{S_p} \cos k_x x \, \sin k_y y \, \psi(y) \alpha_p(x) dx dy \, . \qquad (2.79)$$

Since (2.79) is the same integral as (2.71), we can obtain the expression for $\mathcal{I}_{pmn}$ by substituting p for q in (2.72). From (2.78), the entire expression for Z_{qp} may be written as follows:

$$\begin{aligned} Z_{qp} = & \\ & \frac{j\omega\mu_0 K^2 l_x^4}{16ab \sin^2 K l_x} \zeta_q \zeta_p \sum_{m=1}^{\infty} \sum_{n=0}^{\infty} \varphi_n \cos k_x x_q \cos k_x x_p [\,\mathrm{Sinc} R_{1n} \, \mathrm{Sinc} R_{2n}]^2 \\ \cdot & \frac{[\sin(k_y Y_0) J_0 \left(\frac{k_y W}{2}\right)]^2 \tan k_z^{(1)} h \, \tan k_z^{(2)} (h-c)}{\left[k_z^{(2)} \tan k_z^{(1)} h - k_z^{(1)} \tan k_z^{(2)} (h-c)\right]} \\ \cdot & \frac{\left[k_z^{(2)} \epsilon_r^* \left(1 - \frac{k_t^2}{k_1^2}\right) \tan k_z^{(2)}(h-c) - k_z^{(1)} \left(1 - \frac{k_t^2}{k_0^2}\right) \tan k_z^{(1)} h\right]}{\left[k_z^{(2)} \epsilon_r^* \tan k_z^{(2)} (h-c) - k_z^{(1)} \tan k_z^{(1)} h\right]} \end{aligned} \qquad (2.80)$$

With the theory for the computation of the impedance matrix complete, we turn to the theory for the excitation vector

2.5 Excitation Vector Formulation

In this section, a surface integral will be set up that provides for evaluating the elements of the excitation vector according to (2.16). This equation may be re-written as

$$V_q = \int\int_{S_f} \bar{H}_q(x=0) \cdot M_\phi \hat{\phi} \rho d\rho d\phi \qquad (2.81)$$

where ρ, and ϕ are cylindrical coordinates referenced to the center of the feeding aperture, as shown in Figure 2.7.

An expression for M_ϕ will be presented first. Then, the magnetic field components parallel to the plane of the aperture (i.e. the $y - z$ plane) will be derived based on the Green's function of Section 2.3. The actual integration of (2.81) is performed numerically, and this is described in Section 3.1.

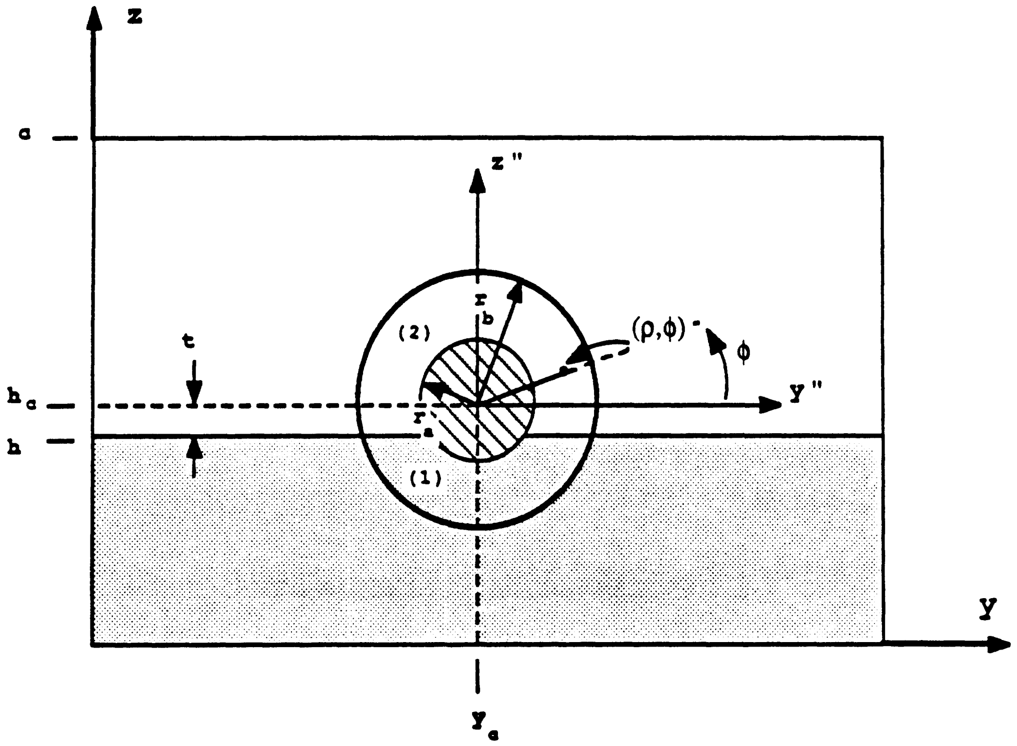

Figure 2.7: Geometry used to set up surface integral for excitation vector.

2.5.1 Coaxial Feed Modeling by an Equivalent Magnetic Current

If the radius of the coaxial feed's inner conductor is assumed to be much smaller than the wavelength ($kr_a \ll 1$), and the coaxial feed line is designed to allow only transverse magnetic (TEM) propagation, we can represent the aperture by an equivalent magnetic frill current given by [25,18]

$$\bar{M}_s = -\frac{V_0}{\rho \ln\left(\frac{r_b}{r_a}\right)}\hat{\phi} \tag{2.82}$$

where

V_0 is the complex voltage present in the coaxial line at the feeding point

r_b is the radius of the coaxial feed's outer conductor

r_a is the radius of the coaxial feed's inner conductor

ρ, ϕ are cylindrical coordinates referenced to the feed's center

Substituting from (2.82) into (2.81) yields (with $ds = \rho d\rho d\phi$)

$$V_q = -\frac{V_0}{\ln\left(\frac{r_b}{r_a}\right)} \int\int_{S_f} H^i_{q\phi}(x=0)\, d\rho d\phi \tag{2.83}$$

where the cylindrical coordinates ρ and ϕ are defined in Figure 2.7, and $H^i_{q\phi}$ is the $\hat{\phi}$ component of the magnetic field evaluated in the plane of the aperture ($x = 0$).

One factor that complicates the integration of (2.83) is that it must be performed in two regions whose boundaries depend on the feed position as can be seen in Figure 2.7. The integration can be broken up as follows:

$$\begin{aligned} V_q &= -\frac{V_0}{\ln\left(\frac{r_b}{r_a}\right)} \int\int_{S_f} H^i_{q\phi}\, d\rho d\phi \\ &= -\frac{V_0}{\ln\left(\frac{r_b}{r_a}\right)} \left[\int\int_{S_f^{(1)}} H^{(1)}_{q\phi}\, d\rho d\phi + \int\int_{S_f^{(2)}} H^{(2)}_{q\phi}\, d\rho d\phi\right] \end{aligned} \tag{2.84}$$

where

$S_f^{(1)}$ is the portion of the feed surface lying below the substrate ($z'' = \rho \sin\phi \le -t$)

$S_f^{(2)}$ is the portion of the feed surface lying above the substrate ($z'' = \rho \sin\phi \ge -t$)

The evaluation of the magnetic field components $H_{q\phi}^{(1)}$ and $H_{q\phi}^{(2)}$ is described next. Once these have been evaluated, the integration of (2.84) is carried out numerically as discussed in Section 3.1.

2.5.2 Evaluation of the Magnetic Field at the Aperture

To evaluate the magnetic field component $H_{q\phi}$, we will first determine the $\hat{y}$ and $\hat{z}$ components, and then perform a coordinate transformation to the cylindrical coordinates ρ and ϕ.

Determination of $\hat{y}$ and $\hat{z}$ components of $\bar{H}_q$.— The magnetic field $\bar{H}_q$ anywhere inside the cavity is given by (2.26)

$$\bar{H}_q^i = \frac{1}{\mu_o} \bar{\nabla} \times \bar{A}_q^i \,.$$

The $\hat{y}$ and $\hat{z}$ components are given by

$$H_{qy}^i = \frac{1}{\mu_0}\left(\frac{\partial A_{qx}^i}{\partial z} - \frac{\partial A_{qz}^i}{\partial x}\right) \tag{2.85}$$

$$H_{qz}^i = -\frac{1}{\mu_0}\frac{\partial A_{qx}^i}{\partial y} \tag{2.86}$$

where, from (2.32) and (2.56),

$$A_{qx}^i = \mu_0 \int\!\!\int_{S_q} \psi(y')\alpha_q(x') G_{xx}^i ds' \tag{2.87}$$

$$A_{qz}^i = \mu_0 \int\!\!\int_{S_q} \psi(y')\alpha_q(x') G_{xz}^i ds' \,. \tag{2.88}$$

Combining the last four equations, we have

$$H_{qy}^i = \int\!\!\int_{S_q} \left(\frac{\partial G_{xx}^i}{\partial z} - \frac{\partial G_{xz}^i}{\partial x}\right) \psi(y')\alpha_q(x') ds' \tag{2.89}$$

$$H_{qz}^i = -\int\!\!\int_{S_q} \frac{\partial G_{xx}^i}{\partial y} \psi(y')\alpha_q(x') ds' \,. \tag{2.90}$$

These components are evaluated in Appendix G (for $i = 1, 2$). Setting $x = 0$ in the resulting expressions yields:

$$\begin{aligned}
H_{qy}^{(1)}(x=0) &= H_{q0} \sum_{m=1}^{\infty} \sum_{n=0}^{\infty} c_{nq} c_{ymn}^{(1)} \sin k_y y \cos k_z^{(1)} z && (2.91) \\
H_{qz}^{(1)}(x=0) &= H_{q0} \sum_{m=1}^{\infty} \sum_{n=0}^{\infty} c_{nq} c_{zmn}^{(1)} \cos k_y y \sin k_z^{(1)} z && (2.92) \\
H_{qy}^{(2)}(x=0) &= H_{q0} \sum_{m=1}^{\infty} \sum_{n=0}^{\infty} c_{nq} c_{ymn}^{(2)} \sin k_y y \cos k_z^{(2)} (z-c) && (2.93) \\
H_{qz}^{(2)}(x=0) &= H_{q0} \sum_{m=1}^{\infty} \sum_{n=0}^{\infty} c_{nq} c_{zmn}^{(2)} \cos k_y y \sin k_z^{(2)} (z-c) && (2.94)
\end{aligned}$$

where

$$\begin{aligned}
H_{q0} &= \frac{\zeta_q K l_x^2}{4ab \sin K l_x} \\
c_{nq} &= \cos k_x x_q \,\mathrm{Sinc}\left[\frac{1}{2}(k_x + K) l_x\right] \mathrm{Sinc}\left[\frac{1}{2}(k_x - K) l_x\right]
\end{aligned}$$

and

$$\begin{aligned}
c_{ymn}^{(1)} &= \frac{c_{zmn}^{(1)}}{k_y d_{2mn}} \left\{ k_z^{(1)} k_z^{(2)} \epsilon_r^* \tan k_z^{(2)} (h-c) \right. \\
&\quad \left. - \left[(k_z^{(1)})^2 + k_x^2 (1 - \epsilon_r^*) \right] \tan k_z^{(1)} h \right\} && (2.95) \\
c_{zmn}^{(1)} &= \frac{\varphi_n k_y \tan k_z^{(2)} (h-c)}{d_{1mn} \cos k_z^{(1)} h} \sin k_y Y_0 \, J_0(k_y \frac{W}{2}) && (2.96) \\
c_{ymn}^{(2)} &= \frac{c_{zmn}^{(2)}}{k_y d_{2mn}} \left\{ k_z^{(1)} k_z^{(2)} \tan k_z^{(1)} h \right. \\
&\quad \left. - \left[(k_z^{(2)})^2 \epsilon_r^* - k_x^2 (1 - \epsilon_r^*) \right] \tan k_z^{(2)} (h-c) \right\} && (2.97) \\
c_{zmn}^{(2)} &= \frac{\varphi_n k_y \tan k_z^{(1)} h}{d_{1mn} \cos k_z^{(2)} (h-c)} \sin k_y Y_0 \, J_0(k_y \frac{W}{2}) \,. && (2.98)
\end{aligned}$$

Coordinate transformation and evaluation of $H_{q\phi}$.— Equations (2.91)-(2.94) give the $\hat{y}$ and $\hat{z}$ components of the magnetic field anywhere inside the cavity. To find the $\hat{\phi}$ component we will perform the necessary coordinate transformation in two steps:

1. move the origin from the corner of the cavity (Figure 1.3) to the center of the coaxial feeding aperture.

Table 2.1: COORDINATE TRANSFORMATION VARIABLES

VARIABLE RELATIONS	UNIT VECTOR RELATIONS
$x'' = x$	$\hat{x}'' = \hat{x}$
$y'' = y - Y_c = \rho \cos\phi$	$\hat{y}'' = \hat{y} = \cos\phi\hat{\rho} - \sin\phi\hat{\phi}$
$z'' = z - h_c = \rho \cos\phi$	$\hat{z}'' = \hat{z} = \sin\phi\hat{\rho} + \cos\phi\hat{\phi}$

2. perform a cartesian to cylindrical coordinate transformation.

Referring to Figure 2.7, let us denote a new coordinate system by (x'', y'', z'') whose origin is at the feed's center $(x, y, z) = (0, Y_c, h_c)$. The relationship between the new and old coordinates are outlined in Table 2.1.

Using these relations, we will make the following substitutions in (2.91)-(2.94) to move the origin to the feed's center, and transform to cylindrical coordinates:

$$\begin{aligned} y \rightarrow y'' + Y_c &= \rho\cos\phi + Y_c \\ z \rightarrow z'' + h_c &= \rho\sin\phi + Y_c \end{aligned}$$

Now, let $\bar{H}^i_{qt}$ represent the projection of $\bar{H}^i_q$ onto the plane of the aperture such that

$$\bar{H}^i_{qt} = H^i_{qy}\hat{y} + H^i_{qz}\hat{z} = H^i_{q\phi}\hat{\phi} + H^i_{q\rho}\hat{\rho} \tag{2.99}$$

where $H^i_{q\rho}$ and $H^i_{q\phi}$ are the $\hat{\rho}$ and $\hat{\phi}$ components respectively.

Using the relations of Table 2.1, we readily obtain

$$H^i_{q\phi} = -\sin\phi H^i_{qy} + \cos\phi H^i_{qz}\,. \tag{2.100}$$

If we substitute from (2.91)-(2.94) into the above, and transform to cylindrical coordinates we obtain

$$H^{(1)}_{q\phi}(x = 0) =$$

$$H_{q0}\left[-\sin\phi\sum_{m=1}^{\infty}\sum_{n=0}^{\infty}c_{nq}c_{ymn}^{(1)}\sin k_y(\rho\cos\phi+Y_c)\cos k_z^{(1)}(\rho\sin\phi+h_c)\right.$$

$$\left.+\cos\phi\sum_{m=1}^{\infty}\sum_{n=0}^{\infty}c_{nq}c_{zmn}^{(1)}\cos k_y(\rho\cos\phi+Y_c)\sin k_z^{(1)}(\rho\sin\phi+h_c)\right] \qquad (2.101)$$

$$H_{q\phi}^{(2)}(x=0)=$$

$$H_{q0}\left[-\sin\phi\sum_{m=1}^{\infty}\sum_{n=0}^{\infty}c_{nq}c_{ymn}^{(2)}\sin k_y(\rho\cos\phi+Y_c)\cos k_z^{(2)}(\rho\sin\phi-c'')\right.$$

$$\left.+\cos\phi\sum_{m=1}^{\infty}\sum_{n=0}^{\infty}c_{nq}c_{zmn}^{(2)}\cos k_y(\rho\cos\phi+Y_c)\sin k_z^{(2)}(\rho\sin\phi-c'')\right] \qquad (2.102)$$

where

$$c''=c-h_c\,. \qquad (2.103)$$

2.6 Current Computation for Two-Port Structures

In the preceeding sections, the theory has been advanced for computing the impedance matrix and excitation vector associated with a one-port discontinuity, such as an open-ended transmission line. This section will present the modifications necessary to extend the theory for treatment of two-port structures. Our approach for computing the network parameters (scattering parameters etc.) of two-ports, requires simultaneous excitation of the strip conductors from both sides of the cavity. We will refer to this as "dual excitation".

2.6.1 Application of Reciprocity Theorem for Dual Excitation

In section 2.2.1 an integral equation (2.3) was derived by applying the reciprocity theorem to the one-port network of Figure 2.5. In an analogous fashion, we will now apply the reciprocity theorem to the two-port network of Figure 2.8.

In Figure 2.8, both magnetic current sources $M_{\phi l}$ and $M_{\phi r}$ are coupled with the electric current source $\bar{J}_s$ on the conducting strips to produce the total fields

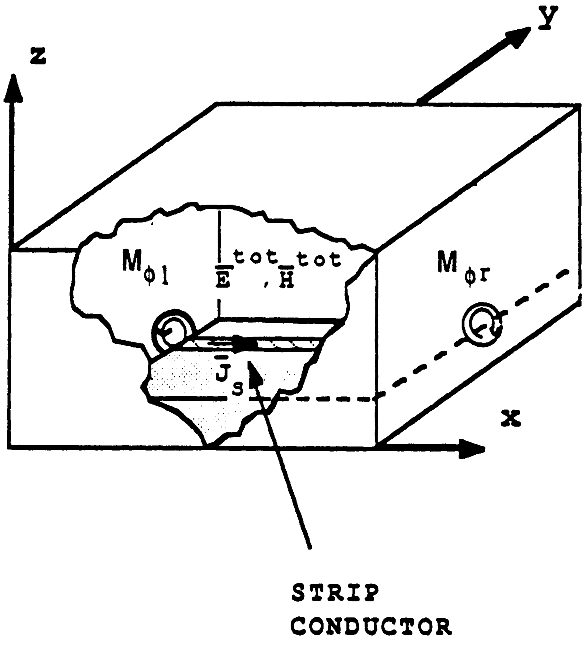

Figure 2.8: In the case of dual excitation, the total fields $\bar{E}^{tot}, \bar{H}^{tot}$ inside the cavity are produced by magnetic currents $M_{\phi l}$, $M_{\phi r}$, and the electric current $\bar{J}_s$.

$\bar{E}^{tot}$, $\bar{H}^{tot}$ inside the cavity. As before, we consider an independent test source $\bar{J}_q$, and associated fields $\bar{E}_q$ and $\bar{H}_q$ as shown in Figure 2.4.

Applying reciprocity theorem between these two sets of sources yields

$$\begin{aligned}\int\!\!\int\!\!\int_V \left(\bar{J}_s \cdot \bar{E}_q - \bar{H}_q \cdot \bar{M}_{sl} - \bar{H}_q \cdot \bar{M}_{sr}\right) dv &= \int\!\!\int\!\!\int_V \bar{J}_q \cdot \bar{E}^{tot} dv \\ &= 0 \end{aligned} \tag{2.104}$$

where the volume V is the interior of the cavity and

$$\bar{M}_{sl} = M_{\phi l}\hat{\phi} \tag{2.105}$$

$$\bar{M}_{sr} = M_{\phi r}\hat{\phi}. \tag{2.106}$$

The right hand side of (2.104) vanishes as described by (2.2). Reducing the remaining volume integrals of (2.104) to the appropriate surface integrals gives

$$\begin{aligned}\int\!\!\int_{S_{strip}} \bar{E}_q(z=h) \cdot \bar{J}_s ds &= \int\!\!\int_{S_{lf}} \bar{H}_q(x=0) \cdot \bar{M}_{sl} ds \\ &+ \int\!\!\int_{S_{rf}} \bar{H}_q(x=a) \cdot \bar{M}_{sr} ds. \end{aligned} \tag{2.107}$$

In the above,

S_{lf} = Surface of coaxial aperture on left hand side ($x = 0$ side) of cavity

S_{rf} = Surface of coaxial aperture on right hand side ($x = a$ side) of cavity.

By comparison with (2.3), (2.107) can be seen as a natural extension to the theory for the case of single excitation.

2.6.2 Expansion of Current and Modified Matrix Equation

The current $\bar{J}_s$ is again expanded according to (2.6)

$$\bar{J}_s = \psi(y) \sum_{p=1}^{N_s} I_p \alpha_p(x)\, \hat{x}$$

The only difference is that we now must consider the basis function for the x-dependence on the last subsection (i.e. closest to the right-most feed) as a special case. This is necessary since at each end of the cavity only a half sinusoidal basis function is required as illustrated in Figure 2.9. Hence, for the right-most subsection we let

$$\alpha_{N_s}(x) = \begin{cases} \frac{\sin[K(x-a)]}{\sin(Kl_x)} & x_{N_s-1} \leq x \leq a \\ 0 & \text{else} \end{cases} \tag{2.108}$$

where the quantities K and l_x are as defined in Section 2.2.2, and N_s represents the index for the right-most subsection. The rest of the basis function expansion is the same as given by (2.7)-(2.9).

Substitution of (2.6) into (2.107) yields

$$\begin{aligned} \sum_{p=1}^{N_s} \left[\int\int_{S_p} \bar{E}_q(x=h) \cdot \psi(y)\, \alpha_p(x)\, \hat{x} ds \right] I_p &= \int\int_{S_{lf}} \bar{H}_q(x=0) \cdot \bar{M}_{sl} ds \\ &+ \int\int_{S_{rf}} \bar{H}_q(x=a) \cdot \bar{M}_{sr} ds \end{aligned} \tag{2.109}$$

which can be expressed as

$$[\mathbf{Z}]\,[\mathbf{I}_d] = [\mathbf{V}_l] + [\mathbf{V}_r] = [\mathbf{V}_d] \tag{2.110}$$

where

$[\mathbf{I}_d]$ is the vector containing the current coefficients for the case of dual excitation

$[\mathbf{V}_l]$ is the excitation vector of the feed on the left ($N_s \times 1$)

$[\mathbf{V}_r]$ is the excitation vector of the feed on the right ($N_s \times 1$)

$[\mathbf{V}_d]$ is the combined excitation vector for dual excitation.

The elements of the excitation vectors $[\mathbf{V}_l]$, and $[\mathbf{V}_r]$ are given by

$$V_{ql} = \int\int_{S_{lf}} \bar{H}_q(x=0) \cdot \bar{M}_{sl} ds \tag{2.111}$$

$$V_{qr} = \int\int_{S_{rf}} \bar{H}_q(x=a) \cdot \bar{M}_{sr} ds \tag{2.112}$$

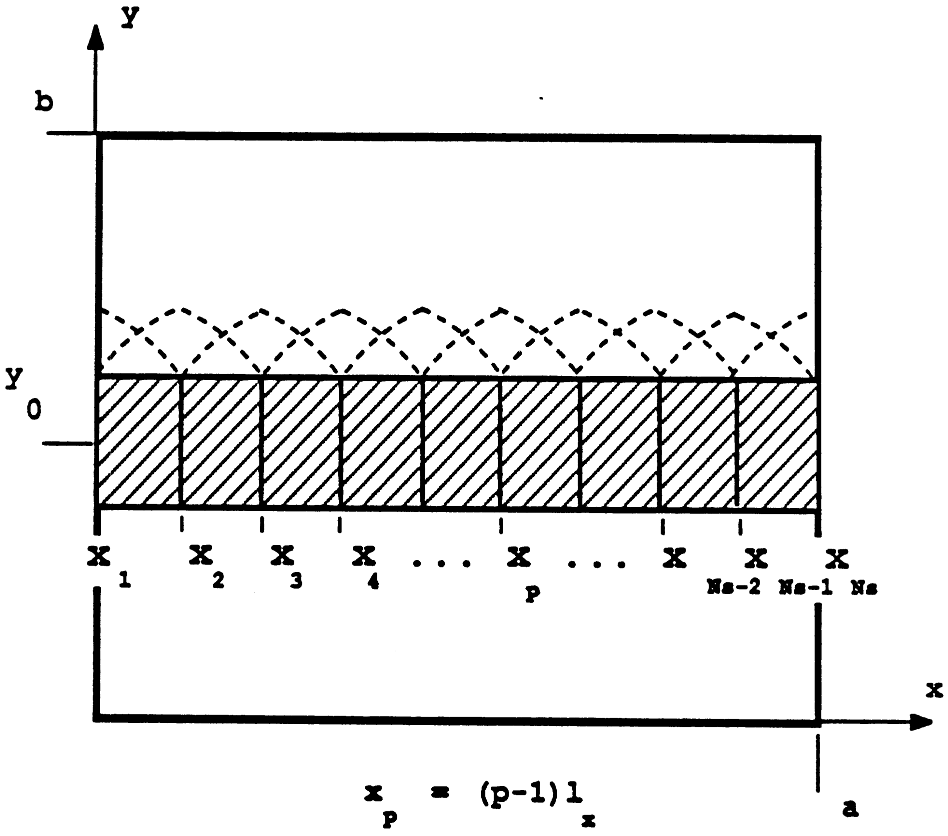

Figure 2.9: Strip geometry for basis function expansion with dual excitation. The case shown corresponds to a thru-line.

We can solve for the current vector by matrix inversion and multiplication according to

$$[\mathrm{I}] = [\mathrm{Z}]^{-1}\,[\mathrm{V}_d] \tag{2.113}$$

2.6.3 Modifications to Impedance Matrix

The elements of the impedance matrix for the case of dual excitation are given by the same integral equation as for the one port case, namely (2.15). The difference is in the integration over the last subsection ($p = N_s$) where $\alpha_p(x)$ is now given by (2.108). The integration for E_{qx} given by (2.70) is also modified for the last subsection ($q = N_s$) in a similar way. It can readily be shown that the surface integration over the last subsection (i.e. closest to the feed on the right) is equivalent to the integration over the first subsection (i.e. closest to the feed on the left). Hence, the elements of the impedance matrix are again given by (2.80) the only change being that ζ_q is as redefined below rather than by (2.74)

$$\zeta_q = \begin{cases} 2 & \text{for } q = 1 \text{ or } q = N_s \\ 4 & \text{else} \end{cases} \tag{2.114}$$

and ζ_p for the dual excitation case is given from (2.114) with q replaced by p.

2.6.4 Modifications to Excitation Vector

We now consider the integrations of (2.111), and (2.112). By analogy with (2.82) we may express the two magnetic currents as follows:

$$\bar{M}_{sl} = -\frac{V_{0l}}{\ln\left(\frac{r_b}{r_a}\right)\rho}\hat{\phi} \tag{2.115}$$

$$\bar{M}_{sr} = +\frac{V_{0r}}{\ln\left(\frac{r_b}{r_a}\right)\rho}\hat{\phi} \tag{2.116}$$

where the positive sign in the second current source indicates that it is taken to be in the opposite sense (Figure 2.8). In the above two equations, V_{0l} is the complex voltage in the coaxial line at the left-hand feed, and V_{0r} is the complex voltage in the coaxial line at the right-hand feed.

Substituting from (2.115) into (2.111) yields

$$V_{ql} = -\frac{V_{0l}}{\ln\left(\frac{r_b}{r_a}\right)} \int\int_{S_f} H_{q\phi}(x=0)\,d\rho\, d\phi\ . \tag{2.117}$$

Similarly, from (2.116) and (2.112),

$$V_{qr} = \frac{V_{0r}}{\ln\left(\frac{r_b}{r_a}\right)} \int\int_{S_f} H_{q\phi}(x=a)\,d\rho\, d\phi\ . \tag{2.118}$$

Now, the integration required for V_{ql} is identical to that carried out in Section 2.5 for V_q (single excitation case). The computation of V_{qr} is only slightly modified as we need to shift the origin to $(x', y', z') = (a, Y_c, h_c)$ instead of to $(0, Y_c, h_c)$. After examining the x-dependence of $\bar{H}_q$ given in Appendix G, it becomes obvious that we need only multiply the result for V_{ql} by $\cos n\pi$ to get the result for V_{qr}. That is

$$V_{qr} = -\frac{V_{0l}}{V_{0r}} \cos n\pi\ V_{ql}. \tag{2.119}$$

Let V_{qd} represent the elements of $[\ \mathbf{V}_d]$ given by

$$V_{qd} = V_{ql} + V_{qr}\ .$$

Then,

$$V_{qd} = \left(1 - \frac{V_{0l}}{V_{0r}} \cos n\pi\right) V_q \tag{2.120}$$

where V_q represents the excitation vector of Section 2.5 with V_0 set equal to unity.

As discussed in Section 2.7, two-port scattering parameters are found by applying even and odd mode excitations to the circuit. The next step here is to find the excitation vectors for these two cases.

For the even mode excitation, we let $V_{0l} = V_{0r} = 1$. In this case, from (2.120) we have

$$V_{qe} = V_q(1 - \cos n\pi)$$

$$= \begin{cases} 0 & \text{for n even} \\ 2V_q & \text{for n odd .} \end{cases} \qquad (2.121)$$

For the odd mode excitation, we let $V_{0l} = -V_{0r} = 1$. Now, using (2.120)

$$\begin{aligned} V_{qo} &= V_q(1+\cos n\pi) \\ &= \begin{cases} 2V_q & \text{for n even} \\ 0 & \text{for n odd} \end{cases} \end{aligned} \qquad (2.122)$$

where

V_{qe} represents the elements of the even excitation vector $[\mathbf{V}_e]$

V_{qo} represents the elements of the odd excitation vector $[\mathbf{V}_o]$.

Using these two excitations, we can compute both the even and odd mode current distributions using the following matrix equations:

$$[\mathbf{I}_e] = [\mathbf{Z}]^{-1}[\mathbf{V}_e] \qquad (2.123)$$

$$[\mathbf{I}_o] = [\mathbf{Z}]^{-1}[\mathbf{V}_o] \qquad (2.124)$$

where

$[\mathbf{I}_e]$ represents the current vector for even excitation

$[\mathbf{I}_o]$ represents the current vector for odd excitation.

2.7 Determination of Network Parameters

The preceeding sections presented the theoretical methods for computing the current distributions for one- and two-port shielded microstrip discontinuities. The next step is to use these currents to determine the associated network parameters that can be used to represent them.

The relevant network parameters include the parameters of uniform microstrip line sections, and the parameters associated with discontinuity structures. The parameters for the uniform line sections are the complex propagation constant (γ_g), and the characteristic impedance (Z_0). For the discontinuity structures, the relevant parameters are one or more of the following:

- input impedance
- reflection coefficient
- scattering parameters
- impedance parameters
- admittance parameters
- equivalent circuit parameters.

Since the aim of this thesis is to concentrate on discontinuity effects, the characteristic impedance is not considered. For a microstrip line Z_0 cannot be strictly defined, and there has been considerable controversy over the most appropriate definition to use [27]-[31]. To avoid potential ambiguities caused by comparing results which may have been normalized to a different Z_0, the author has chosen to work with normalized network parameters where possible. In comparing scattering parameters, the normalizing impedance is whatever impedance corresponds to the microstrip line width in use (i.e. it does not need to be calculated to compare scattering parameters). This is true for both the measurements and the numerical results of the present research, although it may not be true for the results presented from CAD packages.

2.7.1 Network Parameters for One-Port Discontinuities

The simplest one-port discontinuity is an open-ended microstrip line. We will use the open-end as an example to illustrate the methodology for determining one-port network parameters. These include the propagation constant of the line, the reflection coefficient, and the input impedance at various points on the line.

Calculation of the Propagation Constant

In general, the complex propagation constant γ_g is given by

$$\gamma_g = \alpha_g + j\,\beta_g \tag{2.125}$$

For the computation of the current distribution, the theory for which is described in the preceeding sections,

In the development of the preceeding sections, which describes the theory for computation of the current distribution, the dielectric material was assumed to be lossy in general. However, for the discontinuity structures treated in this thesis, only the lossless case is considered for the computation of network parameters. The network parameter theory for the lossy case is a relatively straightforward extension, hence the theory of this section can easily be generalized to handle the lossy case.

In the lossless case $\gamma_g = j\beta_g$, where the phase constant β_g is given by

$$\beta_g = \frac{2\pi}{\lambda_g} \tag{2.126}$$

and λ_g is the microstrip wavelength. This can be determined by calculating the distance between adjacent current maximums. Another parameter that is often used to describe microstrip propagation characteristics is the effective dielectric constant ϵ_{eff}. This may be found from λ_g according to

$$\epsilon_{eff} = \left(\frac{\lambda_0}{\lambda_g}\right)^2 \tag{2.127}$$

where λ_0 is the free space wavelength.

Determination of the Input Reflection Coefficient and Impedance

To determine the input reflection coefficient we first need to establish a reference plane at some point on the line. Two convenient points are just to the right of the coaxial input ($x = 0$) and at the point where the discontinuity begins. Choosing the reference plane at $x = 0$, the voltage reflection coefficient (looking towards the discontinuity) anywhere on the transmission line is given by [5]

$$\Gamma(x) = \frac{SWR - 1}{SWR + 1} e^{-j\pi} e^{-j2\beta_g(x_{max} - x)} \tag{2.128}$$

where x_{max} is the position of a current maximum. SWR denotes the standing wave ratio, which is given by the ratio of the maximum current amplitude $|I_{max}|$ to the minimum current amplitude $|I_{min}|$. That is,

$$SWR = \frac{|I_{max}|}{|I_{min}|} . \tag{2.129}$$

The $e^{-j\pi}$ term in (2.128) arises since, on a lossless line, a current maximum corresponds to a short circuit (i.e. $\Gamma(x_{max}) = e^{-j\pi}$).

From (2.128), the reflection coefficient at the end of the line($x = L_{in}$) is given by

$$\Gamma(L_{in}) = \frac{SWR - 1}{SWR + 1} e^{-j\pi} e^{j2\beta_g d_{max}} \tag{2.130}$$

where

$$d_{max} = l - x_{max}$$

is the distance from the end of the line to a maximum.

The normalized input impedance at any point on the line may be found from the reflection coefficient according to

$$z(x) = \frac{1+\Gamma(x)}{1-\Gamma(x)} \,. \tag{2.131}$$

Equivalent Circuit for an Open-End Discontinuity

An open-end discontinuity in microstrip can be represented as either an effective length extension L_{eff} or by an equivalent capacitance c_{op} as shown in Figure 2.10.

Effective length extension for open-end discontinuity.— The effective length extension represents the length of ideal open circuited transmission line which, if as a continuation of the strip, would present the same reflection coefficient at $x = L_{in}$ as the open-end discontinuity (Figure 2.10). This length is deduced from the fact that the current on an ideal open circuit would go to zero at a distance $\frac{\lambda_g}{4}$ from the last current maximum. Hence, the effective length extension is given by

$$L_{eff} = \frac{\lambda_g}{4} - d_{max} \,. \tag{2.132}$$

This representation gives an intuitive feel for the magnitude of the end effect. On the other hand, the equivalent capacitance representation is better for circuit design purposes.

Equivalent capacitance for open-end discontinuity.— For an open-end in a lossless microstrip environment, the standing wave ratio is infinite ($SWR \rightarrow \infty$); hence, from (2.130)

$$\Gamma_{op} = \Gamma_{op} = e^{j\theta_{op}} \tag{2.133}$$

where

$$\theta_{op} = 2\beta_g d_{max} - \pi \,. \tag{2.134}$$

The associated normalized equivalent capacitance (Figure 2.10) can be expressed as

$$c_{op} = \frac{\sin 2\beta_g d_{max}}{\omega(1-\cos 2\beta_g d_{max})} = \frac{\sin 2\beta_g L_{eff}}{\omega(1+\cos 2\beta_g L_{eff})} . \qquad (2.135)$$

An algorithm for calculating one-port network parameters from the microstrip current, computed numerically, is discussed in the following chapter.

2.7.2 Network Parameters for Two-Port Structures

The network parameters for two-port structures determined by analyzing the currents from the even and odd mode excitations discussed in Section 2.6, and illustrated in Section 3.2.4.

General Representation by Equivalent T-network

In general, a passive symmetric two-port structure can be represented by the T-network equivalent circuit of Figure 2.11. The T-network parameters are given in terms of the normalized impedance parameters according to

$$\begin{bmatrix} V_1 \\ V_2 \end{bmatrix} = \begin{bmatrix} z_{11} & z_{12} \\ z_{21} & z_{22} \end{bmatrix} \begin{bmatrix} I_1 \\ I_2 \end{bmatrix} . \qquad (2.136)$$

Since we have assumed that the two-port structure is passive, reciprocal, and symmetric $z_{11} = z_{22}$ and $z_{12} = z_{21}$.

These impedance parameters are found from the input impedances of the even and odd current distributions. The even mode excitation ($V_{g1} = V_{g2} = V_0$) corresponds to placing an electric wall in the center of the circuit as shown in Figure 2.12a. The odd mode excitation ($V_{g1} = -V_{g2} = V_0$) corresponds to placing a magnetic wall in the center of the circuit as shown in Figure 2.12. The normalized input impedances z_{IN}^e and z_{IN}^o, for these two cases are found by analyzing the two separate current distributions as described in Section 4.2 for one-port analysis.

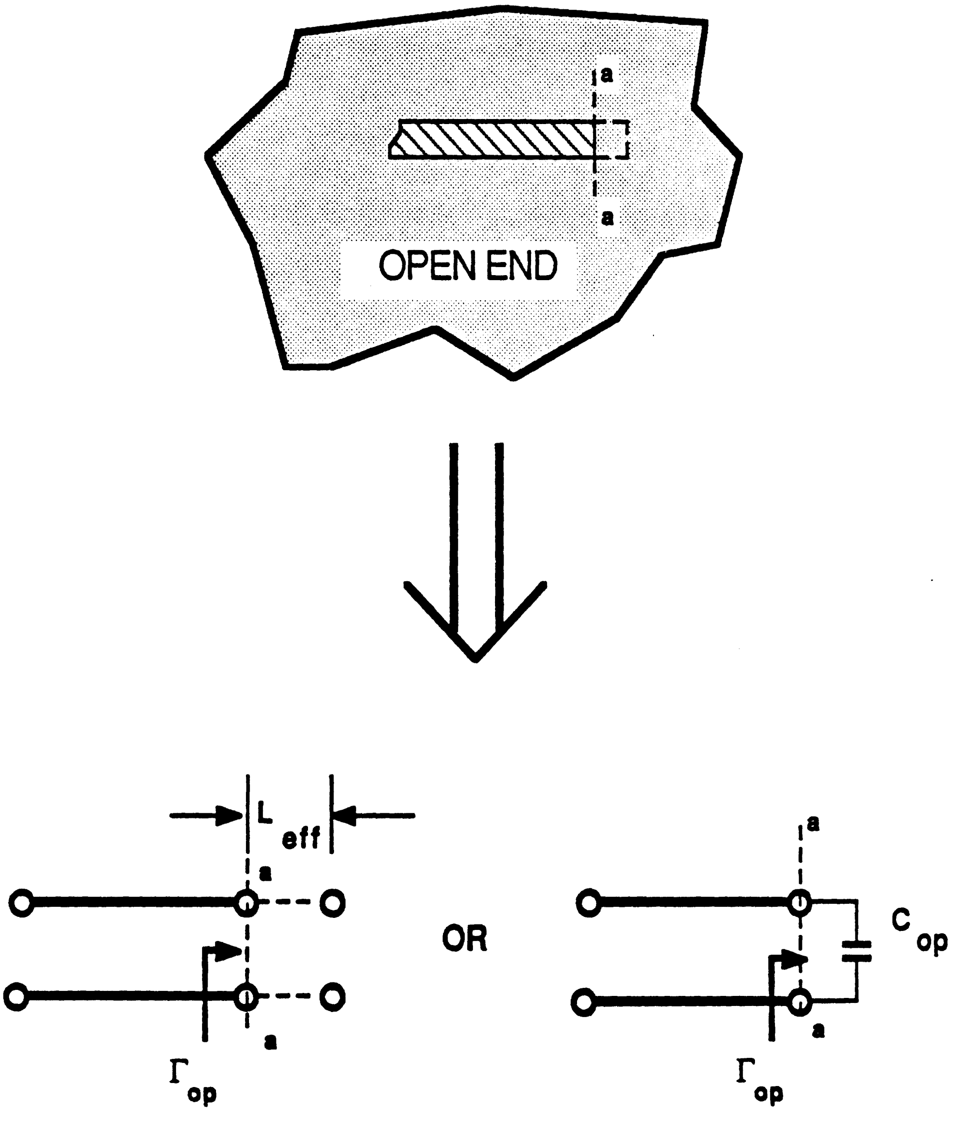

Figure 2.10: Representation for microstrip open end discontinuity.

Once these impedances have been determined, the impedance parameters are found according to

$$z_{11} = \frac{z_{IN}^{e} + z_{IN}^{o}}{2} \tag{2.137}$$

$$z_{12} = \frac{z_{IN}^{o} - z_{IN}^{e}}{2} . \tag{2.138}$$

Derivation of Scattering and Admittance Parameters

The scattering parameters may be derived from the normalized z-parameters by using the following relations

$$S_{11} = S_{22} = \frac{z_{11}^2 - 1 - z_{12}^2}{D} \tag{2.139}$$

$$S_{12} = S_{21} = \frac{2z_{12}}{D} \tag{2.140}$$

where

$$D = z_{11}^2 + 2z_{11} - z_{12}^2 \tag{2.141}$$

Furthermore, it may also be desirable to compute the normalized y-parameters for the network. These may be derived from the scattering parameters using the following relations:

$$y_{11} = y_{22} = \frac{1 - S_{11}^2 - S_{12}^2}{(1 + S_{11})^2 - S_{12}^2} \tag{2.142}$$

$$y_{12} = y_{21} = \frac{2S_{11}S_{12}}{(1 + S_{11})^2 - S_{12}^2} \tag{2.143}$$

2.8 Summary of Theoretical Methodology

In this chapter, the theoretical approach used to compute network parameters for shielded microstrip discontinuities has been described. A combination of reciprocity theorem and the method of moments is used to derive a matrix equation

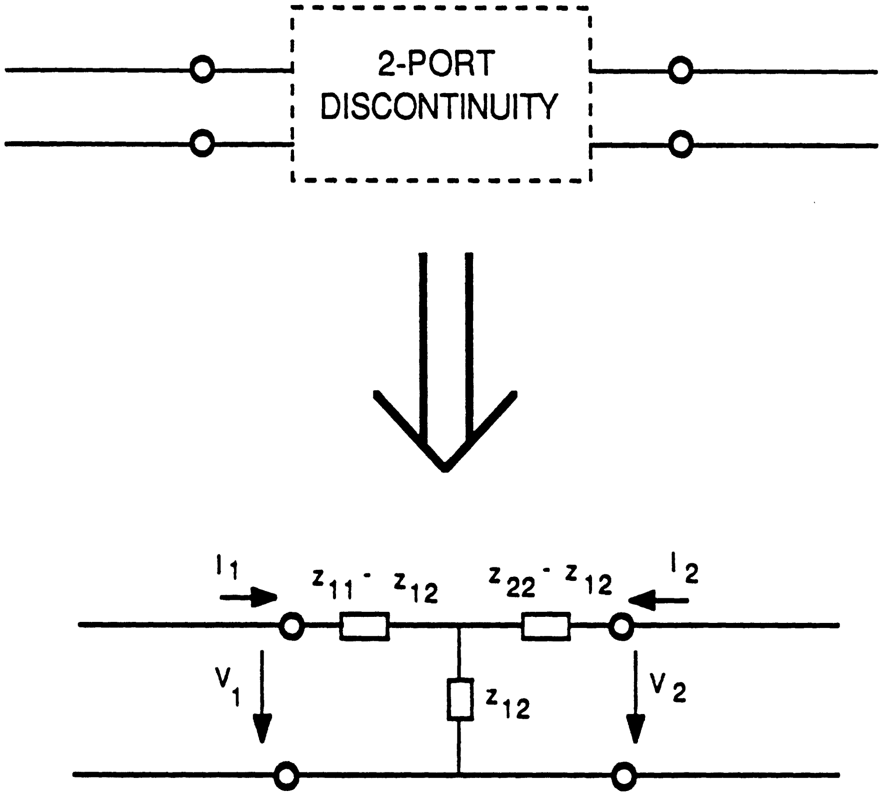

Figure 2.11: Equivalent network representation for generalized 2-port discontinuity.

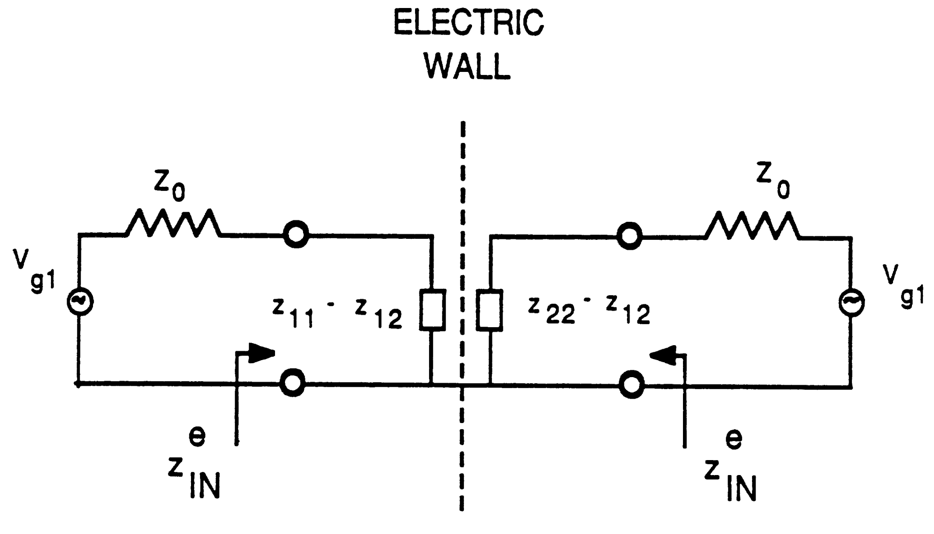

a) Case for even excitation.

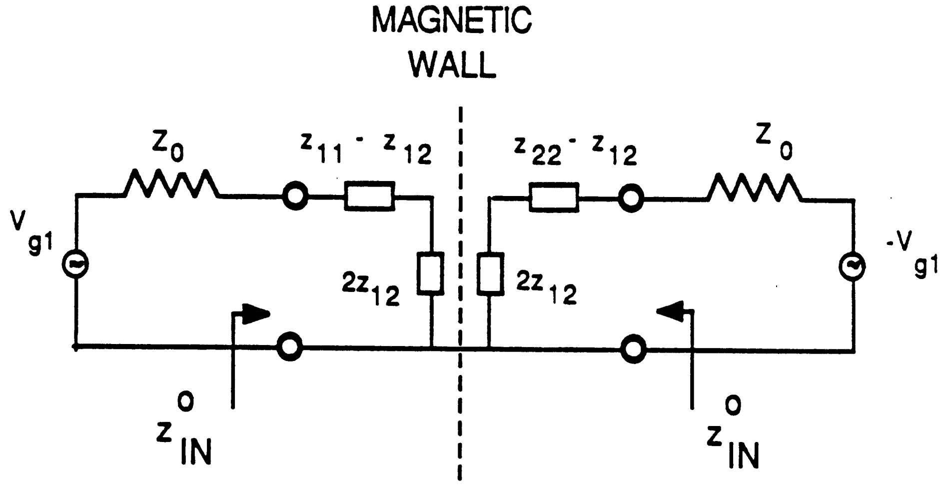

b) Case for odd excitation.

Figure 2.12: The even and odd mode excitations correspond to placing electric and magnetic walls in the center of the two-port structure.

that consists of an impedance matrix, an unknown current vector and an excitation vector. Two types of circuit excitation mechanisms are considered: 1) a coaxial excitation method, and 2) a gap generator method. The matrix equation is solved to compute the current distribution on the conducting strips. Based on this current distribution, the network parameters for one- and two-port discontinuities are calculated.

CHAPTER III

COMPUTATIONAL CONSIDERATIONS

This chapter is divided into two main parts. The first part describes the software design for implementing the theory developed in Chapter 2. First, the formulation used to compute the current distribution is re-arranged to facilitate computer solution. Next, the computer algorithm is discussed, and the computation of the current distribution is described. Algorithms for computing one- and two-port network parameters are also included.

The second part of the chapter focuses on numerical convergence considerations. First, the convergence of the elements of the impedance matrix and excitation vectors is considered. Then a series of numerical experiments are described which are designed to test the stability and convergence of the final results.

3.1 Formulation for Computer Solution

To compute the current distribution given by (2.17) we must first compute the elements of the impedance matrix Z_{qp} and the elements of the excitation vector V_q. The formulations for these elements, given in Chapter 2 are put in a form more convenient for programming below.

3.1.1 Formulation to Compute Impedance Matrix [Z]

The elements of the impedance matrix are given by (2.80). This equation may be re-written in the following form

$$\begin{aligned} Z_{qp} &= \frac{j\omega\mu_0 K^2 l_x^4}{16ab\sin^2 Kl_x}\zeta_q\zeta_p \sum_{n=0}^{NSTOP} \varphi_n \cos k_x x_q \cos k_x x_p \\ &\cdot [\operatorname{Sinc}\left[\frac{1}{2}(k_x+K)l_x\right] \operatorname{Sinc}\left[\frac{1}{2}(k_x-K)l_x\right]]^2 \; [LN(n)] \end{aligned} \tag{3.1}$$

where the vector $LN(n)$ is given by the series

$$LN(n) = \sum_{m=1}^{MSTOP} L_{mn} \tag{3.2}$$

with the series elements L_{mn} given by

$$\begin{aligned} L_{mn} &= \frac{\varphi_n[\sin(k_y Y_0) J_0\left(\frac{k_y W}{2}\right)]^2 \tan k_z^{(1)}h \, \tan k_z^{(2)}(h-c)}{\left[k_z^{(2)} \tan k_z^{(1)}h - k_z^{(1)} \tan k_z^{(2)}(h-c)\right]} \\ &\cdot \frac{\left[k_z^{(2)}\epsilon_r^* \left(1-\frac{k_x^2}{k_1^2}\right) \tan k_z^{(2)}(h-c) - k_z^{(1)}\left(1-\frac{k_x^2}{k_0^2}\right) \tan k_z^{(1)}h\right]}{\left[k_z^{(2)}\epsilon_r^* \tan k_z^{(2)}(h-c) - k_z^{(1)} \tan k_z^{(1)}h\right]} . \end{aligned} \tag{3.3}$$

All of the other parameters are as defined in Chapter 2.

3.1.2 Formulation to Compute Excitation Vector [V]

Excitation vector for coaxial (frill current) excitation

Formulation.— The elements of the excitation vector for the coaxial excitation mechanism (2.84) may be written as

$$\begin{aligned} V_q &= \frac{-V_0\zeta_q K l_x^2}{\ln\left(\frac{r_b}{r_a}\right) 4ab\sin Kl_x} \sum_{n=0}^{NSTOP} \cos k_x x_q \\ &\cdot \operatorname{Sinc}\left[\frac{1}{2}(k_x+K)l_x\right] \operatorname{Sinc}\left[\frac{1}{2}(k_x-K)l_x\right] [MN(n)] \end{aligned} \tag{3.4}$$

where the vector $MN(n)$ is expressed in terms of the series given by

$$MN(n) = \sum_{m=1}^{MSTOP} M_{mn} \, . \tag{3.5}$$

The series elements M_{mn} are given by the following integral

$$\begin{aligned} M_{mn} &= \int\int_{S_f} \mathcal{M}^{i}_{mn}\, d\rho\, d\phi \\ &= \int\int_{S_f^{(1)}} \mathcal{M}^{(1)}_{mn}\, d\rho\, d\phi + \int\int_{S_f^{(2)}} \mathcal{M}^{(2)}_{mn}\, d\rho\, d\phi \qquad (3.6) \end{aligned}$$

In the above, $S_f^{(1)}$ is the portion of the coaxial aperture surface lying above the substrate (region 2) and $S_f^{(2)}$ is the portion of the coaxial aperture surface lying within the substrate (region 1). The integrands $\mathcal{M}^{i}_{mn}$ of (3.6) are given by

$$\begin{aligned} \mathcal{M}^{(1)}_{mn} &= \cos\phi\, c^{(1)}_{zmn} \cos k_y(\rho\cos\phi + Y_c) \sin k_z^{(1)}(\rho\sin\phi + h_c) \\ &\quad - \sin\phi\, c^{(1)}_{ymn} \sin k_y(\rho\cos\phi + Y_c) \cos k_z^{(1)}(\rho\sin\phi + h_c) \qquad (3.7) \end{aligned}$$

for ρ and ϕ in region 1, and

$$\begin{aligned} \mathcal{M}^{(2)}_{mn} &= \cos\phi\, c^{(2)}_{zmn} \cos k_y(\rho\cos\phi + Y_c) \sin k_z^{(2)}(\rho\sin\phi - c'') \\ &\quad - \sin\phi\, c^{(2)}_{ymn} \sin k_y(\rho\cos\phi + Y_c) \cos k_z^{(2)}(\rho\sin\phi - c'')\ . \qquad (3.8) \end{aligned}$$

for ρ and ϕ in region 2. Note that the coefficients $c^{(1)}_{ymn}, c^{(1)}_{zmn}, c^{(2)}_{ymn}$, and $c^{(2)}_{zmn}$, which are given by (2.95)-(2.98), are independent of the integration variables ρ and ϕ.

Numerical Integration.— The elements M_{mn} of the series $MN(n)$ needed to compute the excitation vector for the coaxial (frill current) method are calculated numerically using a 16 point Product Gauss formula approximation [33].

Let us define a pair of dummy variables s and u and a function $\mathcal{F}(s,u)$ such that

$$\int_{\phi_{min}=0}^{\phi_{max}=2\pi} \int_{\rho_{min}=r_a}^{\rho_{max}=r_b} \mathcal{M}^{i}_{mn} d\rho d\phi = \int_{s_{min}=-1}^{s_{max}=1} \int_{u_{min}=-1}^{u_{max}=1} \mathcal{F}(s,u) ds \qquad (3.9)$$

where the correspondence between (u,s) and (ρ,ϕ) is given by the following relations

$$\begin{aligned} u &= \frac{2\rho - (\rho_{max} + \rho_{min})}{\rho_{max} - \rho_{min}} = \frac{2\rho - (r_b - r_a)}{r_b - r_a} \qquad (3.10) \\ \rho &= \frac{1}{2}[u(r_b - r_a) + (r_b + r_a)] \qquad (3.11) \\ s &= \frac{2\phi - (\phi_{max} + \phi_{min})}{\phi_{max} - \phi_{min}} = \phi/\pi - 1 \qquad (3.12) \\ \phi &= \pi(s+1)\ . \qquad (3.13) \end{aligned}$$

The numerical integration can be carried out by generating a set of 16 pairs of points (u_j, s_j) and adding up their contributions according to

$$\int_{\phi_{min}=0}^{\phi_{max}=2\pi} \int_{\rho_{min}=r_a}^{\rho_{max}=r_b} \mathcal{M}^i_{mn} d\rho d\phi \doteq \sum_{j=1}^{16} B_j \mathcal{F}(u_j, s_j) \tag{3.14}$$

where

(u_j, s_j) is the j^{th} pair of integration points

B_j is the weighting factor associated with the j^{th} pair of integration points, and

$\mathcal{F}(s_j, u_j)$ is the transformed integrand found by performing a coordinate transformation on $\mathcal{M}_{mn}$.

Alternatively, once we have chosen the 16 points (s_j, u_j), we can find the corresponding values of ρ and ϕ by (3.11) and (3.13) and obtain the same result. That is

$$\int_{\phi_{min}=0}^{\phi_{max}=2\pi} \int_{\rho_{min}=r_a}^{\rho_{max}=r_b} \mathcal{M}^i_{mn} d\rho d\phi = \sum_{j=1}^{16} B_j \mathcal{M}_{mn}(\rho_j, \phi_j) \tag{3.15}$$

where

$$\begin{aligned} \rho_j &= \frac{1}{2}[u_j(r_b - r_a) + (r_b + r_a)] \\ \phi_j &= \pi(s_j + 1) \end{aligned}$$

and

$$\mathcal{M}^i_{mn}(\rho_j, \phi_j) = \begin{cases} \mathcal{M}^{(1)}_{mn}(\rho_j, \phi_j) & \text{for } -h_c \le \rho_j \sin\phi_j \le -t \\ \mathcal{M}^{(2)}_{mn}(\rho_j, \phi_j) & \text{for } -t \le \rho_j \sin\phi_j \le c'' = c - h_c \\ \text{error condition} & \text{else}\,. \end{cases} \tag{3.16}$$

<u>Gap generator excitation</u>

For the excitation vector, all of the elements of the impedance matrix are set to zero except one, which is given a value of unity. That is,

$$[\mathbf{V}] = \begin{bmatrix} 0 & 0 & \cdots & 1 & \cdots & 0 & 0 & 0 \end{bmatrix}^T . \tag{3.17}$$

Hence, the elements of the excitation vector for this case are given by

$$V_q = \delta_{qg} = \begin{cases} 1 & \text{for } x_q = x_g \\ 0 & \text{else} \end{cases} \tag{3.18}$$

where $x = x_g$ is the position of the gap generator.

3.1.3 Defining the Strip Geometry

The formulations derived above for the computation of the current is general. That is, the same formulation can be used for all of the discontinuities considered in this thesis. However, the strip geometry differs between the cases. The strip geometry is specified by the position vector x_q (or x_p) and the number of sections N_s. The following discussion illustrates how these parameters are determined for various structures.

For an open-ended line (Figure 2.5) and a thru-line (Figure 2.9) the position vector is given by

$$x_p = (p-1)l_x \, . \tag{3.19}$$

The only difference between the two cases is the number of subsections N_s.

The strip geometry for a series gap discontinuity is shown in Figure 3.1. Let N_a be the number of subsections required to compute the current on the left hand strip, with N_s being the total number of subsections. The position vector may be written as

$$x_p = \begin{cases} (p-1)l_x & p \le N_a \\ pl_x + G & p > N_a \, . \end{cases} \tag{3.20}$$

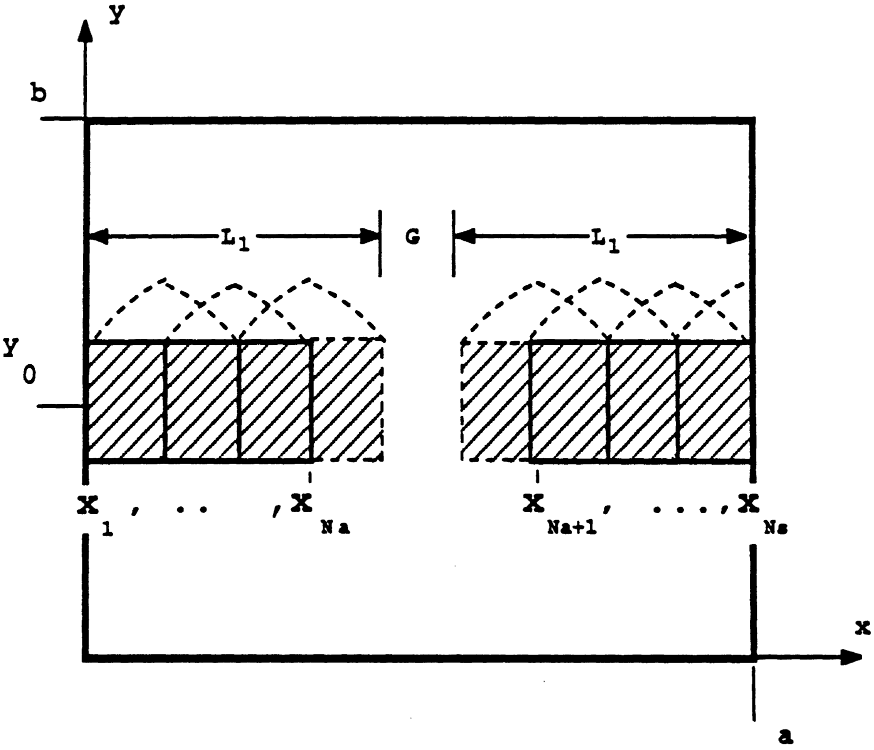

Figure 3.1: Determination of the computational parameters for a series gap is somewhat more complicated than for an open-end or a thru-line.

where G is the length of the gap space.

The strip geometry definition for coupled line structures is only slightly more complicated, than those discussed above. Further details have been omitted.

3.2 Algorithm for Current Computation

The method of moments solution for the current distribution was implemented in a Fortran program named *SHDISC*. The various computation steps are outlined in the flow chart of Figure 3.2 and are summarized below.

3.2.1 Input Data File

A data file is set up first to input the analysis frequencies and the geometrical parameters of the problem to be solved. Also, in this data file several flags may be set or cleared to direct the program flow, and file names are assigned to output files that will contain the results of the computations.

One important flag indicates whether or not the $LN(n)$ and $MN(n)$ vectors are to be calculated or read in from a storage file. These vectors are independent of the subsection length l_x and the strip geometry in the x-direction described by x_p. Hence, once they have been calculated they need not be re-calculated unless the cavity geometry or the frequency has changed. For example, the same $LN(n)$, $MN(n)$ vectors may be used to calculate the current distributions for an open-end discontinuity, a thru-line, and series gap discontinuities with different gap spacings. This is important because approximately 50% to 90% of the computation time (depending on the size of the impedance matrix) is spent on evaluating the vectors $LN(n)$ and $MN(n)$ vectors.

There is also a flag to choose between gap generator and coaxial excitation.

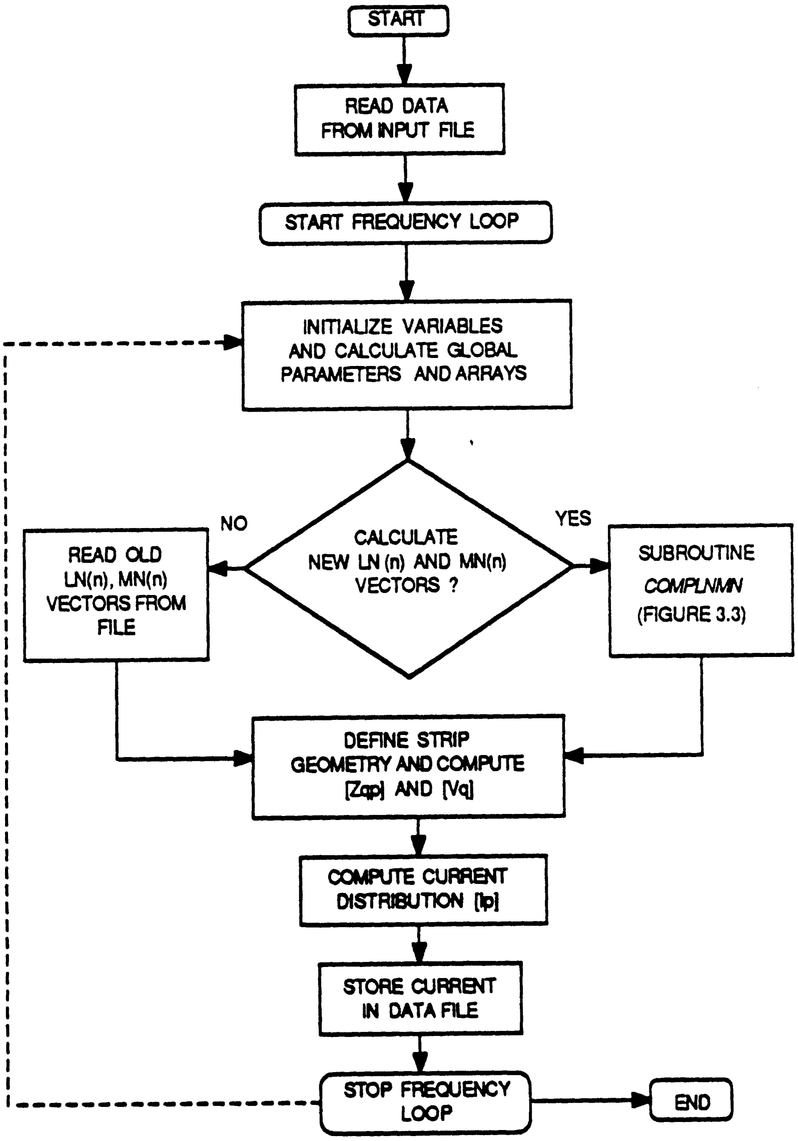

Figure 3.2: Flow chart for program *SHDISC* to compute current distribution.

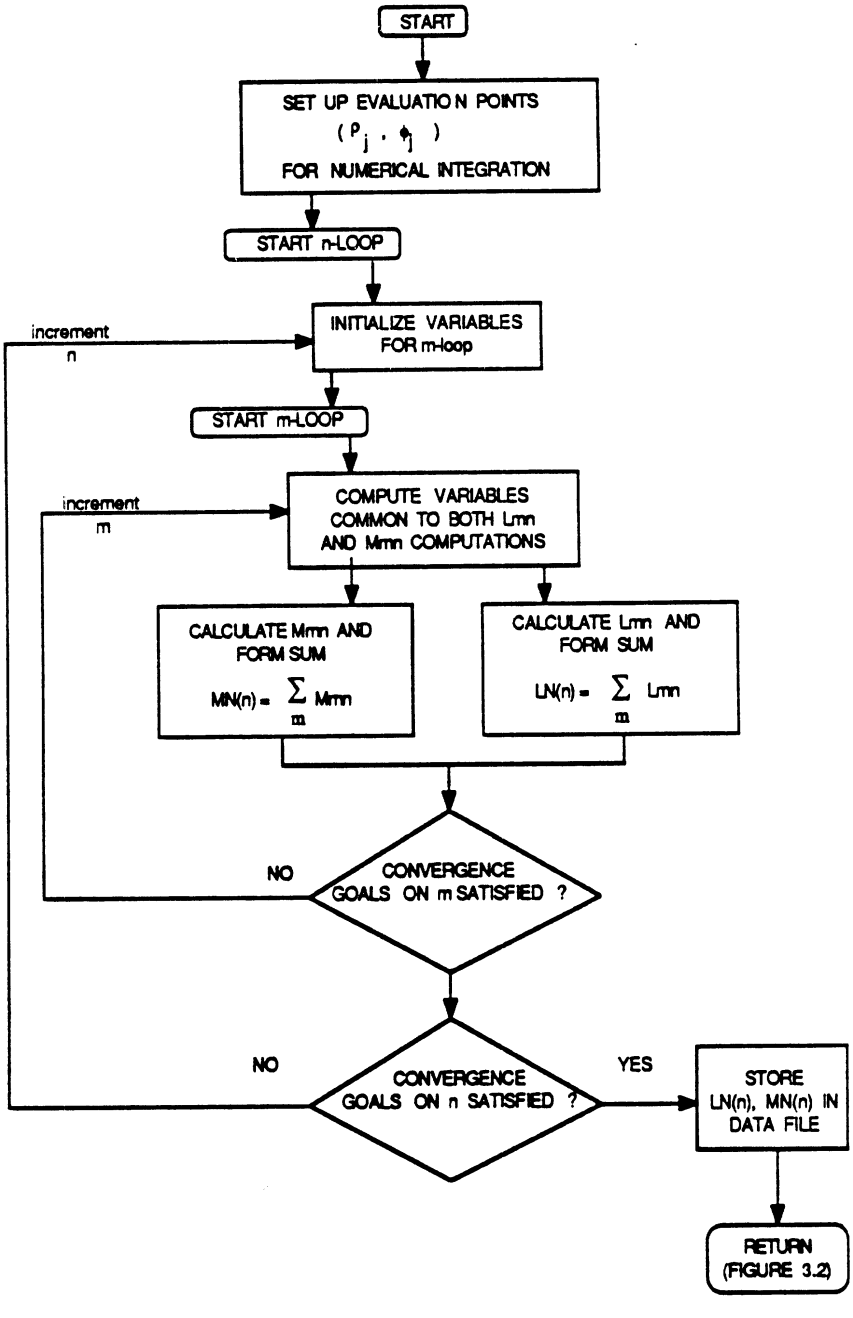

Figure 3.3: Flow chart for subroutine that computes vectors $LN(n)$, and $MN(n)$.

3.2.2 Computation of $LN(n)$ and $MN(n)$ Vectors

After the input data file is read and the global parameters and arrays have been calculated, the program flow is directed to the subroutine "`COMPLNMN`", if the $LN(n)$ and $MN(n)$ vectors have not been previously computed. A flow chart for this subroutine is given in Figure 3.3. The first step is to set up the integration points ρ_j and ϕ_j to be used in the numerical integration for computing M_{mn} as discussed in Section 3.1.2. After this, the computation of $LN(n)$ and $MN(n)$ for each n is carried out by adding up the L_{mn}'s and M_{mn}'s over the summation index m.

The summations over m are terminated in one of two ways. The first is to test error functions which describe the fractional change in $LN(n)$ and $MN(n)$ with the addition of the last L_{mn} and M_{mn} respectively. The other way that the summations over m are terminated is if the specified maximum index value $MSTOP$ is reached before the error goals have been satisfied. The truncation of the computations over the n-index is determined in a similar way. This time, however, the error functions describe the fractional change in the summation of $LN(n)$ and $MN(n)$ over n. As in the summation over m, the computation is also terminated if the maximum n-index $NSTOP$ is reached before the error goal has been reached. For the convergence experiments which are described shortly, the error goals are set to very low values so that the computations on m and n are carried out to $MSTOP$ and $NSTOP$ respectively.

3.2.3 Computation of the Impedance Matrix and Excitation Vectors

After the $LN(n)$ and $MN(n)$ vectors have either been calculated or read in from a storage file, the strip geometry is defined. This is done based on the type of discontinuity to be analyzed and the geometry specified in the input file, as discussed in Section 3.1.3. Next, the elements of the impedance matrix and excitation vector are computed. To gain insight into the nature of these matrices, we will examine plots of a typical impedance matrix and typical one- and two-port excitation vectors.

Typical impedance matrix.— Figure 3.4 shows the amplitude distribution of a typical impedance matrix. It is seen that the amplitude of the diagonal elements is the greatest and the amplitude tapers off uniformly as one moves away from the diagonal. Another observation is that the matrix is symmetric such that $Z_{qp} = Z_{pq}$ for any p and q, and the amplitude for any row or column displays the same distribution with respect to the diagonal element.

Typical excitation vectors.— Figure 3.5 shows the amplitude distribution for the excitation vector for a typical one-port (open-end) structure. It is seen that the amplitude is highest over the first subsection, which is closest to the feed. The amplitude then tapers off rapidly over the subsequent subsections.

The even and odd excitation vectors for a typical two-port (thru-line) structure is shown in Figure 3.6. The amplitude distribution is symmetric around the center of the cavity for the even case, and asymmetric for the odd case. Next to each feed (i.e. near $x = 0$ and $x = a$) the amplitude distribution has the same shape as for the one-port case, which is expected from (2.120).

3.2.4 Computation of the Current Distribution

In the matrix equation (2.17), which describes the solution for the current distribution, matrix inversion and multiplication is implied. While this is correct mathematically, it is not efficient numerically. There are several approaches for solving systems of equations without matrix inversion. Most of these are readily

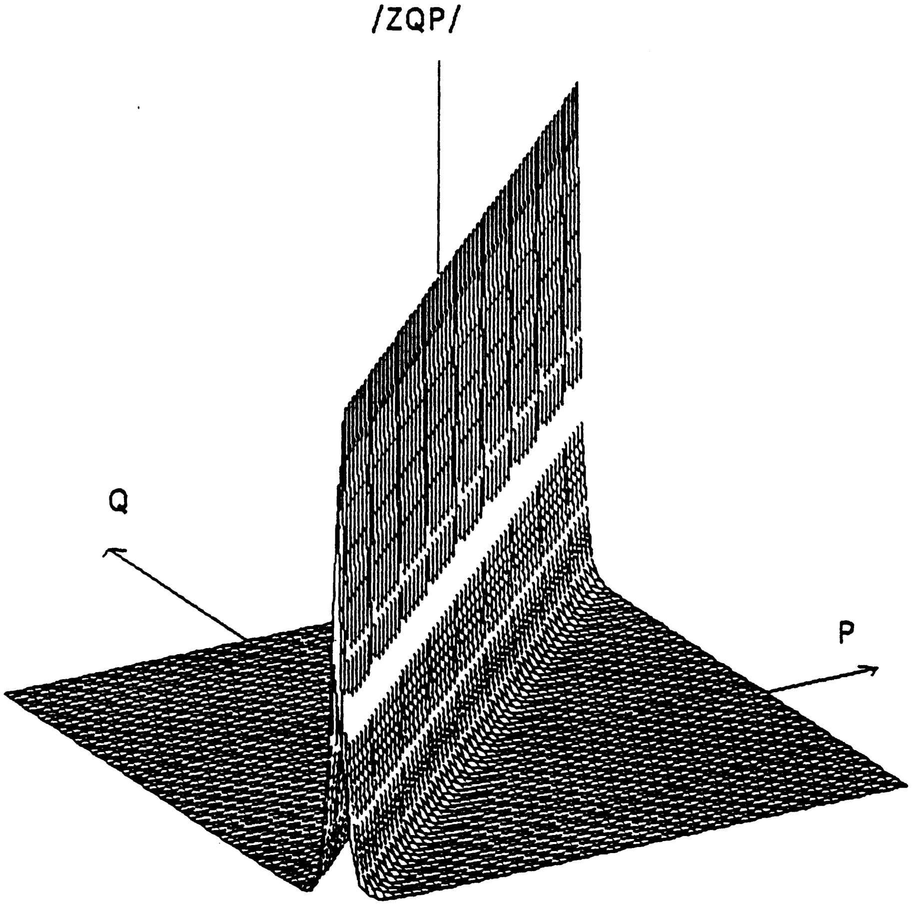

Figure 3.4: A plot 3-dimensional plot of the impedance matrix for a typical open-end shows that it is diagonally dominant and well behaved.

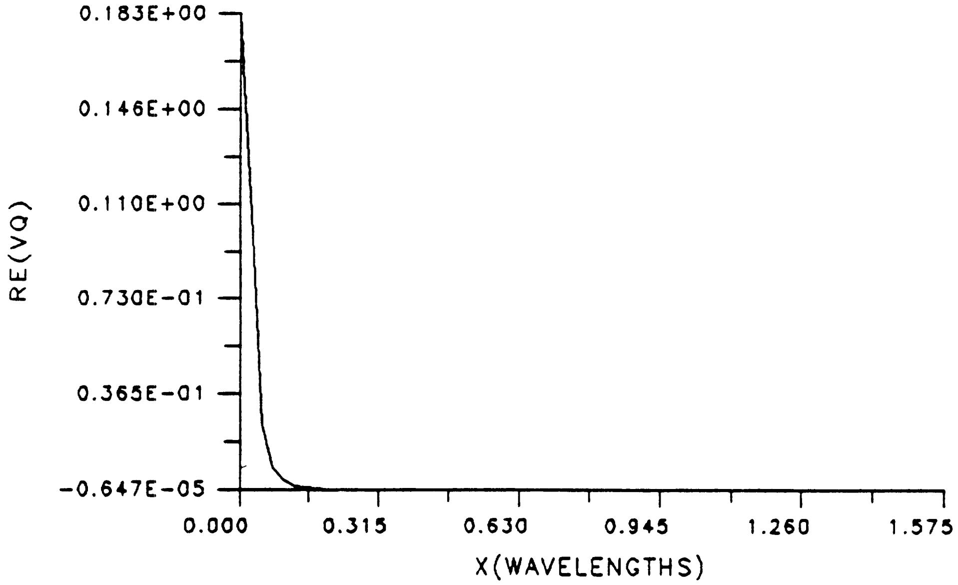

Figure 3.5: The amplitude distribution for the excitation vector is highest for Q=1, which corresponds to the position of the feed.

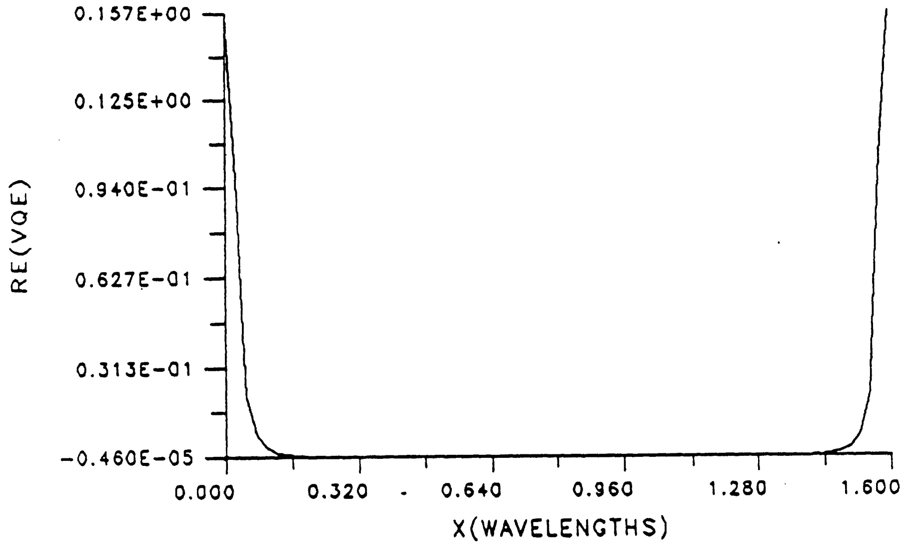

a. The amplitude distribution for the even case is symmetric

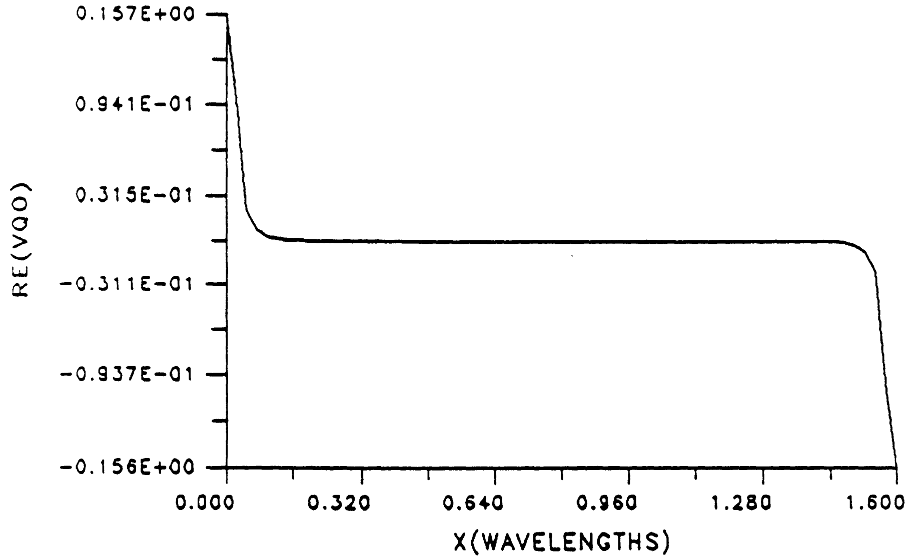

b. The amplitude distribution for the odd case is asymmetric

Figure 3.6: Excitation vector for two port coaxial excitation.

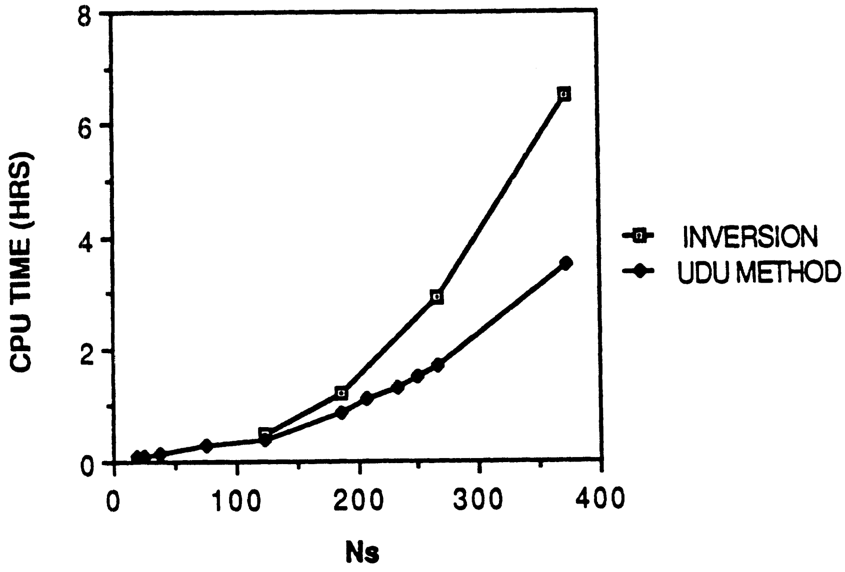

Figure 3.7: A comparison of computation times for two different methods of matrix equation solution shows the advantage of using alternatives to matrix inversion .

available as subroutines in standardized libraries (e.g. Numerical Analysis and Applications Software -NAAS).

For this work, a subroutine was employed that uses UDU factorization and back substitution. This method (also called LDL in some texts) takes advantage of the symmetry of the impedance matrix to speed computations. Figure 3.7 shows a comparison of computing times observed for a typical problem using matrix inversion versus the UDU factorization method. These computations were performed on an Apollo DN3000 work station. The speed advantage of the latter method becomes increasingly significant after a matrix size of about 150 × 150. Matrix sizes for problems studied in this thesis typically vary between about 50 × 50 and 250 × 250.

Typical open-end current distribution.— When the impedance matrix of Figure 3.4 is inverted, the amplitude distribution is as shown in Figure 3.8. Multiplying by the excitation vector of Figure 3.5 yields the current distribution of

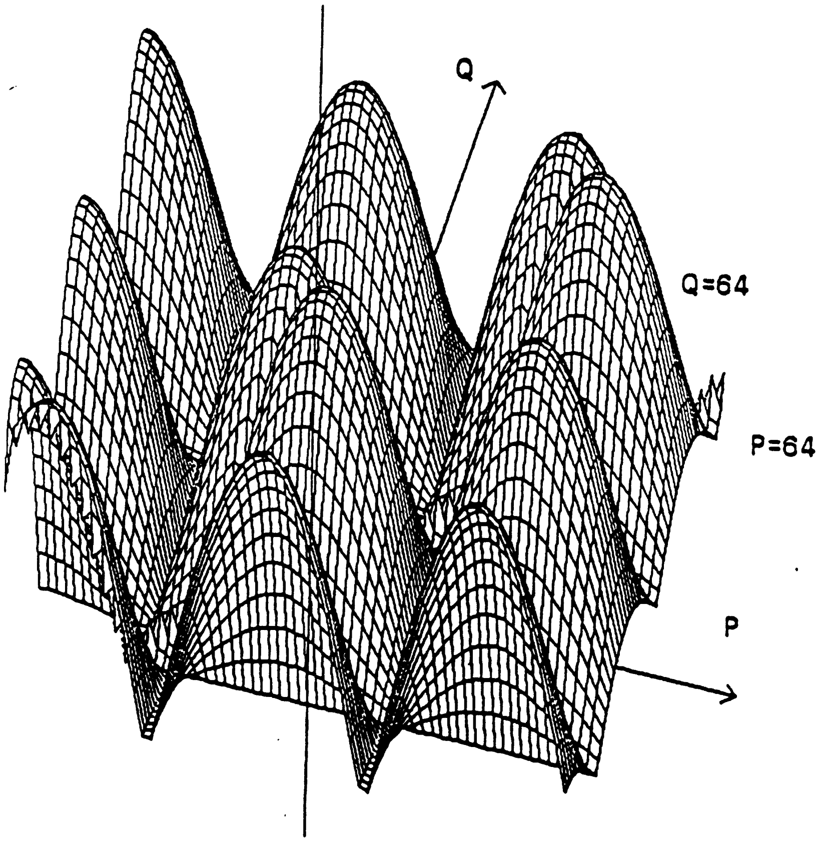

Figure 3.8: This 3-dimensional plot of the magnitude of the elements of the inverted impedance matrix shows that each row and column has a sinusoidal shape.

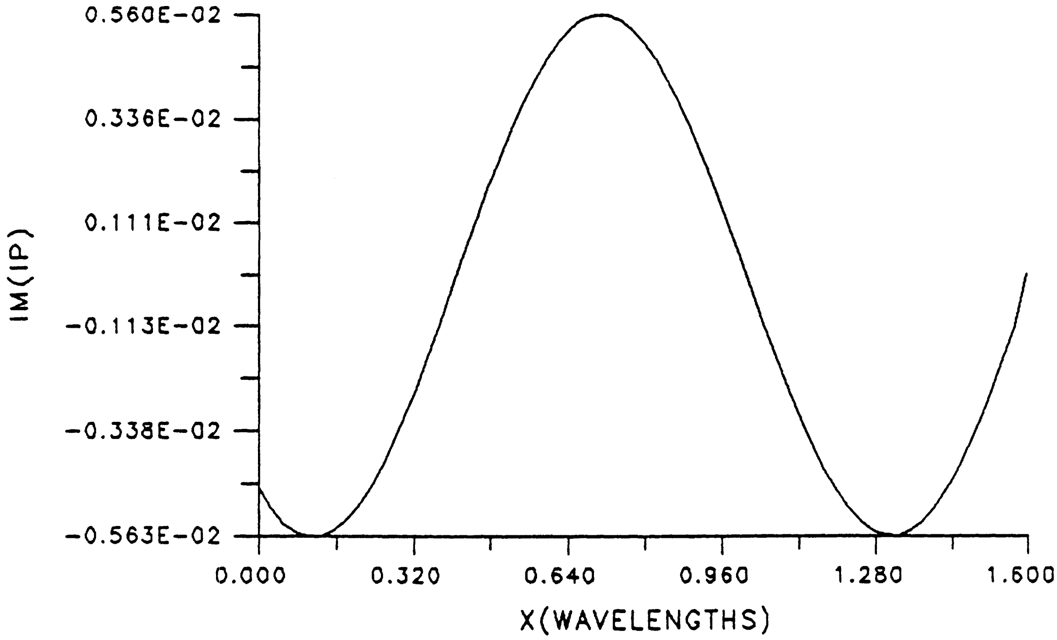

Figure 3.9: The imaginary part of current distribution for an open-end discontinuity displays a sinusoidal behavior.

Figure 3.9. It can be seen that the sinusoidal shape of the current has the same general shape exhibited by the first column of the impedance matrix. This is not surprising given the shape of the excitation vector. The multiplication can be thought of as a weighted summation of the first few rows of the inverted impedance matrix.

A typical current for gap generator excitation is shown in Figure 3.10. For this computation the gap generator was located at a short distance ($\sim .3\lambda_d$)from the wall. The current is seen to be discontinuous around the region of the gap generator, however, is otherwise well behaved. The effect of this discontinuity can be minimized by locating the gap generator source at the beginning at the beginning of the first subsection ($q = 1$).

Typical two-port current distributions.— The current computation for two-port structures is similar. In this case, even and odd currents are computed using excitation vectors shaped like those of Figure 3.6. The current distributions for a

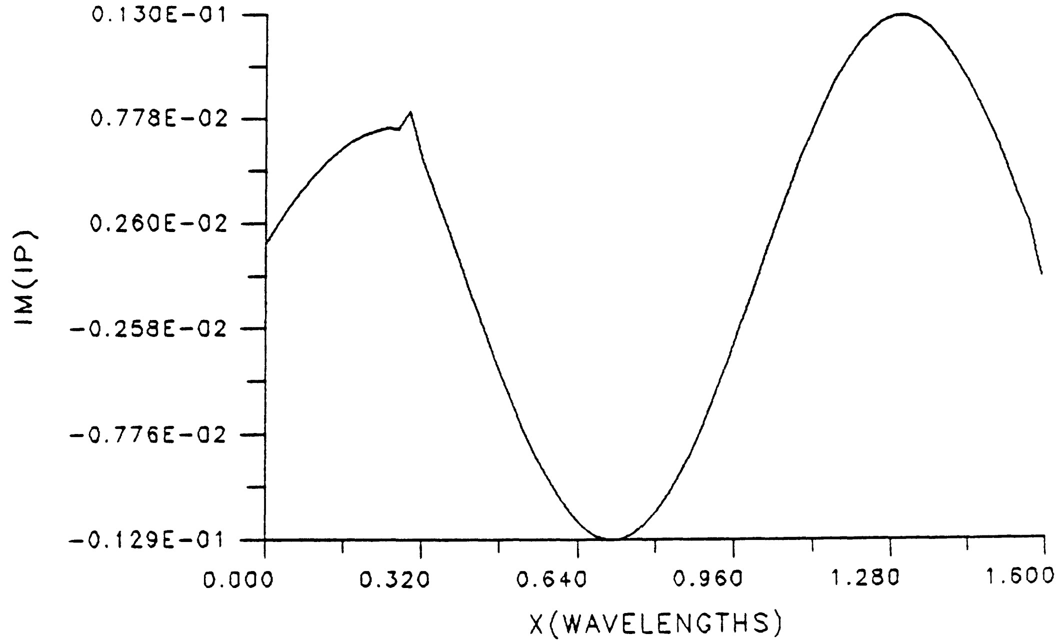

Figure 3.10: The current for gap generator excitation is discontinuous around the position of the source, but is otherwise well behaved.

series gap are shown in Figure 3.11. Due to the symmetry of the structure, the even current is symmetric, and the odd current is asymmetric around the middle of the cavity.

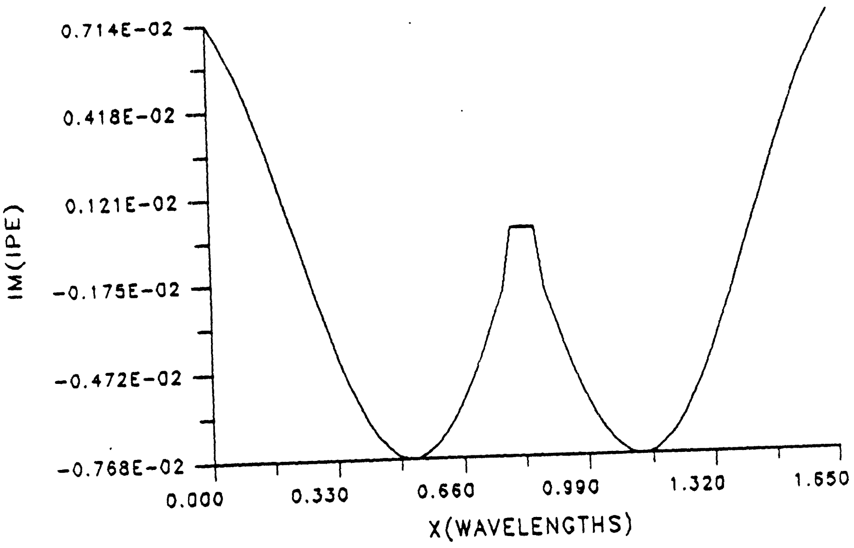

a. Even current

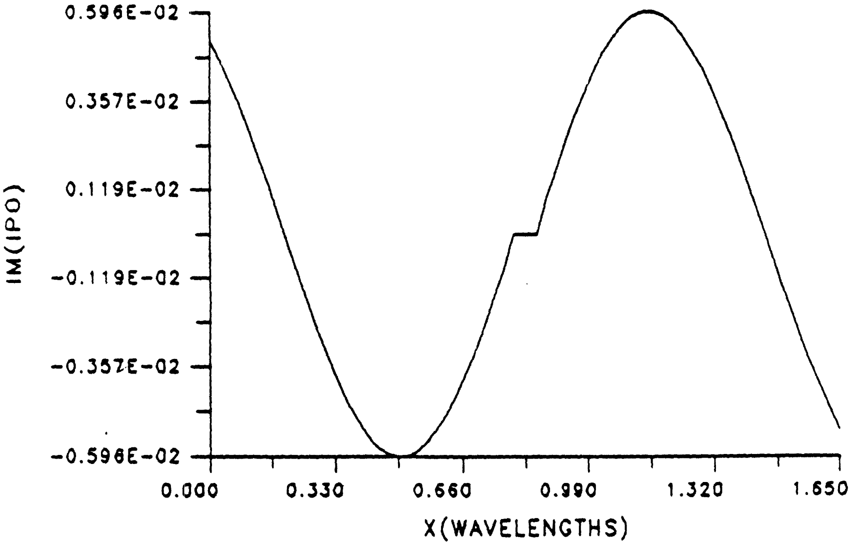

b. Odd current

Figure 3.11: Current distributions for a typical series gap discontinuity

3.3 Algorithms for Computing Network Parameters

3.3.1 Algorithm to Compute One-port Network Parameters

A Fortran program was written to compute one-port network parameters as discussed above [1]. A flow chart for the program *ONENET* is shown in Figure 3.12. The program first reads in the current distribution from a storage file created with *SHDISC*.

The next step is to perform a cubic spline fit to the current. This is necessary to accurately determine the positions of the minimum and maximum current values. The subroutine used to perform this spline fit is a modification of a program appearing in [34]. In a cubic spline fit, each interval between two points is represented by a different cubic equation of the form

$$I(x) = a_p(x - x_p)^3 + b_p(x - x_p)^2 + c_p(x - x_p) + d_p \tag{3.21}$$

Once the spline fit coefficients a_p, b_p, c_p, and d_p have been found, determining the positions of the current minima and maxima is straightforward. First, the two points surrounding an extremum are found by searching for a sign change in the slope of the current ($I'(x_p) = c_p$) evaluated at successive points. Next, the actual position of the extremum is found to within the accuracy of the curve fit. This is done by finding the root of $I'(x) = 0$ which lies within the interval $(x_p \leq x \leq x_{p+1})$.

The microstrip wavelength (λ_g) is then computed as the average distance between each pair of current minima and maxima. With the knowledge of the wavelength, the effective dielectric constant ϵ_{eff}, and the phase constant β_g can be calculated according to (2.127) and (2.126).

---

[1] In this thesis the only one-port structure considered is the open-end discontinuity.

Finally, the equivalent circuit parameters for the open-end are computed. To do this, the reflection coefficient Γ_{op} and impedance z_{op} are calculated. Then, the effective length extension and equivalent capacitance are computed from (2.132) and (2.135) respectively.

3.3.2 Algorithm to Compute Two-port Network Parameters

The program for computing two-port network parameters *TWONET* is very similar to that for one-port parameters. A flow chart is given in Figure 3.13. The first step is to read in the even and odd current distributions. These are analyzed separately. The analysis is performed in the subroutine *SPLIMP* following the same steps as in the one port case to compute λ_g, β_g, ϵ_{eff}, $\Gamma(L_1)$, and $z(L_1)$ for each of the distributions. Next, the impedance, scattering, and admittance parameters are calculated using the relations of Section 2.7. This whole process is repeated for each of the analysis frequencies.

3.4 Convergence Considerations Z_{qp} and V_q

In this section, the convergence of the elements of the impedance matrix Z_{qp} and the excitation vector V_q are discussed. The series involved in the computation of these elements are functions of two summation indices m and n. In theory, the summations are infinite; however, for computation we must truncate them at some point where the error due to this truncation is negligible.

3.4.1 Convergence of Impedance Matrix Elements Z_{qp}

We will now consider the convergence behavior of the matrix with respect to the summation indices m and n.

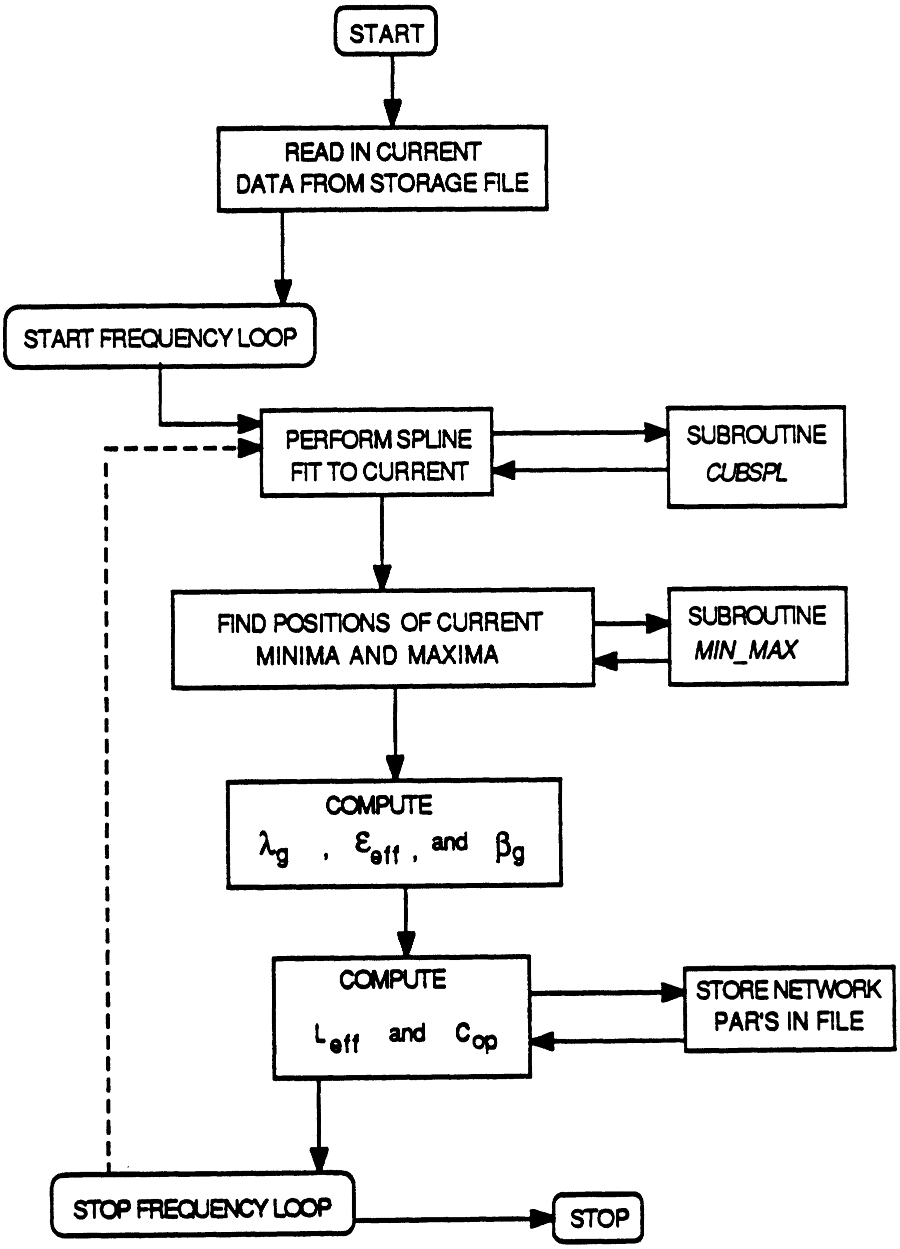

Figure 3.12: Flow chart for computation of one-port network parameters

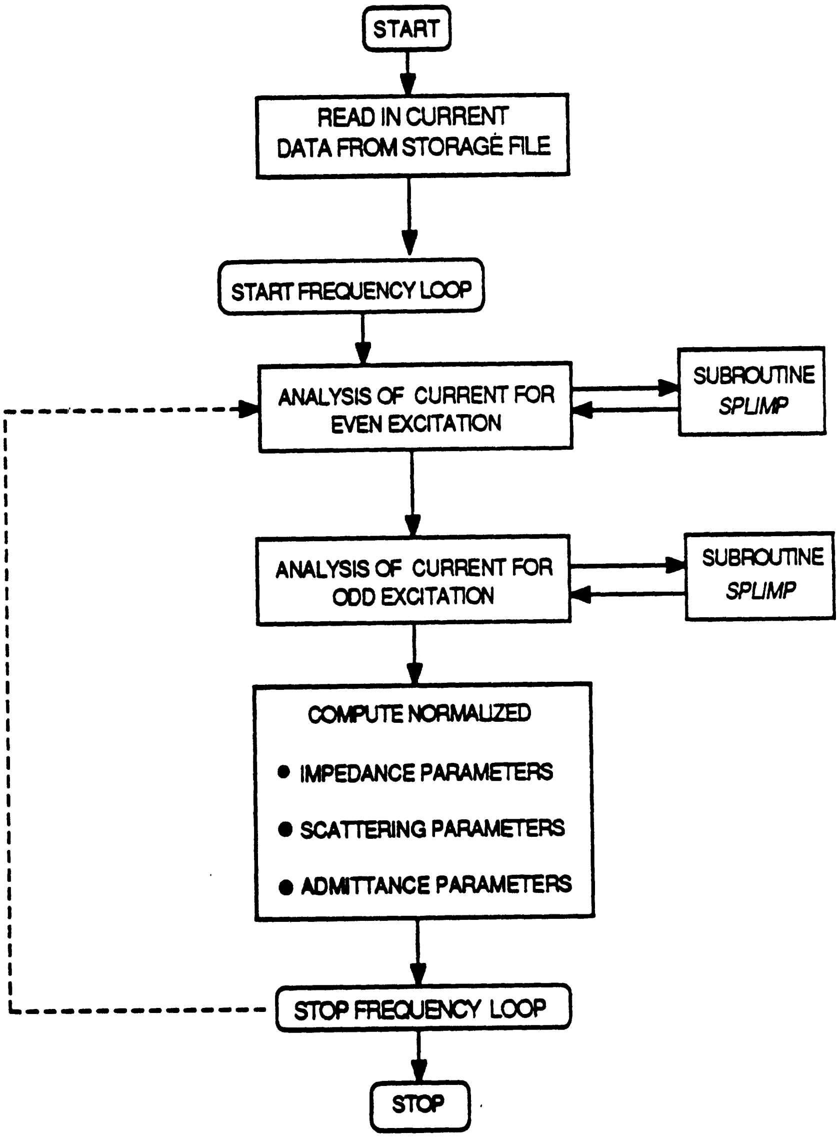

Figure 3.13: Flow chart for computation of two-port network parameters

Convergence of Z_{qp} with m.— As can be seen from (3.1), the convergence of the impedance matrix with respect to m is described by the convergence of $LN(n)$ with m. Recall that $LN(n)$ is given in terms of the series of (3.2)

$$LN(n) = \sum_{m=1}^{MSTOP} L_{mn} \,. \tag{3.22}$$

Figure 3.14 shows the typical variation of $LN(n)$ with m and n. Most of the contributions from $LN(n)$ to the impedance matrix are concentrated in the first several n values. The convergence over m is good. Further analysis, for this case shows that the change in $LN(n)$ appears to be negligible after about $m = 500$.

Convergence of Z_{qp} with n.—

This computation of Z_{qp} over n is illustrated for a typical impedance matrix in Figure 3.15. This figure shows the convergence behavior for one row (the 32^{nd}) of the 64 x 64 element impedance matrix of Figure 3.4. This behavior is representative of that for any row. After only a few terms the diagonal element ($p = q = 32$) rises above the others, and after adding 100 terms the amplitude distribution is well formed.

3.4.2 Convergence of Excitation Vector Elements V_q

We now turn our attention to the convergence of the excitation vector. In the following discussion, we consider only the one-port excitation vector since the two-port excitation vectors are derived from the one-port case (Section 2.6.4).

Convergence of V_q with m.—

As can be seen from examining (3.4), the convergence of V_q with respect to m is described by the convergence of $MN(n)$ with respect to m. $MN(n)$ is given by (3.5)

$$MN(n) = \sum_{m=1}^{MSTOP} M_{mn} \,. \tag{3.23}$$

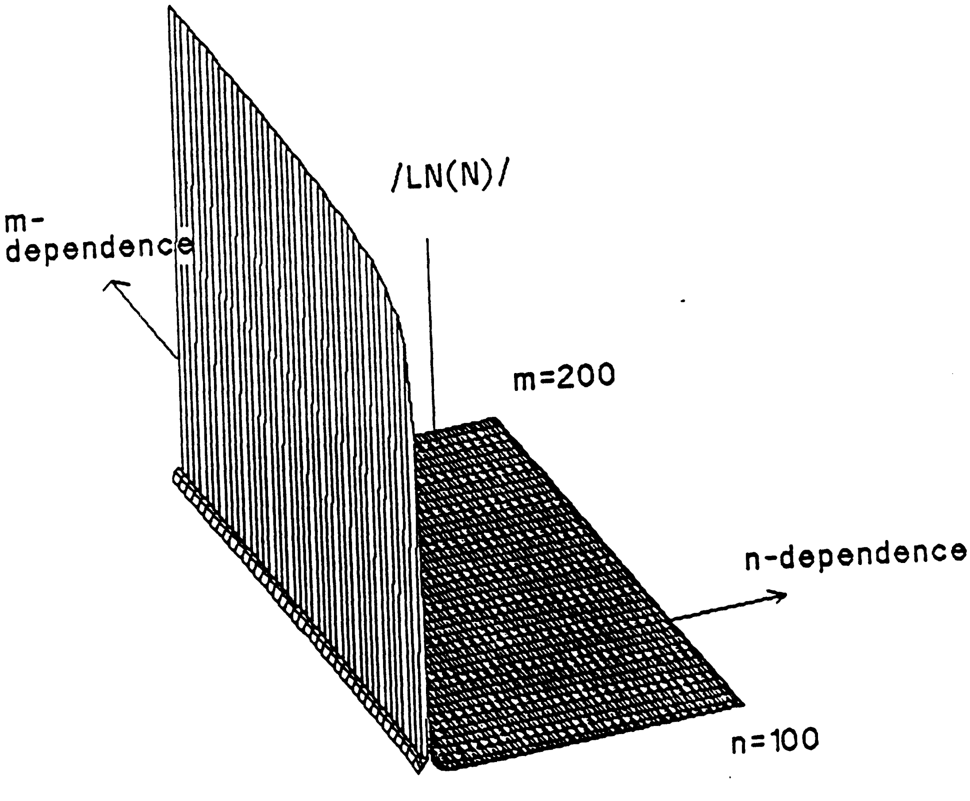

Figure 3.14: 3-dimensional plot illustrating computation of $LN(n)$ over m and n.

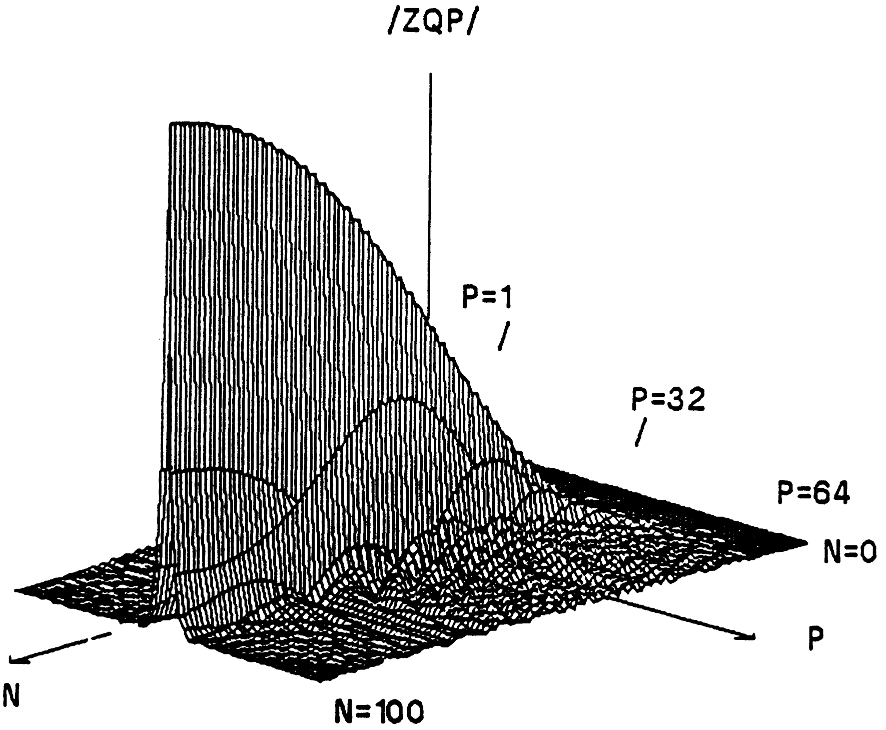

Figure 3.15: The formation of an impedance matrix for one row ($Q = 32$) versus the summation index n.

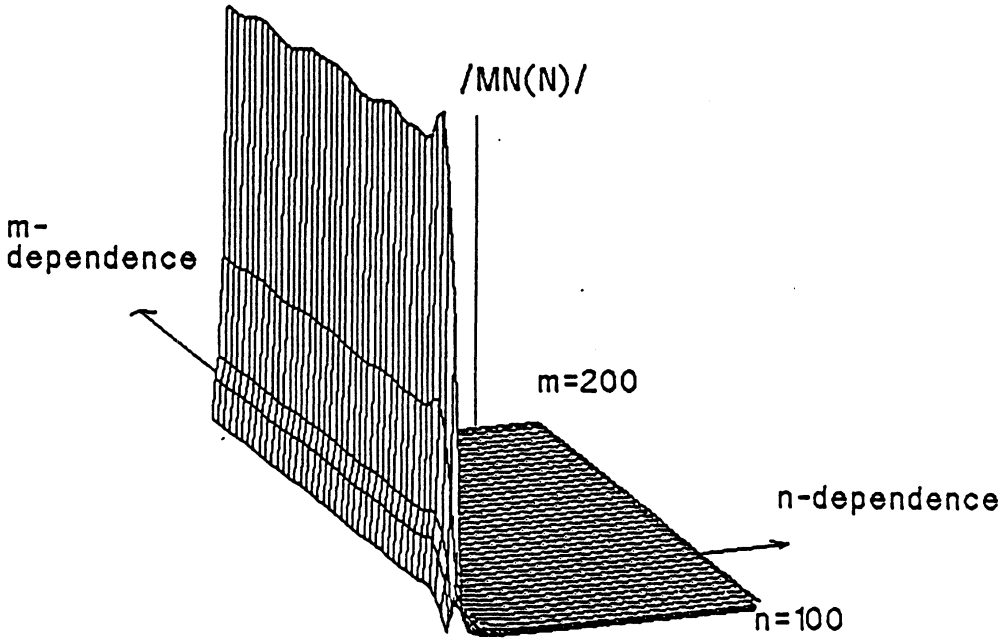

Figure 3.16: 3-dimensional plot illustrating computation of $MN(n)$ over m and n.

A plot of $MN(n)$ with m and n, shown in Figure 3.16, shows that the convergence of MN(n) on m is not as good as that for $LN(n)$. The series exhibits a damped oscillation around the convergent value, which may take more than 1000 terms to determine. However, good results for network parameters are obtained by stopping at $m = 500$. This is discussed further in the section 3.5.

Convergence of V_q with n.— Figure 3.17 illustrates the computation of the elements of V_q as a function of the summation index n. As in the case of the impedance matrix, the amplitude distribution for the excitation vector has been well defined after adding the first 100 terms.

3.5 Convergence of Network Parameters

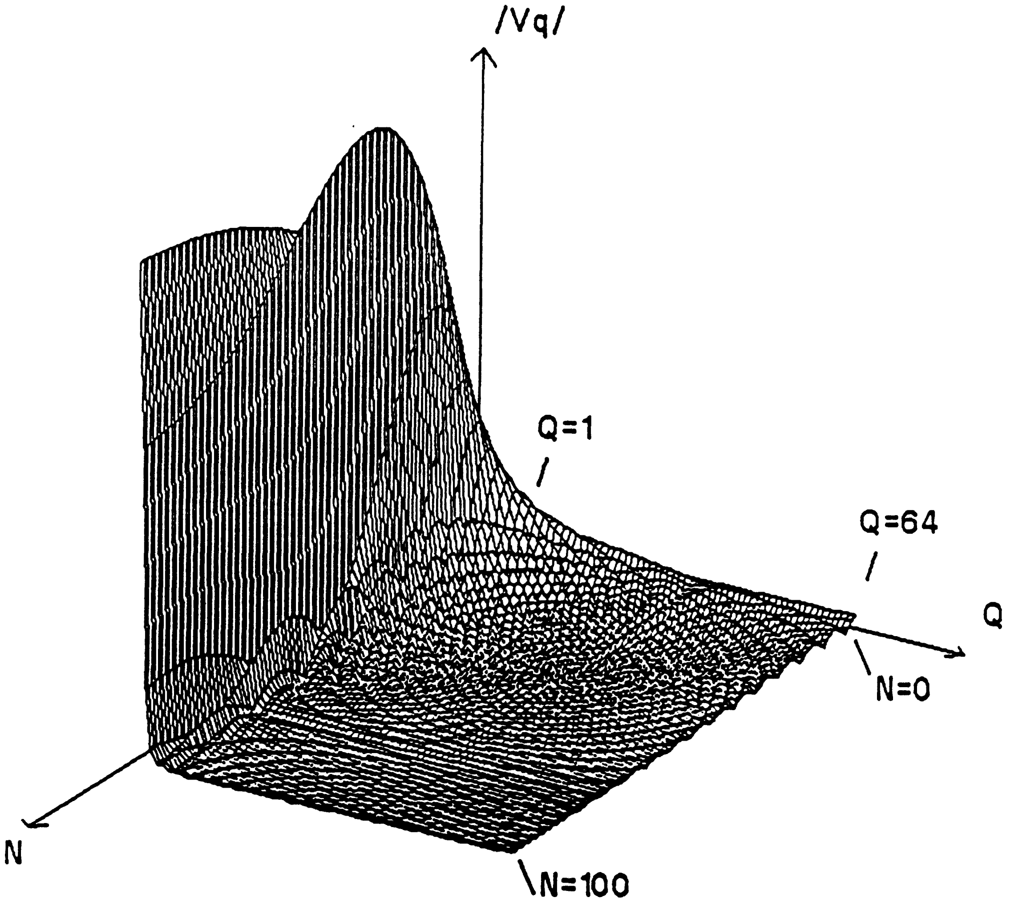

Figure 3.17: The formation of an excitation vector versus the summation index n.

The previous section described how the elements of the impedance matrix and excitation vectors converge on the summation indices m and n. This convergence is important to examine; yet the question remains: how are the final results affected by various convergence related parameters?

To answer this question, a series of numerical experiments were carried out. These experiments investigate the convergence behavior of the network parameters for an open-end discontinuity with respect to the number of samples per wavelength N_x $(= 1/l_x)$, and the truncation points $NSTOP$, $MSTOP$ for the summations over n and m respectively. From an efficiency point of view, we would like to minimize both the sampling rate and the truncation points. To examine these issues, of numerical experiments were performed at different frequencies and for different geometries, and a summary is given here.

In this summary, the numerical experiments have been grouped into three separate categories which are named Experiment A, Experiment B, and Experiment C. Each of these explores a different aspect of the convergence behavior [2].

3.5.1 Numerical Experiment A: Effect of K-value

Objective

In the first experiment, the objective was to investigate how the value for K (K-value) used in the basis functions (2.8) and (2.9) affects the convergence on N_x of the L$_{eff}$ and ϵ_{eff} computations.

Procedures and results

---

[2] Unless otherwise noted, the parameters used for the plots shown in this section are the following: $\epsilon_r = 9.7, W = h = .025'', a = 3.5'', b = c = .25'', f = 18\text{GHz}$.

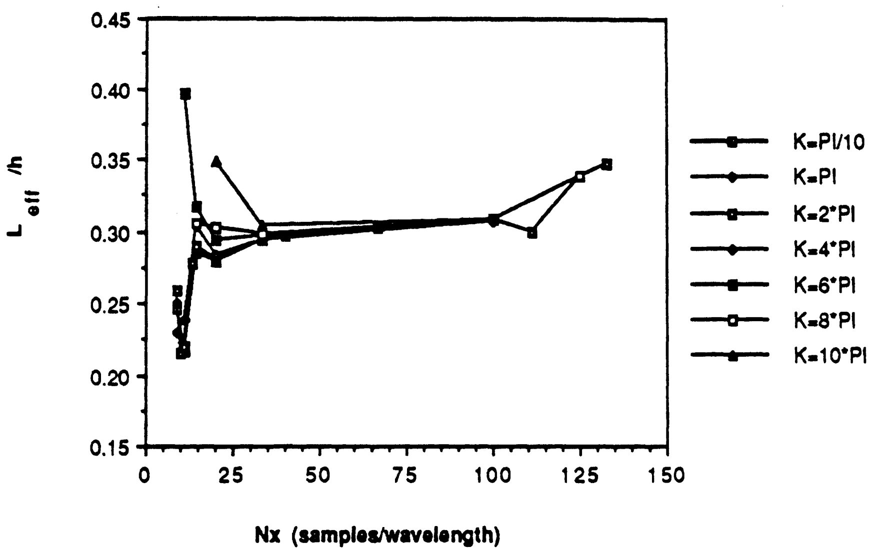

Figure 3.18: Convergence of L_{eff} versus sampling for several different K-values.

Using the programs discussed previously, data was generated to plot L_{eff} and ϵ_{eff} versus N_x for several different K-values. Figure 3.18 shows the convergence behavior of L_{eff} for a typical case. It is seen that a relatively flat convergence region exists for all the K-values between about 40 and 100 samples per wavelength (λ_d). Outside this region the solution behaves differently for different K-values.

At first glance, it appears that the best convergence is achieved for higher K-values (e.g. $K = 8\pi$); however, quite the opposite conclusion results from examining the ϵ_{eff} computation. As can be seen from Figure 3.19, the best convergence for ϵ_{eff} is obtained for low K-values.

Based on these observations, it was theorized that it may be possible to improve the L_{eff} computation by choosing a larger K-value at the end of the line, while keeping the K-value over the rest of the line at a low value. This was investigated by modifying the program *SHDISC* to use $K = 2\pi$ for all the subsections except

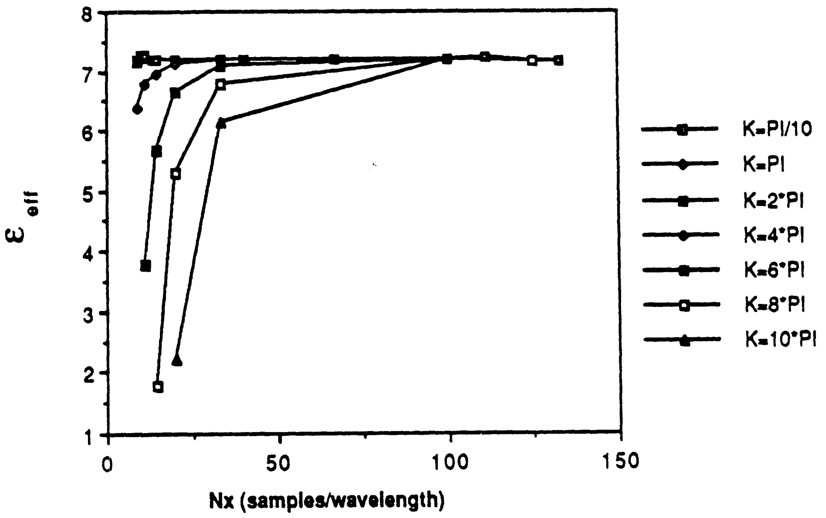

Figure 3.19: Convergence of ϵ_{eff} versus sampling for several different K-values.

the last $\lambda_d/8$ portion of the strip. Over the last $\lambda_d/8$ portion, the K-value was varied to examine its effect on the L_{eff} and ϵ_{eff} computations. It was found that a constant value of $K = 2\pi$ over all the subsections yields the best convergence behavior for L_{eff}. As expected, changing the K-value just at the end of the strip had very little effect on the ϵ_{eff} result.

Some comments will now be made on the L_{eff} convergence behavior for low and high sampling rates. Referring back to Figure 3.18, it was found that a minimum sampling limit was observed that varies with the K-value. This limit may be expressed by the following

Observation III.1 *For the sinusoidal basis functions of (2.8) and (2.9), there exists a lower sampling limit which depends on K and l_x as follows*

$$Kl_x < \frac{\pi}{2} \tag{3.24}$$

or

$$N_x > \frac{2K}{\pi}. \tag{3.25}$$

If the sampling rate is lower than this limit, obvious errors in the current distribution and the network parameters (e.g. negative L_{eff}*) result.*

This limit has a physical basis in that if it is violated, more than one quarter of a sinusoid is represented by each half basis function. This means that the basis function tries to peak before it reaches the end of the section.

Before examining the convergence behavior for high sampling rates, it will be useful to define the matrix condition number. The matrix condition number gives a measure of the relative sensitivity of the errors in the matrix solution to a change in the matrix elements. It may be defined as [35]

$$\mathrm{Cond}\,(\mathbf{Z}) = ||\mathbf{Z}|| * ||\mathbf{Z}^{-1}||\,. \tag{3.26}$$

Matrices with low condition numbers are said to be *well conditioned*; matrices with high condition numbers are said to be *ill conditioned.* In general the condition number, and therefore the accuracy of the matrix solution, degrades as the matrix size increases.

This degradation in the condition number is responsible for the non-convergent behavior exhibited in Figure 3.18 for high sampling rates. Figure 3.20 shows how the reciprocal condition number (RC $= 1/\mathrm{Cond}(\mathbf{Z})$) is degraded as Nx increases. As N_x increases, the matrix order (N_s) also increases for a fixed physical length of line. Hence, the gradual degradation in the condition number observed out to about $N_x = 130$ was expected.

Not expected was the large jump in RC which occurs at about 140 samples per wavelength. This jump indicates that the matrix suddenly becomes ill conditioned and, the associated current distribution is completely erratic. This erratic current condition was found to be independent of K, however, as discussed in the next section it is directly related to the length of the cavity a, and the number of terms added in the summation over n ($NSTOP$).

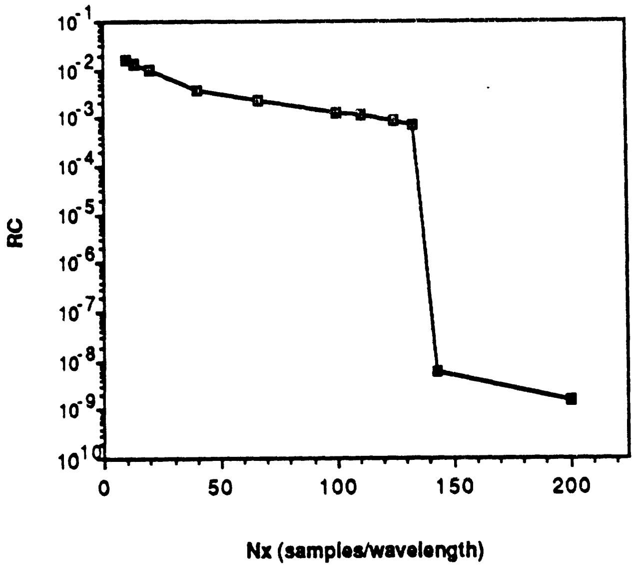

Figure 3.20: Reciprocal matrix condition number versus sampling.

3.5.2 Numerical Experiment B: L_{eff}, ϵ_{eff} Convergence on n and m

Objective

The objective of this next experiment was to determine the appropriate truncation points $NSTOP$ and $MSTOP$ for the double summations involved with computing the impedance matrix and excitation vector elements.

Procedures and Results

First, several program runs were executed for different values of $NSTOP$, with $MSTOP$ fixed at 1000. Data was generated to plot L_{eff} and ϵ_{eff} versus n for several l_x values. Figure 3.21 shows that for all the l_x values $NSTOP = 500$, gives good convergence. The same can be said for the convergence of ϵ_{eff} with n

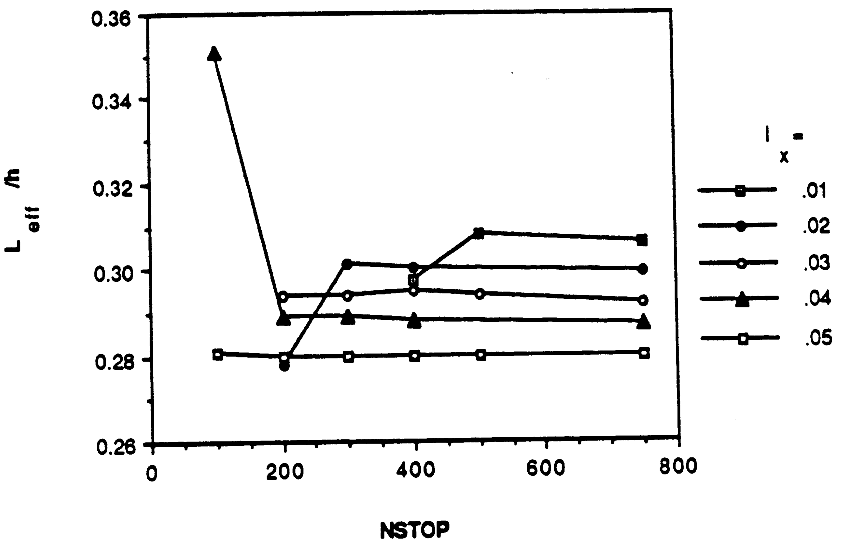

Figure 3.21: The convergence of L_{eff} on n was found to depend on l_x, but is satisfied in all cases after 500 terms have been added.

(Figure 3.22).

To investigate the convergence behavior with respect to the summation index m, $NSTOP$ was fixed at 500, and the program was run for different values of $MSTOP$. Figure 3.23 shows that L_{eff} converges well on m also after about 500 terms. Unlike the convergence on n behavior, the convergence on m does not depend on l_x. The convergence behavior of ϵ_{eff} (not shown) on m, was found to be similar to that for L_{eff}.

The dependence of the n convergence on l_x observed in Figures 3.21 and 3.22 warrants further consideration. It is seen that for large l_x values the solution converges faster on n. This variation of the convergence behavior with different l_x values is also reflected in the reciprocal condition number as seen in Figure 3.24. It is also seen that the condition for erratic current, discussed in Section 3.5.1, is a function of both $NSTOP$ and l_x. Further experimentation with different geometries and frequencies, lead to the formulation of the following observation:

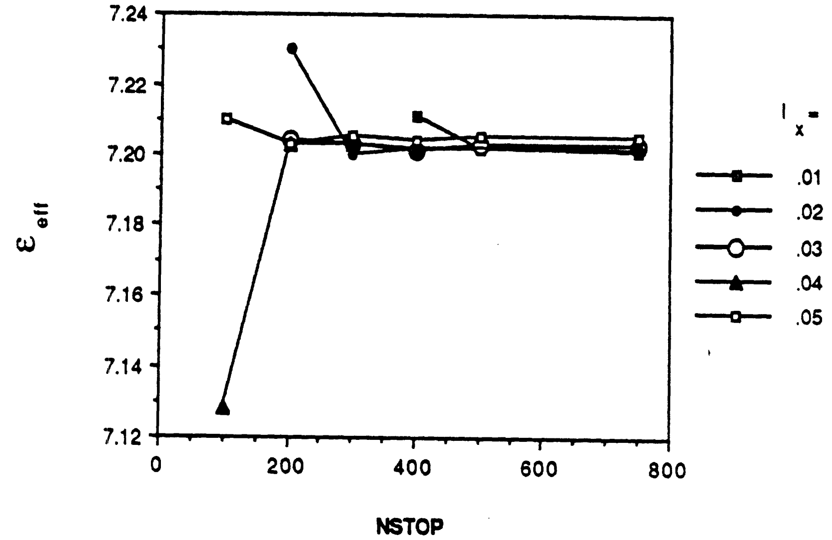

Figure 3.22: The convergence of ϵ_{eff} on n shows similar behavior as that for L_{eff}, and is satisfied in all cases after 500 terms have been added.

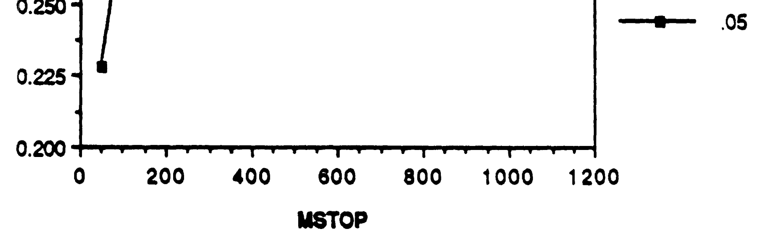

Figure 3.23: The convergence of L_{eff} on m is also satisfied after 500 terms.

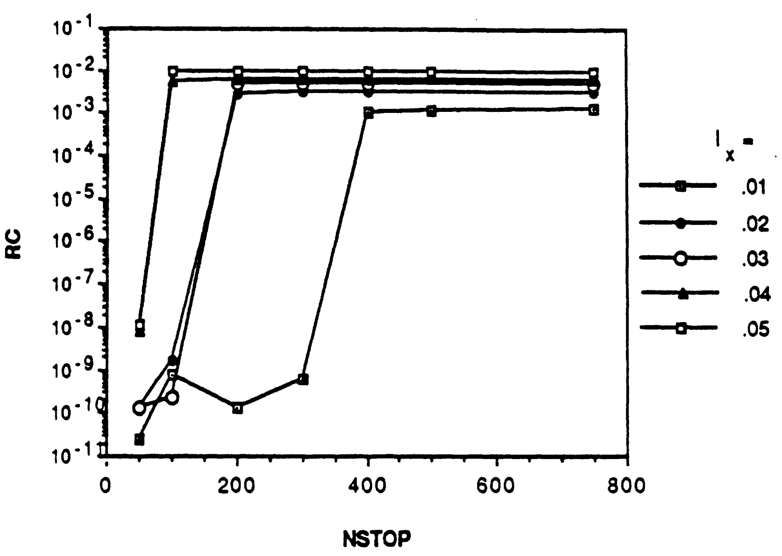

Figure 3.24: A plot of the reciprocal condition number versus NSTOP shows that the condition for erratic current depends on both $NSTOP$ and l_x .

Observation III.2 *The condition for erratic current is given by a simple relation between the cavity length a, the truncation point* $NSTOP$*, and the subsection length* l_x *which may be expressed as*

$$NSTOP * l_x < a \tag{3.27}$$

or

$$\frac{NSTOP}{N_x} < a \tag{3.28}$$

This will be referred to as the **erratic current condition.** *This condition places an upper limit on* N_x *and, correspondingly, a lower limit on the* l_x *value that can be used to generate useful current results.*

The erratic current condition was tested against several cases where erratic currents were observed, and it appears to give an exact prediction.

3.5.3 Numerical Experiment C: Optimum Sampling Range

Objectives

The objective in this last experiment was to examine the effect of varying l_x on the reciprocal matrix condition number, while keeping the matrix size constant. It was hoped that an optimum value, or range of values, for l_x could be found for which the matrix condition number is maximized.

Procedures and Results

To keep the matrix size constant, the number of sections N_s was fixed at 100, and the length of the open-ended line ($L' = L_{in}/\lambda_d$) was allowed to vary such that

$$L' = 100 * l_x$$

for all cases. Data was then generated to plot RC versus l_x as shown in Figure 3.25. As suspected, an optimum sampling range was found, outside of which the matrix is ill conditioned. The experiment was repeated at three different frequencies and for several different shielding geometries. In all cases, an optimum sampling range was found, but it was different for each of them.

To examine this sampling range further the following postulate was advanced, based on the erratic current condition of Experiment B.

Postulate III.1 Postulate:.— *Let* N_{x1} *and* N_{x2} *correspond to the minimum and maximum desired sampling rates. These rates are defined as those values between which the reciprocal condition number is greater than* 10^{-4} *for a fixed matrix size*

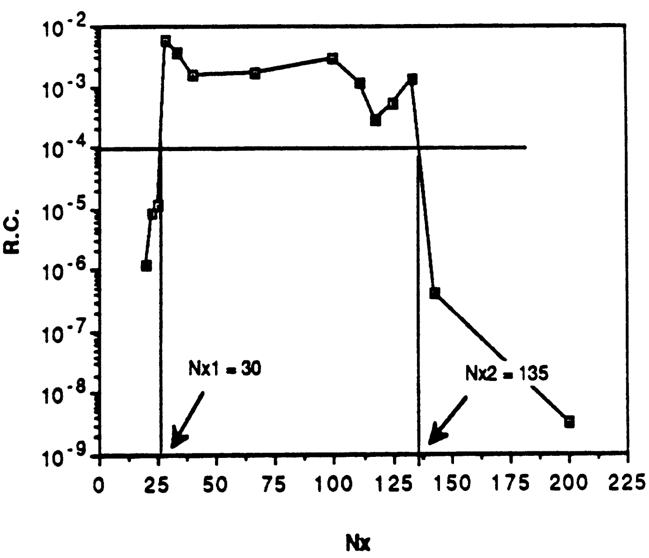

Figure 3.25: The effect on the reciprocal condition number of varying only l_x indicates the existence of an optimum sampling range

of 100×100. [3]

Let l_{x1} *and* l_{x2} *be the subsection lengths corresponding to* N_{x1} *and* N_{x2} *respectively. That is*

$$l_{x1} = 1/N_{x1} \tag{3.29}$$

$$l_{x2} = 1/N_{x2}\,. \tag{3.30}$$

We now postulate the existence of two constants r_1 *and* r_2 *such that*

$$l_{x1} = \frac{r_1 a}{NSTOP} \tag{3.31}$$

$$l_{x2} = \frac{r_2 a}{NSTOP}\,. \tag{3.32}$$

The definition of the sampling range is illustrated in Figure 3.25. This postulate

---

[3] Based on observation, a value of RC = 10^{-4} appeared to be a good value to use as a lower limit.

Table 3.1: RESULTS FOR OPTIMUM SAMPLING RANGE EXPERIMENT

f (GHz)	a	l_{x2}	l_{x1}	l_{xavg}	r_2	r_1	r_{avg}
2	1.58	.0035	.0125	.008	1.1	4.0	2.5
8	6.33	.017	.07	.043	1.3	5.5	3.4
8	1.0	.0029	.0125	.008	1.5	6.3	3.9
18	3.5	.0074	.033	.020	1.1	4.7	2.9
18	1.0	.0023	.0125	.0074	1.2	6.3	3.7
min.	-	-	-	-	1.1	4.0	2.5
max.	-	-	-	-	1.5	6.3	3.9
avg.	-	-	-	-	1.2	5.4	3.3

was applied to the observations from several test runs and the results for the sampling range parameters are summarized in Table 3.1.

The data of Table 3.1 shows that, although Postulate 3.1 is only approximately true, an optimum sampling range can be specified in terms of the multipliers r_1 and r_2. This range is formulated in the observation below. In selecting the multiplier r_2, the maximum observed value from Table 3.1 is used, and in selecting the multiplier r_1 the minimum observed value is used. This is done to define a range for which condition number for the cases of Table 3.1 is always greater than 10^{-4}.

Observation III.3 *An optimum sampling range (or criteria) may be defined by the following choice of subsection length l_x*

$$\frac{1.5a}{NSTOP} \leq l_x \leq \frac{4a}{NSTOP}. \tag{3.33}$$

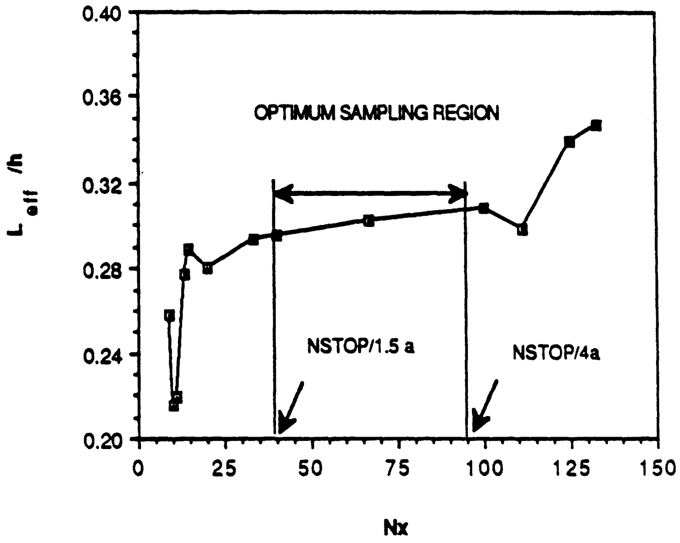

Figure 3.26: The optimum sampling range is seen to correspond directly with the flat convergence region for the L_{eff} computation.

A good average value to use is

$$l_x = \frac{3a}{NSTOP} \tag{3.34}$$

The above observation is very significant. Based on the knowledge of only two parameters, a and $NSTOP$, an optimum sampling range (or range of subsection lengths) can be determined. The erratic current condition is automatically avoided by sampling within this range, and the best accuracy in the matrix solution should be guaranteed.

To support this last claim, consider the plot of Figure 3.26. It is seen that the optimum sampling region specified by 3.33 coincides directly with the flat convergence region for the L_{eff} calculation! This consistency between the optimum sampling region and the flat convergence region for the L_{eff} calculation was observed in all the cases of Table 3.1.

3.6 Summary of Computational Considerations

In this chapter, the software design for the computation of the current distribution, and the network parameters for discontinuities has been described. The programming language used is Fortran. The convergence of the solution with respect to the relevant parameters has been explored extensively by performing a series of numerical convergence experiments. The results from these experiments lead to some simple, but very useful relationships governing the convergence and stability of the solution. A summary of the main findings is given in Chapter 6.

CHAPTER IV

EXPERIMENTAL METHODOLOGY

As part of this research an experimental study of microstrip discontinuities was performed. In conducting this study, the author spent fifteen months at Hughes Aircraft Company[1]. Hence, parts of the study were performed at Hughes; the rest was performed at the University of Michigan.

The chapter gives a description of the study and the procedures used to obtain measured data. First, a general discussion of the experimental approach is given. This consists of the use of Automatic Network Analyzer (ANA) techniques in conjunction with a method for de-embedding (or removing) the effects of the test fixture from the measurements. Next, a comparison of various de-embedding methods is presented. It is concluded that the method most suitable for the measurements of this thesis is the thru-short-delay (TSD) method. The implementation of this method for use with the present research is then explained. Finally, the procedures used to obtain measurements of effective dielectric constant, open-end and series gap discontinuities, and coupled line filter structures are explained. A complete error analysis for these measurements is beyond the scope of this thesis, however, an attempt is made to give a reasonable estimate of measurement uncertainties. To this end a perturbation analysis approach is developed and applied to approximate the effect of connection repeatability errors on de-embedding accuracy.

---

[1] Hughes Aircraft Company, Microwave Products Division, Torrance, CA

4.1 Discussion of Experimental Approach

4.1.1 ANA Error Correction

A basic ANA provides for two-port, error corrected S-parameter measurements in a coaxial or waveguide environment. Error correction is achieved by using a set of standards whose electrical characteristics can be determined to a high degree of certainty. For example, the standards used in a typical coaxial calibration are a 50 ohm load, a short circuit, an open circuit (whose fringing capacitance has been determined apriori), and a thru connection. Measurements on these standards are used to construct an error model for the ANA system which accounts for various system imperfections such as finite coupler directivities, connector mismatches, unflat frequency responses, and source and load impedance mismatches [36].

4.1.2 Difficulties with Microstrip Measurements

Measured data on microstrip discontinuities is very limited, particularly at higher frequencies (above 10GHz). This is due to the many difficulties involved with performing accurate microstrip measurements. The key difficulties associated with these measurements are summarized in Table 4.1. These difficulties are not unique to microstrip and apply to measurements in other planar transmission media as well.

The main difficulty is that in order to measure a microstrip circuit, it is generally mounted in a test fixture with either coaxial-to-microstrip or waveguide-to-microstrip transitions (also called launchers). Figure 4.1 shows the basic configuration for test fixture measurements. The transitions invariably introduce unwanted

Table 4.1: DIFFICULTIES WITH MICROSTRIP MEASUREMENTS

- Separation of microstrip test fixture parasitics from measurements
- Inadequate microstrip calibration standards
- Non-repeatability of microstrip connections
- Effect of variations in substrate material properties
- Effect of variations of metallization dimensions and substrate thickness
- Effect of substrate mounting techniques

parasitics and a reference plane shift to the measurements. These effects must be accurately accounted for and removed from the measurements, or incorporated into the ANA system error model.

One alternative to the use of a test fixture is to employ coplanar wafer probing [37]. However, to measure microstrip structures with coplanar probes requires the use of coplanar-to-microstrip transitions. Since the issues with removing the effect of these transitions are the same as for the other transitions mentioned above, the term "test fixture" as used below will be assumed to include the case of coplanar probing.

Another main difficulty with the measurements is the inadequacy of microstrip calibration standards. Conventional calibration standards are much more difficult to realize in microstrip than in waveguide and coax. Perfect short circuits are complicated by the non-uniform nature of the fringing fields in microstrip, thin-film resistors do not provide the same quality of 50 ohm terminations as in conventional media, and the open-end capacitance is not known to a high enough degree of accuracy for it to be used directly as a calibration piece [2]. Hence, conventional ANA

---

[2] A rigorous numerical solution, such as that developed here may provide

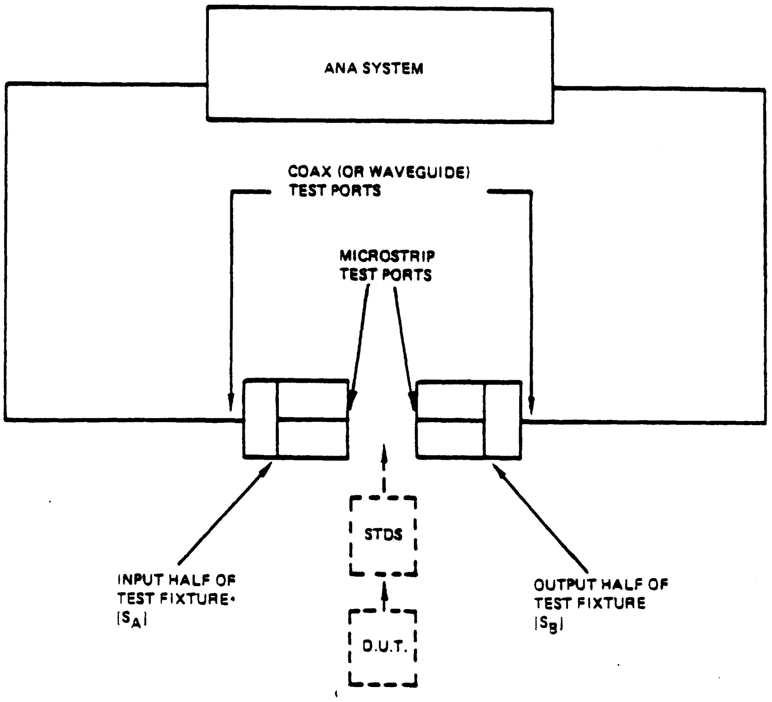

Figure 4.1: Microstrip test fixture approach for de-embedded measurements.

calibration (Section 4.1.1) in microstrip is not easily performed. This difficulty is overcome through the use of de-embedding techniques as discussed below.

The third factor complicating these measurements is the non-repeatability of microstrip connections. Microstrip connections are much harder to make, and much less repeatable than connections in coax and waveguide. This is a key limiting factor to the accuracy of microstrip measurements at higher frequencies. To address this issue, a microstrip connection repeatability study was carried out [14,15]. Details of this study are included in Appendix H, and the results are summarized in Section 4.3 below.

The remaining factors of Table 4.1 can also be important. These factors include the effect of variations in substrate material properties, variations in metalization and substrate thickness dimensions, and substrate mounting techniques. The ef-

---

the required accuracy to alleviate this problem.

fects of these factors on measurements is considered further in Section 4.3, and some consideration is also given in the repeatability study (Appendix H). Their effect can be minimized by paying careful attention during material selection, and during the fabrication and mounting of test circuits.

Before discussing de-embedding methods, a few comments will be made on resonator techniques, since they have been widely used for microstrip measurements.

4.1.3 Resonator Techniques

One way of minimizing transition effects is to incorporate the transition into a resonant circuit which is lightly coupled to a source and detection system [1]. The majority of existing experimental microstrip data have been obtained using such resonator techniques [38]-[41]. The main advantage of this approach is that unwanted transition effects, such as poor VSWR or contact repeatability have minimal effect on measurement accuracy. Also, useful measured data can be obtained without the use of an ANA.

However, the coupling necessary for adequate sensitivity is sufficient to provide some reactive loading of the resonant system which is not easily accounted for. In addition, the measurement procedure is tedious and is not practical for measurements over a broad range of frequencies.

4.1.4 The De-embedding Approach

The preferred approach to removing test fixture effects is called de-embedding. De-embedding refers to the process by which test fixture effects are removed from the measurements. With the exception of time-domain de-embedding, which will be discussed in Section 4.2.2, the de-embedding process consists of two steps:

1. Test fixture (or error) characterization
2. Error extraction.

A microstrip test fixture can be characterized either by an equivalent circuit model (this is generally valid only at low frequencies) or by performing measurements with a number of planar standards inserted within the fixture. The electrical parameters of the fixture, for example the S-parameters for each fixture half, are then used to mathematically move the effective calibration reference planes from the coax or waveguide test ports to the desired microstrip test ports (Figure 4.1).

4.2 Comparison of De-embedding Methods

In this section, several de-embedding methods are compared in terms of their applicability for our measurement requirements. Specifically, the method used must:

- be usable at high frequencies (10GHZ and higher)
- allow the de-embedding of arbitrary transition effects
- allow the connection of any standards used to be similar to those made to the discontinuity structures
- use standards whose electrical characteristics are "known" to a reasonable degree of certainty.

Also, the electrical characteristics of any standards used must be They must be well established theoretically, or determined from independent measurements.

4.2.1 Fixture Equivalent Circuit Modeling

One method of fixture characterization is to propose an equivalent circuit model for the fixture. The simplest model uses a section of ideal transmission line to model each half of the test fixture. In this case, launcher parasitics are completely neglected and de-embedding is performed by simple transmission line rotations around the Smith chart.

Launcher parasitics can be at least partially taken into account by using more complicated equivalent circuit for the fixture whose parameters are fitted to a set of measurements on a reference circuit (e.g. a straight section of transmission line [42]). This approach while an improvement over simple transmission line rotations, lacks generality. It also tends to be unreliable for high frequency use, since fixture parasitics become more difficult to model as frequency increases.

4.2.2 Time Domain De-embedding

Another method of de-embedding makes use of transformations back and forth between the frequency and time domains. This method, which follows from Hines and Stinehelfer [50], involves the use of a Fourier transform to obtain a time domain response from frequency-domain data. In concept, fixture effects can be eliminated by isolating (or gating) the time response of the desired circuit and then transforming back to the frequency domain to obtain the de-embedded frequency response. However, for adequate resolution, it is necessary to use long input and output lines and collect data over a broad range of frequencies. Even then, although useful for many applications ,such as fixture development, this technique is not as accurate as full matrix de-embedding in the frequency domain [51].

4.2.3 Full Matrix De-embedding

The remaining de-embedding methods to be discussed fall into the category of full matrix de-embedding. In full matrix de-embedding, each half of the test fixture is characterized by matrix parameters (e.g. scattering matrix $[S]$, or transmission matrix $[T]$) as a "black box". This is done by measuring planar standards for which the network parameters are known, or can be determined to a reasonable degree of certainty. Examples of such standards are microstrip delay lines, offset microstrip open-ends, and varactor diodes Once the fixture has been characterized, inverse matrix operations can be used to deduce the electrical parameters of the unknown device or circuit.

These matrix operations vary little between full matrix de-embedding methods; conversely, the fixture characterization process differs considerably depending on the type of standards used. Most methods use one of the following combinations of standards:

1. Delay line and reflection standards [44]-[47]
2. 1-port offset reflection standards [52]
3. Varactor diode standards [53]-[55]

The relative merits of different fixture characterization approaches based on the use of these standards are compared in Table 4.2. Based on this comparison, the use of delay line and reflection standards, and in particular, a method based on the thru-short-delay (TSD) approach was adopted for this thesis. A discussion of this choice is given below.

In the TSD method (Figure 4.2), two-port measurements made on a thru (zero length delay) line, a "short" circuit, and a delay line provide enough information to characterize the fixture. As byproducts of the procedure, calculations of the propagation constant γ_g, and the reflection coefficient Γ_s are provided.

Since the original paper [44], it has been pointed out that the "short" implied

Table 4.2: FULL MATRIX DE-EMBEDDING METHODS

APPROACH	TSD (TRL, LRL etc.)	S.C. + 4 O.C.'S	VARACTOR DIODE
AUTHORS	Franzen and Speciale, Bianco et. al., Engen and Hoer, Maury et. al.	da Silva and McPhun	Bauer and Penfield, Peck and Peterson
CONCEPT	o Thru, delay and reflection stds. o Network par's of stds. theoretically known or not critical o Fixture network parameters computed from 1- and 2-port meas.	o Offset reflection stds. o Short used to establish reference plane. o Fixture network parameters computed from 1-port meas.	o Reverse bias varactor diodes used as variable capacitance stds. o Stds. characterized by independent measurements o Fixture network parameters computed from 1-port meas.
ADVANTAGES	o Stds. easy to realize in microstrip o Connections to stds. same as connections to mstrip discontinuities o Provides calculation of propagation constant γ_g o Provides calculation of reflection coefficient Γ_s	o Open circuit stds. easy to realize o Connections to stds. same as connections to mstrip discontinuities o Provides calculation of propagation constant γ_g	o Multiple known loads possible with a single connection o Connections to stds. similar to connections to active devices
DRAWBACKS	o Connection repeatability important for accuracy	o Perfect short circuit difficult to realize o Connection repeatability important for accuracy	o Connections to diodes dissimilar to mstrip discontinuities. o Characterization of stds. tends to be complicated

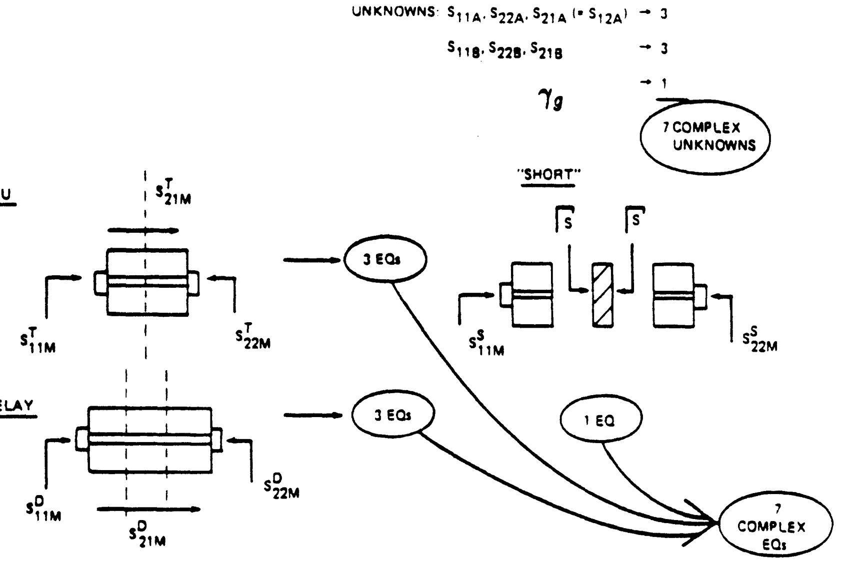

Figure 4.2: Fixture characterization by the TSD technique (Note: the "short" can be any highly reflecting standard).

in TSD, need not be perfect. In fact, any highly reflecting standard may be used in its place [45,46]. The only requirement is that the same reflection coefficient Γ_s must be presented to both microstrip test ports. This is important since, as discussed above, a perfect short is difficult to achieve in microstrip. This variation of the TSD method, that uses an arbitrary reflection standard, has been called the thru-reflect-line (TRL) method. Another variation, called the line-reflect-line method (LRL) [47], allows the use of a non-zero length thru line. Since both of these variations are derived from TSD, the overall approach will be referred to as TSD in this thesis. The understanding will be that the "short" is non-critical.

The main advantage of the TSD approach over the alternatives of Table 4.2 is that the TSD standards are easiest to realize in microstrip. da Silva and McPhun, suggest the use of 4 microstrip open circuits, and a short circuit. As far as this author can determine a perfect short is required to accurately establish the reference plane. To use varactor diode standards a rather complicated modeling procedure must be carried out to characterize the diodes prior to use.

In addition, the fixture hardware may be designed so that the connections made to the TSD standards are made in the same way as the connections to the microstrip discontinuity test circuits. This is not the case with varactor diode standards as the introduction of the diode mounting structure adds parasitics during fixture characterization that, in general, are not present when measuring discontinuity circuits.

One drawback to the TSD method is that good microstrip connection repeatability, and microstrip circuit fabrication repeatability are important for accuracy. This is also true (probably to a greater degree since more standards are required) for da Silva and McPhun's approach. In this area, the varactor diode approach is attractive since several different capacitances can be realized by varying the diode's reverse bias voltage. However, this advantage may be partially offset by the nonrepeatability of returning to the exact same bias voltage during calibration that was used during the characterization of the diodes.

One-tier vs. Two-tier De-embedding.— As discussed by Lane [43], full matrix de-embedding can be performed using either a one-tier or a two-tier approach. The choice between these two options is controversial, and it depends on the application and fixture hardware.

Referring to Figure 4.1, one-tier de-embedding involves making a direct calibration at the microstrip test ports. In this approach, fixture effects are included in the error model used to represent the ANA system imperfections. This approach has been used in coplanar waveguide [37], and also in microstrip [56]. One-tier de-embedding is more straight forward and in some ways easier to implement than two-tier de-embedding. Also, with the speed of current ANAs, the one-tier approach can display de-embedded measurements in essentially real time.

In contrast, two-tier de-embedding involves calibrating first at the coaxial or waveguide terminals. Measurements are then made on various microstrip standards to determine the S-parameters of each half of the test fixture. These are stored and later used to mathematically transform the measurements to the microstrip test ports.

One advantage of two-tier de-embedding for the present application is that it provides for better monitoring of the de-embedding process. Measurements can be made with several different connections made to each of the standards used for fixture characterization. These measurements can be stored in files and then compared in order to screen out bad connections. The remaining connection trials can then be averaged to reduce connection repeatability errors. For this reason the TSD method was implemented as a two-tier procedure, as described next.

4.3 Implementation of TSD De-embedding

4.3.1 Software and Hardware Considerations

Computer programs for performing TSD fixture characterization and de-embedding were provided by Hughes. As part of this work, modifications were made to these programs to customize them for the present application. The mathematics used are described in detail elsewhere [48,49].

A flow chart for the measurement procedure used is shown in Figure 4.3. The programs used to carry out this measurement procedure are set up to process several measurement frequencies simultaneously. First, ANA system calibration is performed with coaxial standards. The S-parameters of each of the TSD standards are then measured and stored in data files. To reduce connection repeatability errors, repeated measurements are performed with two to five connections made to each of the standards. These measurements are then used to obtain an average set of S-parameters for each fixture measurement.

The averaged S-parameters of the standards and the physical length of the delay line are then input to the fixture characterization program. This program performs calculations to provide measured values for $\epsilon_{eff}, \Gamma_s(=\Gamma_{op})$, and the S-parameters $[S_a]$, $[S_b]$ for each half of the test fixture.

Finally, measurements are made with the D.U.T. (i.e. the desired discontinuity circuit) connected within the fixture. Again, repeated measurements are made to reduce connection errors. The averaged D.U.T. S-parameters are then processed along with the fixture characterization data to obtain the de-embedded measurement. If necessary, the reference planes established by the de-embedding (in the middle of the thru line) are moved by performing simple transmission line rotations. The phase constant used for these rotations is based on the measured effective dielectric constant.

The instrumentation used for the measurements of this thesis was almost exclusively HP8510 ANAs which were available to the author at both the University and at Hughes. The only exception is that an HP8409 ANA with a high frequency waveguide extension was used to perform connection repeatability measurements in the 26.5-40GHz frequency range.

The test fixture that was used for the discontinuity measurements was also provided by Hughes. A picture of the test fixture is shown in Figure 4.4. The fixture employs a pair of 7mm coaxial "Eisenhart" launchers [57] and is usable to 18GHz. The shielding is provided by placing U-shaped covers on top of the microstrip carriers. This forms a cavity similar to Figure 1.3.

Another fixture, usable to 40GHz was also developed by the author for use with this thesis. This fixture was used in the connection repeatability study (Appendix H), but not for discontinuity measurements. The reason for this was logis-

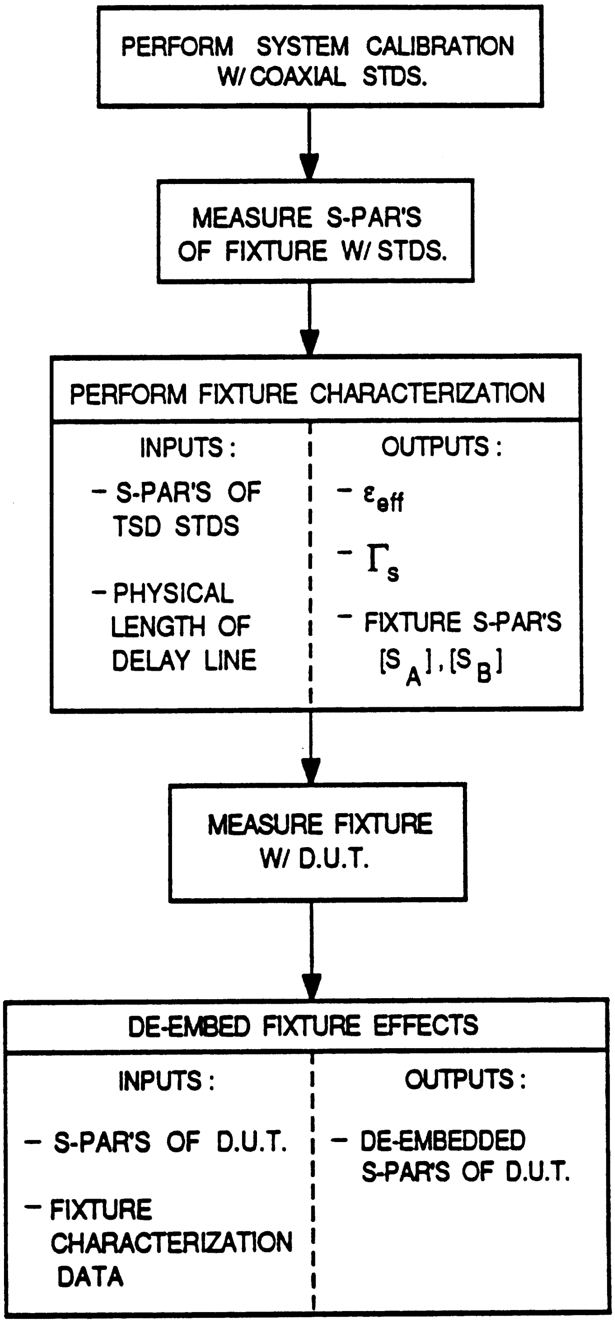

Figure 4.3: Procedure used in this work for measurement and de-embedding.

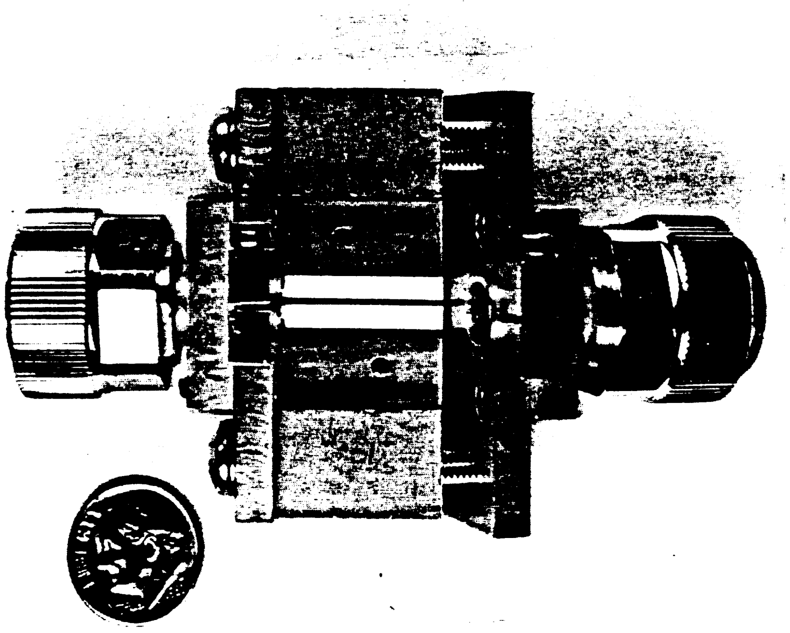

Figure 4.4: 7mm coaxial/microstrip test fixture (partially disassembled).

tical and not technical. All of the discontinuity measurements were performed at the University, and at the time these experiments were planned (substrates ordered etc.), facilities were not available to make measurements above 18GHz. Hence, the 7mm fixture was used for all the discontinuity measurements.

4.3.2 Connection Approaches For TSD De-embedding

There are three basic connection alternatives for TSD characterization of a coaxial fixture. Each of these must rely on at least one of the following assumptions:

1. repeatability of connections made from the coaxial-to-microstrip transition (launcher) to the microstrip line (i.e. coax/microstrip connection repeatability)
2. repeatability of microstrip/microstrip interconnects

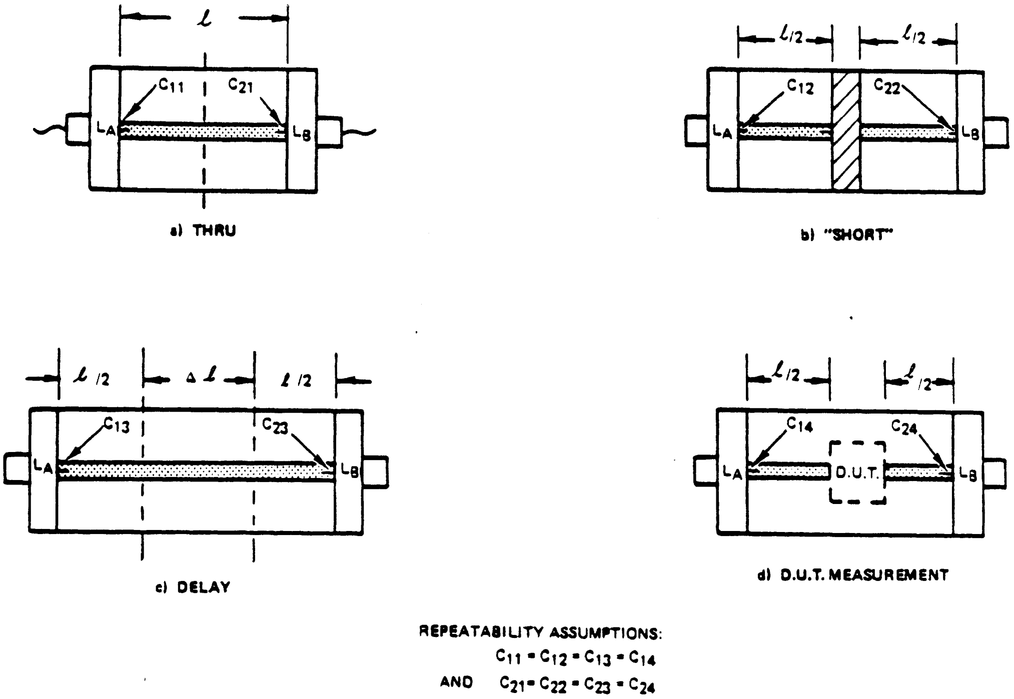

Figure 4.5: The TSD Connection approach used for the present work, relies on repeatable coax/microstrip connections.

3. uniformity of electrical characteristics between different transitions (launcher-to-launcher uniformity).

In the first connection approach (Figure 4.5), continuous substrates are used to realize the three standards, which are connected between the same pair of launchers (L_a, L_b). In the second method (Figure 4.6), the TSD standards, and the D.U.T., are connected between the same two launcher/microstrip assemblies using microstrip-to-microstrip interconnects (e.g. ribbon bonds). In the third approach, each of the standards would be constructed complete with their own intact launchers. While this has practical advantages, such as improving the durability of the standards, launcher-to-launcher uniformity is not generally a good assumption for microwave de-embedding (Appendix H).

In all of the above approaches, it is important to have good uniformity between various microstrip line sections as mounted in the fixture hardware. If the fixture must be removed from the coaxial measurement ports to insert either the stan-

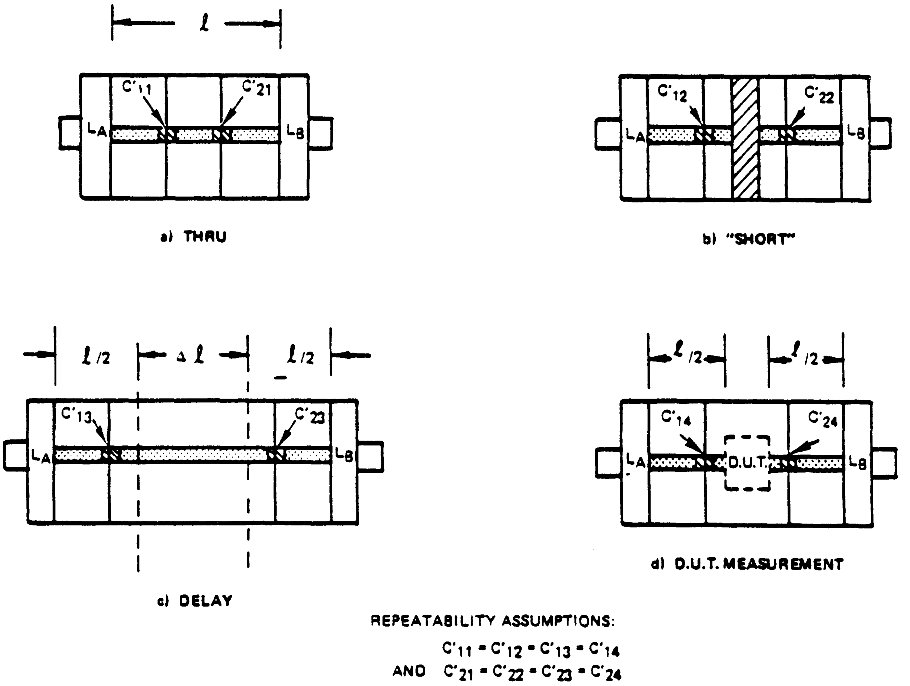

Figure 4.6: TSD Connection approach relying on repeatable microstrip/microstrip connections.

dards or the D.U.T., de-embedding accuracy is also subject to uncertainties due to repeated coax/coax connections. However, the study results suggest that these uncertainties are negligible compared to other errors.

The results of the repeatability study (Appendix H) clearly favor the connection approach of Figure 4.5 relying on repeatable coax/microstrip connections, and this was the approach adopted for the present work.

4.3.3 Measurement of Effective Dielectric Constant

As mentioned previously, one of the byproducts of the TSD method is the calculation of the propagation constant $\gamma_g (= \alpha_g + j\beta_g)$. For the alumina substrates used, the loss factor α was found to be too small to measure by this method, or conversely the measurement sensitivity is not great enough. Using Super Compact this loss (combined dielectric and conductor losses) is estimated to be .05dB/cm at 10GHz. For the delay length used here this translates to a total loss of .01dB which is less than the error due to connection repeatability.

The phase constant β is measurable, and may be used to calculate the effective dielectric constant ϵ_{eff} by the following relation:

$$\epsilon_{eff} = \left(\frac{\beta c}{\omega}\right)^2 \tag{4.1}$$

where c is the velocity of light and ω is the radian frequency.

The value of ϵ_{eff} calculated from the TSD procedure relies mainly on the delay line length Δl, and the difference in measured transmission phase between the thru and delay line standards.

Figure 4.8 shows a typical ϵ_{eff} measurement resulting from a single TSD fixture characterization procedure. A sketch of the standards used is given in Figure 4.7. The "raw" measurement shown is the actual measurement, and the "fitted" result was obtained by performing a least squares polynomial curve fit to the measurements. As supported by the theoretical results of Chapter 5, the actual ϵ_{eff} should follow a smooth curve. Hence, deviations from the fitted curve indicate imperfections in the measurement. In this work, the fitted curve is generally used for any post de-embedding transmission line rotations.

4.3.3 Measurement of Open-end Discontinuity

A measurement of the reflection coefficient and related capacitance of a microstrip open-end discontinuity was obtained based on using an open-ended microstrip line as the reflection standard in place of the "short" of Figure 4.2. A measurement of the reflection coefficient $\Gamma_s(= /\Gamma_{op}/e^{j\theta_{op}})$ results from the fixture characterization procedure. Figure 4.9 shows a representative plot of the measured (de-embedded) reflection coefficient of the open-end standard of Figure 4.7. The phase angle shows an increasingly negative phase shift with frequency, as expected.

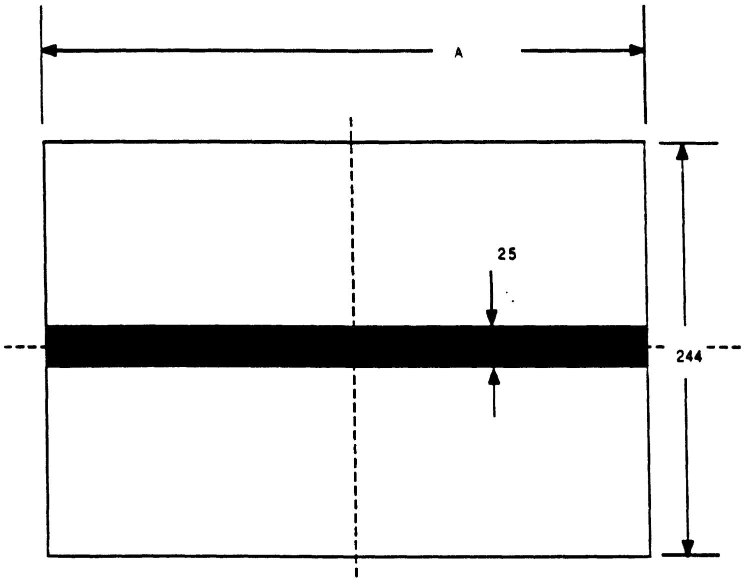

STD.	DIM. A
THRU	730
DELAY	824

a) Thru and delay line standard

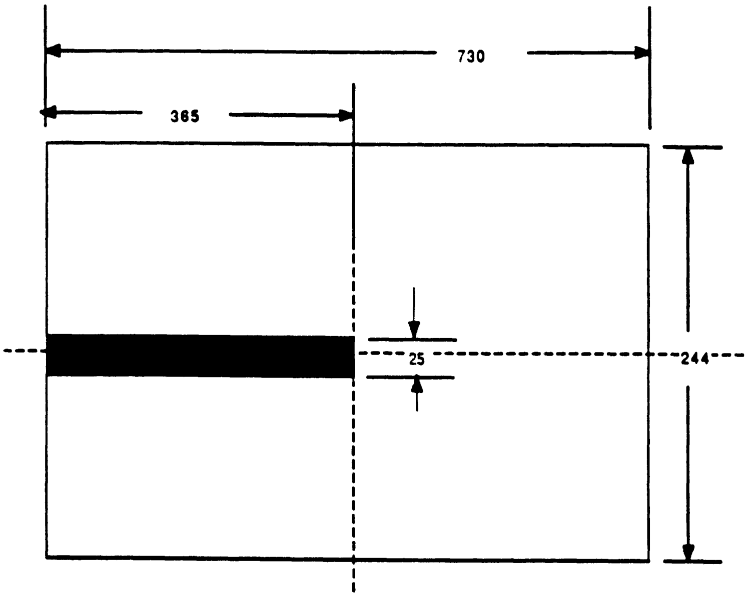

b) Open-end standard

Figure 4.7: Sketch of TSD standards used for measurements of ϵ_{eff}, and open-end and series gap discontinuity circuit. Note: all dimensions of Figure are in mils (1 mil=.001″), $h = .025'', \epsilon_r = 9.7$.

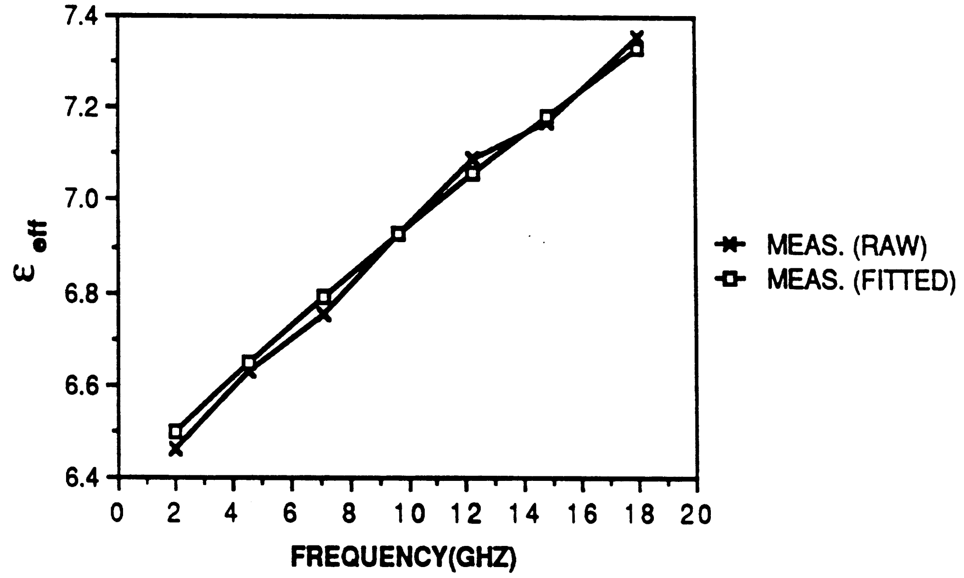

Figure 4.8: Typical effective dielectric constant measurement resulting from TSD fixture characterization. (Shielding dimensions: $b = c = .25''$).

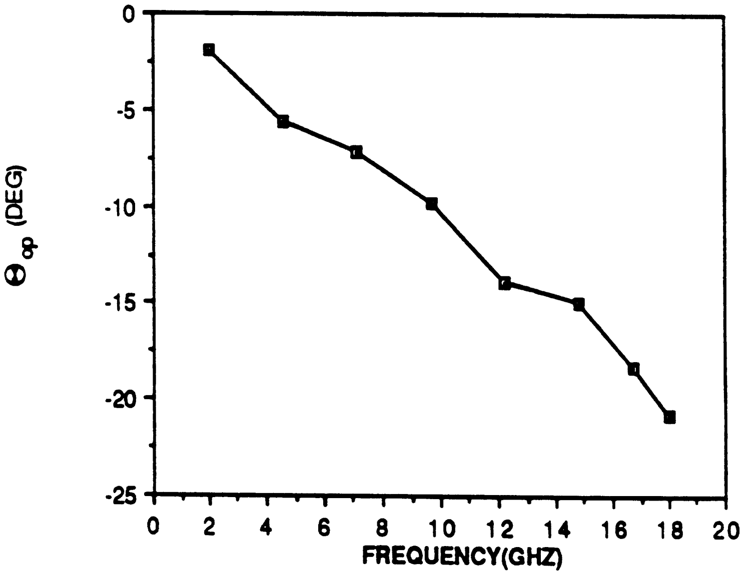

Figure 4.9: Angle of open-end reflection coefficient resulting from a typical fixture characterization procedure.

The reflection coefficient angle θ_{op} is related to the normalized capacitance by the relation given by (2.135)

$$c_{op} = \frac{-\sin\theta_{op}}{\omega(1+\cos\theta_{op})}\,. \tag{4.2}$$

A calculation of c_{op} based on measurements is shown compared to numerical results in Chapter 5.

4.3.4 Measurement of Series Gap Discontinuities

Measurements were performed on three series gap test circuits of different gap widths 15mil, 9mil, and 5mil. A sketch of the test circuit layout is shown in Figure 4.10. The TSD standards of Figure 4.7 were used for fixture characterization. Because the length of the input/output lines L_1 and L_2, to the left and right of the series gap respectively, are shorter than half the thru line of Figure 4.7, the reference planes established by the de-embedding are not at the desired positions of a-a and b-b (Figure 4.10). A transmission line rotation is used, in each case, to move the reference planes to the desired positions. The phase constant used for this rotation is calculated from the fitted effective dielectric constant discussed in Section 4.3.2. The length of rotation is given by the difference in physical length between L_1, L_2, and half the thru line length. The measured results are discussed in Chapter 5.

4.3.5 Measurement of Coupled Line Filters

The last measurements to be described were made on two different coupled line band pass filters. The first filter is the two resonator coupled line filter depicted in the sketch of Figure 4.11. The TSD standards used for this measurement are

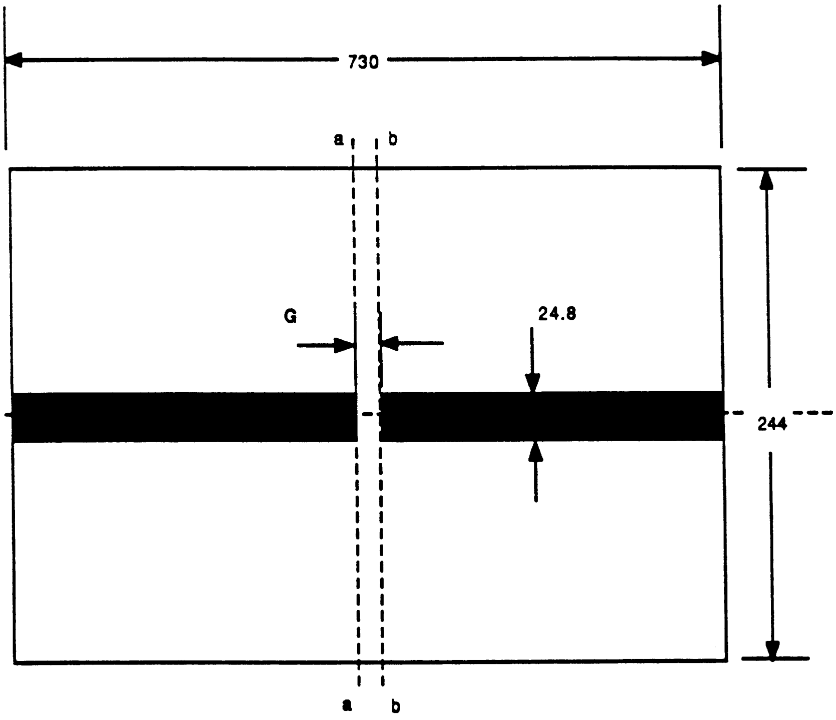

TEST CKT.	DIM. G
A	15
B	9
C	5

Figure 4.10: Sketch of series gap discontinuity test circuit. Note: all dimensions in mils, $h = 25, \epsilon_r = 9.7$. (Shielding dimensions: $b = c = .25''$).

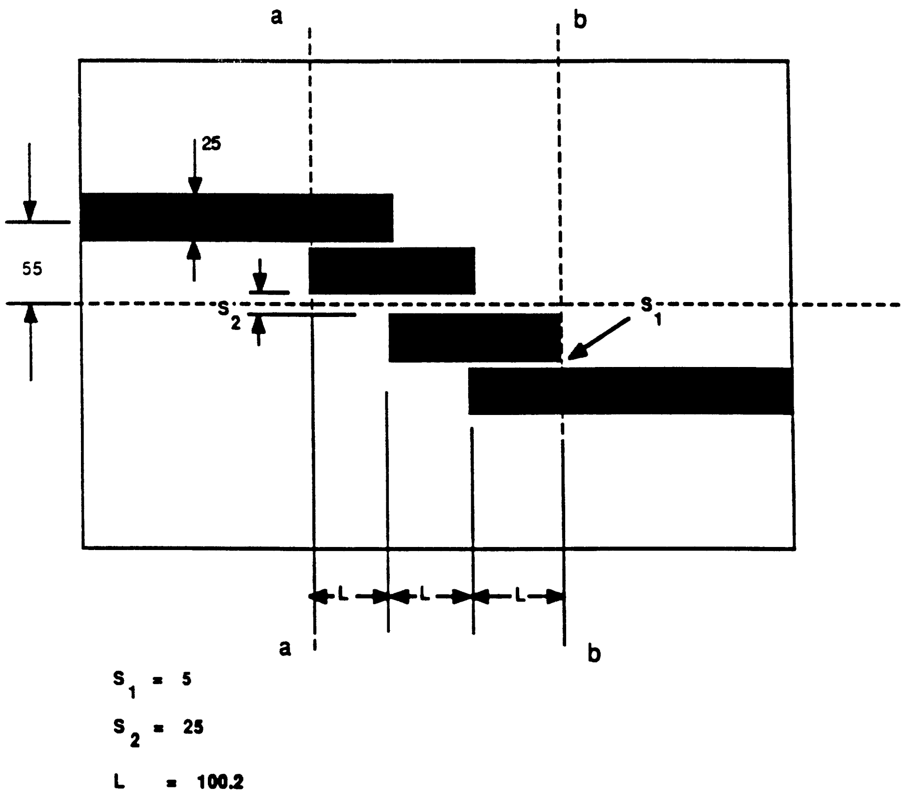

Figure 4.11: Sketch of two resonator coupled line filter. Note: all dimensions in mils. $h = 25, \epsilon_r = 9.7$. (Shielding dimensions: $b = .4''$, $c = .25''$).

shown in Figure 4.12. As in the case of the series gap measurement, a transmission line rotation was required after de-embedding to adjust the reference planes to the desired positions a-a and b-b of Figure 4.11.

The other filter measured is the four resonator filter of Figure 4.13. In this filter, the line widths of the filter structure are 11.9 mils (.302mm) which corresponds to about a 65 ohm impedance level. Since the ANA provides for measurements in a 50 ohm environment, a quarter wave transformer was designed to transform from this 65 ohm impedance level to approximately 50 ohms at the coax/microstrip connection points. By including the same transformer on the input and output portions of the TSD standards (Figure 4.14), its effects can be effectively removed through the de-embedding process.

The result is that microstrip calibration reference planes are established at the

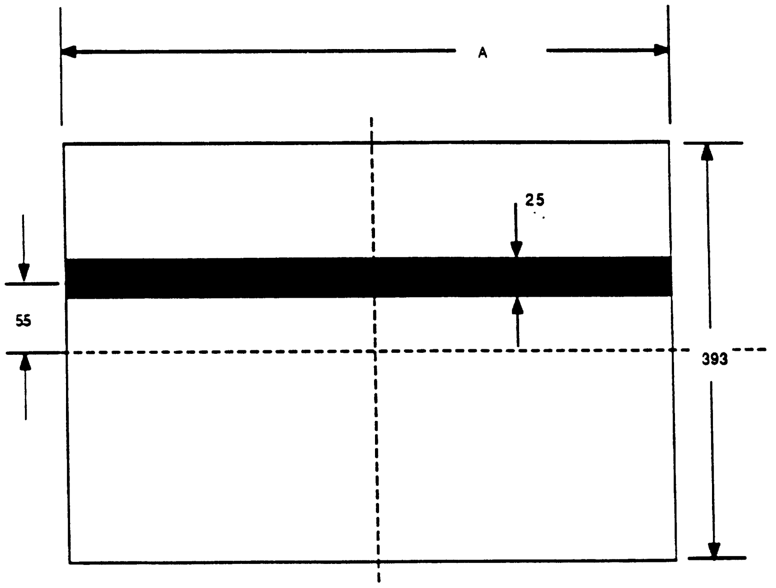

STD.	DIM. A
THRU	730
DELAY	824

a. Thru and delay line standards.

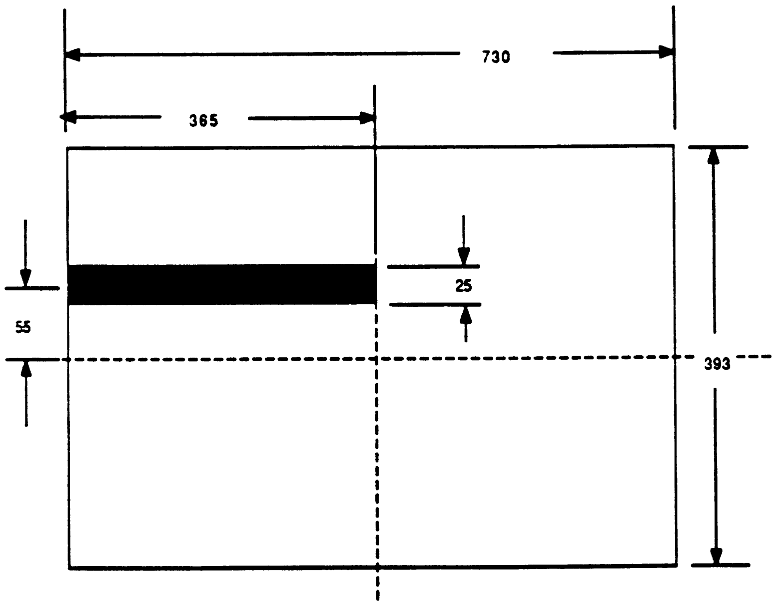

b. Open end standard.

Figure 4.12: Sketch of TSD standards for two resonator filter measurement. Note: all dimensions in mils, $h = .025''$, $\epsilon_r = 9.7$.

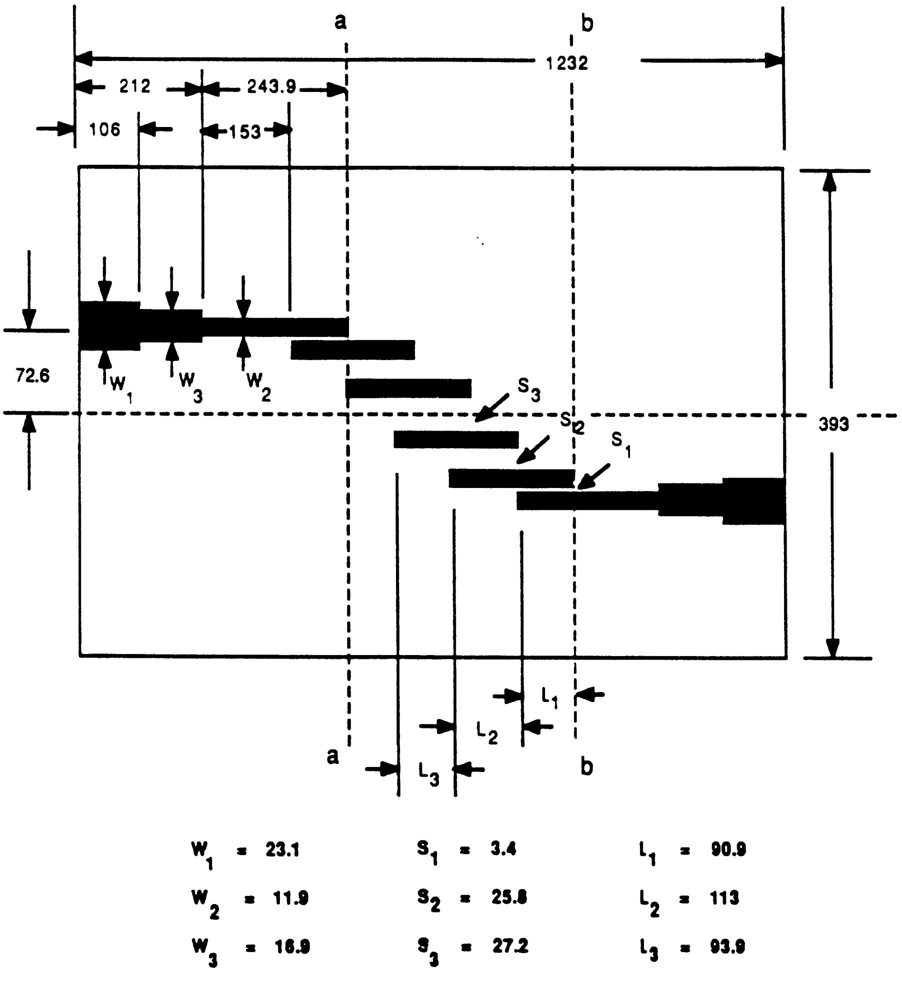

Figure 4.13: Sketch of four resonator coupled line filter. Note: all dimensions in mils, $h = .025'', \epsilon_r = 9.7$. (Shielding dimensions: $b = .4'', c = .25''$).

planes a-a and b-b of Figure 4.13. The de-embedded scattering parameters are referenced to approximately 65 ohms. Note that no transmission line rotations are required to adjust the reference planes for this measurement since the input and output line sections L_1 and L_2 are the same length as half the thru line.

The measured results for both of these filters is discussed in the next chapter.

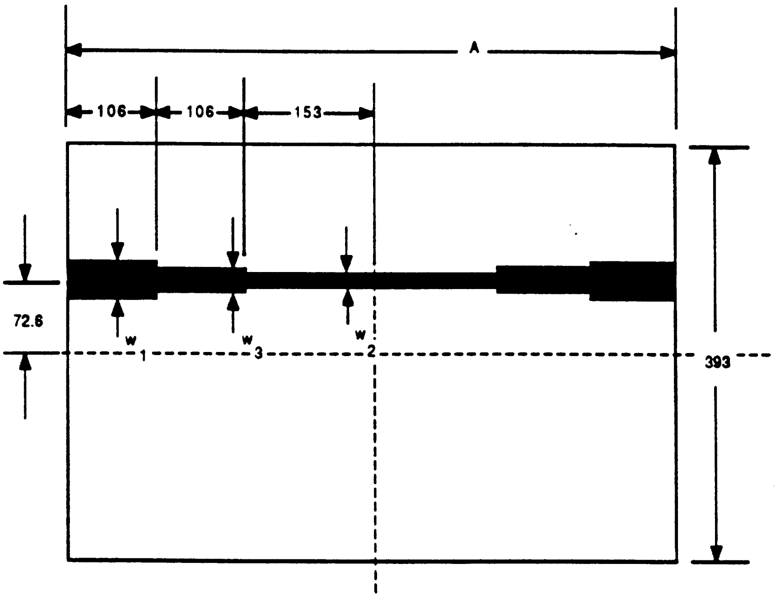

STD.	DIM. A
THRU	730
DELAY	824

a. Thru and delay line standards.

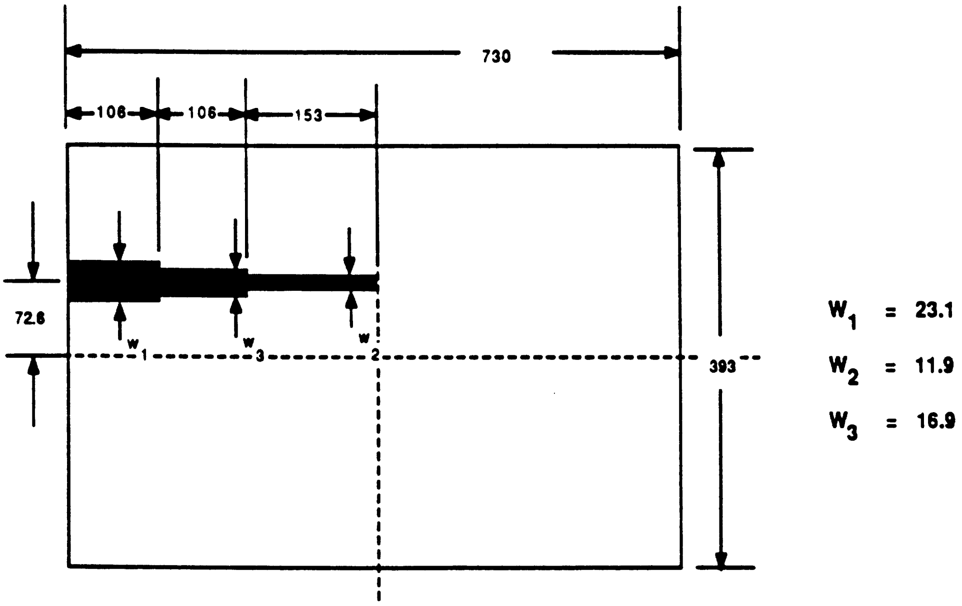

b. Open end standard.

Figure 4.14: Sketch of TSD standards for four resonator filter measurement. Note: all dimensions in mils, $h = .025'', \epsilon_r = 9.7$.

4.4 A Perturbation Analysis of Connection Errors in TSD De-embedding

As part of this thesis, an approach was developed to analyze the uncertainties in TSD de-embedding results arising from connection repeatability errors. The analysis consists of perturbing the S-parameters of the TSD standards and the D.U.T. with a set of error vectors that are representative of the variations of each S-parameter (S_{11}, S_{12} etc.) measurement with repeated connections. Software was written to allow processing the perturbed S-parameter data in the same way as the measurement data is processed (Figure 4.3). This perturbation analysis, allows for an approximation of how connection errors —which are inevitable— propagate through the TSD mathematics and limit the precision of the final results.

The *precision* of a measurement process is not the same as accuracy. *Accuracy* refers to how close the result of an experiment comes to the true value. Since the true value is usually unknown, as it is for the present measurements, true measurement accuracy is often impossible to evaluate. *Precision* on the other hand is a measure of how reproducible a result is. Measurement reproducibility is something for which a reasonable estimate can usually be made, and this is the purpose of the following discussion.

An examination of the measurement procedure (Figure 4.3) shows that any variations in the final results are due to uncertainties in the fixture measurements of the standards and the D.U.T.. The precision of these fixture measurements is affected by two factors. First is the non-repeatability of the fixture connections, which for the present measurements includes both coax/coax and coax/microstrip connections. The second factor affecting the precision is random errors due to ANA instrumentation or the non-repeatability of the system calibration procedure, which is believed to be negligible compared to other error sources. For convenience, the following definition is advanced:

Definition IV.1 *The combined effect of the random errors in the ANA instrumentation and the errors due to connection non-repeatability will be referred to as* **connection errors.**

The repeatability experiments presented in Appendix H explore the errors in microstrip fixture measurements caused by non-repeatable microstrip connections. In these measurements, the resulting spread of the data in each case includes both random ANA errors, and those due to coax/coax connection non-repeatability in addition to the repeatability issue being studied. Hence, the results presented actually represent the total connection errors associated with each repeatability issue.

These connection errors are present during the measurement of each of the three TSD standards (Figure 4.2) and also during the measurement of the D.U.T., which in the present application is a discontinuity structure.

4.4.1 Basic Approach to Perturbation Analysis

The perturbation approach developed to analyze the effect of these connection errors is outlined in Figure 4.15. First, an analysis frequency is chosen. The analysis is performed at a single frequency to prevent the data processing from becoming too cumbersome. In this work a frequency of 10GHz was chosen since it is about in the middle of the frequency range used for the discontinuity measurements.

After the analysis frequency has been chosen, the next step is to derive a representative set of error vectors for the type of connection used. Figure H.4 shows one way of looking at the coax/microstrip connection repeatability data. There, the average set of S-parameters are used to normalize the S-parameters from each of the connection trials by way of vector division. Another way to look at this data is to perform a vector subtraction between the S-parameters from each

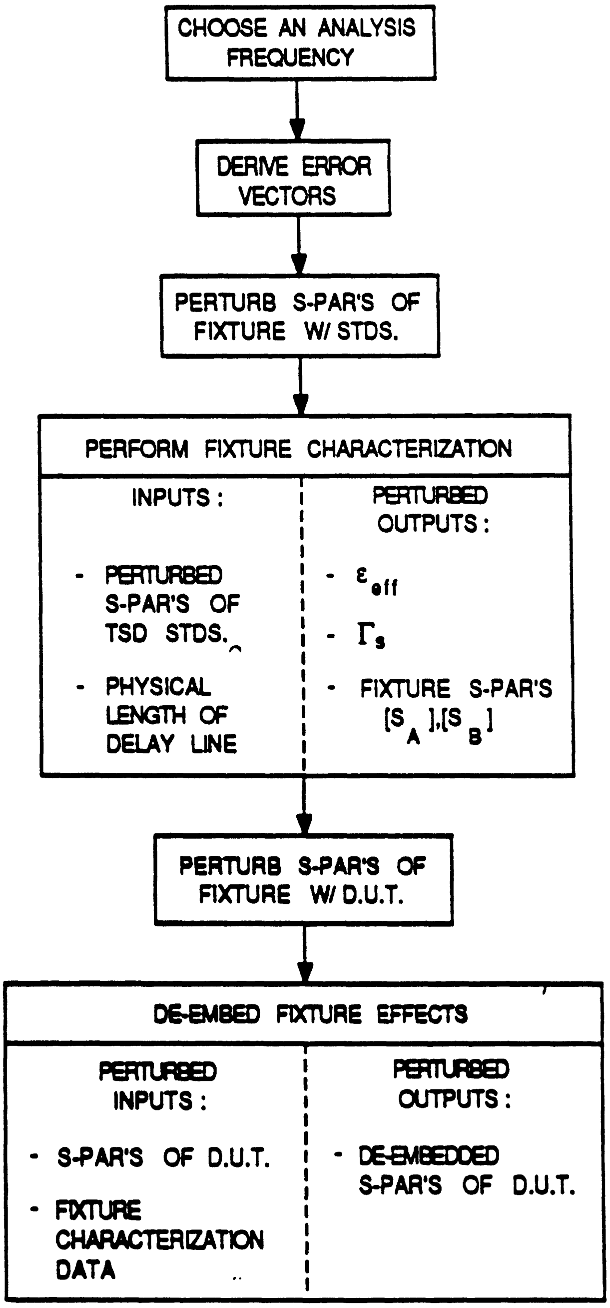

Figure 4.15: Flow chart illustrating approach for perturbation analysis of connection errors.

of the connection trials and the average S-parameters. In this case the result is a set of error vectors that represents the vector perturbation of each of the S-parameter measurements from the average.

This idea is illustrated in Figure 4.16. This figure shows a typical set of S_{11} and S_{12} measurements resulting from 10 connections on a thru line[3]. The error vector ΔS_{11} shown is given by

$$\Delta S_{11} = S_{11m} - S_{11avg} \tag{4.3}$$

where S_{11m} is the measurement for a single connection trial and S_{11avg} is the average of 10 connections. The error vectors $\Delta S_{12}, \Delta S_{21}$, and ΔS_{22} are defined analogously. Thus, for each connection trial we may define four error vectors.

Error vectors so derived, are used in the analysis to perturb the S-parameters for each of the TSD standards and the D.U.T.. To do this, a nominal (or average) set of S-parameters are obtained from measured data. The different error vectors are then added to the nominal S-parameters in an order determined by setting up a permutation table similar to that shown in Table 4.3.

To understand how this permutation table is used, consider the following example. Assume that each fixture connection can be made in one of ten possible ways and let these connections be numbered 1 through 10. Associated with each connection is a set of four error vectors may be derived as discussed above. For this example, assume that the same set of error vectors can be used for all fixture measurements. The final de-embedded result will depend on which of the 10 possible connections was made to each of the standards during fixture characterization and to the D.U.T. before measurement and de-embedding. For 4 fixture measurements, and 10 possible connections for each, there are 10^4 permutations of different con-

---

[3] Note: In Figure 4.16 and the other polar representations that follow, the Smith chart lines drawn only have meaning when the scale is 1.0. When magnified scales are indicated (e.g. SCALE=0.1), only the relative magnitudes and phases of the points plotted are important.

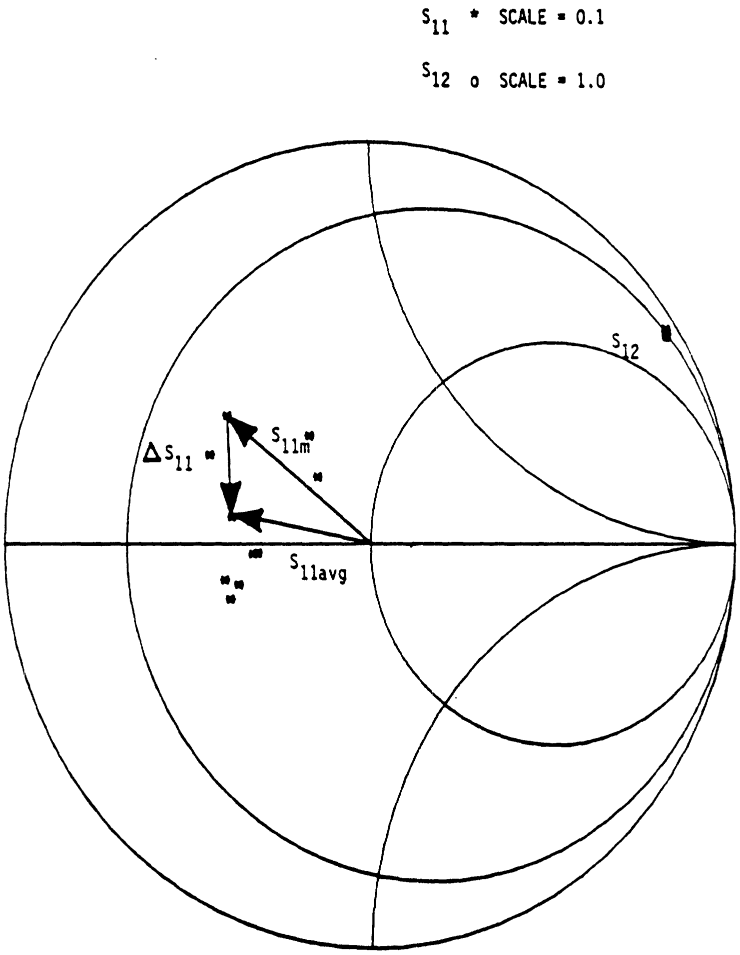

Figure 4.16: Variation of S_{11} and S_{12} for 10 connections made to a typical thru (or delay line) standard. Error vectors may be defined as the vector perturbation of each of the measurements from the average.

Table 4.3: CONNECTION PERMUTATION TABLE EXAMPLE

CONNECTION COMB. NO.	THRU	"SHORT" (OPEN)	DELAY	D.U.T.
1	1	2	5	5
2	6	5	1	9
3	1	6	10	10
4	3	3	7	4
5	7	5	6	4

nection combinations. Table 4.3 only shows 5 of these permutations. Each of the connection combinations is assigned a number, and each row of the table describes the corresponding connections for each of the fixture measurements. The order of the connections is chosen randomly by using a a pseudo-random number generator to set up each column of the table. In this way a large number of repeated de-embedding procedures can be synthesized with a relatively small set of measured data.

Once the perturbed sets of S-parameter data on the standards and the D.U.T. have been obtained, the fixture characterization and de-embedding operations are the same as those of Figure 4.3. The only difference is that instead of processing measured data for different frequencies, the software is used to process perturbed S-parameters for different connection combinations.

4.4.2 Perturbation Analysis and Results

The above gives a brief description of the basic approach used to analyze connection errors. A critical step in the analysis is the selection of a representative set of error vectors for the connection errors of a given microstrip fixture measurement. To be statistically rigorous, a different set of error vectors is required for each different fixture measurement that is made, since the error vectors may differ with the device or circuit being measured. In addition, these error vectors should be derived from a large number of connections in each case.

Obtaining this extensive of a data set would be a formidable task. One problem is that the measurements themselves, and the associated data processing is very time consuming. Second, there is a limit on the number of connections that can be made between a particular set of connectors and a particular microstrip test line. As the number of connections is increased, the wear on the fixture hardware (and the experimenter) gradually degrades the performance of the connection and from a statistical point of view the population average μ will not be a constant.

Because of these difficulties, some simplifying assumptions are made to allow an approximate analysis to be carried out. In doing this, the author has attempted to make the best use of the available connection repeatability data to derive error vectors for each of the fixture measurements. These error vectors are described below. The main assumption made is that the error vectors used represent a random sample of the possible connection errors. Within the limits of this assumption, the resulting analysis gives a reasonable approximation to the related uncertainties.

In the analysis which follows an analysis is carried out to estimate the precision of the measurements made of ϵ_{eff}, and the open-end and series gap discontinuities. An approximation of the precision of the coupled line filter structures is not included because the repeatability data currently available is not sufficient to derive error vectors for these measurements.

Error Vectors used for Delay Lines, and Filters

Based on the repeatability measurements for a microstrip thru line presented in Figure H.4, a set of error vectors were derived in the manner described above. These are shown plotted in Figure 4.17.

The difference observed in this Figure between the S_{12} and S_{21} error vectors (Figure 4.17b) may concern some readers, since for a passive two port structure we would expect the S_{12} and S_{21} measurement to be identical. However, The difference is very small and not considered significant. They are due to a residual systematic error in the ANA that is not removed by the calibration. In the de-embedding algorithm (Figure 4.3) the two measurements are averaged and set equal. However, to avoid amiguities in the perturbation analysis to follow only the S_{12} data is processed.

Also, in the perturbation analysis it will be assumed that the error vectors of Figure 4.17 are representative of the connection errors in the measurement of both the thru and the delay line standards of Figure 4.7. The only difference between these standards and the thru line that was measured for the connection repeatability study is the length of the line. Otherwise, the type of connection used for each is the same. The vector subtraction performed in deriving the error vectors essentially normalizes them to the average (though in a different way than a vector division does). Because of this it is reasonable to assume that the error vectors do not vary greatly between different fixture measurements, provided the magnitudes of the average S-parameters are similar. This is true for both the thru

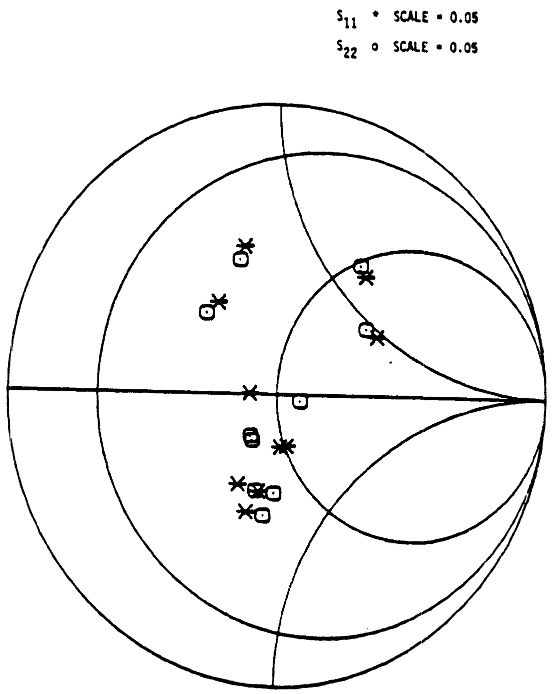

a. Error vectors for S_{11} and S_{22} measurement.

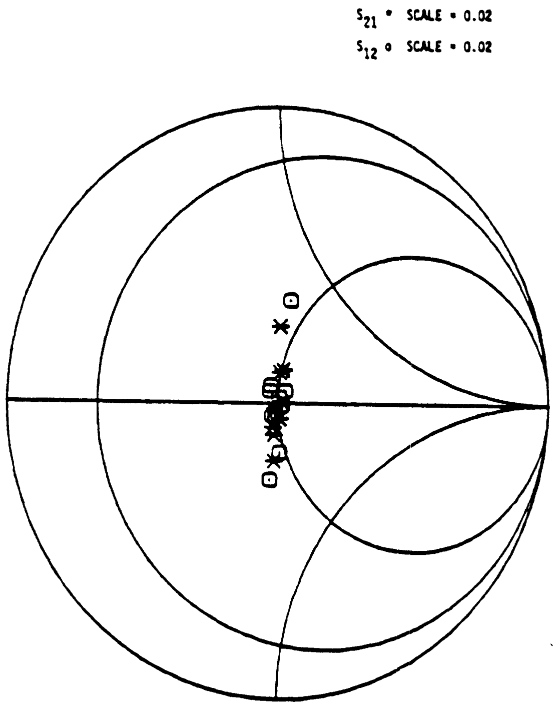

b. Error vectors for S_{12} and S_{21} measurement.

Figure 4.17: Error vectors for thru or delay line standards. These were also used to perturb the S-parameters of the two and four resonator filter structures.

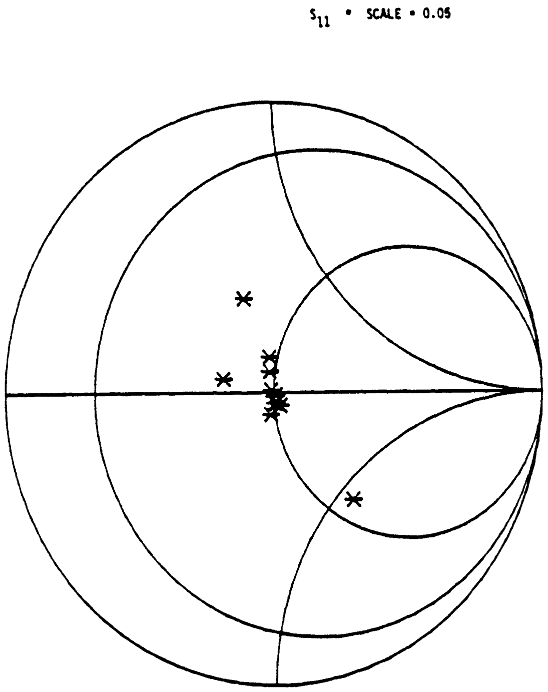

Figure 4.18: Error vectors for measurement of open-end reflection standard.

and delay line standards.

Error Vectors For Open-End Standard

In contrast, the reflection coefficient measurement for an open-end is not similar to that for a thru line and a different set of error vectors is needed. Hence, a new set of error vectors were derived from measurements of 11 repeated connections made to the open-end standard and these are shown in Figure 4.18. Since the magnitude of S_{11} and S_{22} are about the same, it is assumed that the same error vectors can be used to perturb both of these measurements.

Error Vectors For Series Gap Measurements.

For the series gap measurements, repeatability data was obtained for four connections on two of the gap circuits, and five connections on the third. Error vectors were derived separately for each of the gaps and compared. It was seen that the magnitude of the error vectors did not differ significantly between the three sets. These error vector sets were then combined to form a larger set of error vectors representing 13 possible connections. These are shown in Figure 4.19.

4.4.3 Connection Errors in ϵ_{eff} and Open-end Measurement

Using the method described above, a perturbation analysis was carried out to analyze the effects of connection errors on the ϵ_{eff}, Γ_{op}, and c_{op} measurements which are calculated as part of the TSD procedure as described previously.

To do this, nominal S-parameter measurements were taken from measurements on the standards of Figure 4.7 at $f = 10$ GHz. The error vectors discussed above were used to perturb these nominal parameters according to two different permutation tables, one with 20 connection permutations and the other with 100 permutations. These permutation tables are similar to Table 4.3, except that a different set of error vectors are used for the open-end standard. Also, the connection combinations for the S_{11} and S_{22} measurements were allowed to vary independently so that the permutation tables had 5 columns instead of 4.

The statistical data are calculated for each parameter based on the observed results for the different connection combinations. The average is calculated by summing up the results for each of the different combination numbers and dividing by the number of permutations. The estimated standard deviation s for the data is given by

$$s = \text{Std.Deviation} = \sqrt{\frac{\sum x_i^2 - \frac{(\sum x_i)^2}{N}}{N-1}} \qquad (4.4)$$

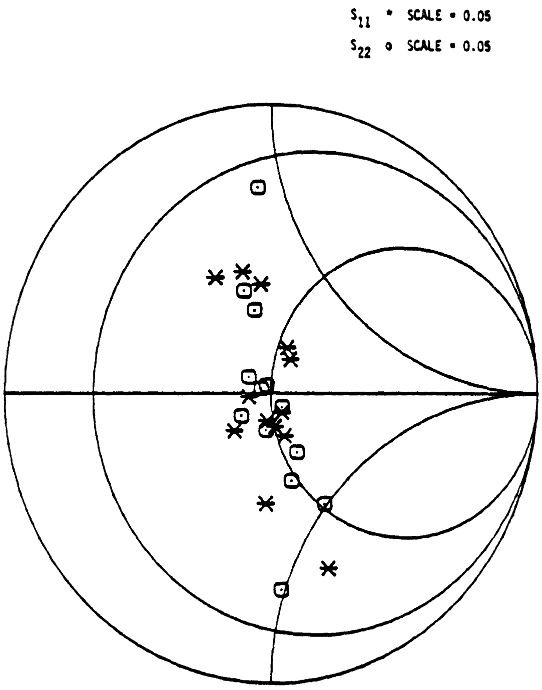

a. Error vectors for S_{11} and S_{22} measurement.

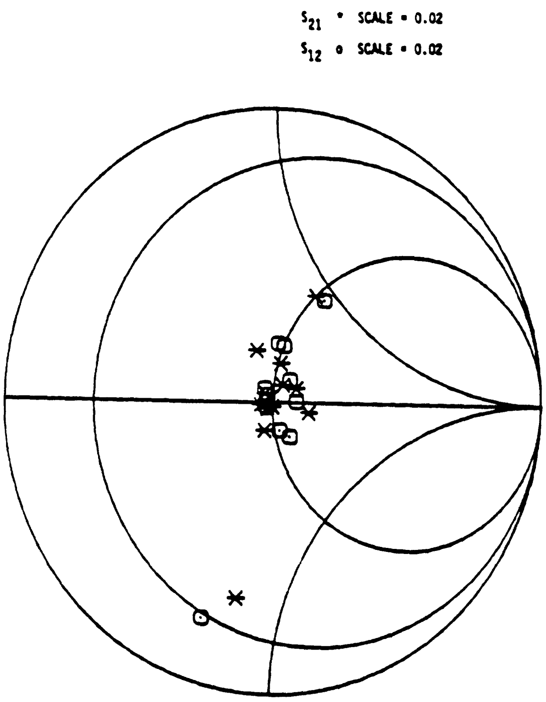

b. Error vectors for S_{12} and S_{21} measurement.

Figure 4.19: Combined error vectors for series gap measurements.

where

N = number of trials

x_i = observed result for the parameter of interest for connection combination i

The results of the perturbation analysis are summarized in Table 4.4. It is seen that the results for 100 connection permutations are not significantly different than those for 20 permutations. The range of observed values increase slightly for each of the parameters. This is reasonable since more worst case connection combinations are possible with a greater number of permutations. On the other hand, the standard deviation values are seen to change by a much smaller amount. It appears that 100 is a sufficient number of permutations from which to base the statistical observations.

The results of the analysis indicate that the uncertainty in ϵ_{eff} and the open-end parameters due to connection errors can be appreciable. The standard deviations for these parameters is about .5% (of the average) for ϵ_{eff}, and about 8% for the open-end parameters. These standard deviation values were used to derive error bars for the measurements of ϵ_{eff} and the open-end parameters presented in the next chapter.

Table 4.4: PERTURBATION ANALYSIS RESULTS FOR ϵ_{eff} and OPEN-END MEASUREMENTS

PARAMETER	PERMUTATIONS	MIN VALUE	MAX VALUE	AVG VALUE	RANGE	STD. DEV.
ϵ_{eff}	20	6.851	6.978	6.922	.127	.0302
	100	6.850	6.998	6.922	.147	.0312
θ_{op}	20	-11.8	-9.2	-10.3	2.6	.799
(DEG)	100	-12.0	-8.7	-10.2	3.3	.837
c_{op}	20	1.285	1.650	1.440	.365	.110
(pF-Ohm)	100	1.210	1.670	1.420	.465	.115

4.4.5 Connection Errors in Measurement of Series Gap Discontinuities

Next, the perturbation analysis was carried through the de-embedding of the three series gap discontinuity circuits measured for this thesis. For this part, nominal S-parameters were taken from each of the series gap measurements at $f = 10\text{GHz}$. The error vectors of Figure 4.19 were then used to perturb this data, and both 20 and 100 connection permutations were synthesized.

Figure 4.20 illustrates the information that can be gained from this perturbation analysis. Shown is the spread in final de-embedded S_{11} and S_{12} data for gap circuit C ($G = 5mil$) caused by connection errors. The perturbation analysis results (100 permutations) for all three gap circuits are summarized in Table 4.5. From these results it is seen that the S_{11} data shows relatively constant behavior with respect to the statistical parameters, while the change in the S_{12} data is significant. This is because in each case the amplitude of the S_{11} measurement is relatively large compared to the corresponding error vectors (Figure 4.19).

One important observation is that for large gap widths the uncertainty in the phase of S_{12} can be appreciable. This is because the magnitude of the nominal S_{12} value begins to approach the magnitude of the connection error. At first glance it appears that the uncertainty in the magnitude of the S_{12} measurement increases as the gap width is reduced. This is not the case since if the range and standard deviation values are divided by the average to calculate these parameters on a percentage basis, the opposite is true. Hence, the measurement uncertainty caused by connection errors increases as the magnitude of the S-parameter being measured decreases.

The standard deviation data from this analysis is used in constructing error bars for the series gap measurements presented in Chapter 5.

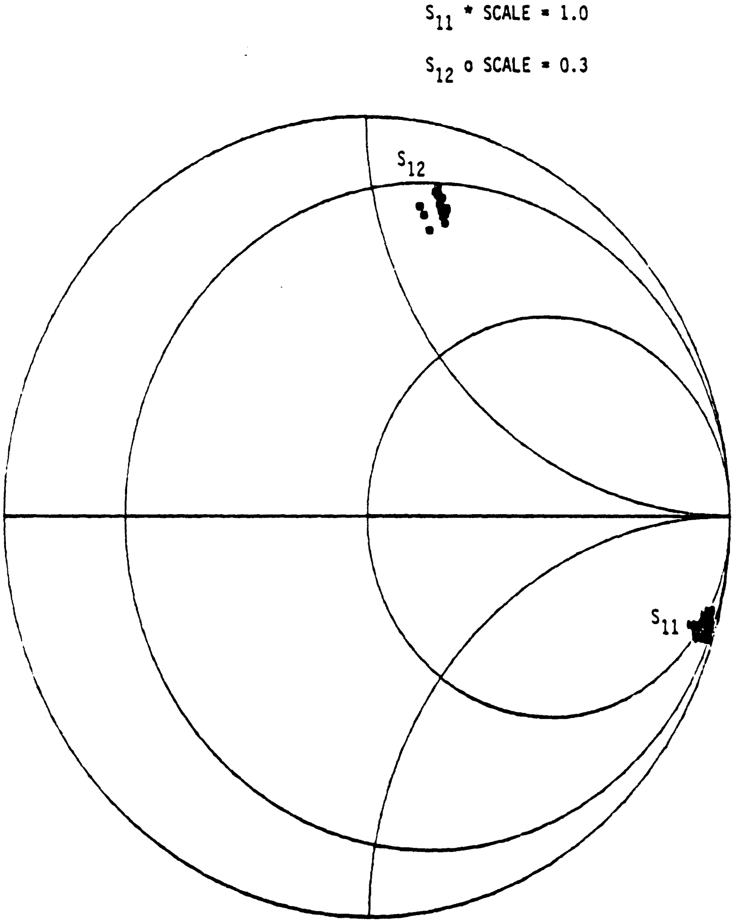

Figure 4.20: This plot of the final de-embedded result for a 5 mil series gap discontinuity illustrates the information obtained through the perturbation analysis (f=10GHz, 20 connection permutations).

Table 4.5: PERTURBATION ANALYSIS RESULTS FOR SERIES GAP MEASUREMENTS

TEST CKT.	PARAMETER	MIN VALUE	MAX VALUE	AVG VALUE	RANGE	STD. DEV.
A (G=15mil)	$\|S_{11}\|$	.964	1.02	.991	.056	.014
	$\angle S_{11}$	-8.2	-2.5	-4.7	5.7	1.33
	$\|S_{12}\|$	.07	.088	.081	.019	.004
	$\angle S_{12}$	76.9	95.1	83.5	18.2	3.2
B (G=9mil)	$\|S_{11}\|$	.963	1.00	.982	.041	.011
	$\angle S_{11}$	-14.2	-7.7	-11.1	6.5	1.29
	$\|S_{12}\|$	.117	.141	.132	.023	.005
	$\angle S_{12}$	77.1	88.8	81.3	11.7	2.0
C (G=5mil)	$\|S_{11}\|$	.940	.983	.962	.043	.011
	$\angle S_{11}$	-20.1	-14.2	-16.7	5.9	1.28
	$\|S_{12}\|$	.220	.254	.240	.034	.007
	$\angle S_{12}$	72.7	78.9	75.2	6.2	1.1

4.5 Summary of Experimental Methodology

The experimental methods used in this thesis are summarized below.

- The TSD method is used to de-embed the test fixture effects from the measurements. An open-end is used in place of the "short" circuit as the reflection standard
- The measurements of ϵ_{eff} and Γ_{op} are obtained as by products of the TSD procedure
- A perturbation analysis approach is used to help approximate measurement uncertainties

CHAPTER V

NUMERICAL AND EXPERIMENTAL RESULTS

In this chapter numerical and experimental results obtained through the present research are presented for the network parameters of shielded microstrip discontinuities. Included here are results for the effective dielectric constant , open-end and series gap discontinuities, and coupled line filters. Where possible comparisons are made to available data from other theoretical solutions. One case for an open-end is compared to to other full-wave solutions. However, since the emphasis in this study is to compare with measured data, extensive comparisons are made to available CAD models since this data is easier to generate for an arbitrary test case. Also, it is useful to include data from these CAD models in the study since they are widely applied to design shielded microstrip circuits.

The CAD models of *Super Compact* and *Touchstone* are based on a combination of different theoretical techniques, most often embodied in simplified closed form solutions, curve fit expressions or look-up tables [1]. These models do not provide a means to account for the effects of the shielding box of Figure 1.3. In the case of *Touchstone*, no shielding effects are included, and for *Super Compact* only a cover height is provided for, and this does not apply to the open-end or series

---

[1] In the manuals for these programs, references are listed for each discontinuity model, the reader is referred to these manuals for further information about the theoretical basis for the CAD models.

gap discontinuities. It is generally believed that as long as the dimensions of the shielding are large relative to the substrate thickness that the shielding will have a negligible effect. To simulate a complicated circuit containing many discontinuities, the discontinuities are assumed to be independent of one another and their respective models are used to generate a matrix representation for each discontinuity. The overall circuit performance is predicted by mathematically cascading the matrices together.

In contrast, the full-wave solution presented here accurately treats the entire geometry of the shielded microstrip circuit as a boundary value problem. Any interactions between, for example, the fringing fields on an open-ended line and an adjacent conducting strip are automatically included in the analysis. Because of this, the method is expected to provide better accuracy than CAD model predictions. Still, as will be seen shortly, the CAD models give quite reasonable results in many cases. However, in other cases, particularly where shielding effects become significant, the accuracy of the CAD models is questionable.

One case where shielding effects are noticeable is when the frequency approaches the cutoff frequency for the onset of higher order modes. As will be discussed next, as the size of the shielding box increases the cutoff frequency for the onset of higher order modes decreases.

5.1 Cutoff Frequency for Higher Order Modes

Higher order modes occur in open microstrip in the form of surface waves and radiation modes. Surface wave modes may be minimized by keeping the substrate electrically thin at the operating frequency. However, the first surface wave mode has a cutoff frequency of zero.

This is not the case for shielded microstrip, where the nature of higher order modes are quite different. The shielding forms a waveguide structure that eliminates radiation and surface waves. Instead, the higher order modes take the form of waveguide modes. As a consequence, below the waveguide cutoff frequency, only the dominant microstrip mode can exist.

For the present problem of Figure 1.3, the cutoff frequency for higher order modes may be approximated by analyzing the infinite dielectric-loaded waveguide of Figure 5.1. The closeness of the solution for the propagating modes of the dielectric-loaded waveguide to the solution for shielded microstrip has been observed in the past, both analytically [58], and numerically [59]. The solution for the propagation characteristics of the dielectric-loaded waveguide takes the form of trancendental equations [26,60] that must be solved either numerically or graphically. The analysis is carried out with LSE and LSM modes which are TE and TM respectively relative to the normal to the air-dielectric interface ($\hat{z}$). The cutoff frequency for the first propagating mode within the structure depends on the geometry. The following definition will help clarify what is meant by cutoff frequency as used in this thesis.

Definition V.1 *For the purposes of this thesis the* **cutoff frequency** f_c *will be defined as the first frequency where non-evanescent waveguide modes can exist inside the cavity. It will correspond to either an LSM or an LSE mode depending on which has the lowest cutoff frequency.*

A numerical solution to the dielectric-loaded waveguide problem was formulated by a student at the University [61]. This program has been used to analyze the cutoff frequencies for several of the shielding geometries considered in this thesis. The plot of Figure 5.2 shows the variation of the cutoff frequencies with shielding sized for a square waveguide three different substrates enclosed. It is seen that for the alumina ($\epsilon_r = 9.7$) substrate, the highest achievable cutoff frequency is limited to about 50GHz , while for a given shielding size, much higher cutoff frequencies are possible with the use of the thinner quartz ($\epsilon_r = 3.8$), or GaAs ($\epsilon_r = 12.7$)

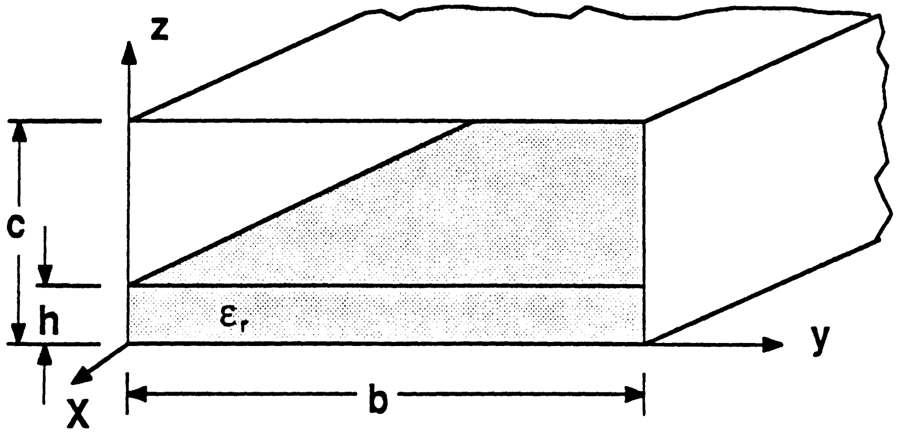

Figure 5.1: The cutoff frequency for higher order modes in shielded microstrip may be approximated by analyzing an infinite dielectric-loaded waveguide.

substrates.

These cutoff frequencies have been found to give a good prediction of the onset of higher order effects observed in the current distributions computed with the new method. As an example, Figure 5.3 shows the current distribution on an open-ended line operating below the cutoff frequency. For the indicated geometry, f_c is about 17.9 GHz. As the frequency is raised above the cutoff frequency, the current becomes more and more distorted as shown in Figure 5.4.

This distortion may be explained as follows. Above cutoff, the microstrip current excites a waveguide mode which travels down the cavity until it reaches the wall at $x = a$, it is then reflected back and forth inside the cavity and interacts with the microstrip current. This waveguide behavior can take place, even though the cavity is not at resonance, because the microstrip current has an external energy source via the coaxial excitation.

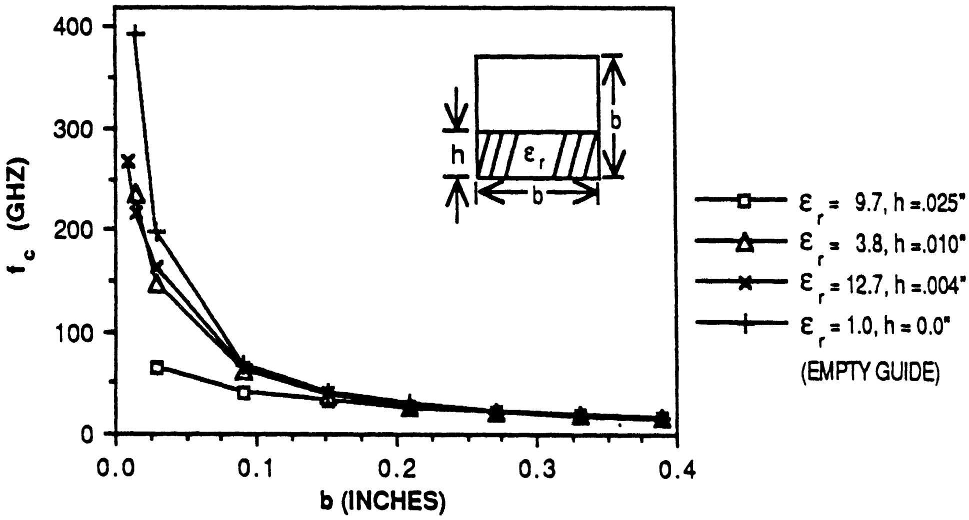

Figure 5.2: Variation of cutoff frequencies with shielding for three commonly used substrates enclosed in a square waveguide ($b = c$). Also shown is empty guide case ($\epsilon_r = 1, h = 0$).

5.2 Effective Dielectric Constant Results

Effective dielectric constant results are presented in this section for 50 ohm lines on three common substrates: alumina, quartz and gallium arsenide (GaAs). As discussed in Section 2.7, the microstrip effective dielectric constant ϵ_{eff} is computed from the current distribution. The current can be associated either with a thru line or an open-ended line. Although a calculation of the effective dielectric constant was not among the primary objectives of this work, its determination is an integral part of the solution for discontinuity effects, and the comparisons which follow also lend insight into the relationship between substrate geometry and shielding effects.

Effective Dielectric Constant Results for an Alumina Substrate

Figure 5.5 shows ϵ_{eff} for a 25 mil thick alumina substrate. The numerical re-

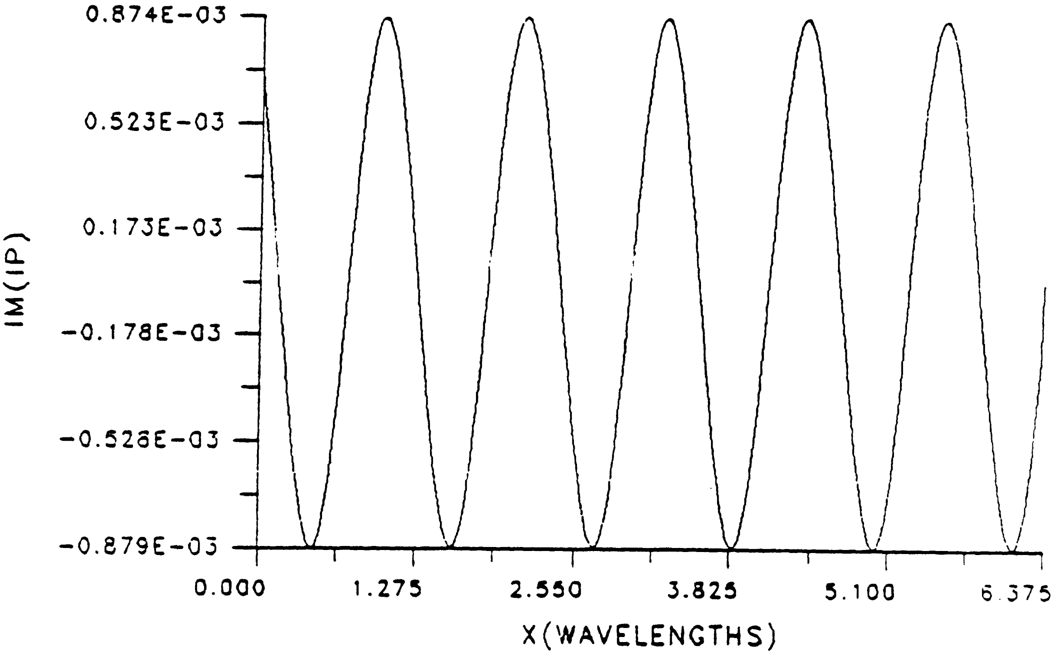

Figure 5.3: Below the cutoff frequency f_c, the microstrip current on an open-ended line forms a uniform standing wave pattern (f = 16GHz,ϵ_r = 9.7, W/h = 1.57, h = .025", b = c = .275").

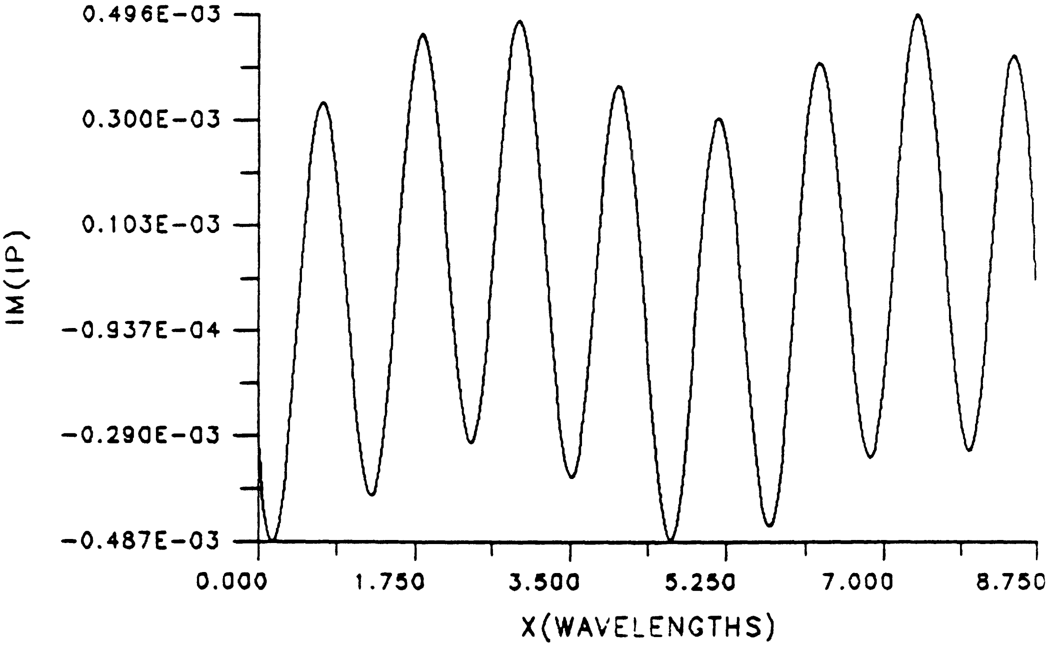

Figure 5.4: As the frequency is increased above f_c, more and more distortion is observed in the open-end current distribution (f = 22GHz,ϵ_r = 9.7, W/h = 1.57, h = .025",b = c = .275").

sults are compared to measurements, and to CAD package results. Note that *Super Compact* allows only the cover height to be varied while the calculation provided by *Touchstone* neglects shielding effects. For the shielding geometry used here, it is seen that the difference between the numerical and CAD package results are within experimental error. However, interestingly enough, better agreement between the CAD results and the numerical results is observed at higher frequencies. This may be due to the fact that the side walls, which are not included in the *Super Compact* analysis, are electrically closer to the strip at low frequencies.

The measured data is obtained as a byproduct of the TSD fixture characterization procedure (Section 4.3). The data shown represents the average of ten separate procedures. These procedures were conducted over a period of about four years at both Hughes (not all by the author) and at the University. At least three or four different sets of TSD standards were used over this period, however, the mechanical dimensions and substrate parameters are designed to be identical. The error bars shown in Figure 5.5 represent the standard deviation ($\pm s$) of the different measurements.

This data is shown here in lieu of the result from a single measurement, since it gives a more representative view of the involved measurement uncertainty. In this case the error bars shown represent the combined effect of connection errors, variations in ϵ_r, differences in substrate mounting, and errors in specifying the physical difference between the length of the thru and delay line standards. The major error source is believed to be the variations in ϵ_r which can be significant for alumina substrates [62,63].

To see how ϵ_{eff} varies with shielding, consider the plot of Figure 5.6. This plot compares numerical and *Super Compact* results for three different shielding geometries. The notation used to describe different shielding and substrate geometries is explained in Table 5.1. The case for cavity CA is the same as that of

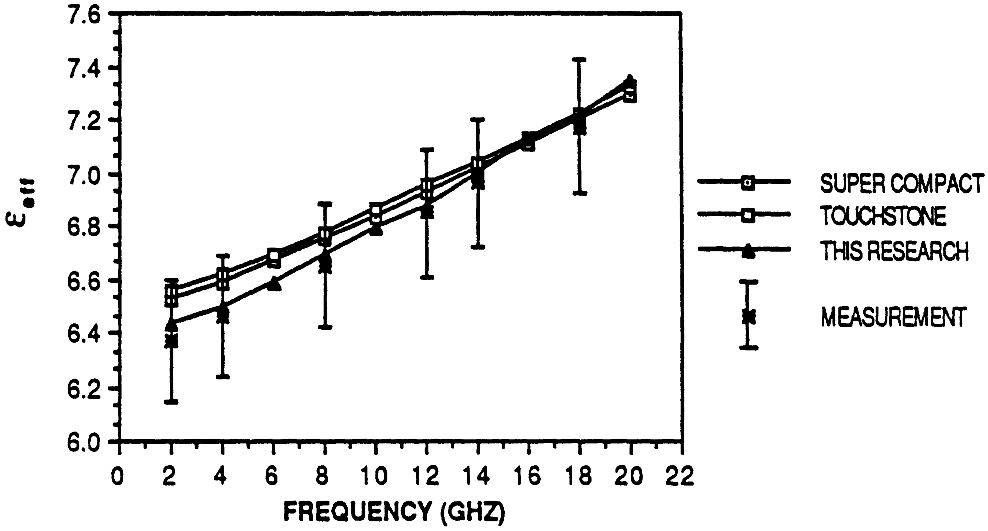

Figure 5.5: Effective dielectric constant comparison for an alumina substrate compared to measurements and CAD package results ($\epsilon_r = 9.7, h = .025'', b = c = .25''$).

Figure 5.5. For the other two cases, where the shielding is closer to the microstrip, the agreement is not as good.

Effective Dielectric Constant for a Quartz Substrate

The effect of shielding on ϵ_{eff} for a quartz substrate is displayed in Figure 5.7. In this case the *Super Compact* analysis is seen to give good results for both of the two larger shielding geometries . However, the numerical results again show a reduced value as the size of the shielding is reduced further.

The reduction of the effective dielectric constant, relative to *Super Compact*, can be explained as follows. For a larger shielding geometry, the field distribution on the microstrip more closely resembles the open microstrip case, with most of the electric field concentrated in the substrate. In this case, most of the electric field lines originate on the microstrip conductors and terminate on the ground plane

Table 5.1: CAVITY NOTATION USED TO DENOTE DIFFERENT GEOMETRY AND SUBSTRATE PARAMETERS

CAVITY	ϵ_r	W (in)	h (in)	b (in)	c (in)	f_c (GHz)
CA	9.7	.025	.025	.250	.250	21.8
CC	9.7	.025	.025	.100	.100	37.5
CF	9.7	.025	.025	.075	.075	41.7
QCB	3.82	.0157	.010	.122	.080	45.8
QCE	3.82	.0157	.010	.100	.100	73.0
QCG	3.82	.0157	.010	.050	.05	102.5

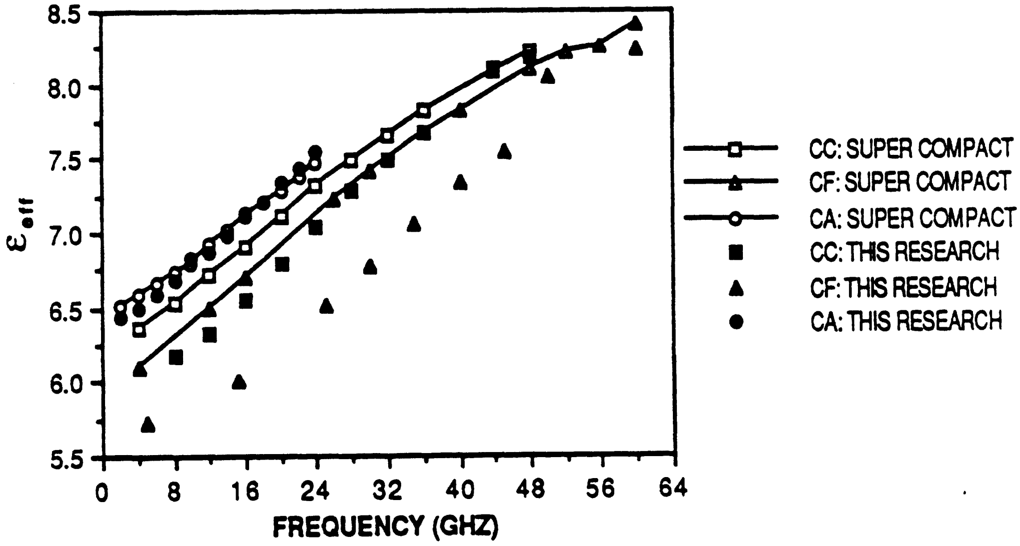

Figure 5.6: The effects of shielding on ϵ_{eff} are apparent as the size of the shielding cavity is reduced (see Table 5.1 for geometry.)

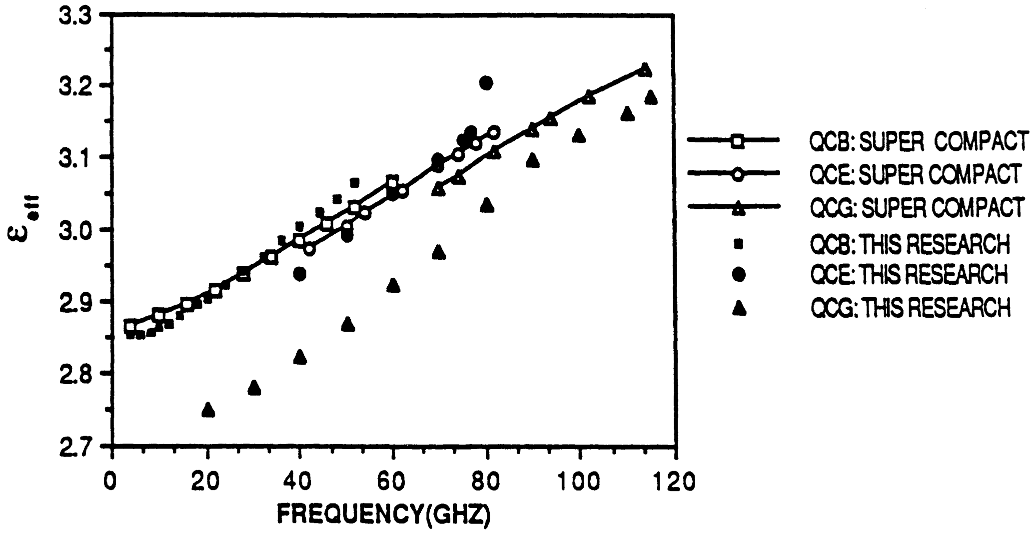

Figure 5.7: Shielding effects are also significant for the quartz substrate shown here (see Table 5.1 for geometry).

below. As the cavity size is reduced, the ground planes of the top and side-walls are brought closer to the microstrip lines. The electric field distribution is now less concentrated in the substrate, as more field lines can terminate on the top and side walls. As a result, a proportionally larger percentage of the energy propagating down the line does so in the air region, and the dielectric constant is reduced.

Effective Dielectric Constant for a GaAs Substrate

Figure 5.8 shows a comparison of the effective dielectric constant for a 4 mil thick GaAs substrate. This is a typical substrate geometry used for MMIC purposes. The agreement between the numerical and CAD model predictions this case is excellent. The differences observed in the case of the other two substrates was not seen for the GaAs substrate of Figure 5.8. because of how thin the substrate is relative to the size of the cavity.

Hence, all of the effective dielectric constant results presented above demon-

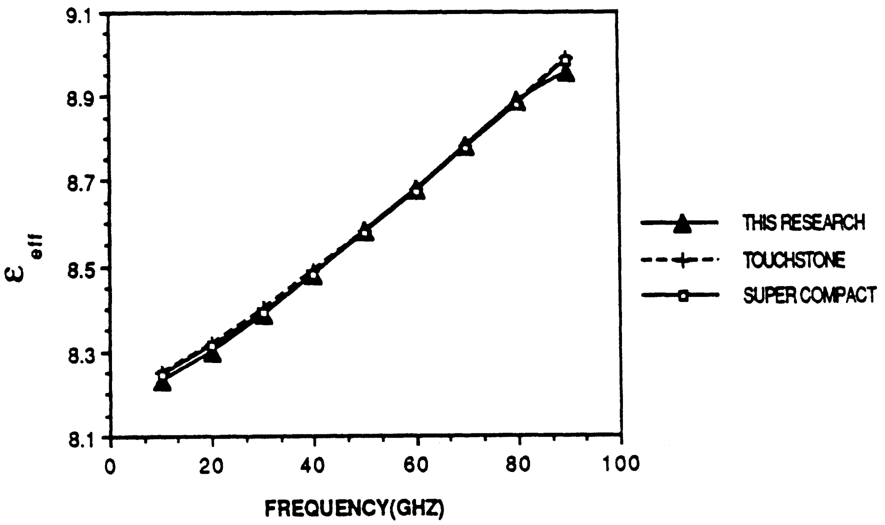

Figure 5.8: The numerical and CAD package results display excellent agreement for the case of a thin GaAs substrate ($\epsilon_r = 12.7, h = .004'', b = c = .07'', f_c = 81\text{GHz}$).

strate that the CAD package predictions are valid when two conditions are met: 1) the shielding is large with respect to the substrate height, and 2) the frequency is below the cutoff frequency. When the dimensions of the shielding becomes comparable to the substrate height, the CAD results are no longer accurate. This suggests the need for an improved CAD formulation valid for small as well as large shielding geometries. The present method could be used as the basis for deriving such a formulation.

5.3 Results for Open-end Discontinuity

As discussed in Section 2.7, an open-end discontinuity can be represented by an effective length extension L_{eff}, by a shunt capacitance c_{op}, or by the associated reflection coefficient Γ_{op} $(= S_{11})$. Each of these three representations will be used in this section.

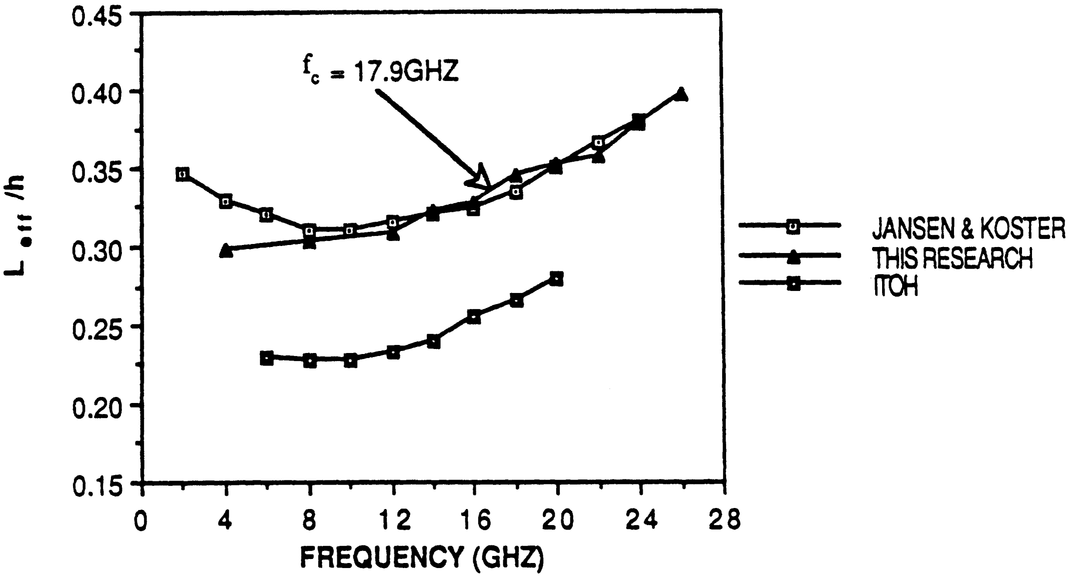

Figure 5.9: Effective length extension of a microstrip open-end discontinuity, as compared to results from other full-wave analyses (ϵ_r = 9.6, W/h = 1.57, b = .305″, c = .2″, h = .025″).

The plot of Figure 5.9 compares L_{eff} results to those of Jansen et al. [64] and Itoh [10]. The results from this research are almost identical to those obtained by Jansen et al. for frequencies above 8 GHz, but show a reduced value for lower frequencies. Jansen et al. speculate that the large difference in the results obtained by Itoh are due to an inadequate choice of basis functions.

The case of Figure 5.9 was chosen to compare the coaxial and gap generator excitation methods used in the method of moments solution [2]. Table 5.2 shows that the results computed for this case by the two methods are equivalent. This equivalence is also observed for the computations of two-port scattering parameters for the structures considered herein. Hence, as far as computing network parameters is concerned either method gives good results. Since the coaxial method is more

---

[2] The inner and outer radii of the coax feed was taken to be .007″ and .016″ respectively.

Table 5.2: COMPARISON OF L_{eff}/h COMPUTATION FOR THE TWO TYPES OF EXCITATION METHODS

f (GHz)	4	8	12	14	16	18	20
GAP GENERATOR	.298	.305	.309	.321	.324	.344	.353
COAXIAL EXCITATION	.299	.304	.309	.322	.327	.344	.352

realistically based, this conclusion lends validity to the use of the gap generator method.

The results shown in Figure 5.10 illustrate the effect of the shielding on the open-end discontinuity. The normalized open-end capacitance c_{op} is plotted for three different cavity sizes. The results show that reducing the cavity size raises f_c (as expected), and it lowers the value of c_{op}. For comparison, data obtained from *Super Compact* and *Touchstone* and measurements (see Section 4.3) are included. The errors bars on the measurements represent the estimated standard deviation ($\pm s$) of the connection errors for this measurement from Table 4.4.

Similar shielding effects are observed for an open-end on a a quartz substrate as shown in Figure 5.11. In this case it is seen that the *Super Compact* result gives a good value for low frequencies, and where the frequency is well below the cutoff frequency for a given shielding size. Or stated another way, the shielding effects are less severe for a smaller shielding cavity! This conclusion defies common sense, but is strongly supported by the numerical results. Note that Jansen's results (Figure 5.9) show a similar rise in the open-end effect as the cutoff frequency is approached.

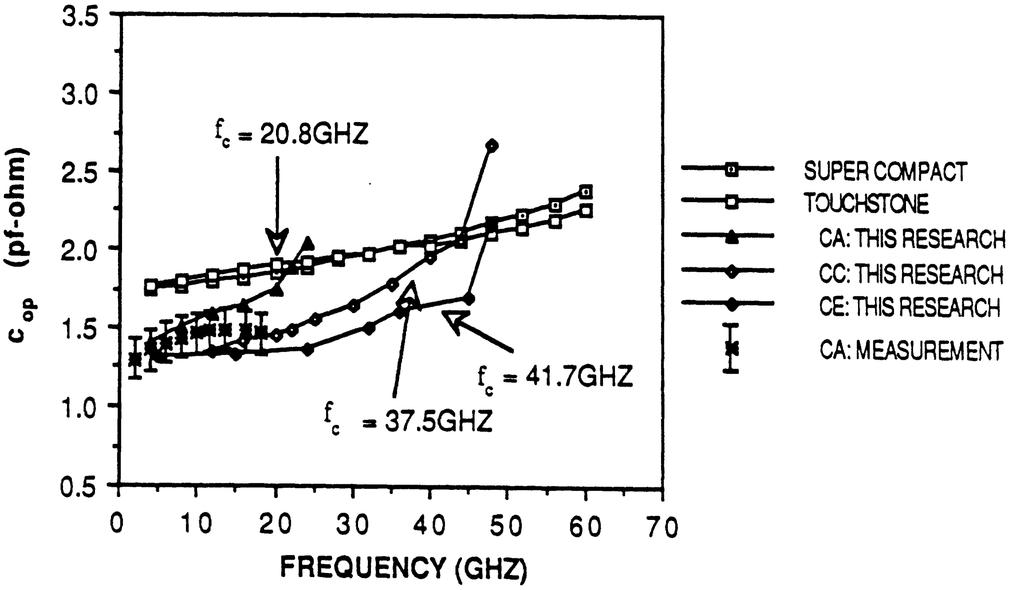

Figure 5.10: A comparison of the normalized open-end capacitance for three different cavity sizes shows that shielding effects are significant at high frequencies (see Table 5.1 for cavity geometries).

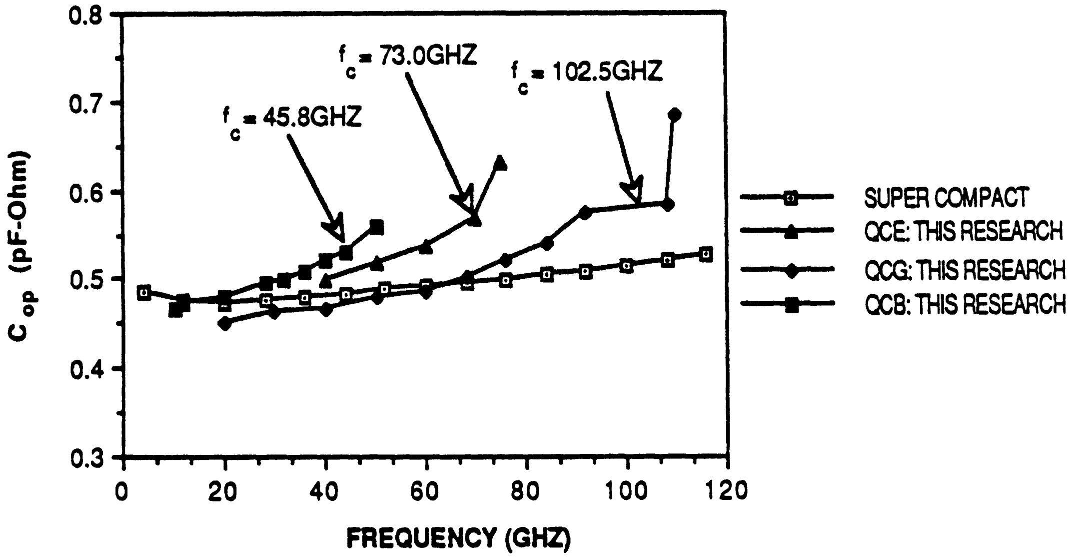

Figure 5.11: Nomalized open-end capacitance for three different cavity sizes for a quartz substrate. This data also shows an increase in the capacitance as the cutoff frequency is approached (see Table 5.1 for cavity geometries).

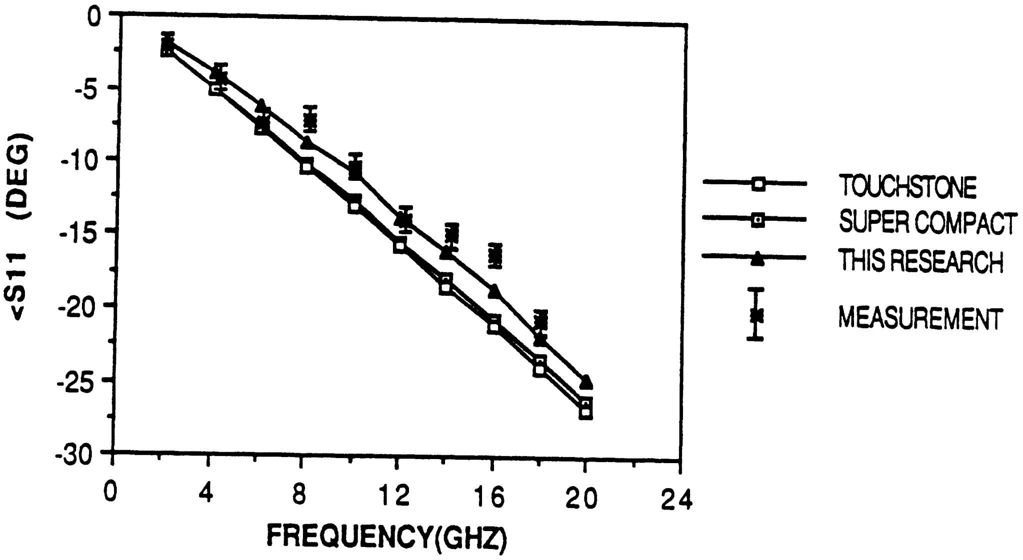

Figure 5.12: Numerical and measured results show good agreement for the angle of S11 of an open circuit ($\epsilon_r = 9.7$, W = h =.025″, b = c =.25″).

As a last example of the open-end effect, Figure 5.12 shows results for the angle of S_{11} of an open-end compared to measurements (see Chapter 4). The measurement is seen to favor the numerical results, although the differences observed are not overly significant for this shielding geometry. The error bars the approximate standard deviation of the connection errors associated with this measurement (Table 4.4).

5.4 Results for Series Gap Discontinuities

Numerical and experimental results have been obtained for series gap discontinuities with three different gap spacings (G) 15 mil (i.e. .015″), 9 mil, and 5 mil. The test circuits and the shielding dimensions used for the measurements are those of Figure 5.12.

Numerical results for the magnitude of S_{21} for these gaps are shown plotted in Figures 5.13- 5.15. For comparison, results obtained using *Super Compact*, and *Touchstone* are also shown plotted along with measured data. The error bars associated with the standard deviation of connection errors (Table 4.5), are on the order of ±.5dB and are too small to show on the plots.

With one exception, the measured data best follows the results of this research. In contrast, the *Touchstone* analysis had the least agreement with the measurements. This may in part be due to the fact that *Touchstone* does not include any shielding effects either the side walls or the shielding cover into account. However, the *Super Compact* model for the series gap does not appear to include the effect of the cover.

The one exception where the numerical result appears to be slightly off from the measurement is in the plot of the magnitude of S_{21} of the 5 mil gap. Based on numerical investigation it appears that by using a smaller subsection length in the method of moments computations, the value for S_{21} can be improved (i.e. it approaches the measurement). However, as discussed in section 3.5, the subsection length cannot be decreased arbitrarily as other implications must be considered. The best approach may be to minimize the size of the matrix by using a small subsection length around the region of the gap and a larger subsection length over the uniform line sections.

Results for the angle of S_{21} and S_{11} for the 15 mil series gap are shown in Figures 5.16 and 5.17. The error bars in these charts represent the estimated standard deviation from the perturbation analysis (Table 4.4). Although the measurements tend to favor the numerical results, the differences are not too significant. The phase of the S-parameters for the other two series gaps behave in a similar way as

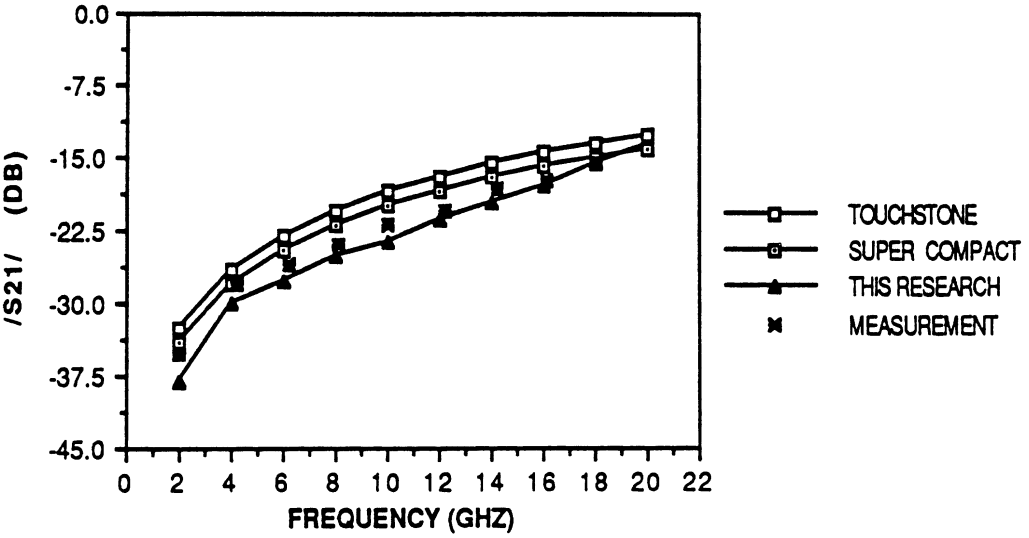

Figure 5.13: Magnitude of S_{21} for series gap circuit A (G = 15 mil).

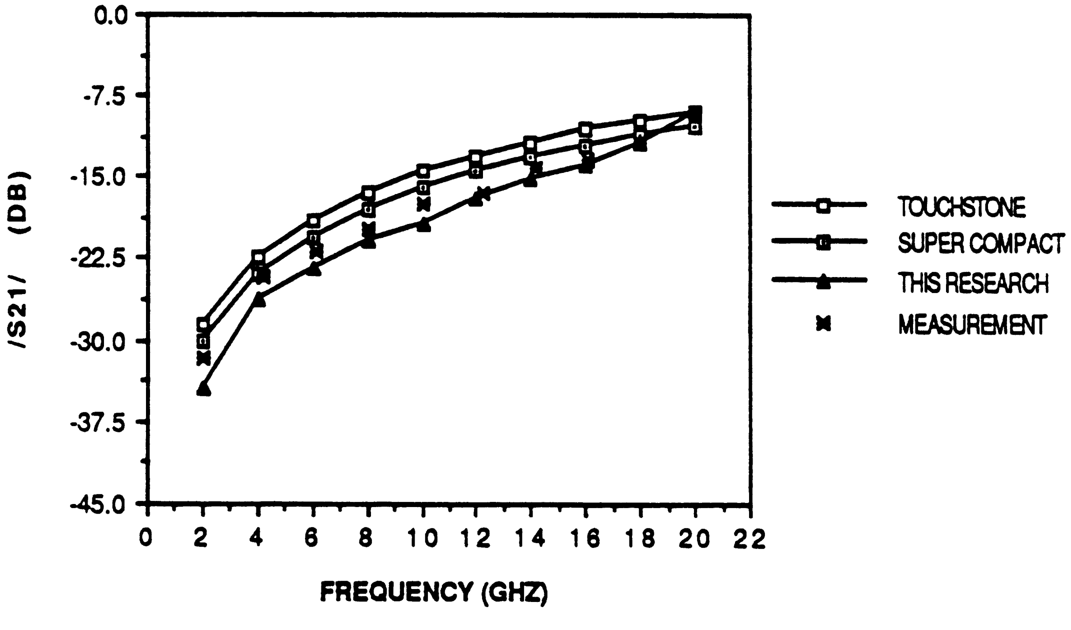

Figure 5.14: Magnitude of S_{21} for series gap circuit B (G = 9 mil).

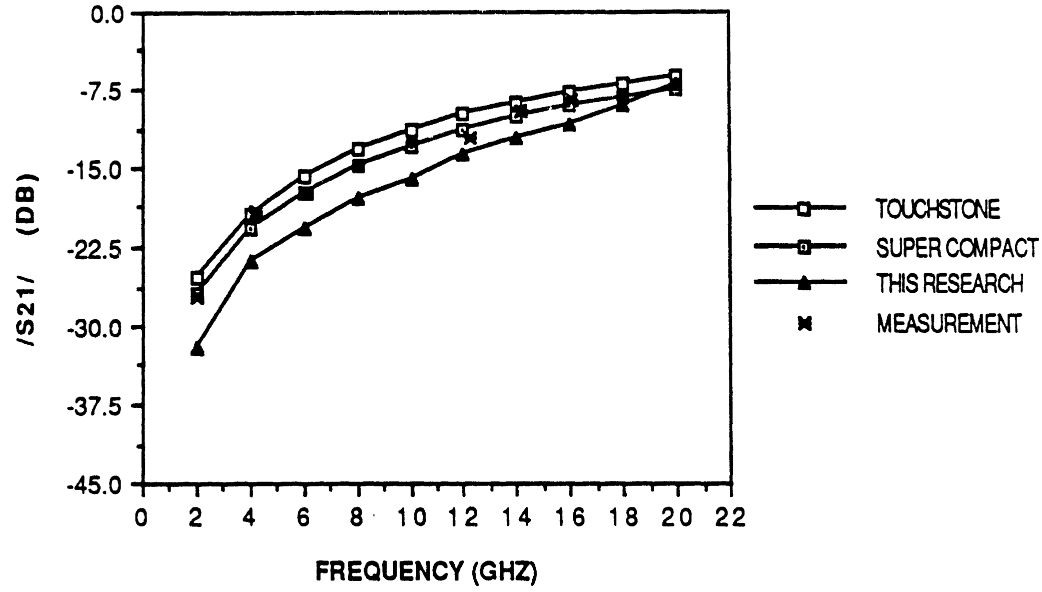

Figure 5.15: Magnitude of S_{21} for series gap circuit C ($G = 5$ mil).

that for the 15 mil gap and have been omitted from this treatment.

The measurements made on the series gap discontinuities are seen to further verify that the theory developed here gives good results. For the large shielding dimensions used for the measurements ($b, c \gg h$) the CAD models are seen to give reasonable results. The behavior of series gaps for small shielding dimensions was not studied, instead emphasis was placed on obtaining results for coupled line filters since their behavior is more complicated and therefore more interesting.

5.5 Results for Coupled Line Filters

The last results to be discussed were obtained for the two and four resonator filters discussed in Section 4.3. For brevity only the amplitude and phase of the transmission coefficient S_{21} will be discussed. Note that for the shielding geometry of both filters, the cutoff frequency f_c. is approximately 13.9GHz. Above this, the

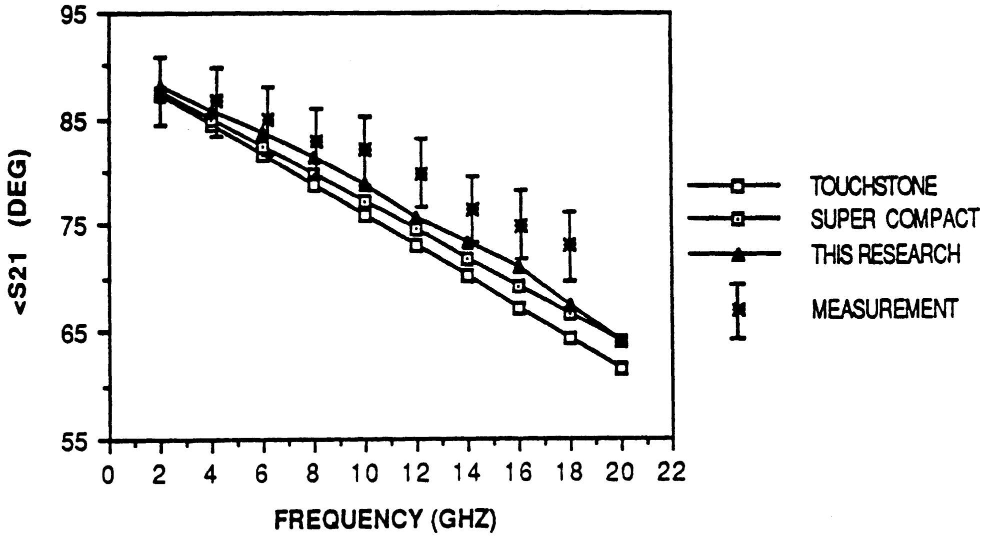

Figure 5.16: Angle of S_{21} for series gap circuit A (G = 15 mil).

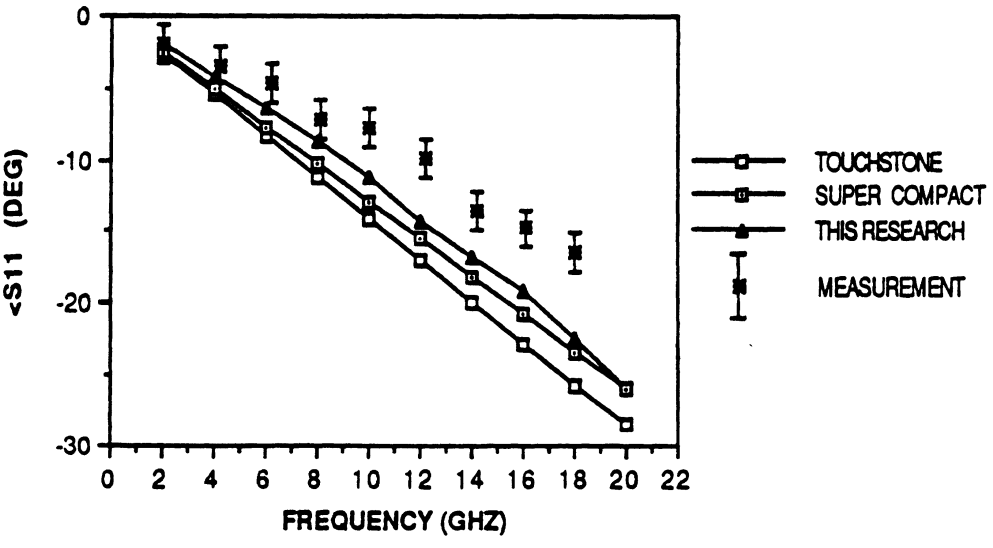

Figure 5.17: Angle of S_{11} for series gap circuit A (G = 15 mil).

filter measurements are distorted due to waveguide moding within the test fixture [3].

The measured and numerical results of this research are compared to CAD model predictions. The CAD package analysis for coupled line filters is performed by cascading two different types of discontinuity elements together: coupled microstrip lines, and open-end discontinuities. As mentioned previously, neither of the packages studied here account for shielding in the open-end discontinuity, however, *Super Compact* does include the effect of the cover height in the model for coupled lines.

Two Resonator Filter

Figure 5.18 shows a comparison of the measured and predicted response of the two resonator filter. From this plot, it is seen that the analysis from both the numerical and the CAD packages give a very good prediction of the response of the filter in the pass band. Outside the pass band the amplitude response is seen to more closely follow the numerical results.

Close examination of the phase plot (Figure 5.18b) shows that the the numerical results are shifted up in frequency by a small amount as compared to the measurements. It is believed that this discrepancy, though small, is related to the thin-strip approximation used for the current distribution. In the theoretical solution, the current is assumed to be uni-directional and to have a symmetric variation in the transverse direction as described by (2.7). In the coupling region

---

[3] Because energy can propagate in a waveguide mode, significant coupling occurs between the two coaxial feeds of the fixture, and the resulting measurement uncertainty is large. Hence, for all the filter results presented, the measurements are only good up to $f_c = 13.9$ GHz.

of the filter the close proximity of the adjacent strip conductors will cause the current to become non-symmetric and may require a more general definition of the current as the strip becomes wide.

However, note that the thin-strip approximation used here already gives a very good result. If in the magnitude plot of Figure 5.18, the response for the numerical results of this research are shifted down slightly, the agreement with the measurement will practically be exact.

Four Resonator Filter

The results for the four resonator filter are shown in Figure 5.19. In this case, numerical results for S_{21}, demonstrate excellent agreement with measurements up to the cutoff frequency. Note that for this filter the strip widths are about half as wide as those in the two resonator filter. Hence, the error due to the thin strip approximation is reduced. As in the case of the two resonator filter, the CAD models fail to predict the filter response in the rejection band, whereas the numerical results follow the measurements closely. For the four resonator filter, this is true for both the phase as well as the magnitude of S_{21}.

In the phase response, the CAD models display a large error compared to measurements between about 6 and 8.5GHz, while the numerical results track the measured phase very well. Below about 5.5GHz, the measured phase is seen to be different from the predictions of both the CAD models and the numerical results. This is most likely due to a phase error in the measurements. In the TSD technique, the delay line for the measurements should ideally be $\frac{\lambda_g}{4}$ at the measurement frequency. When the electrical length becomes either too short or too close to a multiple of $\frac{\lambda_g}{2}$ phase ambiguities can result. A good rule of thumb is for the delay line to be between $\frac{\lambda_g}{8}$ and $\frac{3\lambda_g}{8}$ [4]. At 5.5GHz the delay line used for the measurements is slightly less than $\frac{\lambda_g}{8}$; hence, this is most likely the source of the phase error.

We will now examine what happens as the top cover is brought closer to the circuitry. The results of Figure 5.19 show that even for large shielding dimensions the CAD models do not adequately predict the filter response in the rejection band. Figure 5.20a shows *Super Compact* predictions for the four resonator filter with two different cover heights. These predictions indicate that lowering the cover height should significantly narrow the pass band, and reduce the amplitude in the rejection band.

A significantly different prediction is observed in the numerical results for this case presented in Figure 5.20b. A narrowing of the pass band response is also observed in the numerical predictions, but not by nearly as much as in the *Super Compact* prediction. More importantly, the amplitude in the rejection band is seen to increase instead of decrease!

To prove that the numerical prediction is indeed the correct one, an additional measurement was made of the filter for the low cover height case. As can be seen from Figure 5.20b the measured data falls practically on top of the numerical predictions for both cover heights.

5.6 Summary of Numerical and Experimental Results

In this chapter results were presented for the effective dielectric constant of uniform microstrip lines, and the network parameters for open-end and series gap

---

[4] Multiple lines are needed for broadband measurements.

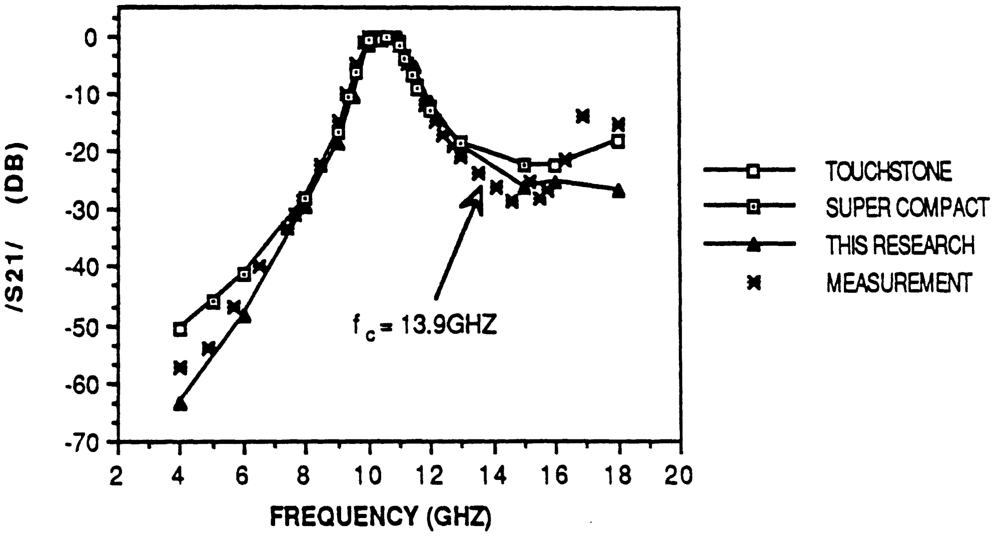

a. Amplitude of S_{21}

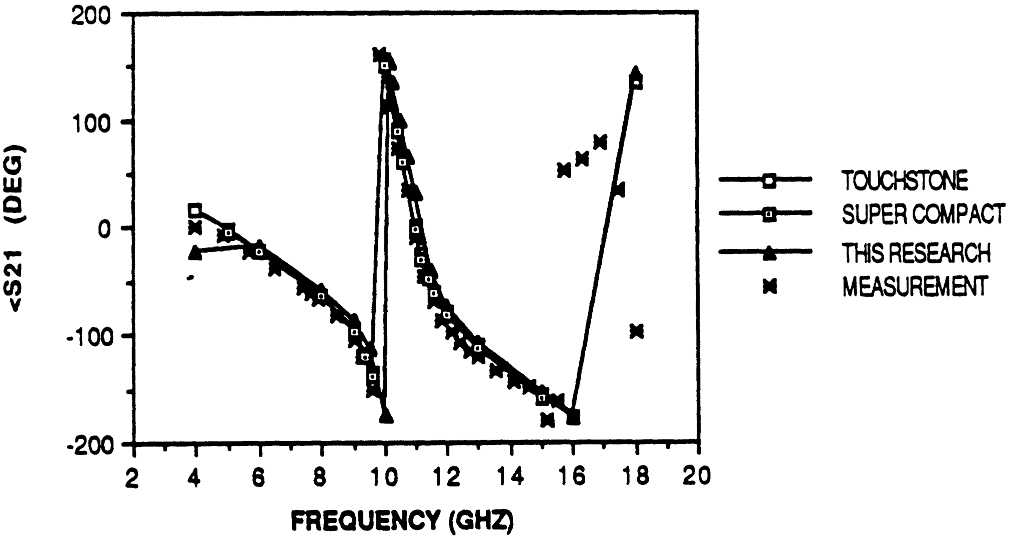

b. Phase of S_{21}

Figure 5.18: Results for transmission coefficient S_{21} of two resonator filter ($\epsilon_r = 9.7, W = h = .025"; b = .4'', c = .25''$).

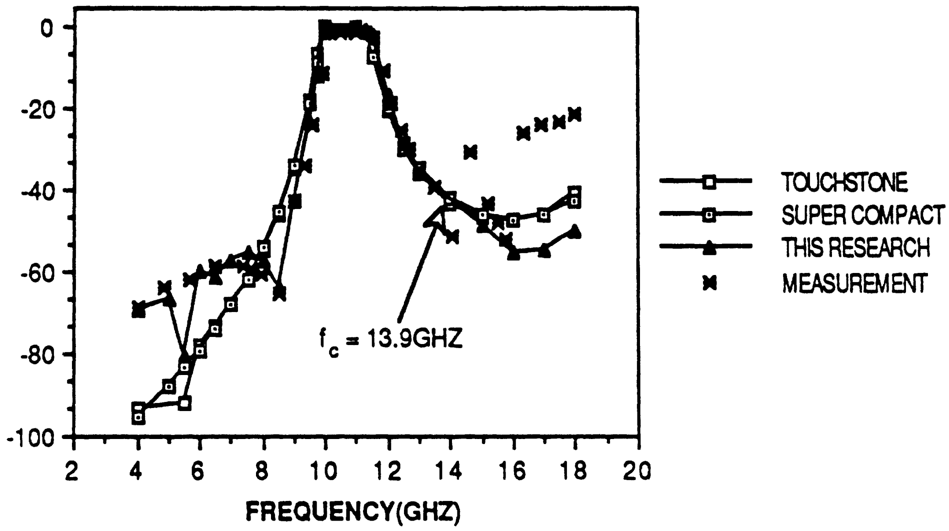

a. Amplitude of S_{21}

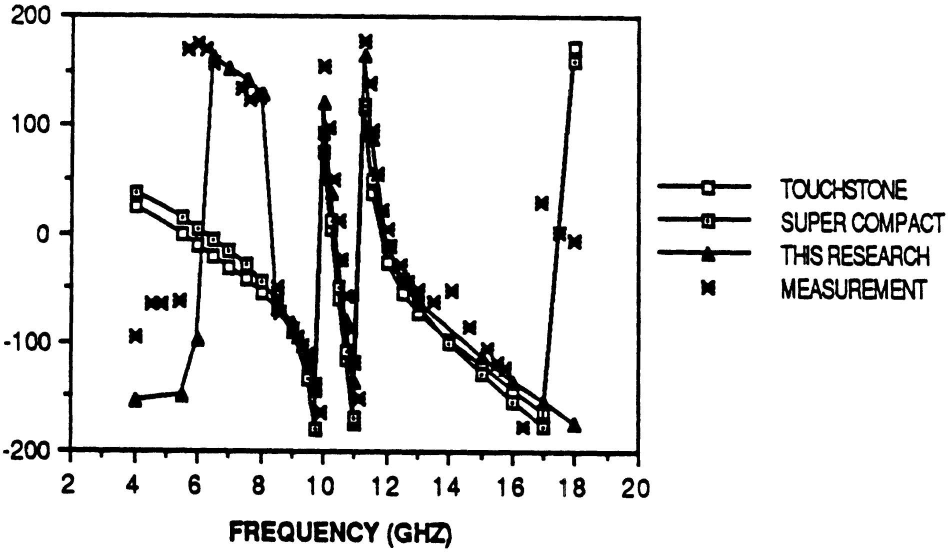

b. Phase of S_{21}

Figure 5.19: Results for transmission coefficient S_{21} of four resonator filter ($\epsilon_r = 9.7, W = .012'', h = .025''; b = .4'', c = .25''$).

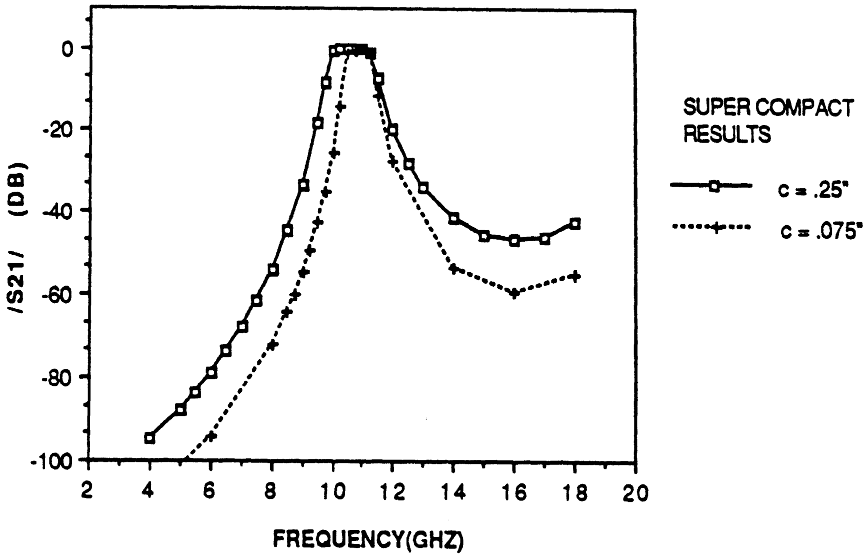

a. Super Compact predictions

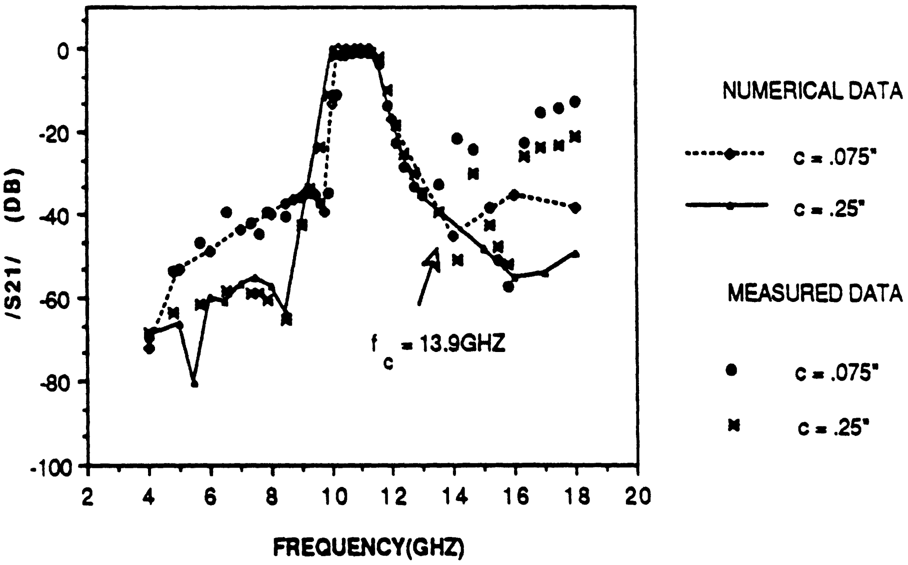

b. Numerical results of this research compared to measurements

Figure 5.20: Results for lowering the shielding cover on the amplitude response of four resonator filter ($\epsilon_r = 9.7, W = .012'', h = .025''; b = .4''$).

discontinuity and for two coupled line filters. The higher order modes in shielded microstrip are described to be essentially waveguide modes. In fact, the cutoff frequency f_c for a partially filled rectangular waveguide gives a good prediction of the onset of higher order mode behavior in the computed microstrip current distribution. A wealth of numerical and experimental data is presented for the above mentioned structures, and comparisons are made to other full-wave analysis and to commercially available CAD packages. Conclusions based on these comparisons are summarized in the next chapter.

CHAPTER VI

CONCLUSIONS AND RECOMMENDATIONS

The results from the research presented in this thesis lead to several conclusions regarding different aspects of shielded microstrip discontinuity characterization. These conclusions have been separated into appropriate categories as addressed herein.

6.1 Conclusions from Theoretical Work

In the theoretical work (Chapter 2) a method of moments formulation for the shielded microstrip problem is derived based on a more realistic excitation model than used with previous techniques. This result follows directly from the reciprocity theorem, with the use of a frill current model for the coaxial feed. The reciprocity theorem is applied in a similar way for the case of gap generator excitation. The impedance matrix formulation for gap generator excitation is seen to be identical to that for the coaxial excitation method developed here. The difference between the two methods is therefore only in the excitation vector used on the right hand side of the matrix equation. In solving for the impedance matrix elements, all of the required integrations are solved in closed form. Conversely, for the excitation vector of the coaxial excitation method, numerical integration is required.

6.2 Conclusions from Computational Work

Computational considerations for implementing the theoretical solution are explored extensively (Chapter 3). A graphical presentation is given that illustrates the different steps in the computation of microstrip currents. The current for the coaxial excitation method is shown to be uniform along the strip, while a discontinuity in the current is evident in the current for the gap generator method. The effect of this discontinuity is minimized by positioning the gap generator at the beginning of the first strip subsection. The gap generator method is more computationally efficient than the coaxial excitation method since numerical integration is not required.

Several numerical experiments are presented (Chapter 3) that explore the convergence and the stability of the solution. The parameters explored are the subsection length l_x, the sampling rate $N_x(= 1/l_x)$, the value for K used in the basis functions, the summation truncation points $NSTOP$ and $MSTOP$, and the cavity length a. A value of $K = 2\pi$ appears to be the best choice. The main conclusions drawn from these experiments may be summarized as follows:

- A value of $K = 2\pi$ is a good value to use in the sinusoidal basis functions.
- A minimum sampling limit exists such that the condition $Kl_x < \frac{\pi}{2}$ must be satisfied in order to obtain useful current results. For a value of $K = 2\pi$, $l_x = .25$ is the largest subsection length that can be used.
- Good convergence on n and m is achieved after 500 terms have been added on each.
- A maximum sampling limit exists in the form of an erratic current condition which may be defined by the simple formula $NSTOP{*}l_x < a$. ($NSTOP{*}l_x \geq a$ must hold for useful results.)

- An optimum sampling range may be specified that automatically avoids the erratic current condition, and guarantees the best accuracy in the matrix solution. This range is given approximately by $\frac{1.5a}{NSTOP} \leq l_x \leq \frac{4a}{NSTOP}$.
- The optimum sampling range was found to correspond directly with the flat convergence region for the L_{eff} and ϵ_{eff} computations.

6.3 Conclusions from Experimental Study

From the experimental study (Chapter 4), a comparison of various measurement techniques lead to the choice of the TSD de-embedding method for the measurements of this thesis. Various microstrip connection repeatability issues are explored experimentally (Appendix I). The results indicate that, for the hardware tested, the best connection approach is to make the required fixture connections at the coax/microstrip connection points, rather than relying on the repeatability of microstrip/microstrip interconnects. Still, connection errors remain an important consideration for the measurements. To examine this, a perturbation analysis is developed that allows for an approximation to be made of the effects of connection errors on the precision of the final de-embedded results. It is seen that connection errors affect the phase of the S-parameter measurements most, and the amount of resulting measurement uncertainty increases as the magnitude of the parameter being measured decreases.

6.4 Conclusions Based on the Results

Numerical and experimental results are presented for several microstrip structures (Chapter 5). Conclusions based on these results are described below.

The effect of higher order modes on the current distribution is demonstrated. As the frequency is increased above the cutoff frequency, the current becomes increasingly distorted due to higher order modes. On the other hand, as long as the cavity size is such that the frequency is below the cutoff frequency, the current is uniform and undistorted regardless of how thick the substrate is. This is in contrast to the case of open microstrip, where the first surface wave mode has a zero cutoff frequency and the onset of higher order modes depends strongly on the substrate thickness. The cavity resonance technique, mentioned in Chapter 1, does not allow for the current distribution to be studied.

A comparison of effective dielectric constant results shows good agreement between the CAD package results, the numerical results from this research, and measurements for large shielding dimensions ($b, c \gg h$). The effects of shielding on the effective dielectric constant are examined. Only one of the packages studied takes shielding into account for the effective dielectric constant calculation, and then only cover effects are considered. A comparison of the CAD package results with numerical results show that good agreement is obtained when the shielding dimensions are large with respect to the substrate thickness, while for small shielding dimensions, the difference between the CAD package results and numerical results becomes significant.

For the open-end discontinuity, good agreement with other full-wave solutions and with measurements is demonstrated. A comparison of open-end capacitance for different cavity sizes shows that, as the cutoff frequency is approached, the capacitance increases in each case. Choosing a small cavity with a high cut-off frequency extends the region where the capacitance is relatively constant. The open-end models used in the two CAD packages studied here do not include shielding and cannot show this effect.

A comparison of numerical and measured results for series gap discontinuities portrays good agreement for all three gap widths studied. The agreement with measurements is very good for the two larger gap widths, but for the smallest gap width it is seen that one of the CAD models give a slightly better prediction of the behavior of the magnitude of S_{21} than the numerical results. The effects of shielding on the behavior of series gaps is not explored extensively.

Good agreement is also demonstrated for the two and four resonator coupled line filters. For both filters, the numerical results of this research give a better prediction of the overall filter response than provided by the CAD models. This is especially true in the rejection bands of the filters. For the two resonator filter, a slight frequency shift is observed in the numerical results compared to the measurements. This is most likely due to the thin-strip approximation used for the current distribution, and is not a limitation of the method itself.

In contrast, for the four resonator filter, which has thinner strip widths, the present method gave an excellent prediction of the filter performance in every way, whereas discrepancies are observed in the CAD model predictions. Reducing the cover height is seen to narrow the pass band response and raise the amplitude of the filter's rejection band response. The numerical results of this research give an excellent prediction of this effect, and this is proven by measured data.

6.5 Recommendations

The data comparisons performed here have demonstrated the validity of the theoretical methods. However, there are a few areas where improvements can be made to the theory.

Further numerical investigation for series gap discontinuities indicates that as the gap width becomes small, a smaller subsection length is required for accurate computation of the scattering parameters. However, the improvement in the result is limited because a smaller subsection length increases the matrix size and degrades the condition number (Section 3.5). One way to extend this limit would be to use a variable subsection length in the computations. That is, use a small subsection length close to the discontinuity where the current is disturbed, and use a larger subsection length over the uniform sections of strip. In this way the size of the matrix would be maximized for a given problem.

The thin strip approximation as used here provides an accurate solution for the discontinuity structures studied. In one case, that of the two resonator filter, it appears that a more general current distribution may improve the solution. The thin strip approximation uses a unidirectional current. The method presented here may be generalized in a straight forward way to allow for two component current distributions. This will also allow for more complicated structures to be considered, yet it will be more computation intensive. It may be possible to improve the filter analysis by changing the formulation to allow the transverse variation of the longitudinal component of the current to be non-symmetrical without actually adding a transverse current component. To be able to discern which approximations are most appropriate for a given problem detailed comparisons should be made between results obtained with a more general current distribution and those obtained with the present method.

The experimental work has shown that good measured data on microstrip discontinuities can be obtained with the TSD technique. On the other hand it is shown that the measurement uncertainties due to connection errors, and other repeatability issues can be appreciable. In applying the technique for millimeter-wave measurements close attention is required to minimize the associated uncertainties: The following suggests some guidelines for doing so:

1. Connection repeatability errors can be reduced by first selecting the best available fixture and connection technique, and then by averaging measurements from repeated connections made for each fixture measurement.

2. Variations in ϵ_r can be minimized by fabricating the standards. and the discontinuity circuits from the same substrate, or by using substrates from

the same "lot", or manufacturing run.

3. Variations in substrate and line width geometry, though not a major error source, should be monitored carefully during all steps of fabrication. This can be done by performing careful measurements of the fabrication masks, the substrates to be used, and the surface metalization geometry after etching.

4. In the area of substrate mounting, care must be taken to use the exact same technique in bonding the substrates onto carriers.

5. Finally, if the physical delay line length is used in the fixture characterization procedure, it should be carefully measured and input to the program for each set of standards that are used.

Because of its susceptibility to connection repeatability errors, the TSD technique is not necessarily the best technique for high frequency measurements, and research into improved de-embedding methods should continue. In considering the trade-offs between alternative approaches that already exist, the sensitivity of each technique to the unavoidable measurement repeatability issues discussed here should be analyzed and compared. Ultimately, the best de-embedding method for a particular application depends on the required accuracy, the type of test fixture, and the nature of the device or circuit being tested.

APPENDICES

APPENDIX A

REVIEW OF METHOD OF MOMENTS

The general steps involved for in the computation of surface currents using the method of moments can be summarized as follows:

1. Formulate an integral equation for the electric or magnetic field in terms of the surface current density $\bar{J}_s$ on the conductors. It is generally possible to put this equation in the form

$$L_{op}\left(\bar{J}_s\right) = \bar{g}\begin{pmatrix} \bar{E} \\ \bar{H} \end{pmatrix} \tag{A.1}$$

   where L_{op} is an integral operator, and $\bar{g}$ is a vector function of either the electric field $\bar{E}$ or magnetic field $\bar{H}$ associated with $\bar{J}_s$.

2. Expand $\bar{J}_s$ into a series of basis functions $\bar{J}_p$ so that

$$\bar{J}_s = \sum_{p=1}^{N_s} I_p \bar{J}_p \tag{A.2}$$

   where the I_p's are complex coefficients and N_s is the number of sections the conductor is divided into.

3. Determine a suitable inner product and define a set of test (or weighting) functions $\bar{W}_q$. The result may be expressed as

$$\sum_{p=1}^{N_s} I_p \left\langle \bar{W}_q, L_{op}\left(\bar{J}_p\right)\right\rangle = \left\langle \bar{W}_q, \bar{g}\right\rangle \tag{A.3}$$

where the inner product is defined as

$$\left\langle \bar{a}, \bar{b} \right\rangle = \int_S \int \bar{a} \cdot \bar{b} ds \, .$$

In Galerkin's method, the weighting functions are taken to be test currents $\bar{J}_q$ which are identical in form to the basis functions $\bar{J}_p$.

4. Solve the inner product equation (A.3) and form a matrix equation of the form

$$[\mathbf{Z}]\,[\mathbf{I}] = [\mathbf{V}] \tag{A.4}$$

   where [**Z**] is termed the impedance matrix, and [**V**] is called the excitation vector.

5. Solve for the current coefficient vector by matrix inversion and multiplication according to

$$[\mathbf{I}] = [\mathbf{Z}]^{-1}\,[\mathbf{V}] \, . \tag{A.5}$$

APPENDIX B

DERIVATION OF INTEGRAL EQUATION FOR ELECTRIC FIELD

Starting with Maxwell's equations

$$\bar{\nabla} \times \bar{E} = -j\omega\mu\bar{H} \tag{B.1}$$

$$\bar{\nabla} \times \bar{H} = j\omega\epsilon\bar{E} + \bar{J} \tag{B.2}$$

$$\bar{\nabla} \cdot \bar{J} = -j\omega\rho \tag{B.3}$$

$$\bar{\nabla} \cdot \left(\epsilon\bar{E}\right) = \rho \tag{B.4}$$

$$\bar{\nabla} \cdot \left(\mu\bar{H}\right) = 0\,, \tag{B.5}$$

We define $\bar{A}$ such that

$$\bar{H} = \frac{1}{\mu}\bar{\nabla} \times \bar{A}\,. \tag{B.6}$$

Substituting (B.6) into (B.1) yields

$$\bar{\nabla} \times (\bar{E} + j\omega\bar{A}) = 0\,. \tag{B.7}$$

Since $\bar{\nabla} \times \bar{\nabla}\phi = 0$ for an arbitrary vector function ϕ, we let

$$\bar{E} + j\omega\bar{A} = -\bar{\nabla}\phi\,. \tag{B.8}$$

Making use of (B.6) and (B.8) in (B.2) yields

$$\bar{\nabla} \times \frac{1}{\mu}\bar{\nabla} \times \bar{A} = -j\omega\epsilon(j\omega\bar{A} + \bar{\nabla}\phi) + \bar{J} \tag{B.9}$$

or

$$-\nabla^2\bar{A} + \bar{\nabla}(\bar{\nabla}\cdot\bar{A}) = \omega^2\mu\epsilon\bar{A} - j\omega\mu\epsilon\bar{\nabla}\phi + \mu\bar{J}\,. \tag{B.10}$$

We use the Lorentz condition

$$\bar{\nabla}(\bar{\nabla}\cdot\bar{A}) = -j\omega\mu\epsilon\bar{\nabla}\phi \tag{B.11}$$

in (B.10) to obtain

$$\nabla^2\bar{A} + k^2\bar{A} = -\mu\bar{J} \tag{B.12}$$

where $k^2 = \omega^2\mu\epsilon$. From (B.9) and (B.11) the electric field may be expressed as

$$\begin{aligned} \bar{E} &= -j\omega\bar{A} + \frac{1}{j\omega\mu\epsilon}\bar{\nabla}(\bar{\nabla}\cdot\bar{A}) \\ &= -j\omega(1 + \frac{1}{k^2}\bar{\nabla}\bar{\nabla}\cdot)\bar{A}\,. \end{aligned} \tag{B.13}$$

We now define a dyadic Green's function $\bar{\bar{G}}$ to be a solution of

$$\nabla^2\bar{\bar{G}} + k^2\bar{\bar{G}} = -\bar{\bar{I}}\delta(\bar{r} - \bar{r}')\,. \tag{B.14}$$

To relate $\bar{\bar{G}}$ to $\bar{A}$, we will derive a vector-dyadic extension of Green's theorem. The vector Green's theorem is given by [23,19]

$$\begin{aligned} &\iiint_V \left\{\bar{Q}\cdot[\bar{\nabla}\times\bar{\nabla}\times\bar{P}] - \bar{P}\cdot[\bar{\nabla}\times\bar{\nabla}\times\bar{Q}]\right\} dv = \\ &\qquad \iint_{S_w+S_s} \hat{n}\cdot[\bar{P}\times(\bar{\nabla}\times\bar{Q}) - \bar{Q}\times(\bar{\nabla}\times\bar{P})]ds \end{aligned} \tag{B.15}$$

For the shielded microstrip cavity problem of Figure 2.4, the volume V is the interior of the cavity, and S_w and S_s are the surface of the cavity walls, and the surface of a small volume enclosing the source region $(\bar{J})$ respectively. The unit normal vector $\hat{n}$ is directed outward from V, and we will denote $\hat{n}' = -\hat{n}$ to be the inward directed normal vector. $\bar{P}$ and $\bar{Q}$ are arbitrary vector fields.

After applying a few vector identities, (B.15) may be re-written as follows:

$$\begin{aligned} &\iiint_V \left\{\bar{P}\cdot[\bar{\nabla}\times\bar{\nabla}\times\bar{Q}] - [\bar{\nabla}\times\bar{\nabla}\times\bar{P}]\cdot\bar{Q}\right\} dv = \\ &\qquad \iint_{S_w+S_s} \left[(\hat{n}'\times\bar{P})\cdot(\bar{\nabla}\times\bar{Q}) + \hat{n}'\times(\bar{\nabla}\times\bar{P})\cdot\bar{Q}\right] ds \end{aligned} \tag{B.16}$$

With the equation in this form, we can replace $\bar{Q}$ by a dyadic function $\bar{\bar{T}}$. The result is the vector-dyadic Green's theorem given by

$$\begin{aligned}&\int\!\!\int\!\!\int_V \left\{\bar{P}\cdot[\bar{\nabla}\times\bar{\nabla}\times\bar{\bar{T}}]-[\bar{\nabla}\times\bar{\nabla}\times\bar{P}]\cdot\bar{\bar{T}}\right\}dv = \\ &\qquad \int\!\!\int_{S_w+S_s}\left[(\hat{n}'\times\bar{P})\cdot(\bar{\nabla}\times\bar{\bar{T}})+\hat{n}'\times(\bar{\nabla}\times\bar{P})\cdot\bar{\bar{T}}\right]ds\,. \end{aligned} \tag{B.17}$$

We may now replace $\bar{P}$ with $\bar{A}$ and $\bar{\bar{T}}$ with $\bar{\bar{G}}$ and make use of vector-dyadic identities to yield

$$\begin{aligned}&\int\!\!\int\!\!\int_V (\nabla^2\bar{A}\cdot\bar{\bar{G}}-\bar{A}\cdot\nabla^2\bar{\bar{G}})dv = \\ &\qquad \int\!\!\int_{S_w+S_s}\left\{(\hat{n}'\times\bar{A})\cdot\bar{\nabla}\times\bar{\bar{G}}+(\hat{n}'\times\bar{\nabla}\times\bar{A})\cdot\bar{\bar{G}}\right. \\ &\qquad \left. +\hat{n}'\cdot\left[\bar{A}(\bar{\nabla}\cdot\bar{\bar{G}})\right]-\hat{n}'\cdot\left[(\bar{\nabla}\cdot\bar{A})\bar{\bar{G}}\right]\right\}ds\,. \end{aligned} \tag{B.18}$$

If we require that the components of $\bar{A}$ and $\bar{\bar{G}}$ satisfy the same boundary conditions on S_w and S_s, it can be shown that the entire surface integral on the right hand side of (B.18) vanishes. Substitution from (B.11) and (B.14) for $\nabla^2\bar{A}$ and $\nabla^2\bar{\bar{G}}$ we obtain

$$\begin{aligned}\int\!\!\int\!\!\int_V (\nabla^2\bar{A}\cdot\bar{\bar{G}}-\bar{A}\cdot\nabla^2\bar{\bar{G}})dv &= \int\!\!\int\!\!\int_V \left\{(-\mu\bar{J}-k^2\bar{A})\cdot\bar{\bar{G}}\right. \\ &\qquad \left.-\bar{A}\cdot\left[-\bar{\bar{I}}\delta(\bar{r}-\bar{r}')-k^2\cdot\bar{\bar{G}}\right]\right\}dv \\ &= -\mu\int\!\!\int\!\!\int_V \bar{J}\cdot\bar{\bar{G}}dv+\bar{A}(\bar{r}) \\ &= 0\,. \end{aligned} \tag{B.19}$$

Hence,

$$\bar{A}=\mu\int\!\!\int\!\!\int_V \bar{J}\cdot\bar{\bar{G}}dv\,. \tag{B.20}$$

Finally, substituting from (B.20) into (B.13) produces the following integral equation for the electric field

$$\begin{aligned}\bar{E} &= -j\omega\mu(1+\frac{1}{k^2}\bar{\nabla}\bar{\nabla}\cdot)\int\!\!\int\!\!\int_V \bar{J}\cdot\bar{\bar{G}}dv \\ &= -j\omega\mu\int\!\!\int\!\!\int_V \left[(1+\frac{1}{k^2}\bar{\nabla}\bar{\nabla}\cdot)(\bar{\bar{G}})^T\right]\cdot\bar{J}dv \end{aligned} \tag{B.21}$$

where $(\bar{\bar{G}})^T$ represents the transpose of $\bar{\bar{G}}$.

APPENDIX C

EIGENFUNCTION SOLUTION FOR GREEN'S FUNCTION

The boundary conditions on the cavity walls are applied here in order to derive the functional form of the Green's function. First, the general solution to the homogeneous differential equations for the components of the Green's function is presented. Then, the boundary conditions on the walls are used to arrive at an eigenfunction expansion for each of the Green's function components. The particular solution for the Green's function is found by integrating the inhomogeneous differential equation across the source region.

GENERAL SOLUTION TO HOMOGENEOUS D.E.'s FOR GREEN'S FUNCTION

Consider the homogeneous forms of equations (2.28) and (2.30)

$$\nabla^2 \bar{A}^i + k_i^2 \bar{A}^i = 0 \tag{C.1}$$

$$\nabla^2 \bar{\bar{G}}^i + k_i^2 \bar{\bar{G}}^i = 0 \tag{C.2}$$

where $i = 1, 2$ denotes that these equations hold in each region respectively.

The relationship between $\bar{A}^i$ and $\bar{\bar{G}}^i$ is given by (B.20) which reduces to

$$\frac{1}{\mu_0} \bar{A}^i = \hat{x} \cdot \bar{\bar{G}}^i , \tag{C.3}$$

since we consider an infinitesimal current source $\bar{J}$ for the Green's function derivation. The components of $\bar{A}^i$ and $\bar{\bar{G}}^i$ are related as follows:

$$A_x^i = \mu_0 G_{xx}^i \tag{C.4}$$

$$A_z^i = \mu_0 G_{xz}^i \,. \tag{C.5}$$

With $\bar{\bar{G}}^i$ given by (2.35), it can readily be shown that (C.2) implies

$$\nabla^2 G_{xx}^i + k_i^2 G_{xx}^i = 0 \tag{C.6}$$

$$\nabla^2 G_{xz}^i + k_i^2 G_{xz}^i = 0 \,. \tag{C.7}$$

We apply the method of separation of variables with

$$G_{xx}^i = X_x^i(x) Y_x^i(y) Z_x^i(z) \tag{C.8}$$

$$G_{xz}^i = X_z^i(x) Y_z^i(y) Z_z^i(z) \,. \tag{C.9}$$

The well known general solution of each of the above differential equations may be put in the form

$$\psi = A_1 \cos k_t^i t + A_2 \sin k_t^i t \tag{C.10}$$

where $t = x, y$, or $z; \psi = X_s^i, Y_s^i$, orZ_s^i (where $s = x$ or z) and k_t^i is complex in general. The eigenvalues are related by

$$k_i^2 = k_x^{i2} + k_y^{i2} + k_z^{i2} \,. \tag{C.11}$$

APPLICATION OF BOUNDARY CONDITIONS ON THE CAVITY WALLS

In applying the vector-dyadic Green's theorem of (B.18), it was imposed that $\bar{A}^i$ and $\bar{\bar{G}}^i$ satisfy the same boundary conditions. Hence, A_x^i and G_{xx}^i must satisfy the same boundary conditions on the waveguide walls and on the substrate/air interface and, must have the same functional form in terms of spatial variation. The same holds true for A^i_z and G^i_{xz}.

In order to establish what conditions $\bar{A}^i$ (and correspondingly $\bar{\bar{G}}^i$) must satisfy at the walls, we need first to establish more explicit relations between $\bar{A}^i$ and $\bar{E}^i$. From (B.13)

$$\bar{E}^i = -j\omega\bar{A}^i + \frac{1}{j\omega\epsilon\mu}\bar{\nabla}(\bar{\nabla}\cdot\bar{A}^i)\,. \tag{C.12}$$

The vector potential $\bar{A}^i$ may be expressed as (2.31)

$$\bar{A}^i = A^i_x\hat{x} + A^i_z\hat{z}\,. \tag{C.13}$$

The use of (C.13) in (C.12) yields the following expressions for the electric field components:

$$\begin{aligned} E^i_x &= -j\omega\left[A^i_x + \frac{1}{k_i^2}\frac{\partial}{\partial x}(\bar{\nabla}\cdot\bar{A}^i)\right] \\ &= -j\omega\left[A^i_x + \frac{1}{k_i^2}\frac{\partial}{\partial x}(\frac{\partial A^i_x}{\partial x} + \frac{\partial A^i_z}{\partial z})\right] \end{aligned} \tag{C.14}$$

$$E^i_y = \frac{-j\omega}{k_i^2}\frac{\partial}{\partial y}(\frac{\partial A^i_x}{\partial x} + \frac{\partial A^i_z}{\partial z}) \tag{C.15}$$

$$E^i_z = -j\omega\left[A^i_z + \frac{1}{k_i^2}\frac{\partial}{\partial z}(\frac{\partial A^i_x}{\partial x} + \frac{\partial A^i_z}{\partial z})\right]\,. \tag{C.16}$$

We now will consider the boundary conditions at each of the cavity walls.

Boundary Conditions at $x = 0, a$

Since the cavity walls are assumed to be perfectly conducting, the tangential components of the electric field must vanish at the walls. We have

$$E^i_y(x = 0, a) = 0 \tag{C.17}$$

$$E^i_z(x = 0, a) = 0\,. \tag{C.18}$$

In view of these two equations, (C.14) and (C.16) lead to

$$E^i_y(x=0,a) = \left[\frac{\partial}{\partial y}\left(\frac{\partial A^i_x}{\partial x} + \frac{\partial A^i_z}{\partial z}\right)\right]\Bigg|_{x=0,a} = 0\,. \tag{C.19}$$

$$E^i_z(x=0,a) = -j\omega\left[A^i_z + \frac{1}{k_i^2}\frac{\partial}{\partial z}\left(\frac{\partial A^i_x}{\partial x} + \frac{\partial A^i_z}{\partial z}\right)\right]\Bigg|_{x=0,a} = 0\,. \tag{C.20}$$

(C.19) is satisfied if the following condition is imposed:

$$\left(\frac{\partial A^i_x}{\partial x} + \frac{\partial A^i_z}{\partial z}\right)\Bigg|_{x=0,a} = 0 \tag{C.21}$$

in which case (C.20) leads to

$$A^i_z(x=0,a) = 0\,. \tag{C.22}$$

If (C.22) is placed into (C.21) it is seen that

$$\frac{\partial A^i_x}{\partial x}\Bigg|_{x=0,a} = 0\,. \tag{C.23}$$

The boundary conditions of (C.22) and (C.23) can be satisfied by choosing the following eigenfunction solutions for the x-dependence:

$$X^i_x = \cos k^i_x x \tag{C.24}$$

$$X^i_z = \sin k^i_x x\,. \tag{C.25}$$

for $i = 1, 2$, where

$$k^{(1)}_x = k^{(2)}_x = k_x = \tfrac{n\pi}{a} \quad \text{for } n = 0, 1, 2, \ldots\ \cdot \tag{C.26}$$

Boundary Conditions at $y = 0,\, b$

The tangential component of the electric field must vanish on the walls $y = 0$ and b; hence,

$$E^i_x(y=0,b) = 0 \tag{C.27}$$

$$E^i_z(y=0,b) = 0\,. \tag{C.28}$$

From (C.14) and (C.15)

$$E_x^i(y=0,b) \;=\; -j\omega\left[A_x^i + \frac{1}{k_i^2}\frac{\partial}{\partial x}\left(\frac{\partial A_x^i}{\partial x} + \frac{\partial A_z^i}{\partial z}\right)\right]\Big|_{y=0,b} = 0 \qquad \text{(C.29)}$$

$$E_z^i(y=0,b) \;=\; -j\omega\left[A_z^i + \frac{1}{k_i^2}\frac{\partial}{\partial z}\left(\frac{\partial A_x^i}{\partial x} + \frac{\partial A_z^i}{\partial z}\right)\right]\Big|_{y=0,b} = 0\,. \qquad \text{(C.30)}$$

It follows from the above two equations that the eigenfunction solution for the y-dependence is given by

$$Y_x^i \;=\; \sin k_y^i y \qquad \text{(C.31)}$$

$$Y_z^i \;=\; \sin k_y^i y \qquad \text{(C.32)}$$

(for $i = 1, 2$), where

$$k_y^{(1)} = k_y^{(2)} = k_y = \tfrac{m\pi}{b} \qquad for\ m = 1, 2, 3, \ldots\ . \qquad \text{(C.33)}$$

Note that it is easily shown that $m = 0$ leads to a trivial solution for the y-dependence of both components.

Boundary Conditions at $z = 0,\ c$

Similarly at the walls $z = 0$ and c we have

$$E_x^i(z=0,c) \;=\; 0 \qquad \text{(C.34)}$$

$$E_y^i(z=0,c) \;=\; 0\,. \qquad \text{(C.35)}$$

Making use of (C.14) and (C.15) yields

$$E_x^i(z=0,c) \;=\; -j\omega\left[A_x^i + \frac{1}{k_i^2}\frac{\partial}{\partial x}\left(\frac{\partial A_x^i}{\partial x} + \frac{\partial A_z^i}{\partial z}\right)\right]\Big|_{z=0,c} = 0 \qquad \text{(C.36)}$$

$$E_y^i(z=0,c) \;=\; \left[\frac{-j\omega}{k_i^2}\frac{\partial}{\partial y}\left(\frac{\partial A_x^i}{\partial x} + \frac{\partial A_z^i}{\partial z}\right)\right]\Big|_{z=0,c} = 0\,. \qquad \text{(C.37)}$$

It can readily be shown that the eigenfunction solution for the z-dependence can be written as

$$Z_x^{(1)} \;=\; \sin k_z^{(1)} z \qquad \text{(C.38)}$$

$$Z_z^{(1)} = \cos k_z^{(1)} z \tag{C.39}$$

$$Z_z^{(2)} = \sin k_z^{(2)}(z-c) \tag{C.40}$$

$$Z_z^{(2)} = \cos k_z^{(2)}(z-c) \tag{C.41}$$

where, from (C.11), (C.26), and (C.33), $k_z^{(1)}$ and $k_z^{(2)}$ are given explicitly by

$$k_z^{(1)} = \sqrt{k_1^2 - (\frac{n\pi}{a})^2 - (\frac{m\pi}{b})^2} \tag{C.42}$$

$$k_z^{(2)} = \sqrt{k_0^2 - (\frac{n\pi}{a})^2 - (\frac{m\pi}{b})^2}\,. \tag{C.43}$$

k_1 and k_0 are the wave numbers in region 1 and 2 respectively, and are given by

$$k_1 = \omega\sqrt{\mu\epsilon_1} \tag{C.44}$$

$$k_0 = \omega\sqrt{\mu\epsilon_0}\,. \tag{C.45}$$

REPRESENTATION OF GREEN'S FUNCTION BY EIGENFUNCTION SERIES

We now combine the results obtained above, so that the Green's function may be written in series expansion form. Substituting from (C.24), (C.31),(C.38), and (C.40) into (C.8) and taking the summation over all the possible modes, results in the following for G_{xx}^i:

$$G_{xx}^{(1)} = \sum_{m=1}^{\infty}\sum_{n=0}^{\infty} A_{mn}^{(1)} \cos k_x x \sin k_y y \sin k_z^{(1)} z \tag{C.46}$$

$$G_{xx}^{(2)} = \sum_{m=1}^{\infty}\sum_{n=0}^{\infty} A_{mn}^{(2)} \cos k_x x \sin k_y y \sin k_z^{(2)}(z-c)\,. \tag{C.47}$$

Similarly, if we substitute from (C.25),(C.32),(C.39), and (C.41) into (C.9) we obtain the following for G_{zx}^i

$$G_{zx}^{(1)} = \sum_{m=1}^{\infty}\sum_{n=0}^{\infty} B_{mn}^{(1)} \sin k_x x \sin k_y y \cos k_z^{(1)} z \tag{C.48}$$

$$G_{zx}^{(2)} = \sum_{m=1}^{\infty}\sum_{n=0}^{\infty} B_{mn}^{(2)} \sin k_x x \sin k_y y \cos k_z^{(2)}(z-c)\,. \tag{C.49}$$

The complex coefficients A_{mn}^i and B_{mn}^i $(i = 1,2)$ are determined in Appendix D by the application of boundary conditions at the substrate/air interface $(z = h)$.

APPENDIX D

BOUNDARY CONDITIONS AT SUBSTRATE/AIR INTERFACE

The complex coefficients A^i_{mn}, and B^i_{mn} (for $i = 1, 2$) for the Green's function components given by (2.36)-(2.39) are found here by applying boundary conditions at the substrate/air interface ($z = h$).

Figure D.1 shows a cross section of the cavity in the x–z plane. The application of boundary conditions at the interface is made difficult by the presence of the infinitesimal current source on the substrate surface. We will avoid this difficulty by first solving a similar problem with the current source raised a distance Δh above the substrate. After solving for the boundary conditions at $z = h$ and $z = h + \Delta h$, the equations required to determine the coefficients A^i_{mn}, and B^i_{mn} are obtained by letting Δh go to zero.

FORMULATION

From the consideration of the boundary conditions on the waveguide walls the components of the Green's function are given as

$$G^{(1)}_{xx} = \sum_{m=1}^{\infty}\sum_{n=0}^{\infty} A^{(1)}_{mn} \cos k_x x \, \sin k_y y \, \sin k^{(1)}_z z \tag{D.1}$$

$$G^{(1)}_{zx} = \sum_{m=1}^{\infty}\sum_{n=0}^{\infty} B^{(1)}_{mn} \sin k_x x \, \sin k_y y \, \cos k^{(1)}_z z \tag{D.2}$$

$$G^{(2)}_{xx} = \sum_{m=1}^{\infty}\sum_{n=0}^{\infty} A^{(2)}_{mn} \cos k_x x \, \sin k_y y \, \sin k^{(2)}_z (z - c) \tag{D.3}$$

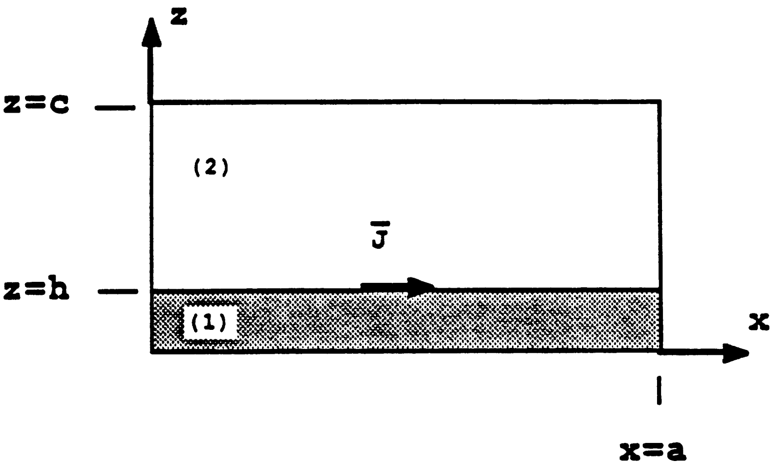

a) Actual position of current source

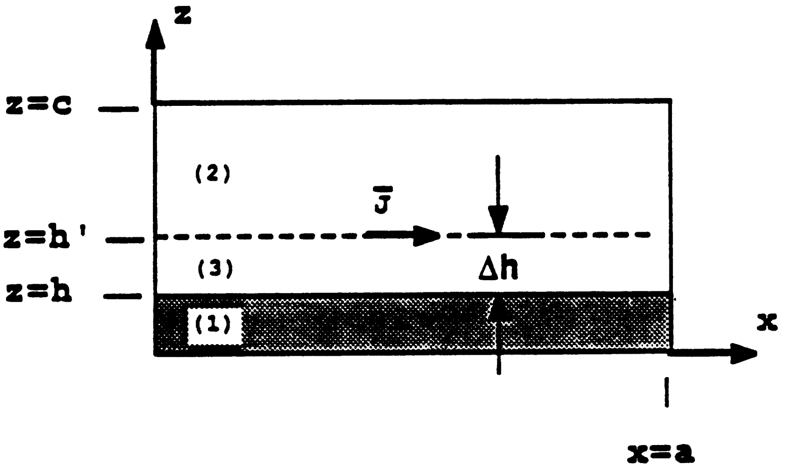

b) Current source raised above interface

Figure D.1: The current source is raised above the substrate/air interface to apply boundary conditions.

$$G^{(2)}_{xz} = \sum_{m=1}^{\infty}\sum_{n=0}^{\infty} B^{(2)}_{mn} \sin k_x x \, \sin k_y y \, \cos k_z^{(2)}(z-c) \, . \tag{D.4}$$

For region 3, the Green's function must satisfy the same differential equation (2.30) as in the other two regions. We will use the form of the general solution given by

$$G^{(3)}_{xx} = \sum_{m=1}^{\infty}\sum_{n=0}^{\infty} \cos k_x x \, \sin k_y y \left[A^{(3)}_{mn} e^{jk_z^{(3)} z} + B^{(3)}_{mn} e^{-jk_z^{(3)} z}\right] \tag{D.5}$$

$$G^{(3)}_{xz} = \sum_{m=1}^{\infty}\sum_{n=0}^{\infty} \sin k_x x \, \sin k_y y \left[C^{(3)}_{mn} e^{jk_z^{(3)} z} + D^{(3)}_{mn} e^{-jk_z^{(3)} z}\right] \tag{D.6}$$

where

$$k_x = n\pi/a \tag{D.7}$$

$$k_y = m\pi/b \tag{D.8}$$

$$k_z^{(1)} = \sqrt{k_1^2 - k_x^2 - k_y^2} \tag{D.9}$$

$$k_z^{(2)} = \sqrt{k_0^2 - k_x^2 - k_y^2} \tag{D.10}$$

$$k_z^{(3)} = k_z^{(2)} \tag{D.11}$$

$$k = \omega\sqrt{\mu_0 \epsilon_1} \tag{D.12}$$

$$k_0 = \omega\sqrt{\mu_0 \epsilon_0} \, . \tag{D.13}$$

Recall, the electric field solution in terms of the vector potential components (C.14)-(C.16)

$$E^i_x = -j\omega\left[A^i_x + \frac{1}{k_i^2}\frac{\partial}{\partial x}\left(\frac{\partial A^i_x}{\partial x} + \frac{\partial A^i_z}{\partial z}\right)\right] \tag{D.14}$$

$$E^i_y = \frac{-j\omega}{k_i^2}\frac{\partial}{\partial y}\left(\frac{\partial A^i_x}{\partial x} + \frac{\partial A^i_z}{\partial z}\right) \tag{D.15}$$

$$E^i_z = -j\omega\left[A^i_z + \frac{1}{k_i^2}\frac{\partial}{\partial z}\left(\frac{\partial A^i_x}{\partial x} + \frac{\partial A^i_z}{\partial z}\right)\right] \, . \tag{D.16}$$

These equations hold in each region respectively (i.e. for $i = 1, 2, 3$).

The solution for the magnetic field can be written using (2.26) and (2.31) as follows:

$$\bar{H}^i = \frac{1}{\mu_o}\bar{\nabla} \times \bar{A}^i = \frac{1}{\mu_o}[\bar{\nabla} \times (A^i_x \hat{x} + A^i_z \hat{z})] \, . \tag{D.17}$$

Separating this into x, y, and z components gives

$$H_x^i = \frac{1}{\mu_0}\frac{\partial A_z^i}{\partial y} \tag{D.18}$$

$$H_y^i = \frac{1}{\mu_0}\left(\frac{\partial A_x^i}{\partial z} - \frac{\partial A_z^i}{\partial x}\right) \tag{D.19}$$

$$H_z^i = -\frac{1}{\mu_0}\frac{\partial A_x^i}{\partial y}. \tag{D.20}$$

APPLICATION OF BOUNDARY CONDITIONS

Boundary Conditions at $z = h$

At $z = h$, the following boundary conditions apply:

$$E_x^{(1)} = E_x^{(3)} \tag{D.21}$$

$$E_y^{(1)} = E_y^{(3)} \tag{D.22}$$

$$H_x^{(1)} = H_x^{(3)} \tag{D.23}$$

$$H_y^{(1)} = H_y^{(3)} \tag{D.24}$$

$$\mu_0 H_z^{(1)} = \mu_0 H_z^{(3)} \Longrightarrow H_z^{(1)} = H_z^{(3)} \tag{D.25}$$

$$\epsilon_1 E_z^{(1)} = \epsilon_0 E_z^{(3)}. \tag{D.26}$$

We will make use of (D.22)-(D.25) to formulate four of the eight equations needed to solve for the complex coefficients in (D.1)-(D.6). We start with (D.25), then substitute from (D.20), and recall the correspondences of (C.3) to obtain

$$\frac{\partial G_{xx}^{(1)}}{\partial y}\Big|_{z=h} = \frac{\partial G_{xx}^{(3)}}{\partial y}\Big|_{z=h}. \tag{D.27}$$

When (D.1)and (D.5) are used the above, and orthogonality is applied, the following is obtained

$$A_{mn}^{(1)} \sin k_z^{(1)} h = A_{mn}^{(3)} e^{jk_z^{(2)} h} + B_{mn}^{(3)} e^{-jk_z^{(2)} h} \tag{D.28}$$

where $k_z^{(2)}$ has been substituted for $k_z^{(3)}$ in accordance with (D.11).

Next, from (D.23),(D.18), and (C.3)

$$\frac{\partial G_{xz}^{(1)}}{\partial y} = \frac{\partial G_{xz}^{(3)}}{\partial y} \, . \tag{D.29}$$

From (D.2),(D.6) and the above

$$B_{mn}^{(1)} \cos k_z^{(1)} h = C_{mn}^{(3)} e^{jk_z^{(2)} h} + D_{mn}^{(3)} e^{-jk_z^{(2)} h} \, . \tag{D.30}$$

The combination of (D.24), (D.19) and (C.3) yields

$$\left(\frac{\partial G_{xx}^{(1)}}{\partial z} - \frac{\partial G_{xz}^{(1)}}{\partial x} \right) |_{z=h} = \left(\frac{\partial G_{xx}^{(3)}}{\partial z} - \frac{\partial G_{xz}^{(3)}}{\partial x} \right) |_{z=h} \, . \tag{D.31}$$

Making substitutions from (D.1),(D.2),(D.5) and (D.6) into this expression and using (D.30) leads to

$$A_{mn}^{(1)} k_z^{(1)} \cos k_z^{(1)} h = j k_z^{(2)} \left[A_{mn}^{(3)} e^{jk_z^{(2)} h} - B_{mn}^{(3)} e^{-jk_z^{(2)} h} \right] \, . \tag{D.32}$$

Now consider (D.22). From (D.15) and (C.3)

$$\frac{1}{\epsilon_r^*} \frac{\partial}{\partial y} \left(\frac{\partial G_{xx}^{(1)}}{\partial x} + \frac{\partial G_{xz}^{(1)}}{\partial z} \right) |_{z=h} = \frac{\partial}{\partial y} \left(\frac{\partial G_{xx}^{(3)}}{\partial x} + \frac{\partial G_{xz}^{(3)}}{\partial z} \right) |_{z=h} \, . \tag{D.33}$$

After appropriate substitutions and some algebra, the following equation is obtained

$$\begin{aligned} A_{mn}^{(1)} (1 - \epsilon_r^*) k_x \sin k_z^{(1)} h + B_{mn}^{(1)} k_z^{(1)} \sin k_z^{(1)} h = \\ -j k_z^{(2)} \epsilon_r^* \left[C_{mn}^{(3)} e^{jk_z^{(2)} h} - D_{mn}^{(3)} e^{-jk_z^{(2)} h} \right] \, . \end{aligned} \tag{D.34}$$

Equations (D.28), (D.30), (D.32), and (D.34) represent 4 of the 8 equations we need.

Boundary Conditions at $z = h'$

We now proceed to the boundary conditions at $z = h'$ (see Figure D.1) we have

$$
\begin{aligned}
E_x^{(2)} &= E_x^{(3)} && \text{(D.35)} \\
E_y^{(2)} &= E_y^{(3)} && \text{(D.36)} \\
E_z^{(2)} - E_z^{(3)} &= \sigma_s && \text{(D.37)} \\
H_z^{(2)} &= H_z^{(3)} && \text{(D.38)} \\
\hat{z} \times (\bar{H}^{(2)} - \bar{H}^{(3)}) &= J_s \hat{x} \Longrightarrow && \\
H_x^{(2)} &= H_x^{(3)} && \text{(D.39)} \\
-(H_y^{(2)} - H_y^{(3)}) &= J_s \, . && \text{(D.40)}
\end{aligned}
$$

Of the above, we will use (D.35), (D.38), and (D.39) to derive three more equations for the complex coefficients.

We start with (D.39) and use (D.18) and (C.3) to obtain

$$\frac{\partial G_{xz}^{(2)}}{\partial y} |_{z=h'} = \frac{\partial G_{xz}^{(3)}}{\partial y} |_{z=h'} \tag{D.41}$$

which yields after substituting from (D.4) and (D.6)

$$B_{mn}^{(2)} \cos k_z^{(2)}(h' - c) = C_{mn}^{(3)} e^{jk_z^{(2)}h'} + D_{mn}^{(3)} e^{-jk_z^{(2)}h'} \, . \tag{D.42}$$

Next, consider the boundary condition of (D.38). This leads to

$$\frac{\partial G_{xx}^{(2)}}{\partial y} |_{z=h'} = \frac{\partial G_{xx}^{(3)}}{\partial y} |_{z=h'} \tag{D.43}$$

Substitution from (D.3) and (D.5) yields

$$A_{mn}^{(2)} \sin k_z^{(2)}(h' - c) = A_{mn}^{(3)} e^{jk_z^{(2)}h'} + B_{mn}^{(3)} e^{-jk_z^{(2)}h'} \, . \tag{D.44}$$

This equation, when combined with (D.3) and (D.5) , shows that

$$G_{xx}^{(2)}(z = h') = G_{xx}^{(3)}(z = h') \, . \tag{D.45}$$

With the above equality, we can substitute from (D.14) into the boundary condition of (D.35), and make use of (C.3) to produce

$$\frac{\partial}{\partial x}\left(\frac{\partial G_{xx}^{(2)}}{\partial x} + \frac{\partial G_{xz}^{(2)}}{\partial z}\right) = \frac{\partial}{\partial x}\left(\frac{\partial G_{xx}^{(3)}}{\partial x} + \frac{\partial G_{xz}^{(3)}}{\partial z}\right) . \tag{D.46}$$

Suffering through the details again we obtain

$$B^{(2)}_{mn}\sin k_z^{(2)}(h'-c) = -j\left[C^{(3)}_{mn}e^{jk_z^{(2)}h'} - D^{(3)}_{mn}e^{-jk_z^{(2)}h'}\right] . \tag{D.47}$$

At this point we have 7 independent equations —(D.28), (D.30),(D.32), (D.34),-(D.42),(D.44), and (D.47)— and we have 8 unknown complex coefficients. The other required equation is obtained by integrating the differential equation of (2.30) across the boundary at $z = h'$.

Integration Across the Source Region at $z = h'$

From (2.30) we have

$$\nabla^2\bar{\bar{G}}^i + k_i^2\bar{\bar{G}}^i = -\bar{\bar{I}}\delta(\bar{r}-\bar{r}') . \tag{D.48}$$

Substitution from (2.35) for $\bar{\bar{G}}^i$ yields

$$(\nabla^2 + k_i^2)\left(G^i_{xx}\hat{x}\hat{x} + G^i_{xz}\hat{x}\hat{z}\right) = -\delta(\bar{r}-\bar{r}')\hat{x}\hat{x} . \tag{D.49}$$

Hence,

$$(\nabla^2 + k_i^2)G^i_{xx} = -\delta(\bar{r}-\bar{r}') = -\delta(x-x')\delta(y-y')\delta(z-z') . \tag{D.50}$$

We now integrate both sides of this equation over a line passing through the source point $\bar{r}'$, and then take the limit as the length of this line vanishes

$$\lim_{\alpha\to 0}\int_{h'-\alpha}^{h'+\alpha}(\nabla^2 + k_i^2)G^i_{xx}dz = -\delta(x-x')\delta(y-y') . \tag{D.51}$$

This may be written as

$$\lim_{\alpha\to 0}\left[\left(\frac{\partial^2}{\partial x^2}+\frac{\partial^2}{\partial y^2}+k_i^2\right)\int_{h'-\alpha}^{h'+\alpha}G^i_{xx}dz + \int_{h'-\alpha}^{h'+\alpha}\frac{\partial^2}{\partial z^2}G^i_{xx}dz\right] = -\delta(x-x')\delta(y-y') \tag{D.52}$$

If we make use of (D.3) and (D.5), we can show that the first integral vanishes as follows:

$$\begin{aligned}
\lim_{\alpha\to 0}\int_{h'-\alpha}^{h'+\alpha} G^{i}_{xx}dz &= \lim_{\alpha\to 0}\left[\int_{h'-\alpha}^{h'} G^{(3)}_{xx}dz + \int_{h'}^{h'+\alpha} G^{(2)}_{xx}dz\right] \\
&= \lim_{\alpha\to 0}\left[\sum_{m=1}^{\infty}\sum_{n=0}^{\infty}\left(\frac{1}{jk_z^{(2)}}\right)\cos k_x x\,\sin k_y y\left(A^{(3)}_{mn}e^{jk_z^{(2)}z} - B^{(3)}_{mn}e^{-jk_z^{(2)}z}\right)\right]\Bigg|_{z=h'-\alpha}^{z=h'} \\
&\quad + \lim_{\alpha\to 0}\left[\sum_{m=1}^{\infty}\sum_{n=0}^{\infty}\left(\frac{-1}{k_z^{(2)}}\right)A^{(2)}_{mn}\cos k_x x\,\sin k_y y\,\cos k_z^{(2)}(z-c)\right]\Bigg|_{z=h'}^{z=h'+\alpha} \\
&= 0
\end{aligned} \tag{D.53}$$

(since each of the limits on the right hand side of the second equality vanishes individually.)

Therefore, (D.52) can be reduced to

$$\lim_{\alpha\to 0}\int_{h'-\alpha}^{h'+\alpha}\frac{\partial^2}{\partial z^2}G^{i}_{xx}dz = -\delta(x-x')\delta(y-y') \tag{D.54}$$

From which we obtain

$$\lim_{\alpha\to 0}\frac{\partial G^{i}_{xx}}{\partial z}\Bigg|_{h'-\alpha}^{h'+\alpha} = -\delta(x-x')\delta(y-y'), \tag{D.55}$$

or

$$\left(\frac{\partial G^{(2)}_{xx}}{\partial z} - \frac{\partial G^{(3)}_{xx}}{\partial z}\right)\Bigg|_{z=h'} = -\delta(x-x')\delta(y-y'). \tag{D.56}$$

Substitution in the above from (D.3) and (D.5), and simplifying yields

$$\begin{aligned}
\frac{ab}{\varphi_n}\left\{A^{(2)}_{mn}k_z^{(2)}\cos k_z^{(2)}(h'-c) \right. &- \left. jk_z^{(2)}(A^{(3)}_{mn}e^{jk_z^{(2)}z} - B^{(3)}_{mn}e^{-jk_z^{(2)}z})\right\} \\
&= -\cos k_x x'\,\sin k_y y'
\end{aligned} \tag{D.57}$$

where

$$\varphi_n = \begin{cases} 2 & \text{for } n = 0 \\ 4 & \text{for } n \neq 0 \end{cases} \tag{D.58}$$

The above represents the final equation needed to evaluate the complex coefficients.

EVALUATION OF THE COMPLEX COEFFICIENTS OF THE GREEN'S FUNCTION

To evaluate the complex coefficients, we will make use of the equations derived above involving A^i_{mn}, B^i_{mn} $(i = 1, 3)$, and $C^{(3)}_{mn}$ and $D^{(3)}_{mn}$. Since we are only interested in $A^{(1)}_{mn}$, $B^{(1)}_{mn}$, $A^{(2)}_{mn}$, and $B^{(2)}_{mn}$ these will be evaluated by eliminating the other complex coefficients.

Now, recall that $h' = h + \Delta h$. If $\Delta h \to 0$ then $h' \to h$ in equations (D.42), (D.44), (D.47), and (D.57).

Starting with (D.42) with $h' \to h$ we can substitute from (D.30) to obtain

$$B^{(1)}_{mn} \cos k^{(1)}_z h = B^{(2)}_{mn} \cos k^{(2)}_z (h - c) \, . \tag{D.59}$$

Similarly, (D.28) and (D.44) yield

$$A^{(2)}_{mn} \sin k^{(2)}_z (h - c) = A^{(1)}_{mn} \sin k^{(1)}_z h \, . \tag{D.60}$$

From (D.34) and (D.47) we get

$$B^{(2)}_{mn} \sin k^{(2)}_z (h - c) = \frac{1}{k^{(2)}_z} \left[A^{(1)}_{mn} \left(\frac{1}{\epsilon^*_r} - 1 \right) k_x \sin k^{(1)}_z h + \frac{B^{(1)}_{mn} k^{(1)}_z}{\epsilon^*_r} \sin k^{(1)}_z h \right] . \tag{D.61}$$

From (D.32) and (D.57)

$$\frac{ab}{\varphi_n} \left[A^{(2)}_{mn} k^{(2)}_z \cos k^{(2)}_z (h' - c) - A^{(1)}_{mn} k^{(1)}_z \cos k^{(1)}_z h \right] = - \cos k_x x' \sin k_y y' \, . \tag{D.62}$$

The combination of (D.60) and (D.62) yields

$$\frac{ab}{\varphi_n} \left[\frac{A^{(1)}_{mn} \sin k^{(1)}_z h}{\sin k^{(2)}_z (h - c)} k^{(2)}_z \cos k^{(2)}_z (h - c) - A^{(1)}_{mn} k^{(1)}_z \cos k^{(1)}_z h \right] = - \cos k_x x' \sin k_y y' \, . \tag{D.63}$$

Solving for $A^{(1)}_{mn}$

$$A^{(1)}_{mn} = \frac{-\varphi_n \cos k_x x' \sin k_y y' \tan k^{(2)}_z (h - c)}{ab \, d_{1mn} \cos k^{(1)}_z h} \tag{D.64}$$

where

$$d_{1mn} = k_z^{(2)} \tan k_z^{(1)} h - k_z^{(1)} \tan k_z^{(2)} (h-c) \tag{D.65}$$

and φ_n is given by (D.58). $A_{mn}^{(2)}$ is found by substitution from (D.64) into (D.60)

$$A_{mn}^{(2)} = \frac{-\varphi_n \cos k_x x' \sin k_y y' \tan k_z^{(1)} h}{ab\, d_{1mn} \cos k_z^{(2)} (h-c)} \,. \tag{D.66}$$

Next, we combine (D.59) and (D.61) to get

$$\begin{aligned} \frac{B_{mn}^{(1)} \cos k_z^{(1)} h \sin k_z^{(2)} (h-c)}{\cos k_z^{(2)} (h-c)} &= \frac{1}{k_z^{(2)}} \left[A_{mn}^{(1)} \left(\frac{1}{\epsilon_r^*} - 1 \right) k_x \sin k_z^{(1)} h \right. \\ &\left. + \frac{B_{mn}^{(1)} k_z^{(1)}}{\epsilon_r^*} \sin k_z^{(1)} h \right] \,. \end{aligned} \tag{D.67}$$

By substituting for $A_{mn}^{(1)}$ from (D.64), the above can be rearranged to find $B_{mn}^{(1)}$ as

$$B_{mn}^{(1)} = \frac{-\varphi_n (1-\epsilon_r^*) k_x \cos k_x x' \sin k_y y' \tan k_z^{(1)} h \tan k_z^{(2)} (h-c)}{ab\, d_{1mn} d_{2mn} \cos k_z^{(1)} h} \tag{D.68}$$

where

$$d_{2mn} = k_z^{(2)} \epsilon_r^* \tan k_z^{(2)} (h-c) - k_z^{(1)} \tan k_z^{(1)} h \,. \tag{D.69}$$

Finally, if we place (D.68) in (D.59), $B_{mn}^{(2)}$ can be expressed as:

$$B_{mn}^{(2)} = \frac{-\varphi_n (1-\epsilon_r^*) k_x \cos k_x x' \sin k_y y' \tan k_z^{(1)} h \tan k_z^{(2)} (h-c)}{ab\, d_{1mn} d_{2mn} \cos k_z^{(2)} (h-c)} \,. \tag{D.70}$$

We now have derived explicit relations for the desired complex coefficients $A_{mn}^{(1)}$, $A_{mn}^{(2)}$, $B_{mn}^{(1)}$, $B_{mn}^{(2)}$. It can be shown that the same relations can be obtained by moving the current source of Figure D.1 into the dielectric region and then bringing it back to the substrate surface.

APPENDIX E

EVALUATION OF MODIFIED DYADIC GREENS FUNCTION

For the purposes of evaluating the electric field (2.66), only the xx component of the modified dyadic Green's function $\bar{\bar{\Gamma}}^i$ is needed. In this appendix, expressions for $\Gamma^{(1)}_{xx}$, and $\Gamma^{(2)}_{xx}$ are derived. Then, each of these are evaluated at the air/dielectric interface ($z = h$) and shown to be equal.

The modified dyadic Greens function was defined in (2.58) as

$$\bar{\bar{\Gamma}}^i = -j\omega\mu_0 \left[\left(1 + \frac{1}{k_i^2} \bar{\nabla}\bar{\nabla}\cdot \right) (\bar{\bar{G}}^i)^T \right] . \tag{E.1}$$

From (2.35)

$$\bar{\bar{G}}^i = G^i_{xx}\hat{x}\hat{x} + G^i_{xz}\hat{x}\hat{z} .$$

The dyadic transpose is

$$(\bar{\bar{G}}^i)^T = G^i_{xx}\hat{x}\hat{x} + G^i_{xz}\hat{z}\hat{x} \tag{E.2}$$

Using (E.2) into (E.1) yields

$$\begin{aligned} \bar{\bar{\Gamma}}^i = & -j\omega\mu_0 \left\{ \left[G^i_{xx} + \frac{1}{k_i^2}\frac{\partial}{\partial x}\left(\frac{\partial G^i_{xx}}{\partial x} + \frac{\partial G^i_{xz}}{\partial z} \right) \right] \hat{x}\hat{x} \right. \\ & + \left[\frac{1}{k_i^2}\frac{\partial}{\partial y}\left(\frac{\partial G^i_{xx}}{\partial x} + \frac{\partial G^i_{xz}}{\partial z} \right) \right] \hat{y}\hat{x} \\ & \left. + \left[G^i_{xz} + \frac{1}{k_i^2}\frac{\partial}{\partial z}\left(\frac{\partial G^i_{xx}}{\partial x} + \frac{\partial G^i_{xz}}{\partial z} \right) \right] \hat{z}\hat{x} \right\} . \end{aligned} \tag{E.3}$$

Hence, the xx component of the modified Green's function is given by

$$\Gamma^i_{xx} = -j\omega\mu_0 \left[G^i_{xx} + \frac{1}{k_i^2}\frac{\partial}{\partial x}\left(\frac{\partial G^i_{xx}}{\partial x} + \frac{\partial G^i_{xz}}{\partial z} \right) \right] . \tag{E.4}$$

Substitution from (2.36) and (2.37) into (E.4) results in

$$\Gamma_{xx}^{(1)} = -j\omega\mu_0 \sum_{m=1}^{\infty}\sum_{n=0}^{\infty} \cos k_x x \, \sin k_y y \, \sin k_z^{(1)} z \left[A_{mn}^{(1)}\left(1-\frac{k_x^2}{k_1^2}\right) - \frac{k_x k_z^{(1)}}{k_1^2} B_{mn}^{(1)}\right]$$

If we use the expressions for $A_{mn}^{(1)}$ and $B_{mn}^{(1)}$ from (2.46) and (2.48) we may write

$$\begin{aligned}
\Gamma_{xx}^{(1)} &= j\omega\mu_0 \sum_{m=1}^{\infty}\sum_{n=0}^{\infty}\Bigg\{\frac{\varphi_n}{abd_{1mn}d_{2mn}\cos k_z^{(1)}h} \\
&\cdot\left[\cos k_x x \, \sin k_y y \, \sin k_z^{(1)} z \, \cos k_x x' \, \sin k_y y' \, \tan k_z^{(2)}(h-c)\right] \\
&\cdot\Bigg[k_z^{(2)}\epsilon_r^*\left(1-\frac{k_x^2}{k_1^2}\right)\tan k_z^{(2)}(h-c) \\
&-k_z^{(1)}\left(1-\frac{\epsilon_r^* k_x^2}{k_1^2}\right)\tan k_z^{(1)}h\Bigg]\Bigg\}
\end{aligned} \tag{E.5}$$

where the expression for d_{2mn} from (D.69) is used to combine terms. Evaluation of (E.5) at $z = h$ gives

$$\begin{aligned}
\Gamma_{xx}^{(1)}(z=h) &= j\omega\mu_0 \sum_{m=1}^{\infty}\sum_{n=0}^{\infty}\Bigg\{\left(\frac{\varphi_n}{abd_{1mn}d_{2mn}}\right) \\
&\cdot\left[\cos k_x x \, \sin k_y y \, \cos k_x x' \, \sin k_y y' \, \tan k_z^{(1)}h \, \tan k_z^{(2)}(h-c)\right] \\
&\cdot\Bigg[k_z^{(2)}\epsilon_r^*\left(1-\frac{k_x^2}{k_1^2}\right)\tan k_z^{(2)}(h-c) \\
&-k_z^{(1)}\left(1-\frac{\epsilon_r^* k_x^2}{k_1^2}\right)\tan k_z^{(1)}h\Bigg]\Bigg\}\,.
\end{aligned} \tag{E.6}$$

Proceeding in a similar fashion for region 2, it can be shown that

$$\begin{aligned}
\Gamma_{xx}^{(2)} &= -j\omega\mu_0 \sum_{m=1}^{\infty}\sum_{n=0}^{\infty} \cos k_x x \, \sin k_y y \, \sin k_z^{(2)}(z-c) \\
&\cdot\Bigg\{\left[\frac{-\varphi_n \cos k_x x' \, \sin k_y y' \, \tan k_z^{(1)}h}{abd_{1mn}\cos k_z^{(2)}(h-c)}\right]\left(1-\frac{k_x^2}{k_0^2}\right) - \frac{k_x k_z^{(2)}}{k_0^2} \\
&\cdot\left[\frac{-\varphi_n(1-\epsilon_r^*)k_x \cos k_x x' \, \sin k_y y' \, \tan k_z^{(1)}h \, \tan k_z^{(2)}(h-c)}{abd_{1mn}d_{2mn}\cos k_z^{(2)}(h-c)}\right]\Bigg\}\,.
\end{aligned}$$

Evaluation of this expression at z=h and rearranging the result produces

$$\Gamma_{xx}^{(2)}(z=h) = j\omega\mu_0 \sum_{m=1}^{\infty}\sum_{n=0}^{\infty}\Bigg\{\left(\frac{\varphi_n}{abd_{1mn}d_{2mn}}\right)$$

$$\cdot\left[\cos k_x x \, \sin k_y y \, \cos k_x x' \, \sin k_y y' \, \tan k_z^{(1)} h \, \tan k_z^{(2)}(h-c)\right]$$

$$\cdot \left[k_z^{(2)} \epsilon_r^* \left(1 - \frac{k_x^2}{k_1^2}\right) \tan k_z^{(2)}(h-c) \right.$$

$$\left. \left. - k_z^{(1)} \left(1 - \frac{\epsilon_r^* k_x^2}{k_1^2}\right) \tan k_z^{(1)} h \right] \right\} . \tag{E.7}$$

Upon comparison of (E.7) with (E.6) we can readily see that

$$\Gamma_{xx}^{(1)}(z=h) = \Gamma_{xx}^{(2)}(z=h) = \Gamma_{xx}(z=h) . \tag{E.8}$$

APPENDIX F

INTEGRATION OVER SUBSECTIONAL SURFACES

Consider the surface integral given by (2.71)

$$\mathcal{I}_{qmn} = \int\int_{S_q} \cos k_x x' \, \sin k_y y' \, \psi(y') \alpha_q(x') \, dx' dy' \, . \tag{F.1}$$

where from (2.7)

$$\psi(y') = \begin{cases} \dfrac{\frac{2}{\pi W}}{\sqrt{1 - \left[\frac{2(y'-Y_0)}{W}\right]^2}} & Y_0 - \frac{W}{2} \leq y' \leq Y_0 + \frac{W}{2} \\ 0 & \text{else} \, . \end{cases} \tag{F.2}$$

From (2.8), for $q \neq 1$

$$\alpha_q(x') = \begin{cases} \frac{\sin[K(x_{q+1} - x')]}{\sin(K l_x)} & x_q \leq x' \leq x_{q+1} \\ \frac{\sin[K(x' - x_{q-1})]}{\sin(K l_x)} & x_{q-1} \leq x' \leq x_q \\ 0 & \text{else} \, , \end{cases} \tag{F.3}$$

and from (2.9), for $q = 1$

$$\alpha_1(x') = \begin{cases} \frac{\sin[K(l_x - x')]}{\sin(K l_x)} & 0 \leq x' \leq l_x \\ 0 & \text{else} \, . \end{cases} \tag{F.4}$$

In the above,

$$l_x = x_{q+1} - x_q = x_q - x_{q-1}$$

and, for our purposes here[1] , we let

$$x_q = (q-1) l_x \, .$$

---

[1] Note that for strip geometries other than an open-end and a thru line, the position function x_q will be more complicated in general (see Section 3.1.4).

Figure F.1 illustrates the strip geometry used to determine the integration limits in equation (F.1). The boundaries of the q^{th} subsection depend on q as follows:

$$S_q = \begin{cases} 0 \leq x' \leq l_x & \\ Y_0 - \frac{W}{2} \leq y' \leq Y_0 + \frac{W}{2} & \text{for } q = 1 \\ & \\ x_{q-1} \leq x' \leq x_{q+1} & \\ Y_0 - \frac{W}{2} \leq y' \leq Y_0 + \frac{W}{2} & \text{else}\,. \end{cases} \tag{F.5}$$

With these subsection boundaries, $\mathcal{I}_{qmn}$ may be expressed as

$$\mathcal{I}_{qmn} = \mathcal{I}^{y'}\mathcal{I}_q^{x'} \tag{F.6}$$

where

$$\mathcal{I}^{y'} = \int_{Y_0-W/2}^{Y_0+W/2} \psi(y') \sin k_y y' \, dy' \tag{F.7}$$

$$\mathcal{I}_q^{x'} = \begin{cases} \int_0^{l_x} \cos k_x x' \, \alpha_q(x') dx' & \text{for } q = 1 \\ \int_{x_{q-1}}^{x_{q+1}} \cos k_x x' \alpha_q(x') dx' & \text{for } q \neq 1\,. \end{cases} \tag{F.8}$$

INTEGRATION OVER y'

From (F.7) and (F.2) we have

$$\mathcal{I}^{y'} = \frac{2}{\pi W} \int_{Y_0-W/2}^{Y_0+W/2} \frac{\sin k_y y'}{\sqrt{1 - \left[\frac{2(y'-Y_0)}{W}\right]^2}} dy'\,. \tag{F.9}$$

Now, let

$$\begin{aligned} \sin\phi &= \tfrac{2(y'-Y_0)}{W} & \Longrightarrow \quad \cos\phi \, d\phi &= \tfrac{2}{W} dy' \\ y' &= \tfrac{W}{2}\sin\phi + Y_0 & \Longrightarrow \quad dy' &= \tfrac{W}{2}\cos\phi \, d\phi \end{aligned} \tag{F.10}$$

with these substitutions

$$\mathcal{I}^{y'} = \frac{1}{\pi} \int_{-\frac{\pi}{2}}^{\frac{\pi}{2}} \sin\left[k_y(\frac{W}{2}\sin\phi + Y_0)\right] d\phi\,. \tag{F.11}$$

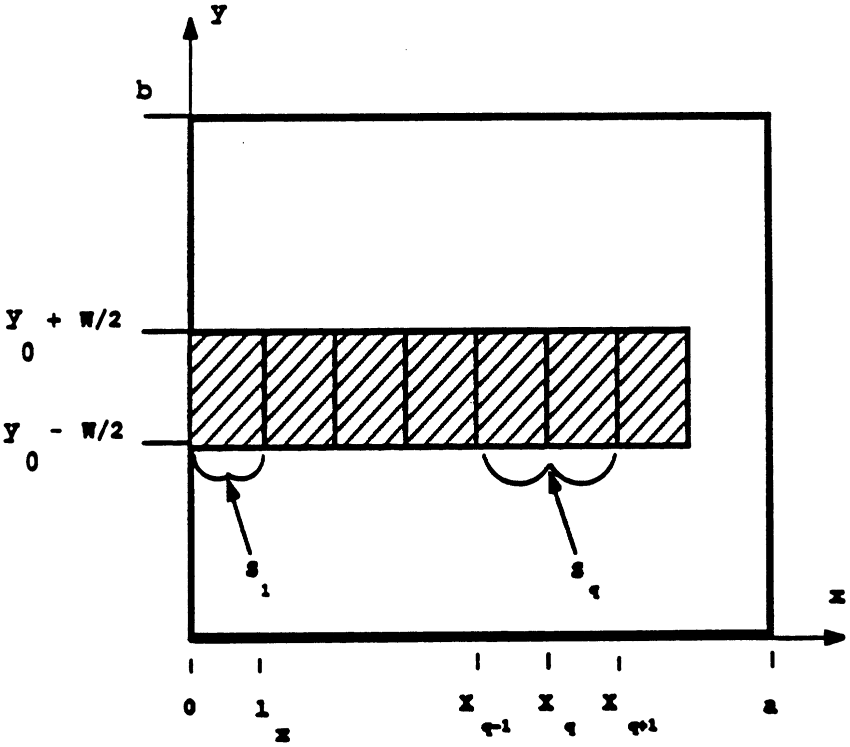

Figure F.1: Strip geometry used in evaluation of surface integrals

The above may be rewritten as

$$\begin{aligned}
\mathcal{I}^{y'} &= \frac{1}{\pi}\left[\int_{-\frac{\pi}{2}}^{\frac{\pi}{2}} \sin(k_y \frac{W}{2} \sin\phi) \cos k_y Y_0 \, d\phi \right. \\
&\qquad \left. + \int_{-\frac{\pi}{2}}^{\frac{\pi}{2}} \cos(k_y \frac{W}{2} \sin\phi) \sin k_y Y_0 \, d\phi \right] \\
&= \int^{(1)y'} + \int^{(2)y'} . \qquad \text{(F.12)}
\end{aligned}$$

Consider the first term of (F.12):

$$\begin{aligned}
\int^{(1)y'} &= \frac{1}{\pi} \cos k_y Y_0 \int_{-\frac{\pi}{2}}^{\frac{\pi}{2}} \sin(k_y \frac{W}{2} \sin\phi) \, d\phi \\
&= \frac{1}{\pi} \cos k_y Y_0 \left[\int_{-\frac{\pi}{2}}^{0} \sin(k_y \frac{W}{2} \sin\phi) \, d\phi + \int_{0}^{\frac{\pi}{2}} \sin(k_y \frac{W}{2} \sin\phi) \, d\phi \right] .
\end{aligned}$$

If, in the second integral above, we let

$$\phi' = -\phi \ ; \ d\phi' = -d\phi$$

then

$$\begin{aligned}
\int^{(1)y'} &= \frac{1}{\pi} \cos k_y Y_0 \left[\int_{-\frac{\pi}{2}}^{0} \sin(k_y \frac{W}{2} \sin\phi) \, d\phi + \int_{0}^{-\frac{\pi}{2}} \sin(-k_y \frac{W}{2} \sin\phi)(-d\phi) \right] \\
&= 0 .
\end{aligned}$$

Hence, (F.12) becomes

$$\begin{aligned}
\mathcal{I}^{y'} &= \int^{(2)y'} = \frac{1}{\pi} \sin k_y Y_0 \int_{-\frac{\pi}{2}}^{\frac{\pi}{2}} \cos(k_y \frac{W}{2} \sin\phi) \, d\phi \\
&= \frac{1}{\pi} \sin k_y Y_0 \left[\int_{-\frac{\pi}{2}}^{0} \cos(k_y \frac{W}{2} \sin\phi) \, d\phi \right. \\
&\qquad \left. + \int_{0}^{\frac{\pi}{2}} \cos(k_y \frac{W}{2} \sin\phi) \, d\phi \right] . \qquad \text{(F.13)}
\end{aligned}$$

If, in the first integral of (F.13), we let

$$\phi' = -\phi \ ; \ d\phi' = -d\phi$$

we obtain

$$\mathcal{I}^{y'} = \frac{2}{\pi} \sin k_y Y_0 \int_0^{\frac{\pi}{2}} \cos(k_y \frac{W}{2} \sin\phi)\, d\phi \,. \tag{F.14}$$

By comparison of the Bessel function of the 2η order given by [65]

$$J_{2\eta}(z) = \frac{2}{\pi} \int_0^{\frac{\pi}{2}} \cos 2\eta\theta \cos(z \sin\theta)\, d\theta$$

with (F.14) we may readily see that

$$\mathcal{I}^{y'} = \sin k_y Y_0\, J_0\left(k_y \frac{W}{2}\right) \tag{F.15}$$

This completes the y'-portion of the integration.

INTEGRATION OVER x'

From (F.8),

$$\mathcal{I}_q^{x'} = \int_{x_{q-1}}^{x_{q+1}} \cos k_x x' \alpha_q(x') dx' \tag{F.16}$$

First we consider the case for $q \neq 1$. Substitution from (F.3) in the above yields

$$\begin{aligned} \mathcal{I}_q^{x'} &= \frac{1}{\sin K l_x} \left[\int_{x_{q-1}}^{x_q} \sin K(x' - x_{q-1}) \cos k_x x'\, dx' \right. \\ &\quad \left. + \int_{x_q}^{x_{q+1}} \sin K(x' + x_{q-1}) \cos k_x x'\, dx' \right] \\ &= \frac{1}{\sin K l_x} \left[\mathcal{I}_q^{(1)x'} + \mathcal{I}_q^{(2)x'} \right] \quad (q \neq 1) \,. \end{aligned} \tag{F.17}$$

For the first integral we have

$$\begin{aligned} \mathcal{I}_q^{(1)x'} &= \int_{x_{q-1}}^{x_q} \sin K(x' - x_{q-1}) \cos k_x x' dx' \\ &= \frac{1}{2} \int_{x_{q-1}}^{x_q} \{ \sin[(K + k_x)x' - K x_{q-1}] + \sin[(K - k_x)x' - K x_{q-1}] \}\, dx' \\ &= -\frac{1}{2} \left\{ \frac{1}{K + k_x} [\cos(K l_x + k_x x_q) - \cos k_x x_{q-1}] \right. \\ &\quad \left. + \frac{1}{K - k_x} [\cos(K l_x - k_x x_q) - \cos k_x x_{q-1}] \right\} \,. \end{aligned} \tag{F.18}$$

We can solve for $\mathcal{I}_q^{(2)x'}$ in a similar fashion to yield

$$\begin{aligned}\mathcal{I}_q^{(2)x'} &= \int_{x_q}^{x_{q+1}} \sin\left[K(x_{q+1}-x')\right]\cos k_x x' dx' \\ &= \frac{1}{2}\left\{\frac{1}{K-k_x}\left[\cos k_x x_{q+1} - \cos(Kl_x + k_x x_q)\right]\right. \\ &\quad \left. + \frac{1}{K+k_x}\left[\cos k_x x_{q+1} - \cos(Kl_x - k_x x_q)\right]\right\} . \qquad (\text{F.19})\end{aligned}$$

Substitution from (F.18) and (F.19) back into (F.17) yields

$$\begin{aligned}\mathcal{I}_q^{x'} &= \frac{1}{\sin Kl_x}\left(\frac{1}{K+k_x} + \frac{1}{K-k_x}\right) \\ &\quad \cdot \left[\frac{1}{2}\left(\cos k_x x_{q+1} + \cos k_x x_{q-1}\right) - \cos Kl_x \cos k_x x_q\right] . \qquad (\text{F.20})\end{aligned}$$

After some manipulation, this expression may be put in the following form

$$\begin{aligned}\mathcal{I}_q^{x'} &= \frac{-4K\cos k_x x_q \sin\left[\frac{1}{2}(k_x+K)l_x\right]\sin\left[\frac{1}{2}(k_x-K)l_x\right]}{\sin Kl_x \ (K+k_x)\ (K-k_x)} \\ &= -\frac{Kl_x^2\cos k_x x_q}{\sin Kl_x}\,\text{Sinc}\left[\frac{1}{2}(k_x+K)l_x\right]\,\text{Sinc}\left[\frac{1}{2}(k_x-K)l_x\right] \qquad (\text{F.21})\end{aligned}$$

where

$$\text{Sinc}(t) = \begin{cases} \frac{\sin t}{t} & t \neq 0 \\ 1 & t = 0 . \end{cases} \qquad (\text{F.22})$$

Recall now the integral for the case $q = 1$ from (F.8)

$$\mathcal{I}_1^{x'} = \int_0^{l_x} \cos k_x x' \alpha_1(x') dx' .$$

Substitution from (F.4) for $\alpha_1(x)$

$$\mathcal{I}_1^{x'} = \frac{1}{\sin Kl_x}\int_0^{l_x} \cos k_x x' \sin(l_x - x') dx' . \qquad (\text{F.23})$$

Comparison of this expression to the integral of (F.19) shows that if we let $x_q \to 0$ and $x_{q+1} \to l_x$ in (F.19) we can obtain the solution for the integral in (F.23). The result is

$$\begin{aligned}\mathcal{I}_1^{x'} &= \frac{1}{2\sin Kl_x}\left\{\frac{1}{K-k_x}\left[\cos k_x l_x - \cos Kl_x\right] + \frac{1}{K+k_x}\left[\cos k_x l_x - \cos Kl_x\right]\right\} \\ &= \frac{1}{2\sin Kl_x}\left(\frac{1}{K-k_x} + \frac{1}{K+k_x}\right)\left[\cos k_x l_x - \cos Kl_x\right] .\end{aligned}$$

The above can be rearranged to give

$$\mathcal{I}_1^{x'} = \frac{-Kl_x^2}{2\sin Kl_x} \text{Sinc}\left[\frac{1}{2}(k_x + K)l_x\right] \text{Sinc}\left[\frac{1}{2}(k_x - K)l_x\right] \quad (\text{for } q = 1)\,. \qquad (\text{F.24})$$

Combination of this with (F.21) yields

$$\mathcal{I}_q^{x'} = -\frac{\zeta_q K l_x^2 \cos k_x x_q}{4\sin Kl_x} \text{Sinc}\left[\frac{1}{2}(k_x + K)l_x\right] \text{Sinc}\left[\frac{1}{2}(k_x - K)l_x\right] \quad (\text{for any } q) \qquad (\text{F.25})$$

where

$$\zeta_q = \begin{cases} 2 & \text{for} \quad q = 1 \\ 4 & \text{for} \quad q \neq 1\,. \end{cases} \qquad (\text{F.26})$$

Finally, substitution from (F.15) and (F.25) back into (F.6) yields

$$\begin{aligned} \mathcal{I}_{qmn} &= \int\int_{S_q} \cos k_x x' \sin k_y y' \psi(y') \alpha_q(x') dx' dy' \\ &= -\frac{\zeta_q K l_x^2 \cos k_x x_q}{\sin Kl_x} \text{Sinc}\left[\frac{1}{2}(k_x + K)l_x\right] \text{Sinc}\left[\frac{1}{2}(k_x - K)l_x\right] \\ &\quad \cdot \sin k_y Y_0 \, J_0(k_y \frac{W}{2})\,. \end{aligned} \qquad (\text{F.27})$$

APPENDIX G

EVALUATION OF MAGNETIC FIELD COMPONENTS

The magnetic field components anywhere inside the cavity are given by the surface integrals of (2.89) and (2.90)

$$H_{qy}^{i} = \int\int_{S_q} \left(\frac{\partial G_{xx}^{i}}{\partial z} - \frac{\partial G_{xz}^{i}}{\partial x} \right) \psi(y') \alpha_q(x') ds' \qquad (G.1)$$

$$H_{qz}^{i} = -\int\int_{S_q} \frac{\partial G_{xx}^{i}}{\partial y} \psi(y') \alpha_q(x') ds' \,. \qquad (G.2)$$

We will evaluate H_{qy}^{i} first.

EVALUATION OF THE $y-$ COMPONENT OF THE MAGNETIC FIELD

From (2.36) and (2.37)

$$\begin{aligned} \frac{\partial G_{xx}^{(1)}}{\partial z} - \frac{\partial G_{xz}^{(1)}}{\partial x} &= \sum_{m=1}^{\infty} \sum_{n=0}^{\infty} k_z^{(1)} A_{mn}^{(1)} \cos k_x x \, \sin k_y y \, \cos k_z^{(1)} z \\ &\quad - \sum_{m=1}^{\infty} \sum_{n=0}^{\infty} k_x B_{mn}^{(1)} \cos k_x x \, \sin k_y y \, \cos k_z^{(1)} z \,. \end{aligned}$$

After appropriate substitutions and some manipulation we may write

$$\begin{aligned} \frac{\partial G_{xx}^{(1)}}{\partial z} - \frac{\partial G_{xz}^{(1)}}{\partial x} &= -\sum_{m=1}^{\infty} \sum_{n=0}^{\infty} \frac{\varphi_n \tan k_z^{(2)}(h-c)}{ab\, d_{1mn} d_{2mn} \cos k_z^{(1)} h} \\ &\quad \cdot \left\{ k_z^{(1)} k_z^{(2)} \epsilon_r^{*} \tan k_z^{(2)}(h-c) - \left[(k_z^{(1)})^2 + k_x^2 (1-\epsilon_r^{*}) \right] \tan k_z^{(1)} h \right\} \\ &\quad \cdot \cos k_x x \, \sin k_y y \, \cos k_z^{(1)} z \, \cos k_x x' \, \sin k_y y' \,. \qquad (G.3) \end{aligned}$$

Similarly, substitution from (2.38) and (2.39) leads to

$$\begin{aligned}\frac{\partial G_{xx}^{(2)}}{\partial z}-\frac{\partial G_{xz}^{(2)}}{\partial x} &= \sum_{m=1}^{\infty}\sum_{n=0}^{\infty}\frac{\varphi_n \tan k_z^{(1)}h}{ab\, d_{1mn}d_{2mn}\cos k_z^{(2)}(h-c)}\\ &\cdot\left\{k_z^{(1)}k_z^{(2)}\tan k_z^{(1)}h-\left[(k_z^{(2)})^2\epsilon_r^*-k_x^2(1-\epsilon_r^*)\right]\tan k_z^{(2)}(h-c)\right\}\\ &\cos k_x x\,\sin k_y y\,\cos k_z^{(2)}(z-c)\,\cos k_x x'\,\sin k_y y'\,. \qquad \text{(G.4)}\end{aligned}$$

We are now ready to evaluate the $y-$component of the magnetic field. Substitution from (G.3) into (G.1) yields

$$\begin{aligned}H_{qy}^{(1)} &= -\sum_{m=1}^{\infty}\sum_{n=0}^{\infty}\frac{\varphi_n\tan k_z^{(2)}(h-c)}{ab\, d_{1mn}d_{2mn}\cos k_z^{(1)}h}\\ &\cdot\left\{k_z^{(1)}k_z^{(2)}\epsilon_r^*\tan k_z^{(2)}(h-c)-\left[(k_z^{(1)})^2+k_x^2(1-\epsilon_r^*)\right]\tan k_z^{(1)}h\right\}\\ &\cdot\cos k_x x\,\sin k_y y\,\cos k_z^{(1)}z\,\left[\mathcal{I}_{qmn}\right] \qquad \text{(G.5)}\end{aligned}$$

Replacement of $\mathcal{I}_{qmn}$ with the expression from Appendix F, yields

$$\begin{aligned}H_{qy}^{(1)} &= \frac{\zeta_q K l_x^2}{4ab\sin K l_x}\sum_{m=1}^{\infty}\sum_{n=0}^{\infty}\frac{\varphi_n\tan k_z^{(2)}(h-c)}{d_{1mn}d_{2mn}\cos k_z^{(1)}h}\\ &\cdot\left\{k_z^{(1)}k_z^{(2)}\epsilon_r^*\tan k_z^{(2)}(h-c)-\left[(k_z^{(1)})^2+k_x^2(1-\epsilon_r^*)\right]\tan k_z^{(1)}h\right\}\\ &\cdot\cos k_x x_q\,\mathrm{Sinc}\left[\frac{1}{2}(k_x+K)l_x\right]\,\mathrm{Sinc}\left[\frac{1}{2}(k_x-K)l_x\right]\sin k_y Y_0\, J_0(k_y\frac{W}{2})\\ &\cdot\cos k_x x\,\sin k_y y\,\cos k_z^{(1)}z\,. \qquad \text{(G.6)}\end{aligned}$$

Similarly, substitution from (G.4) into (G.1) and again making use of (F.27) yields

$$\begin{aligned}H_{qy}^{(2)} &= \frac{-\zeta_q K l_x^2}{4ab\sin K l_x}\sum_{m=1}^{\infty}\sum_{n=0}^{\infty}\frac{\varphi_n\tan k_z^{(1)}h}{d_{1mn}d_{2mn}\cos k_z^{(2)}(h-c)}\\ &\cdot\left\{k_z^{(1)}k_z^{(2)}\tan k_z^{(1)}h-\left[(k_z^{(2)})^2\epsilon_r^*-k_x^2(1-\epsilon_r^*)\right]\tan k_z^{(2)}(h-c)\right\}\\ &\cdot\cos k_x x_q\,\mathrm{Sinc}\left[\frac{1}{2}(k_x+K)l_x\right]\,\mathrm{Sinc}\left[\frac{1}{2}(k_x-K)l_x\right]\sin k_y Y_0\, J_0(k_y\frac{W}{2})\\ &\cdot\cos k_x x\,\sin k_y y\,\cos k_z^{(2)}(z-c)\,. \qquad \text{(G.7)}\end{aligned}$$

We now proceed to the evaluation of H_{qz}^{i}.

EVALUATION OF THE $z-$ COMPONENT OF THE MAGNETIC FIELD

With the use of (2.36), we can write

$$\begin{aligned}\frac{\partial G_{xx}^{(1)}}{\partial y} &= \sum_{m=1}^{\infty}\sum_{n=0}^{\infty} k_y A_{mn}^{(1)} \cos k_x x \cos k_y y \sin k_z^{(1)} z \\ &= -\sum_{m=1}^{\infty}\sum_{n=0}^{\infty} \frac{\varphi_n k_y \tan k_z^{(2)}(h-c)}{ab\, d_{1mn} \cos k_z^{(1)} h} \\ &\quad \cdot \cos k_x x \cos k_y y \sin k_z^{(1)} z \cos k_x x' \sin k_y y' \,. \end{aligned} \tag{G.8}$$

Similarly, from (2.38)

$$\begin{aligned}\frac{\partial G_{xx}^{(2)}}{\partial y} &= \sum_{m=1}^{\infty}\sum_{n=0}^{\infty} k_y A_{mn}^{(2)} \cos k_x x \cos k_y y \sin k_z^{(2)}(z-c) \\ &= -\sum_{m=1}^{\infty}\sum_{n=0}^{\infty} \frac{\varphi_n k_y \tan k_z^{(1)} h}{ab\, d_{1mn} \cos k_z^{(2)}(h-c)} \\ &\quad \cdot \cos k_x x \cos k_y y \sin k_z^{(2)}(z-c) \cos k_x x' \sin k_y y' \,. \end{aligned} \tag{G.9}$$

Substitution from (G.8) into (G.2) and using (F.27) yields

$$\begin{aligned} H_{qz}^{(1)} &= \frac{\zeta_q K l_x^2}{4ab \sin K l_x} \sum_{m=1}^{\infty}\sum_{n=0}^{\infty} \frac{\varphi_n k_y \tan k_z^{(2)}(h-c)}{d_{1mn} \cos k_z^{(1)} h} \\ &\quad \cdot \cos k_x x_q \,\mathrm{Sinc}\left[\frac{1}{2}(k_x+K) l_x\right] \mathrm{Sinc}\left[\frac{1}{2}(k_x-K) l_x\right] \\ &\quad \cdot \sin k_y Y_0 \, J_0(k_y \frac{W}{2}) \cos k_x x \cos k_y y \sin k_z^{(1)} z \end{aligned} \tag{G.10}$$

Likewise, substitution from (G.9) in (G.2) yields

$$\begin{aligned} H_{qz}^{(2)} &= \frac{\zeta_q K l_x^2}{4ab \sin K l_x} \sum_{m=1}^{\infty}\sum_{n=0}^{\infty} \frac{\varphi_n k_y \tan k_z^{(1)} h}{d_{1mn} \cos k_z^{(2)}(h-c)} \\ &\quad \cdot \cos k_x x_q \,\mathrm{Sinc}\left[\frac{1}{2}(k_x+K) l_x\right] \mathrm{Sinc}\left[\frac{1}{2}(k_x-K) l_x\right] \\ &\quad \cdot \sin k_y Y_0 \, J_0(k_y \frac{W}{2}) \cos k_x x \cos k_y y \sin k_z^{(2)}(z-c) \end{aligned} \tag{G.11}$$

In summary, the $\hat{y}$ and $\hat{z}$ components of the magnetic field anywhere in the cavity may be expressed as follows:

$$H_{qy}^{(1)} = H_{q0} \sum_{m=1}^{\infty}\sum_{n=0}^{\infty} c_{nq} c_{ymn}^{(1)} \cos k_x x \sin k_y y \cos k_z^{(1)} z \tag{G.12}$$

$$
\begin{aligned}
H_{qz}^{(1)} &= H_{q0} \sum_{m=1}^{\infty} \sum_{n=0}^{\infty} c_{nq} c_{zmn}^{(1)} \cos k_x x \cos k_y y \sin k_z^{(1)} z && \text{(G.13)} \\
H_{qy}^{(2)} &= H_{q0} \sum_{m=1}^{\infty} \sum_{n=0}^{\infty} c_{nq} c_{ymn}^{(2)} \cos k_x x \sin k_y y \cos k_z^{(2)} (z-c) && \text{(G.14)} \\
H_{qz}^{(2)} &= H_{q0} \sum_{m=1}^{\infty} \sum_{n=0}^{\infty} c_{nq} c_{zmn}^{(2)} \cos k_x x \cos k_y y \sin k_z^{(2)} (z-c) && \text{(G.15)}
\end{aligned}
$$

where

$$
\begin{aligned}
H_{q0} &= \frac{\zeta_q K l_x^2}{4ab \sin K l_x} \\
c_{nq} &= \cos k_x x_q \,\mathrm{Sinc}\left[\frac{1}{2}(k_x + K) l_x\right] \mathrm{Sinc}\left[\frac{1}{2}(k_x - K) l_x\right]
\end{aligned}
$$

and

$$
\begin{aligned}
c_{ymn}^{(1)} &= \frac{c_{zmn}^{(1)}}{k_y d_{2mn}} \Big\{ k_z^{(1)} k_z^{(2)} \epsilon_r^* \tan k_z^{(2)} (h-c) \\
&\quad - \left[(k_z^{(1)})^2 + k_x^2 (1 - \epsilon_r^*) \right] \tan k_z^{(1)} h \Big\} && \text{(G.16)} \\
c_{zmn}^{(1)} &= \frac{\varphi_n k_y \tan k_z^{(2)} (h-c)}{d_{1mn} \cos k_z^{(1)} h} \sin k_y Y_0 \, J_0(k_y \frac{W}{2}) && \text{(G.17)} \\
c_{ymn}^{(2)} &= \frac{c_{zmn}^{(2)}}{k_y d_{2mn}} \Big\{ k_z^{(1)} k_z^{(2)} \tan k_z^{(1)} h \\
&\quad - \left[(k_z^{(2)})^2 \epsilon_r^* - k_x^2 (1 - \epsilon_r^*) \right] \tan k_z^{(2)} (h-c) \Big\} && \text{(G.18)} \\
c_{zmn}^{(2)} &= \frac{\varphi_n k_y \tan k_z^{(1)} h}{d_{1mn} \cos k_z^{(2)} (h-c)} \sin k_y Y_0 \, J_0(k_y \frac{W}{2}) \,. && \text{(G.19)}
\end{aligned}
$$

APPENDIX H

MICROSTRIP CONNECTION REPEATABILITY STUDY

This appendix includes a description of the microstrip connection repeatability study carried out by the author while at Hughes Aircraft Company. In this study, key repeatability issues related to the measurement of microstrip discontinuities with the TSD (thru-short-delay) technique [44,49], are explored experimentally. These include the repeatability of coax/microstrip connections, microstrip/microstrip interconnects, microstrip line fabrication and substrate mounting, and the electrical characteristics of coax-to-microstrip transitions (launchers). Each of these issues has been explored experimentally and the results are presented for two types of coaxial-to-microstrip test fixtures: one usable to 18GHz, and the other to 40GHz.

The objectives met by this study are two-fold. First, trade-offs were explored for choosing between different connection alternatives for de-embedding in microstrip with the (TSD) technique Secondly, data was obtained to assess the uncertainties in microstrip fixture measurements due to the non-repeatability of various microstrip connections.

Finite measurement uncertainties, due to the repeatability issues described above, are inherent in each fixture measurement made on the TSD standards (during fixture characterization), and the D.U.T.. The measurements described next illustrate how experimentation can be used to determine the magnitudes of

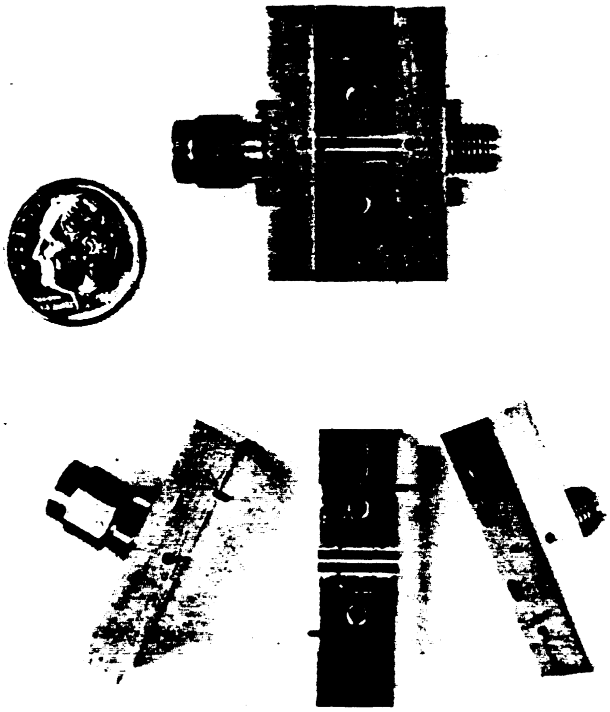

Figure H.1: K-connector (2.9mm) coaxial/microstrip test fixture.

these uncertainties.

DESCRIPTION OF CONNECTION REPEATABILITY EXPERIMENTS

Two types of coaxial test fixtures were used in the experiments. The first, usable to 18 GHz, consists of a pair of 7mm "Eisenhart" launchers [57]. The test circuit used here consists of a 1″ section of 50 ohm microstrip line on an alumina (h = .025″) substrate (Figure 4.4). The other fixture , operable to 40 GHz, uses a pair of Wiltron K-connector (2.9mm) launchers and a .40″ section of 50 ohm microstrip line on a quartz (h = .01″) substrate (Figure H.1).

The repeatability experiments performed are summarized in Table 1. For our purposes, "cycling" a connection refers to disconnecting and reconnecting both the input and output connections simultaneously and repeating the measurement. For the coax/coax repeatability experiment, each fixture was connected to and

Table H.1: SUMMARY OF REPEATABILITY EXPERIMENTS

EXPERIMENT	NUMBER OF TRIALS	FREQUENCY RANGE	DESCRIPTION
1. COAX/COAX			
A) 7 mm FIXTURE	20	0.045-18 GHz	CYCLED CONNECTIONS AT 7 mm COAXIAL MEASUREMENT PORTS
B) K-CONN. FIXTURE	20	0.045-26.5 GHz	CYCLED CONNECTIONS AT K-CONN. COAXIAL MEASUREMENT PORTS
2. COAX/MICROSTRIP			
A) 7 mm FIXTURE	10	0.045-18 GHz	CYCLED PRESSURE CONTACT MADE FROM LAUNCHER TO MICROSTRIP LINE
B) K-CONN. FIXTURE	10	0.045-40 GHz	CYCLED GAP WELD CONNECTION MADE FROM TAB ON K-CONN. SLIDING CONTACT TO MICROSTRIP
3. MICROSTRIP/MICROSTRIP			
K-CONN. FIXTURE	5	0.045-40 GHz	CYCLED TWO GAP WELDED RIBBONS USED TO CONNECT THREE MICROSTRIP LINES TOGETHER
4. MICROSTRIP FABRICATION/ MOUNTING			
K-CONN. FIXTURE	5	0.045-40 GHz	MEASURED FIVE SEPARATE MICROSTRIP LINES WITH SAME LAUNCHERS
5. LAUNCHER-TO-LAUNCHER UNIFORMITY			
A) 7 mm FIXTURE	4	0.045-18 GHz	MEASURED SAME LINE WITH DIFFERENT PAIRS OF 7 mm LAUNCHERS
B) K-CONN. FIXTURE	3	0.045-26.5 GHz	MEASURED SAME LINE WITH DIFFERENT PAIRS OF K-CONN. LAUNCHERS

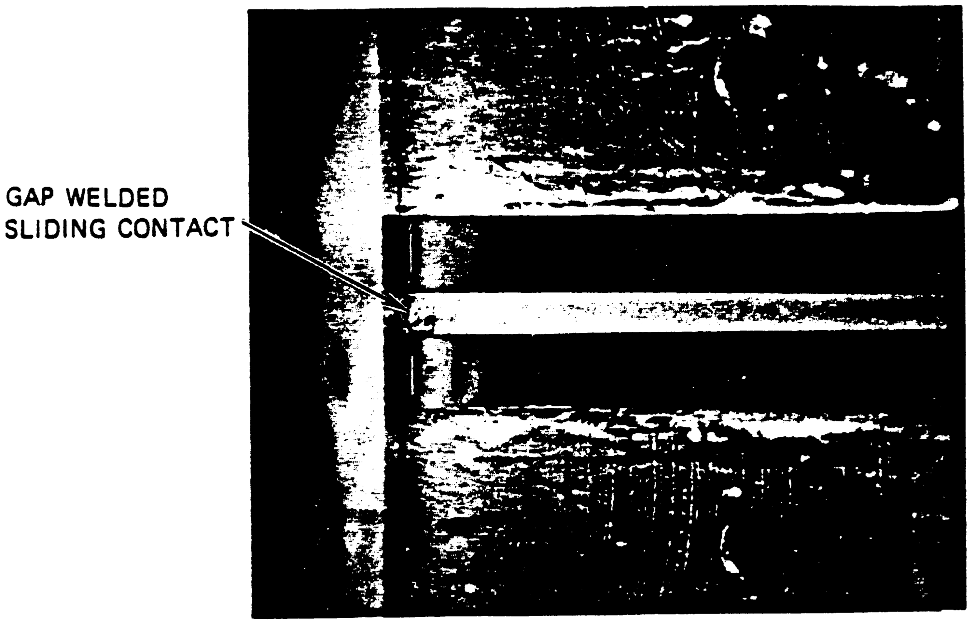

Figure H.2: Coax/microstrip connection technique used with K-connector (2.9mm) launchers.

removed from the coaxial measurement terminals several times, taking care not to disturb the coax/microstrip connection. The 7mm coax/microstrip connection test was performed by cycling pressure contacts made between the wedge shaped center conductors on the Eisenhart launchers, and the microstrip line. For the K-conn. fixture, gap welds used to connect the .018″ tab on the K-conn. "sliding contact" (a small gold plated tab with a sleeve that fits over the launcher's center conductor) to the microstrip line (Figure H.2) were cycled. In order to preserve the microstrip metalization, the minimum amount of weld voltage and pressure needed to secure the tab was used. This made it possible to use the same microstrip line and sliding contacts for all 10 trials.

A similar connection approach was used for the microstrip/microstrip interconnects. Two .020" × .025″ Gold ribbon straps were gap welded across the connection interfaces between three microstrip lines (Figure H.3). To cycle this connection,

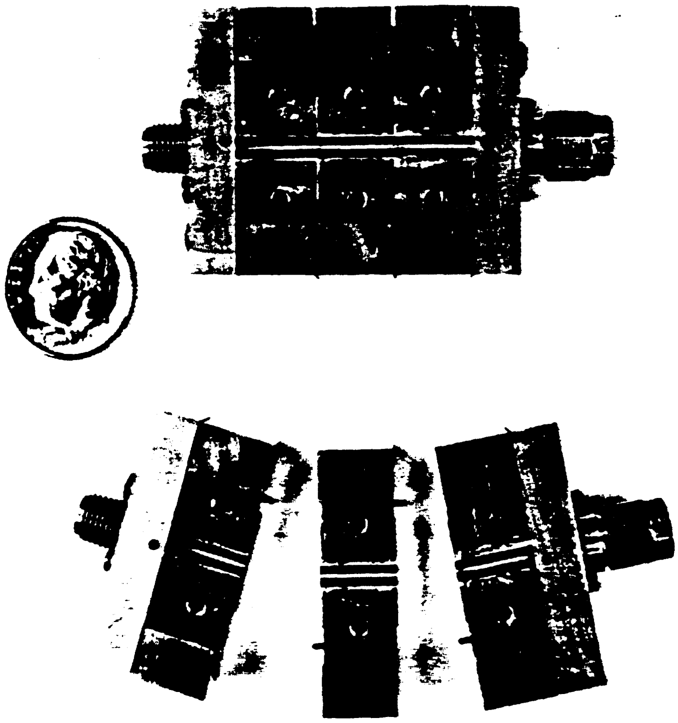

Figure H.3: K-connector multi-line test fixture used for testing microstrip/microstrip interconnects.

the straps were removed and then replaced with new ones. A minimum amount of weld voltage and pressure were used.

Note that none of the repeatability cycling could be performed without removing the fixture from the coaxial measurement ports; hence, coax/coax connection uncertainties are included in all the results. In the microstrip fabrication/mounting experiment, three uncertainty factors are present simultaneously: coax/coax connections, coax/microstrip connections, and the variations in the carrier mounted microstrip lines.

Two automatic network analyzers were employed for the testing; an HP8510 ANA for .045 to 26.5 GHz measurements, and an HP8409 ANA with an in-house frequency extension system for Ka-Band (26.5 to 40GHz) measurements. The HP8510 ANA was operated in step mode with 201 calibration points, and the Ka-Band ANA was operated in phase-locked mode with 51 calibration points.

Calibration was achieved using either 7mm or K-conn. coaxial standards, depending on the fixture. After testing, the S-parameters for each of the measurement trials were stored in separate files so that data processing could be carried out later.

DISCUSSION OF RESULTS

Due to the large volume of data generated, only a sample of the results can be presented. Therefore, we will limit the discussion to the uncertainties in S_{21} (the forward transmission coefficient) due to the repeatability issues discussed above.

Figure H.4a shows the coax/microstrip repeatability measurements made with the 7mm test fixture. At a glance this connection looks very repeatable, yet with some data processing we can get a closer look. A program was written that allows for statistical computations to be made using the data stored on file. With this program, an average set of S-parameters was computed for each experiment. Figure H.4b shows the results of normalizing the S_{21} data to the average S-parameters for the coax/microstrip test. This was achieved by performing a complex division between the S-parameters from each trial and the average S-parameters. After normalization, it is easy to see the variations in phase and magnitude resulting from the repeated connections. For the 7mm coax/microstrip connection, the repeatability in S_{21} is quite good and can be held to within a range of .1dB(+/-.05dB) in amplitude and 1 degree (+/-.5deg.) in phase.

Standard deviation data for each experiment was also computed as a function of frequency. This was done separately for the magnitude and phase angles of the S-parameters using the following formula:

$$\text{Std.Deviation} = s = \sqrt{\frac{\sum x_i^2 - \frac{(\sum x_i)^2}{N}}{N-1}} \qquad \text{(H.1)}$$

where

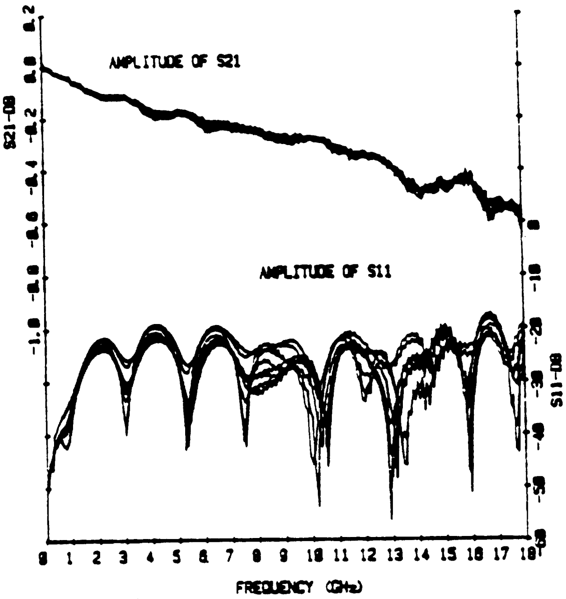

a) Amplitude measurements

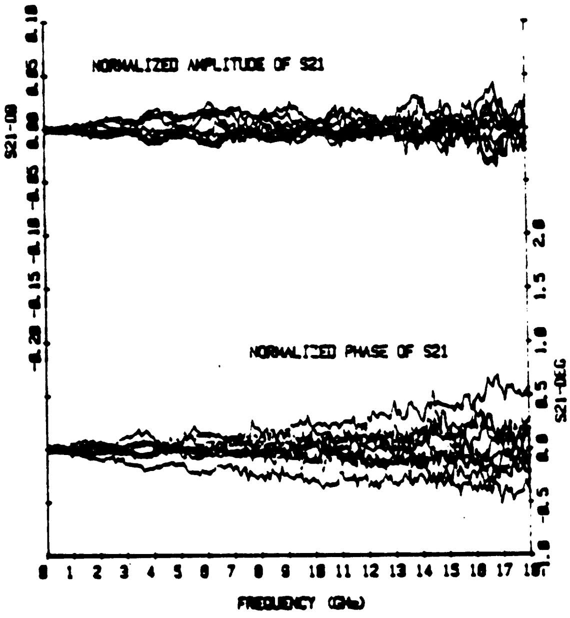

b) S_{21} results normalized to average S-parameters.

Figure H.4: 7mm Coax/microstrip connection repeatability measurements.

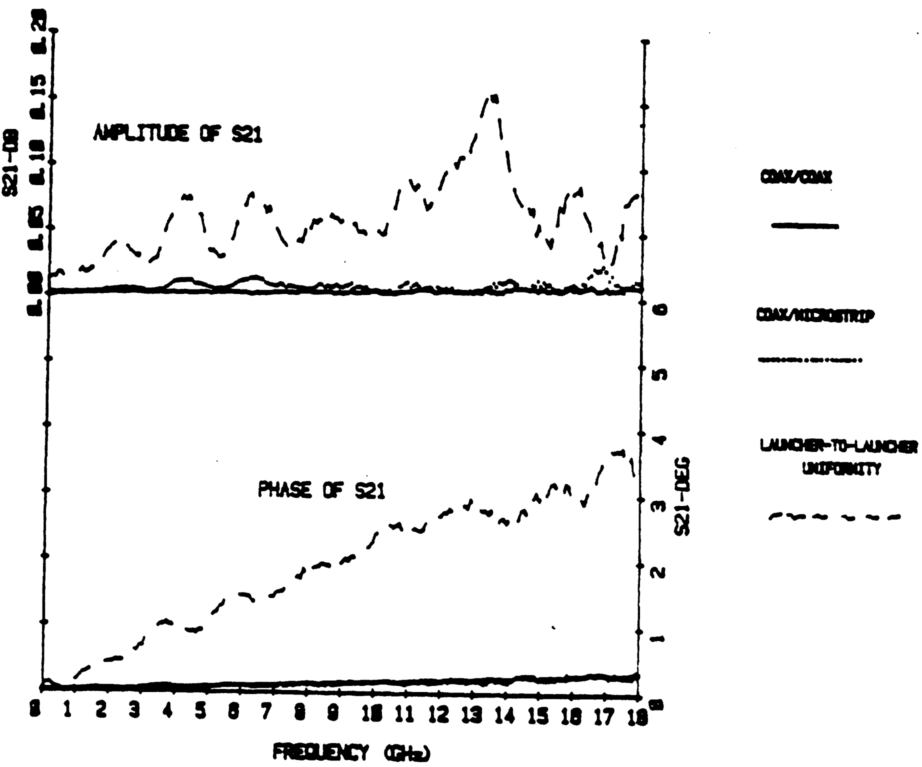

Figure H.5: Standard deviation data for experiments with 7mm fixture

N = number of trials

x_i = magnitude or phase of a particular S-parameter (at a given frequency) for trial i

The standard deviation data on S_{21} for the three experiments performed with the 7mm fixture(Figure H.5), shows clearly that electrical variations between Eisenhart launchers can be significant. This is not surprising, since the center pin on each is individually tuned to achieve good performance. On the other hand, the standard deviation resulting from the coax/microstrip test was almost as good as that from the coax/coax test; thus, the uncertainty contribution to S_{21} caused by the 7mm coax/microstrip connection errors is finite but minimal.

The normalized S_{21} data for the k-connector coax/microstrip experiment (Figure H.6) displays similar repeatability performance to the 7mm coax/microstrip connection to 18 GHz. The approximate range in amplitude is .1dB to 26.5 GHz and .2dB to 40 GHz, and the range in phase is 2 degrees to 26.5 GHz, and 8 degrees to 40GHz. For the microstrip fabrication/mounting experiment (Figure H.7) the amplitude and phase deviation were about the same if one ,apparently erroneous, measurement in the .045 to 26.5GHz band is neglected. The connection repeatability of the microstrip/microstrip interconnects (Figure H.8) was considerably worse than the coax/microstrip connections, with ranges in amplitude of .5dB to 26.5 GHz and .6dB to 40 GHz, and in phase of 10 degrees to 26.5 GHz and as much as 15 degrees to 40 GHz.

A good summary of the K-conn. fixture repeatability experiments is provided by the standard deviation plots of Figure H.9. Admittedly, some of the results (e.g. launcher-to-launcher uniformity) are not entirely conclusive due to the limited number of trials performed, however, some definite trends are apparent.

The erroneous measurement in the fabrication/mounting experiment (Figure H.7) caused the standard deviation in phase below 26.5 GHz to appear much worse than it should. This is supported by the comparatively good standard deviation observed in the 26.5 to 40 GHz band, which follows the coax/microstrip repeatability curve closely. Hence, the measurement uncertainties due to microstrip fabrication/mounting variations are not believed to be a major concern. On the other hand, although the K-conn. launchers are not individually tuned, Figure H.9 indicates significant deviations in S_{21} between the three sets of launchers tested. Consequently, for accurate de-embedding work, launcher-to-launcher uniformity should not be assumed. The standard deviation data for the coax/microstrip and microstrip/microstrip experiments reinforces the S_{21} data of Figures H.6 and H.8. In terms of the TSD connection alternatives discussed in Section 5.3 these results clearly favor an approach relying on repeatable coax/microstrip connections rather

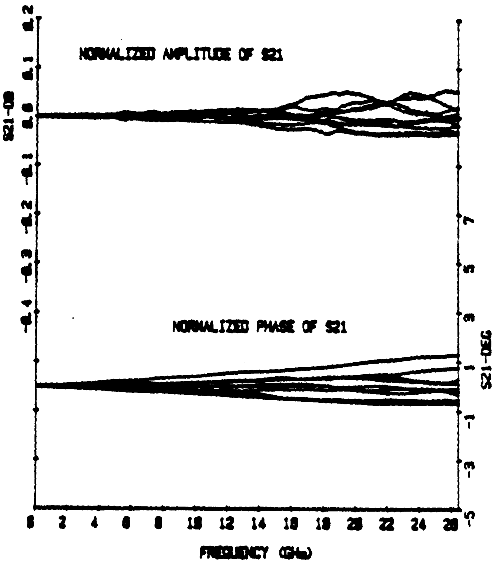

a) Measurements from .045-26.5 GHz

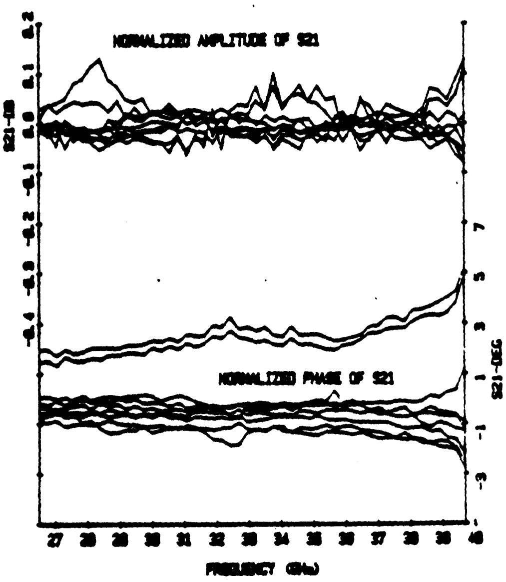

b) Measurements from 26.5-40 GHz

Figure H.6: K-connector coax/microstrip repeatability measurements normalized to average.

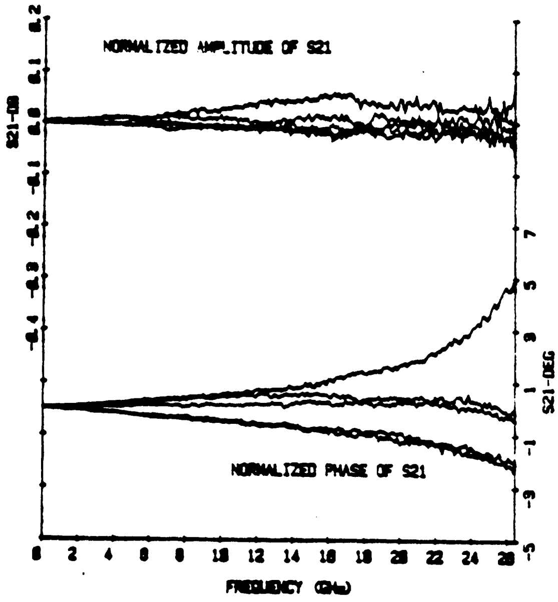

a) Measurements from .045-26.5 GHz

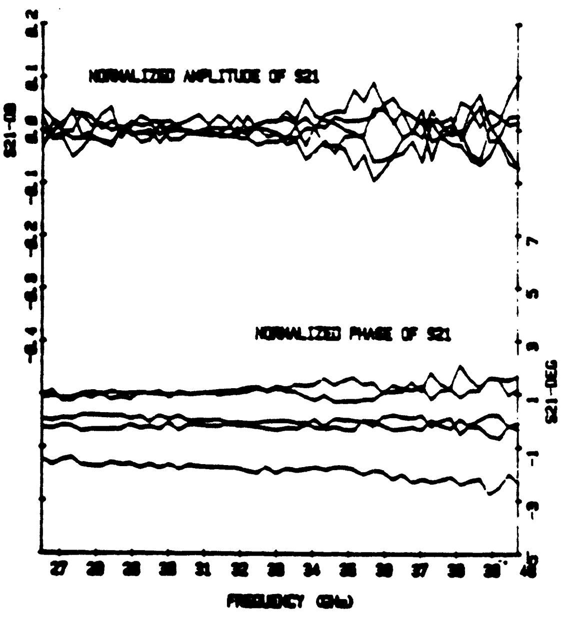

b) Measurements from 26.5-40 GHz

Figure H.7: Microstrip fabrication/mounting repeatability measurements normalized to average.

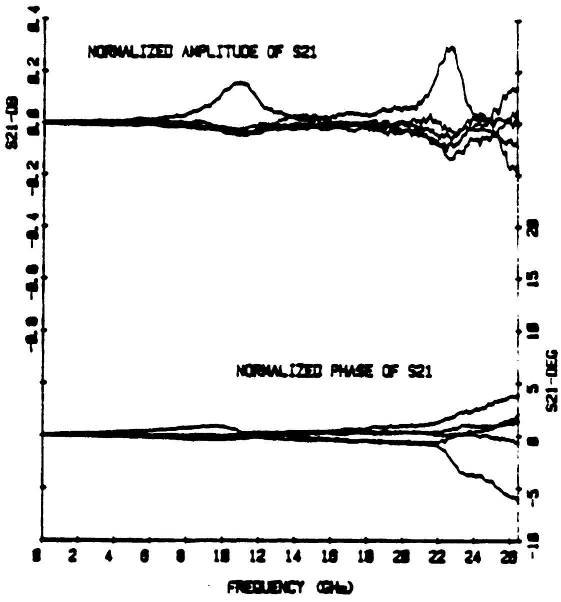

a) Measurements from .045-26.5 GHz

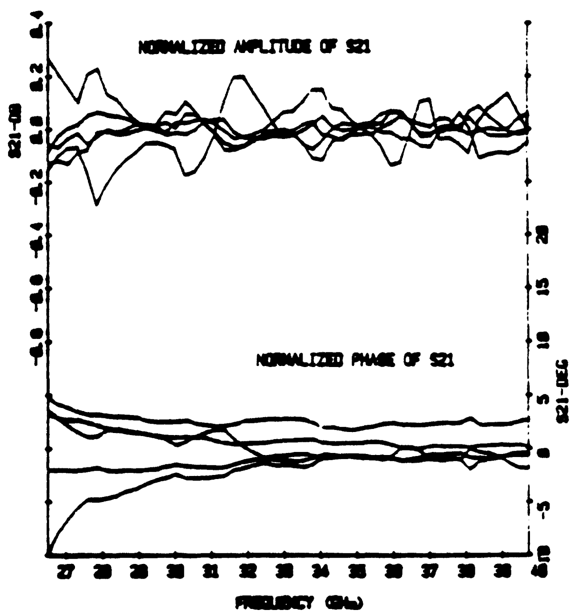

b) Measurements from 26.5-40 GHz

Figure H.8: Microstrip/microstrip interconnect repeatability measurements normalized to average.

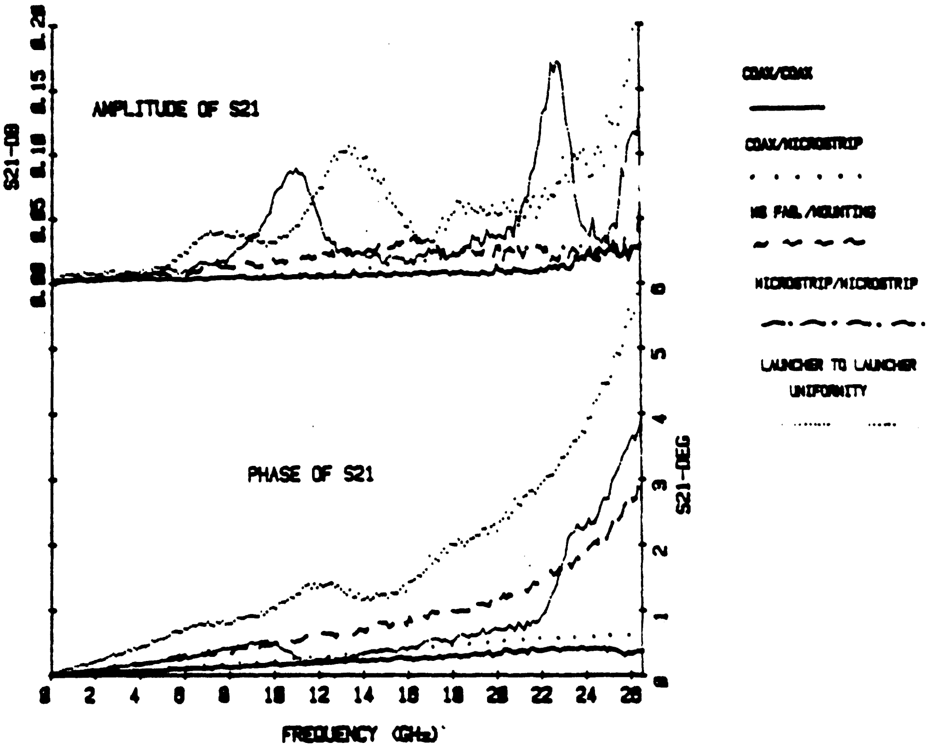

a) Results for experiments conducted from .045-26.5 GHz

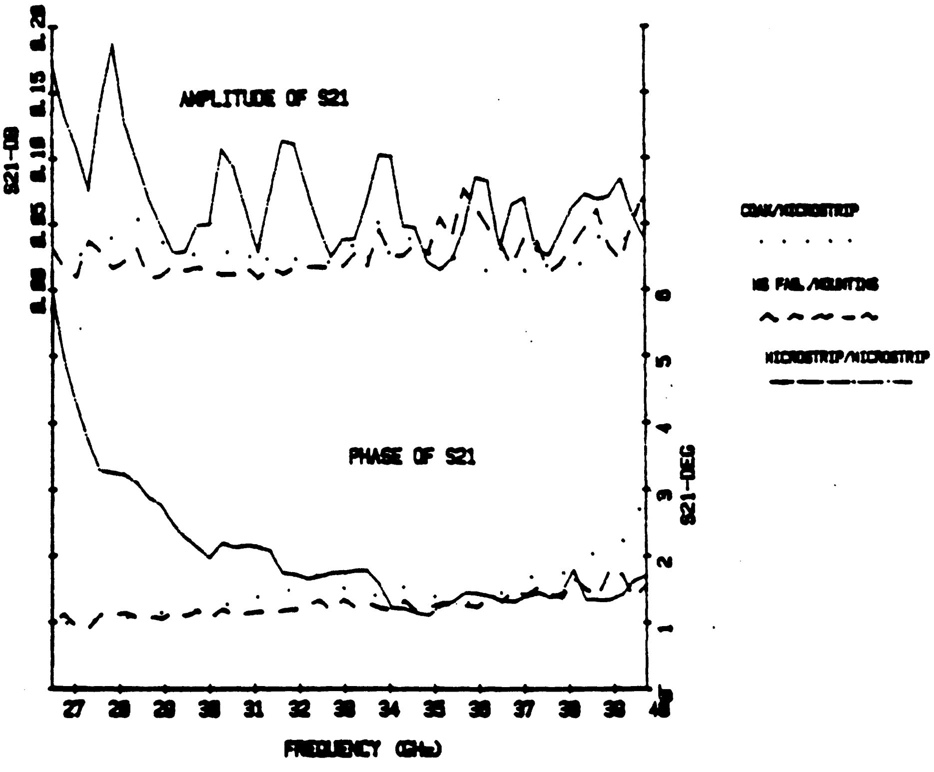

b) Results for experiments conducted from 26.5-40 GHz

Figure H.9: Standard deviation data for experiments with K-connector fixture.

than microstrip/microstrip interconnects for the hardware tested.

BIBLIOGRAPHY

BIBLIOGRAPHY

[1] T.C. Edwards, *Foundations for Microstrip Circuit Design*, John Wiley and Sons, 1981.

[2] K. C. Gupta, R. Garg, and I. J. Bahl, *Microstrip Lines and Slotlines*, Artech House, 1979.

[3] K. C. Gupta, R. Garg, R. Chadha,*Computer-Aided Design of Microwave Circuits*, Artech House, 1981.

[4] Y. C. Shih, T. S. Chu, and T. Itoh, "Comparative Study of Mode Mode Matching Formulations for Microstrip Discontinuity Problems", *1985 IEEE MTT-S Digest*, pp. 435-438.

[5] P. Katehi and N. Alexopoulos, "Microstrip Discontinuity Modeling For Millimetric Integrated Circuits", *1985 IEEE MTT-S Digest*, pp. 571-573.

[6] P. Katehi and N. Alexopoulos,"Frequency-Dependent Characteristics of Microstrip Discontinuities in Millimeter-wave Integrated Circuits", *IEEE Trans. Microwave Theory Tech.* vol. MTT-33 No. 10, Oct. 1985, pp. 1029-1035.

[7] R. Jansen and N. Koster, "A Unified CAD Basis for the Frequency Dependent Characteristics of Strip, Slot, and Coplanar MIC Components", *11th European Microwave Conference*, 1971 pp. 682-687.

[8] R. Jansen, "Hybrid Mode Analysis of End Effects of Planar Microwave and Millimeter-Wave Transmission Lines", *IEEE Proc.*, Vol 128, April 1981, pp. 77-86.

[9] N. Koster and R. Jansen, "The Equivalent Circuit of the Asymmetrical Series Gap in Microstrip and Suspended Substrate Lines", *IEEE Trans. Microwave Theory Tech.*, August 1982, pp. 1273-1279.

[10] T. Itoh,"Analysis of Microstrip Resonators", *IEEE Trans. Microwave Theory Tech.*, vol MTT-24 1974, pp 946-951.

[11] J. Rautio, *A Time-Harmonic Electromagnetic Analysis of Shielded Microstrip Circuits*, Ph.D. dissertation, Syracuse University, August 1986.

[12] J. Rautio, "An Electromagnetic Time-Harmonic Analysis of Shielded Microstrip Circuits",*IEEE Trans. Microwave Theory Tech.*, vol. MTT-35, No. 8, pp726-729.

[13] N. R. Franzen and R. A. Speciale, "A New Procedure for System Calibration and Error Removal in Automated S-Parameter Measurements", *5th European Microwave Conference*,1975, pp. 69-73.

[14] L. Dunleavy and P. Katehi, "Repeatability Issues for De-embedding Microstrip Discontinuity S-parameter Measurements By the TSD Technique" *Automatic RF Techniques Group (ARFTG) Conf. Dig.* June 1986.

[15] L. Dunleavy and P. Katehi, "Eliminate Surprises When De-embedding Microstrip Launches", *Microwaves & RF* August 1987, pp117-122.

[16] R. Collin, *Field Theory of Guided Waves* McGraw Hill 1960, p287

[17] R. Mittra ed., *Computer Techniques for Electromagnetics*, Pergamon Press 1973.

[18] R.Harrington,*Field Computation by Moment Methods* R. Krieger Publishing , 1968.

[19] J. Stratton, *Electromagnetic Theory*, McGraw Hill 1941,p. 250.

[20] J.C. Maxwell, *A Treatise on Electricity and Magnetism* 3rd. ed., vol. 1,New York: Dover 1954 pp 296-297.

[21] E. Denlinger, "A Frequency Dependent Solution for Microstrip Transmission Lines", *IEEE Trans. Microwave Theory Tech.* vol. MTT-19, Jan. 1971, pp30-39.

[22] E. Yamashita, Variational Method for the Analysis of Microstrip-like Transmission Lines" *IEEE Trans. Microwave Theory Tech.*, vol. MTT-16, Aug. 1968, pp529-535.

[23] C.T. Tai, *Dyadic Green's Functions in Electromagnetic Theory* , Intext Educational Publishers 1971.

[24] A. Sommerfeld, *Partial Differential Equations in Physics* vol. VI, Academic Press, 1949, pp257-258.

[25] C. Chi and N. Alexopoulos, "Radiation by a Probe Through a Substrate" *IEEE Trans. Antennas Propagat.* vol. AP-34, Sept. 1986, pp 1080-1091.

[26] R. Harrington, *Time-Harmonic Electromagnetic Fields*, McGraw Hill 1961, pp.111-112.

[27] J. Brews, "Characteristic Impedance of Microstrip Lines", *IEEE Trans. Microwave Theory Tech.* vol. MTT-35, January 1987, pp 30-33.

[28] W. Getsinger, "Measurement and Modeling of the Apparent Characteristic Impedance of Microstrip" *IEEE Trans. Microwave Theory Tech.* vol. MTT-31, August 1983, pp 624-632.

[29] R. Jansen and H. Koster, "New Aspects Concerning the Definition of Microstrip Characteristic Impedance as a Function of Frequency", *1982 IEEE MTT-S Digest*, pp 305-307.

[30] W. Getsinger, "Microstrip Characteristic Impedance", *IEEE Trans. Microwave Theory Tech.* vol. MTT-27, April 1979, p. 293.

[31] B. Bianco et. al., "Some Considerations About the Frequency Dependence of the Characteristic Impedance of Uniform Microstrips", *IEEE Trans. Microwave Theory Tech.* vol. MTT-26, March 1978, pp182-185.

[32] P. Katehi, "A Generalized Method for the Evaluation of Mutual Coupling in Microstrip Arrays", *IEEE Trans. Antennas Propagat.* Vol. AP-35, Feb. 1987, pp 125-133.

[33] A.H. Stroud *Approximate calculation of Multiple Integrals*, Prentice Hall, New Jersey 1971, p255.

[34] C. Gerald, *Applied Numerical Analysis* Adison-Wesley 1978, p 509.

[35] G. Golub and C. Van Loan, *Matrix Computations*, John Hopkins University Press, 1983, pp26-27.

[36] J. Fitzpatrick, "Error Models for Systems Measurement",*Microwave Journal*, May 1978, pp. 63-66.

[37] E. W. Strid and K. R. Gleason, "Calibration Methods for Microwave Wafer Testing", *1984 IEEE MTT-S Digest*, pp. 93-97.

[38] B. Easter,"The Equivalent Circuit of Some Microstrip Discontinuities", *IEEE Trans. Microwave Theory Tech.*, vol. MTT-23, No. 8, August 1975, pp. 655-660.

[39] V. Rizzoli, "A General Approach to the Resonance Measurement of Asymmetric Microstrip Discontinuities", *1980 IEEE MTT-S Digest*, pp. 422-424.

[40] M. Kirschning, R. Jansen, and N. Koster, "Measurement and Computer-Aided Modeling of Microstrip Discontinuities by an Improved Resonator Method", *1983 IEEE MTT-S Digest*, pp. 495-497.

[41] B. Easter, A. Gopinath, and I. Stephenson, "Theoretical and Experimental Methods for Evaluating Discontinuities in Microstrip", *Radio and Elec. Engr.*, Vol. 48, No. 1/2, January/February 1978, pp. 73-84.

[42] H. F. Pues and V. Capelle, "Computer-Aided Experimental Characterization of Microstrip-to-Coaxial Transitions", *14th European Microwave Conference*, 1984, pp. 137-141.

[43] R. Lane, "De-Embedding Device Scattering Parameters", *Microwave Journal*, August 1984, pp. 149-156.

[44] N. R. Franzen and R. A. Speciale, "A New Procedure for System Calibration and Error Removal in Automated S-Parameter Measurements", *5th European Microwave Conference*,1975, pp. 69-73.

[45] B. Bianco et. al. "Launcher and Microstrip Characterization" *IEEE Trans. on Instrum. and Meas.* Vol. IM 25, NO. 4, Dec. 1976, pp. 320-323.

[46] G. Engen and C. Hoer, "Thru-Reflect-Line: An improved Technique for Calibrating the Six-Port Automatic Network Analyzer". *IEEE Trans. Microwave Theory Tech.* vol. MTT-27, No. 12, Dec. 1979, pp 987-993.

[47] M. Maury, S. March, and G. Simpson, "LRL Calibration of Vector Automatic Network Analyzers". *Microwave Journal* May 1987, pp. 387-391.

[48] G. Fillipson, "Characterization of Microstrip Fixtures, A Broad Band Model for a Microstrip Connector", National Defense Research Institute (Linkoping, Sweden), FOA Report no.C30338-E (AD/NASA no. N84-21824/7), Sept. 1983,

[49] D. Brubaker, "Measure S-parameters With the TSD Technique", *: Microwaves & RF*, Nov. 1985, pp. 97-102.

[50] M. Hines and H. Stinehelfer, "Time-Domain Oscillographic Microwave Network Analysis Using Frequency-Domain Data", *mtt* , vol. MTT-22, No.3, March 1974, pp. 276-282.

[51] H.E. Stinehelfer, "Discussion of De-embedding Techniques Using Time-Domain Analysis", *IEEE Proceedings*, Vol. 74, No. 1, Jan 1986. pp 90-94.

[52] E. K. da Silva and M. K. McPhun, "Calibration of an Automatic Network Analyser Using Transmission Lines of Unknown Characteristics Impedance Loss and Dispersion", *Radio and Elec. Engr.*, Vol. 48, No. 5, May 1978, pp. 227-234.

[53] R. Bauer, and P. Penfield, "De-embedding and Unterminating", *IEEE Trans. Microwave Theory Tech.*, Vol. MTT-22, No. 5, March 1974, pp. 310-312.

[54] D.E. Peck and D. F. Peterson,"A Measurement Method for Accurate Characterization and Modeling of MESFET Chips", *1981 IEEE MTT-S Digest*, pp. 310-312.

[55] D.E. Peck,"Measurement Methods for Accurate Microwave Characterization and Modeling of MESFET Chips", Technical Report AFWAL-TR-84-1177, January 1985.

[56] P. R. Shepherd and P. Daly, "Modeling and Measurement of Microstrip Transmission Line Structures", 1985 IEEE MTT-S Digest, pp. 679-682.

[57] R.L. Eisenhart,"A Better Microstrip Connector", *1978 IEEE MTT-S Digest*, pp. 318-320.

[58] E. Hassan "Field Solution, Polarization, and Eigenmodes of Shielded Microstrip Transmission Line", *IEEE Trans. Microwave Theory Tech.*, vol. MTT-34 No. 8, August 1986, pp845-851.

[59] E. Yamashita and K. Atsuki, "Analysis of Microstrip-Like Transmission Lines by Nonuniform Discretization of Integral Equations," *IEEE Trans. Microwave Theory Tech.*, vol. MTT-24, pp. 195-200.

[60] L. Pincherle, "Electromagnetic Waves in Metal Tubes Filled Longitudinally with Two Dielectrics,"' *Phys. Rev*, 66, No. 5, pp. 118-130, 1944.

[61] T. Weller, University of Michigan, Personal Communication March 2, 1988.

[62] Mr. Jim Schellenberg, Hughes Aircraft Company, Personal communication June 14, 1987.

[63] J. Snook, "Substrates for Hybrid Microelectronic Applications", *Microwave System News and Comm. Tech.*, February 1988, pp26-31.

[64] R. Jansen, and H. Koster, "Accurate Results on the End Effect of Single and Coupled Lines for Use in Microwave Circuit Design " *A.E.U.* Band 34 1980, pp 453-459.

[65] G.N Watson,*A Treatise on the Theory of Bessel Functions* 2nd ed., Cambridge University Press 1980, p21.